Fall 10-1-2021

Determination and Application of Hydrogen Transfer Thermochemistry: Studies of Molecules, Nanoparticles, and Metallic Electrodes

Rishi Agarwal
Yale University Graduate School of Arts and Sciences, rga.agarwal@gmail.com

Abstract

Determination and Application of Hydrogen Transfer Thermochemistry: Studies of Molecules, Nanoparticles, and Metallic Electrodes

Rishi G. Agarwal

2021

From the surface of a platinized electrode in a hydrogen fuel cell to the oxygen-evolving complex in photosystem II, the binding and transfer of hydrogen is central to many important chemical transformations in our world. The core thermochemical and kinetic concepts which connect these proton-coupled electron transfers across a continuum of compound sizes, including small molecules, nanoparticles, and bulk materials, are explored. In Chapter 1, the thermochemical basis for this thesis is presented, along with the underlying connections it enables for the study of proton-coupled electron transfer (PCET) across almost any reaction environment.

Methods for measuring the thermochemistry of hydrogen transfer in solution and at solution-solid interfaces have been critical to developing these connections. In Chapter 2, an accessible potentiometric technique for measuring molecular potentials of hydrogenation in nonaqueous and mixed media is developed. The resulting thermochemical values are then exploited in Chapter 3 to measure the hydrogen transfer thermochemistry of cerium oxide nanoparticles (nanoceria). Experiments demonstrate that reactions between colloidal nanoceria and several different molecular PCET reagents reach equilibrium states. These equilibrium states provide direct measurements of the surface O–H bond dissociation free energies of nanoceria; the first for any metal oxide nanomaterial. Furthermore, they demonstrate that, unlike molecules, nanoceria have a broad range of bond strengths to hydrogen. Together, Chapters 2 and 3 provide new methodologies for exploring hydrogen transfer thermochemistry in heterogeneous solution and surface environments.

A clear understanding of a process's thermochemistry is essential to the study of its kinetics. In Chapter 4, the rates of reactions between nanoceria at different levels of reduction and substituted picrylhydrazyl reagents are measured. These rate constants are combined with the nanoceria bond dissociation free energies measured in Chapter 3 to produce Brønsted-Evans Polanyi relationships for the hydrogen transfer reactivity of nanoceria. These relationships show a significant effect of nanoceria hydrogen coverage on the kinetics of its hydrogen transfer reactivity, with broader implications for traditional kinetic analyses of heterogeneous (electro)catalysts.

In Chapter 5, the thermodynamics and kinetics of hydrogen transfers at more industrially relevant model gold and platinum electrocatalysts are explored. Studies employ deuterium oxide solvent isotope effects as a mechanistic tool for the study of hydrogen transfer at these electrocatalytic interfaces. Although such isotope effects have previously been explored, these studies provide novel insights through the development of a novel methodology for preparing ultrapure deuterated electrolytes. The robustness of this procedure is demonstrated via voltammetry of highly sensitive single crystal facets of platinum. Product solvent isotope effects for the hydrogen evolution reaction at polycrystalline gold electrodes in perchloric acid electrolytes are then explored through studies with a homebuilt differential electrochemical mass spectrometer. Kinetic analysis demonstrates that the product solvent isotope effect for the hydrogen evolution reaction at polycrystalline gold electrodes is significantly larger than previous measures of the kinetic solvent isotope effect. This finding provides new insights into the kinetically invisible steps of the hydrogen evolution reaction on polycrystalline gold electrodes.

In this thesis, molecular concepts and techniques are applied to study the thermochemistry and mechanism of hydrogen transfer in more complex solution environments and on material surfaces. This interdisciplinary approach enables new connections between and insights into these critical processes.

Determination and Application of Hydrogen Transfer Thermochemistry: Studies of Molecules, Nanoparticles, and Metallic Electrodes

A Dissertation

Presented to the Faculty of the Graduate School

Of

Yale University

In Candidacy for the Degree of

Doctor of Philosophy

by

Rishi G. Agarwal

Dissertation Director: James M. Mayer

December 2021

Table of Contents

List of Figures

List of Schemes

List of Tables

Acknowledgments

Graduate school often feels like a solitary endeavor. Wrought iron meeting the hardened hammer of knowledge. This is for the people who brought me along a more generous and more fruitful path. To those listed and those not, I am eternally grateful.

To Jim. When I joined, I knew that I had found an advisor with whom I could have fantastic scientific debates and learn from for a long time. As I leave, I feel incredibly lucky to have found an advisor who truly prioritizes the mentorship of their students above all else. Your ability to be both a brilliant scientist and a selfless mentor is a testament to your commitment to your craft. It is a quality I admire greatly, and will continue to aspire towards as I build my own career.

To my committee. Thank you to Profs. Pat Holland and Hailiang Wang for your support and wisdom. Pat, thank you for pushing me into becoming a departmental leader and for your dedication to the health of our department.

To the Mayer group. Laboratory work is more than just the experiments you do. Thank you to members past and present for chatting with me about puzzling results, changing pump oil, and being such a fun team. A few special thanks:

Jen, you took me under your wing when I first joined and I cannot thank you enough for that. Your friendship has truly transformed my life for the better. *Julia*, you enabled the lab to be a well-oiled machine by being incredibly selfless. I admire you for that and am so thankful. *Brian*, I sometimes felt alone as the only person in my class to join the lab, but you were always there to support me and remind me to have a little fun. I will see you at a Bonchon soon. *Anna*, it is easy to lose one's self in the monotony of graduate school. Thank you for dumb conversations and carrot flavored candies, you are one of the most genuine people I know. *Catherine*, I am so glad we got to work more together in my final few years. Your steadfast commitment and humble attitude continue to be an inspiration. *Daniel,* watching your predecessors

leave is one of the hardest parts of graduate school. Thank you for being my old head buddy through a crazy last year.

To Prof. Marc Koper and his group. Thank you for being remarkably collaborative and showing me new ways to view my research. The opportunity to work with you all was truly once in a lifetime.

To the Roundbottoms. Playing with you all was an absolute joy. From seeing the joy of those who had never picked up a soccer ball to our mud-soaked makeup championship, I will cherish so many moments.

To my cohort. I cannot believe how lucky I am to have joined graduate school with such a wonderful group of misfits. Your friendship inside and outside the department was a constant source of joy. Special thanks to *Julia*, *Sam*, and *Matt* for being the best inorganic crew, and to *Zach* for being a delightful roommate.

To Ginger, Rachel, Chris, and Nick. The best part about getting into science is the people. Thank you for all the wonderful conversations, dinners, and adventures.

To my family. I am so lucky to have your love and support. *Ashwin,* thank you for being my confidant, best friend, and role model. *Mom and Dad,* thank you for teaching me how to question. *Sonia,* thank you for joining our weird little family and being a spark of joy. And *Yashna*, where to begin. You more than anyone else have helped to make graduate school the best time of my life. I love you and cannot wait for the many adventures to come.

Chapter 1

The Universality of Proton-Coupled Electron Transfer Thermochemistry

Adapted from Agarwal, R. G.; Coste, S. C.; Groff, B. D.; Heuer, A. M.; Noh, H. N.; Parada, G. P.; Wise, C. W.; Nichols, E. N.; Warren, J. J.; Mayer, J. M. "Free Energies of Proton-Coupled Electron Transfer and Their Applications." *Chem. Rev.* **2021**, https://doi.org/10.1021/acs.chemrev.1c00521. RGA and JMM wrote and created figures for the sections included below. AMH collected data shown in Appendix A. The authors thank Dr. Eric Wiedner, Dr. Aaron Appel, and Dr. Morris Bullock of Pacific Northwest National Laboratory for their insights and feedback.

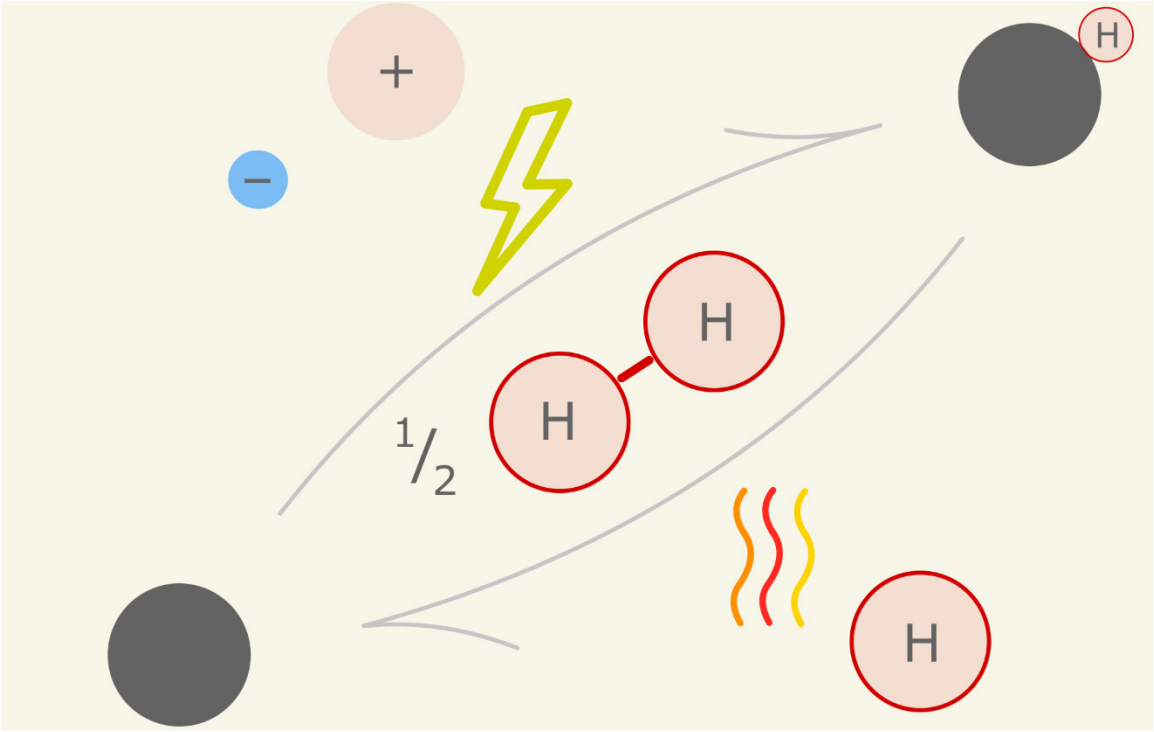

1.1 Introduction

The widespread occurrence of proton-coupled electron transfer (PCET) reactions in chemical processes has drawn broad interest from a myriad of scientific communities. PCET is involved in chemical synthesis from the bench to the industrial plant, and is common in nature, biology, materials, and chemical energy processes. This chapter describes methods for the measurement Gibbs free energies—heretofore denoted as free energies —for the transfer of hydrogen to and from a wide range of

substrates and reagents. An emphasis is placed on solution-phase reactivity, and building a shared understanding of PCET thermochemistry across the full range of molecules, materials, and reaction environments. While PCET reactions can be broadly defined as those that involve transfers of electrons and protons (ne^-/mH^+), the material covered here is restricted to reactions involving equal numbers of e^- and H^+ ($n = m$, eq 1.1). Even with these confines this is a very broad class of reactions, from the cathodic $4e^-/4H^+$ reduction of O_2 to H_2O in fuel cells (eq 1.2) to the $1e^-/1H^+$ oxidation of the tyrosine residue (eq 1.3) that facilitates water oxidation in the photosynthetic oxygen-evolving complex. It is therefore unsurprising that there have been many previous reviews of the PCET field which cover reaction chemistry,[1-3] computation and theory,[4] electrochemical aspects,[5] biochemical and biomimetic systems,[6-9] photo-initiated reactions,[10,11] organic synthesis,[12,13] hydride transfer,[14,15] and more.[16,17]

$$X + ne^- + nH^+ \rightarrow XH_n \quad (1.1)$$

$$O_2 + 4e^- + 4H^+ \rightarrow 2H_2O \quad (1.2)$$

$$TyrOH \rightarrow TyrO^\bullet + e^- + H^+ \quad (1.3)$$

The thermochemistry of PCET reagents provides the foundation for understanding their reaction chemistry. Eleven years ago, our laboratory presented the first comprehensive listings of solution thermochemical values for PCET substrates.[3] We are delighted that it has been widely used and that it seems to have influenced several burgeoning areas of chemistry, including photo-redox,[7,11,18,19] N_2 reduction,[20-23] and redox-mediated systems.[24-26]

Unfortunately, we have found several systematic mathematical errors in that review which shifted the absolute values of reported bond dissociation free energies (BDFEs). One purpose of this chapter is to correct the values in the 2010 review.[3,27] These corrections systematically decrease previously reported BDFEs by between 1.6

and 4.8 kcal mol^{-1}, depending on the solvent. We note that the differences between prior BDFE values in the same solvent are typically correct, just not the absolute values. Furthermore, the discussion provided in the previous review remains relevant and we refer the reader to those sections for further context.[3]

In summarizing what has been learned about PCET thermochemistry over the past decade and advocating for new directions, this chapter goes well beyond simply correcting values. We provide a thorough breakdown of the thermochemical cycles used (Section 1.2), which we hope provides a simplified analysis for newcomers and new insights to already expert practitioners. Furthermore, we demonstrate the experimental and theoretical advantages of using potentials of hydrogenation, denoted $E°$(V vs H_2), to describe the thermochemistry of PCET reactions. In particular, $E°$(V vs H_2) is shown to be effectively equivalent to more widely reported BDFEs in solution while also being far easier to measure directly (Section 1.2.2.2). In fact, we highlight a recently published method which enables direct measurement of $E°$(V vs H_2) for many compounds under any buffered solvent condition amenable to electrochemical analysis (Section 1.2.2.3).[28] Thermochemical cycles based on this method, and future ones like it, will be important to fulfilling the growing interest in measuring reaction thermodynamics in real systems where significant non-idealities exist (Section 1.2.3).

The increasing centrality of PCET thermochemistry over the past decade has greatly increased the quantity and standard of measurement methods and data. These advances have, in most cases, made previously used approximations unnecessary. Examples of approximations include the use of peak potentials from irreversible electrochemical couples in Bordwell's early pathbreaking studies,[29] and Abraham parameters for estimating transfer free energies between solvents.[3] The higher standard of data included in this chapter enabled a novel analysis of the solvent dependence of free energies for ne^-/nH^+ PCET half reactions (Section 1.3.1). Over a wide range of systems, both BDFEs and $E°$(V vs H_2) values are shown to be highly

insensitive to solvent identity across a wide range of molecules and solvents. Importantly, this is not the case for ne^-/nH^+ PCET potentials measured against a pure-electron transfer reference such as ferrocene. This is because the overall thermochemical equations will involve the transfer of charged species (e^- and/or H^+), if a hydrogen-based reference is not used. As a result, we advocate for the use of $H_{2(g)}$, $H^\bullet$, and the standard reversible hydrogen electrode (RHE) as reference states for both aqueous and non-aqueous thermochemistry. We hope that this transition is speeded by expanded experimental use of H_2-based reference electrodes to more easily and more accurately determine PCET thermochemistry.

The advantages of referencing PCET thermochemistry to $H_{2(g)}$ are most apparent in the connections it enables to studies in complex reaction media and related fields. We highlight the growing interest in engineering solution conditions to improve system performance, such as in the use of organic/aqueous mixtures to solubilize redox mediators for oxygen reduction,[26,30] and to perturb solvation environments for CO_2 reduction (Section 1.3.1.3).[31,32] Additionally, we provide an introduction to the many connections between PCET thermochemistry at molecules and (nano)materials (Section 1.3.2). This includes the measurement of hydrogen adsorption energies for gas/solid reactions by temperature-programmed desorption methods, as well as electrochemical and thermal studies of solid/solution interfaces. These highlights emphasize the centrality of PCET thermochemistry and the connections it enables.

1.2 Thermochemical Background

The free energy of the ne^-/nH^+ oxidation of a PCET reagent (XH_n) can be described by multiple thermochemical formalisms. The simplest case, with $n = 1$, involves the making or breaking of only one X–H bond to give $X^\bullet$ and $H^\bullet$ ($H^+ + e^-$). The "gold standard" thermochemical descriptor for such a process is the bond dissociation free energy (BDFE) of X–H (eq 1.4). When $n > 1$, the average BDFE (or free energy

per H• dissociated) has typically been the preferred value for tabulation. However, most tables of X–H bond strengths instead give bond dissociation enthalpies (BDEs). This choice is in part historical as widely reported gas-phase BDEs were easier to measure and to connect with early computational approaches. When studies of solution-phase bond strengths became more common, most tried to parallel the known gas-phase values and report BDEs. Excellent resources exist for BDEs, such as Luo's Comprehensive Handbook of Chemical Bond Energies (2007) and the iBonD Databank from Tsinghua and Nankai Universities that lists 7,600 BDEs and 35,000 pK_a values.[33,34] However, free energies are more important for reactions in solution. This is because $\Delta G°$ values determine equilibrium constants and are used in both Linear Free Energy Relations and treatments derived from Marcus theory.

$$X–H \rightarrow X^{\bullet} + H^{\bullet} \qquad \Delta G° = \text{BDFE} \qquad (1.4)$$

Another important thermochemical parameter is the free energy of hydrogenation. This extrinsic thermochemical value is more commonly cited for gas-phase reactions, and is directly related to the potential of hydrogenation, $E°$(V vs H_2), by eq 1.5. Here we report the intrinsic $E°$(V vs H_2) because it does not scale with sample size or the number of electrons transferred in a reaction, thereby making comparisons across reaction types more facile. Furthermore, we discuss the experimental advantages of measuring $E°$(V vs H_2) from an ne^-/nH^+ electrochemical potential ($E°(X/XH_n)$, eq 1.6), and practical value of reporting these potentials to describe PCET reactions (Sections 1.2.2.2, 1.2.2.3, and 1.2.3).

$$X + {}^{n}/_{2}H_{2(g)} \rightarrow XH_n \qquad \Delta G°_{\text{hydrogenation}} = -nFE°(\text{V vs } H_2) \qquad (1.5)$$

$$X + nH+ + ne^- \rightarrow XH_n \qquad E°(X/XH_n) \qquad (1.6)$$

In this section, we provide an overview of methods and thermochemical cycles used to obtain the values presented in the Tables below, with a specific emphasis on the similarities between BDFE and $E°$(V vs H_2). In all of the equations, schemes, and

tables, H_2 is always gas-phase (1 atm standard state) and all other species are solution-phase unless otherwise specified (1 M or, more precisely, at standard state[35]).

1.2.1 Traditional Methods for the Measurement of BDFEs

Relative BDFEs can be accurately determined by equilibration, and this gives absolute BDFEs when the value for one of the PCET reagents is known (eq 7). Lucarini and co-workers, for instance, used this approach to determine phenol BDFEs.[36] Similarly, Kreevoy et al. used equilibration to measure the relative hydride affinities of NAD^+ analogs (a type of heterolytic bond strength).[14,37,38]

$$X–H + Y \rightarrow X + Y–H \qquad \Delta G° = BDFE(XH) – BDFE(YH) \qquad (1.7)$$

Solution BDFEs ($BDFE_{(solv)}$) can be derived from known bond dissociation enthalpies (BDEs), but only with certain assumptions. If the BDE of X–H is known in the solution of interest, then the conversion requires the absolute entropies of XH, $X^\bullet$ and $H^\bullet$ in the solvent (eq 1.8). The thermochemistry of $H^\bullet$ solvation has been well estimated in various solvents, as discussed below, but the entropies for HX and $X^\bullet$ are almost never known experimentally. If the BDE is only known for gas-phase species, additional energies of solvation are needed to convert a $BDE_{(g)}$ to a $BDFE_{(solv)}$, which are also almost never known.

$$BDFE(XH)_{(solv)} = BDE(XH)_{(solv)} – T\mathit{S}°(H^\bullet) – T[\mathit{S}°(X^\bullet) – \mathit{S}°(XH)] \qquad (1.8)$$

In practice, the conversion of BDEs to BDFEs uses the assumption that the absolute entropies for $X^\bullet$ and XH are very similar and cancel, presumably because these species are very similar in size and polarity (eq 1.9).[39,40]

$$BDFE(XH)_{(solv)} = BDE(XH)_{(solv)} – T\mathit{S}°(H^\bullet) \qquad (1.9)$$

Bordwell, Parker, Tilset, and others have found this to be a good assumption for the organic and organometallic systems they studied.[41-44] However, there may be significant deviations when $X^\bullet$ and/or XH can engage in hydrogen bonding with the

solvent.[3,45] In addition, there can be large entropy terms when high-spin transition metal complexes are involved.[40,46] The concerns about these assumptions emphasize the need for direct measurements of free energies to describe PCET reaction thermochemistry, especially when comparing across conditions.

1.2.2 Square Scheme Approaches to BDFEs and Potentials of Hydrogenation

Many BDFEs have been determined by measuring a pK_a and a one-electron reduction potential ($E°$), in a method which essentially parses the BDFE into the free energies for electron transfer (ET) and proton transfer (PT) (eq 10).

$$\text{BDFE} = 23.06E° + 1.37\text{p}K_a + C_G \qquad (1.10)$$

This approach was first popularized by Bordwell, although he used it to derive BDEs.[41] The development of this method required the definition of an unusual free energy constant, C_G. While the use of one constant makes eq 10 elegant in its simplicity, it also buries the fact that C_G is a composite value that is challenging to measure (see below). As a result, widespread adoption of this approach has left the field with complex terminology that can confuse even well-versed practitioners. After all, this chapter is being written in part because our group made thermochemical errors when calculating C_G values a decade ago. Below we describe the traditional analysis, and then, in Section 1.2.3, we advocate for the adoption of new terminology based on potentials of hydrogenation to make this powerful new method more accessible to the research community – both intuitively and experimentally.

1.2.2.1 BDFE Analysis using C_G

Scheme 1.1. Square scheme of PCET thermochemistry.

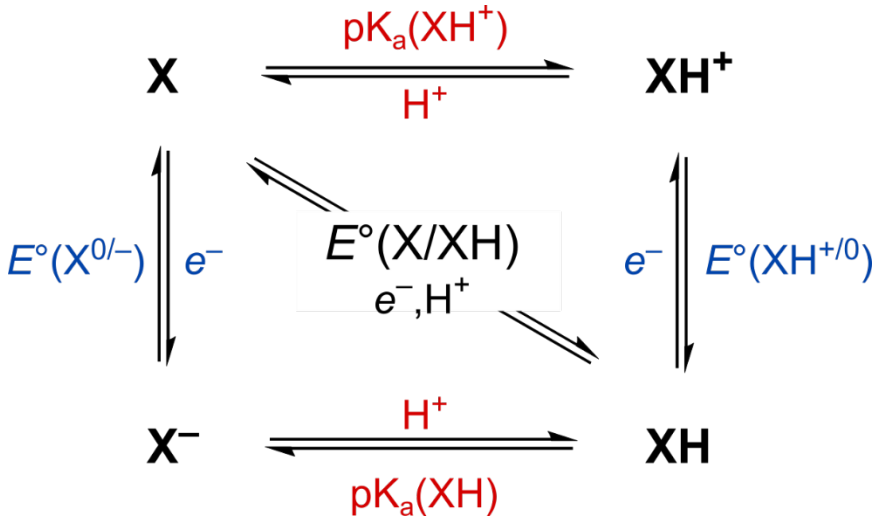

Division of the overall free energy for a solution-phase PCET process into the components for electron and proton transfer is best visualized using a square scheme (Scheme 1.1). Following this roadmap and eq 1.10, the overall free energy for the PCET process is calculable by adding together the appropriate $E°$ and pK_a values, via the bottom left (eqs 1.11 and 1.12) or top right corners. However, the resulting equation describes the transfer of e^- and H^+ (eq 1.6 where n = 1), as opposed to the desired transfer of $H^•$. This thermochemical quandary was first solved with the advent of C_G, or $E°(H^+/H^•)$, since its addition neatly converts e^- plus H^+ to $H^•$ (eq 1.13). As a result, when the C_G and the $E°(X/X^-)$ use the same reference electrode—recommended by IUPAC to be the $Cp_2Fe^{+/0}$ couple in organic solvents[47,48]—then the sum of eqs 1.11-1.13 gives the BDFE in kcal mol^{-1} (eq 1.4).

$$X^- \rightarrow X^• + e^- \qquad \Delta G° = FE°(X^•/X^-) \qquad (1.11)$$

$$XH \rightarrow X^- + H^+ \qquad \Delta G° = 1.36pK_a(XH) \qquad (1.12)$$

$$H^+ + e^- \rightarrow H^• \qquad \Delta G° = C_G = -FE°(H^+/H^•) \qquad (1.13)$$

$$X–H \rightarrow X^• + H^• \qquad \Delta G° = \text{BDFE} \qquad (1.4)$$

However, the calculation of C_G involves multiple steps.[28] The first is the determination of $E°(H^+/H_2)$ against the appropriate reference electrode (eq 1.14). Addition of this quantity switches the reference potential to $H^+/H_{2(g)}$ in the solvent of interest, and it changes the overall thermodynamic equation to describe the potential of hydrogenation (Section 1.2.2.2). Next, the well-known free energy of H_2 dissociation in the gas-phase is added (eq 1.15).[49] The last step is addition of the free energy for solvating $H^•$ in the solvent of interest (eq 1.16). The sum of eqs 1.15 and 1.16 gives $\Delta G°_f(H^•)$ (eq 1.17), which itself is of practical use and whose values are compiled for a range of solvents in Table 1.1.

$$H^+ + e^- \rightarrow {}^1/_2H_2 \qquad \Delta G° = -FE°(H^+/H_2) \qquad (1.14)$$

$${}^1/_2H_2 \rightarrow H^•_{(g)} \qquad {}^1/_2\Delta G°_{diss}(H_2) \qquad (1.15)$$

$$H^•_{(g)} \rightarrow H^•_{(solv)} \qquad \Delta G°_{solvation}(H^•) \qquad (1.16)$$

$${}^1/_2H_2 \rightarrow H^•_{(solv)} \qquad \Delta G°_f(H^•) \qquad (1.17)$$

In this paragraph we describe, for the interested reader, the nuances of properly calculating $\Delta G°_{solvation}(H^•)$. While the solvation term described by eq 1.16 is intractable to measure directly, the solvation of $H^•$ has been shown to be well-described by that of H_2.[50] Other workers have used noble gases as models for $H^•$ and recent papers have argued the merits of both of these approaches, though values derived from the two methods differ by only 1 kcal mol^{-1} at 298 K.[51-53] For simplicity and consistency, here we choose to use the H_2 assumption for all solvents. This assumption can be broadly applied, as solvation data for H_2 is available for numerous solvents.[54-56] We note that calculation of $\Delta G°_{solvation}(H^•)$ is complicated by the need to convert the standard state of $H^•$ in the solvent from the reported unit mole fraction ($\chi = 1$) to 1 molar.[28,35] A sign error in applying this conversion resulted in systematic errors for the BDFEs reported in our original publication.[27] A complete and corrected

walk-through of the underlying equations is provided in Section 5 of the Supplementary Information of our recently published work.[28]

Table 1.1. Key Thermodynamic Constants in Common Solvents.

Solvent	$TS°(H^•)^{a,b}$	$\Delta G°_f(H^•)^{a,c}$	$E°(H^+/H_2)^{d,e}$	$C_G{}^e$
Gas-phase	8.17[f]	48.59[f]	--	--
Water	2.95[56]	52.8[56]	0.00[g]	52.8[57,g]
Acetone	6.50[54]	51.9[54]	--	--
Acetonitrile (MeCN)	6.37[54]	52.0[54]	−0.028[58]	52.6[58]
Benzene	6.23[55]	52.1[55]	--	--
CCl_4	6.16[55]	51.9[55]	--	--
Chlorobenzene	5.83[55]	52.1[55]	--	--
N,*N*-dimethylacetamide (DMA)	--	--	−0.79[59]	--
N,*N*-dimethylformamide (DMF)	6.07[54]	52.3[54]	−0.662[58]	67.6[58]
Dimethylsulfoxide (DMSO)	6.16[56]	52.6[56]	−0.67[60,h]	68[h]
1,4-dioxane	6.25[54]	52.2[54]	--	--
n-hexane	6.30[54]	51.7[54]	--	--
Isopropanol (IPA)	--	--	−0.494[58]	--
Methanol (MeOH)	5.71[56]	51.9[56]	−0.501[61]	63.4
Toluene	6.10[54]	52.0[54]	--	--
Tetrahydrofuran (THF)	6.43[54]	52.0[54]	−0.343[i]	59.9

[a] Values in kcal mol^{-1} at 298 K. [b] $TS°(H^•) = T[S°(H^•_{(g)}) + \Delta S_{solv}°(H^•)]$ where H_2 data is used to approximate $H^•$ solvation, and the standard state is 1M in solution unless otherwise specified. [c] Adapted and expanded from ref [28]. [d] Potentials are in V. [e] $E°$ and C_G are vs $Cp_2Fe^{+/0}$ unless otherwise stated. [f] Values involve $H^•_{(g)}$ at 1 atm gaseous standard state from ref [49]. [g] Value referenced to SHE. [h] $E°(H^+/H_2)$ in DMSO was determined from the $E_{1/2}$ of a quasi-reversible wave and therefore both it and the corresponding C_G are not reported to the same level of accuracy as other values in this table. [i] Value is an average of those presented in refs [28,62,63] with corrections for $TS°(H^•)$ where necessary.[64] Standard state is defined by an absolute pK_a scale.[65]

1.2.2.2 Potential of Hydrogenation

As shown in the section above, determination of the C_G term needed to measure BDFEs is complex and inaccessible to the beginning practitioner. Below, we introduce a more experimentally accessible, and equally robust, thermochemical value that one necessarily calculates in the process of determining a BDFE. The addition of eqs 1.11, 1.12, and 1.14 (Scheme 1.2) gives the potential of hydrogenation, or $E°$(V vs H_2).In this Scheme, the sum of eqs 1.11 and 1.12 gives an electrochemical potential,

$E°$(X/XH, vs $Cp_2Fe^{+/0}$), and eq 1.14 changes the reference state to $E°(H^+/H_2)$. The resulting term, $E°$(V vs H_2), is quite universal as it is equivalent to an electrochemical potential and directly related to the free energy of hydrogenation via, eq 1.5.

Similar to a BDFE, $E°$(V vs H_2) describes a full reaction without charged species. In this case, the two half reactions are described by $E°$(X/XH, vs $Cp_2Fe^{+/0}$) and $E°(H^+/H_2$, vs $Cp_2Fe^{+/0})$ so that the overall reaction describes the addition of $H_{2(g)}$. While we could describe the potential of hydrogenation as a half-reaction versus an electrochemical reference, we believe that this characterization would cloud the universality of the value described above. As a result, we choose to use the abbreviation $E°$(V vs H_2), which specifies the reference state as $H_{2(g)}$. Values of $E°$(V vs H_2) are also easily compared with BDFEs, as they only differ by $\Delta G°_f(H^\bullet)$ in the solvent of interest (eq 1.18). Values of $\Delta G°_f(H^\bullet)$ are 52.2 ± 0.6 across a wide range of solvents, aqueous or non-aqueous, protic or aprotic (Table 1.1). As a result, solution-phase values of $E°$(V vs H_2) and BDFE are effectively equivalent. In the following paragraphs (and in Sections 1.2.2.3 and 1.2.3), we discuss the practical aspects of measuring $E°$(V vs H_2) as well as the experimental and theoretical advantages.

Scheme 1.2. Calculation of $E°$(V vs H_2) from the 1e^- reduction potential and pK_a.

$$X + e^- \xrightarrow{E° \text{ vs. } Cp_2Fe^{+/0}} X^- \qquad (1.11)$$

$$X^- + H^+ \xrightarrow{0.0592[pK_a(XH)]} XH \qquad (1.12)$$

$$^1/_2H_2 \xrightarrow{-E° \text{ vs. } Cp_2Fe^{+/0}} H^+ + e^- \qquad (1.14)$$

$$X + {}^1/_2H_2 \xrightarrow{E°(\text{V vs } H_2)} XH \qquad (1.5)$$

$$\text{BDFE}(X–H) = 23.06E°(\text{V vs } H_2) + \Delta G°_f(H^\bullet) \qquad (1.18)$$

$E°$(V vs H_2) is referenced against the standard H^+/H_2 potential or $E°(H^+/H_2)$ — the third line in Scheme 1.2 (eq 1.14). In aqueous electrochemistry, this is commonly

denoted as the Standard Hydrogen Electrode or SHE, and denotes the standard potential for proton reduction in a theoretical ideal solution where the activity of protons is one and the pressure of $H_{2(g)}$ is 1 atm. While a close approximation to this value can be measured in aqueous solvents using a clean Pt wire, determination of SHE in non-aqueous solvents has only become readily available since the advent of a new open-circuit potential (OCP) method by Roberts and Bullock (Figure 1.1) ,who also successfully used a clean Pt wire.[66] As compared to aqueous solutions, proton transfer under non-aqueous conditions is significantly slowed, and preparation of electrolytes where the proton activity is unity is often not possible. As a result, the new OCP method needed to be performed under non-standard proton activities and extrapolated to standard state. The robustness of this extrapolation was proved by the authors, who demonstrated a Nernstian shift of the OCP with changes in buffer pK_a.[66] This is therefore a robust methodology for measuring the non-aqueous equivalent of SHE (or $E°(H^+/H_2)$) in any solvent suitable for electrochemistry where the pK_a scale is known. We note that the generality of this method is limited by the assumption that Pt should be able bind hydrogen at SHE in any solvent. This point has not been proven, but we would expect it to be true in the absence of strong solvent adsorption to the Pt surface. This is because of the relative solvent independence of PCET reactions (Section 1.3.1), and our current understanding that PCET thermochemistry at material interfaces shares many of the same features as that for molecules (Section 1.3.2).

We refer readers to the original article for full details of the method,[66] but in brief, the OCP of a clean platinum wire electrode is measured in a buffered electrolyte solution in the presence of 1 atm H_2. This is a direct measurement of the reduction potential of the acid component of the buffer (eq 1.19), and is termed $E°'(HA/H_2)$ with the prime (') indicating that it is specific to the buffer used (eq 1.20). The sum of eqs 1.19 and 1.20 give $E°(H^+/H_2)$ for that solvent (eq 1.14), with H^+ and H_2 at their standard states (hence SHE).

$$HA + e^- \rightarrow {}^1/_2H_2 + A^- \qquad E°'(HA/H_2) \text{ or } E°_{RHE} \qquad (1.19)$$

$$A^- + H^+ \rightarrow HA \qquad -pK_a(HA) \qquad (1.20)$$

Equation 1.19 is equivalent to a Reversible Hydrogen Electrode reference state (RHE). RHE is commonly used in aqueous PCET electrochemistry and electrocatalysis as both a physical reference electrode and a theoretical reference state. In RHE electrodes the potential is measured with a clean Pt wire in electrolyte sparged with 1 atm H_2, but unlike SHE, the standard state for proton activity is set (or measured) as that of the electrolyte. This means that changes in pH (aqueous solutions) or buffer pK_a (organic solutions) do not shift $E°_{RHE}$ from zero, making the reference state independent of proton activity. The great value of this reference state is emphasized in the next sections.

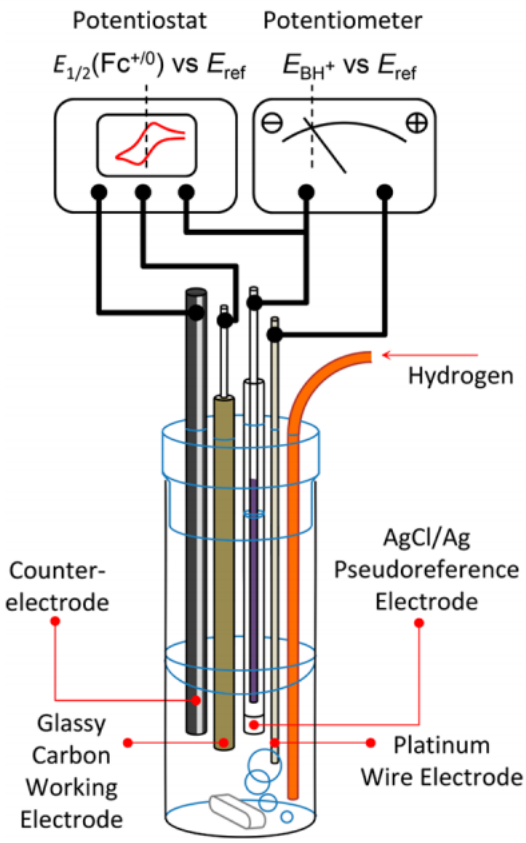

Figure 1.1. Roberts and Bullock's schematic of the four-electrode cell configuration used for H_2 open circuit potential (OCP) measurements. The analyte solution consists of an acid:base:H_2 mixture of known composition. The Ag/AgCl pseudoreference is calibrated to $Cp_2Fe^{+/0}$ after determination of the OCP. Potentiostat and potentiometer are shown as separate devices to illustrate the principle of the measurement. Reprinted with permission from ref [66]. Copyright 2013 American Chemical Society.

1.2.2.3 Direct Electrochemical Measurements of PCET Thermochemistry

Direct electrochemical measurements of reversible PCET processes are often possible in aqueous solutions. Under acidic, basic, or buffered conditions, proton transfer in water is often sufficiently rapid that reversible electrochemical responses are observed for PCET redox couples such as quinone + $2e^-$ + $2H^+$ → hydroquinone.[67] The resulting values of $E°(X/XH_n)$ are PCET potentials, similar to eq 1.6, measured under various conditions and corrected to standard states and aqueous SHE.

Our laboratory has recently developed a direct electrochemical measurement of $E°'(X/XH_n)$ in organic and mixed solutions using an OCP method similar to that of

Roberts and Bullock's for $E°'(HA/H_2)$.[28] This is a significant advance as cyclic voltammograms (CVs) of PCET couples are almost always irreversible in non-aqueous solvents due to the slower proton transfer rates. As a result, $E_{1/2}$ values determined from these voltammograms do not provide accurate measures of the underlying PCET thermochemistry.[28,68] OCP measurements have a longer timescale than CV, allowing more time for protons and other nuclei to equilibrate. The strategy of using OCP measurements, or redox potentiometry, to evaluate the thermodynamics of sluggish electroreductions has previously been explored in biochemical systems, as well as towards the measurement of molecular hydricities and nanoparticle fermi levels.[69-71] More details on the method and its development are provided in Chapter 2.

$$X + ne^- + nHA \rightarrow XH_n + nA^- \qquad E°'(X/XH_n \text{ vs } Cp_2Fe^{+/0}) \qquad (1.21)$$

$$nHA + ne^- \rightarrow {}^{n}/_{2}H_2 + nA^- \qquad E°_{RHE} \qquad (1.22)$$

The PCET electrochemical potential derived from OCP measurements (eq 1.21) can be combined with the measurement of $E°_{RHE}$ (eq 1.22) to give $E°(V \text{ vs } H_2)$ (Scheme 1.3). This addition requires that the two measurements be made using the same solvent, buffer and electrolyte, and then the contributions of the buffer cancel. The resulting reaction, at the bottom of Scheme 1.3, and shown earlier as eq 1.5, is simply the potential of hydrogenation of X to XH_n. This reaction is, therefore, independent of the buffer or ferrocene reference. The advantages of this approach are described in the following section.

Scheme 1.3. Calculation of $E°$(V vs H_2) directly from $E°'$(X/XH_n).

$$X + nHA + ne^- \xrightarrow{E°' \text{ vs } Cp_2Fe^{+/0}} XH_n + nA^- \quad (1.21)$$

$$^n/_2H_2 + nA^- \xrightarrow{-E°' \text{ vs } Cp_2Fe^{+/0}} nHA + ne^- \quad (1.22)$$

$$X + {}^n/_2H_2 \xrightarrow{E°(\text{V vs } H_2)} XH_n \quad (1.5)$$

Scheme 1.3 is *thermochemically* equivalent to the route to $E°$(V vs H_2) in Scheme 1.2 using pK_a and $E°$. However, these two methods are not *experimentally* equivalent because one OCP potential takes the place of two separate pK_a and $E°$ measurements, eqs 1.11 and 1.12. The pK_a(XH) and $E°(X/X^-)$ are often measured under different conditions from each other and from $E°(H^+/H_2)$, introducing potential systematic errors in the analysis. In particular, ion-pairing with the electrolyte and homoconjugation of the buffer acid and base can shift the proton activity in organic solvents significantly from that predicted from ideal pK_a measurements. In our experience, the OCP approach outlined in Scheme 1.3 is the most accurate measurement of PCET thermochemistry when experimentally accessible.

1.2.3 Advantages of Potentials of Hydrogenation

As discussed above, values of $E°$(V vs H_2) are experimentally accessible, they are equivalent to proton-coupled electrochemical potentials, $E°$(X/XH_n, vs H^+/H_2), and they are directly related to free energies of hydrogenation. However, potentials of hydrogenation are not commonly reported, especially for reactions in non-aqueous environments.[28] Instead, common practice for electrochemists is to report proton-coupled potentials vs $Cp_2Fe^{+/0}$, and common practice for thermochemists is to report BDFEs (or BDEs). Below we demonstrate the advantages of instead reporting $E°$(V vs H_2), and discuss how this suggested new paradigm promotes connections between the thermal and electrochemical communities.

Reporting of proton-coupled potentials as $E°$(V vs H_2) has significant advantages over potentials versus ferrocene or other electron-only references.

Because electrochemical PCET involves the transfer of both protons and electrons, the proton activity of solution affects the measured potential. While a pure electron reference does not move with proton activity, use of $E°_{RHE}$ does. As shown in Scheme 1.2 and Scheme 1.3, this removes all charged species from the overall reaction. Thus, the $E°$(V vs H_2) for an ne^-/nH^+ couple is independent of changes in the proton activity of the solvent. This independence leads to $E°$(V vs H_2) to have very similar values in a range of solvent conditions (Section 1.3.1). The solvent independence is furthered by the use of the same $H_{2(g)}$ reference for all measurements.

Reporting of $E°$(V vs H_2) instead of BDFEs allows for a direct comparison with a large database of electrochemical values without any conversions. While $E°$(V vs H_2) values are perhaps not as conceptually simple as BDFEs (eqs 1.4 and 1.5), they require one less step to calculate. $E°$(V vs H_2) is converted to a BDFE (or an average BDFE) by addition of $\Delta G°_f(H^•)$, eq 1.18. This free energy has been reported in many but not all solvents (e.g., not in DMA, MeOH, and IPA (Table 1.1)). Still, $\Delta G°_f(H^•)$ varies little with solvent and, if necessary, can be well estimated by averaging values for similar solvents.

The advantages of this approach are particularly evident for studies in mixed solvents. Thermochemical measurements of PCET reactivity have traditionally been inaccessible in mixed solvents due to the lack of established pK_a scales. In fact, this is a barrier to applying a square scheme approach (Section 1.2.2) even in many pure solvents, as pK_a scales are not ubiquitous and reagent instability can make measurements challenging. However, both issues can be solved by measuring $E°$(V vs H_2) via Scheme 1.3, as this method removes the need to measure a pK_a. In Scheme 1.3, pK_a measurement is effectively replaced by the OCP measurement of $E°_{RHE}$ which is readily accessible by experiment in any medium that is amenable to electrochemical analysis, Figure 1.1.[28,59,66,72-75]

The approach in Scheme 1.3 should be broadly applicable to PCET reagents with O–H and N–H bonds in almost any polar medium.[28] Currently, the generality of this scheme is limited by the OCP method for determining $E°'(X/XH_n)$, eq 1.21. In our experience, the method will not be successful if there is no Faradaic response for the X/XH_n couple in the solution window for voltammetry. This is consistent with the understanding that electrochemical equilibria can only be reached if electrode kinetics are sufficiently fast to enable current flow.[76] We therefore suspect that electrode kinetics are the main barrier to measuring $E°'(X/XH_n)$ for PCET reactions that involve C–H bonds by the OCP method.[28] Nevertheless, the promise of this methodology is significant as it greatly increases access to the direct measurement of $E°$(V vs H_2) using widely available electrochemical setups. Furthermore, the measurement of $E°'(X/XH_n)$, where $n > 1$, is also made simple by this method as a single measurement replaces the alternative of $2n$ free energies measurements required by a square scheme approach. This new method has enabled a broad analysis of the solvent dependence of BDFEs and $E°$(V vs H_2) values (Section 1.3.1).

Values of $E°$(V vs H_2) have the additional advantage that they are readily compared to other free energies of hydrogen addition (eq 1.5), in solution or in the gas-phase. In aqueous solution, tabulated electrochemical potentials vs RHE are equivalent to $E°$(V vs H_2). There is also a long history of tabulating energies of gas-phase hydrogen addition to both molecules and materials (see Section 1.3.2). BDFEs can also be compared to gas-phase measurements, although the overall reaction is slightly different and a correction of ~4 kcal mol^{-1} must be applied to account for the free energy of solvation for $H^•$, Table 1.1. For both $E°$(V vs H_2) and BDFE, practical comparison of solution- and gas-phase values requires the assumption that the solvation of X and XH_n are very similar. This assumption is discussed in Section 1.3.1.1 below.

Overall, potentials of hydrogenation have the unique advantage of being universal. When solution-phase potentials are reported in this way they are not only solvent-independent, but become comparable to a broad base of previously reported thermochemical values. While we hope that $E°$(V vs H_2) values will be widely adopted, we recognize that a new term brings the potential of further convoluting the literature. As a result, we have striven to clearly define the relationships between $E°$(V vs H_2) and more established thermochemical values, such as BDFEs. We anticipate that using $E°$(V vs H_2) instead of BDFEs will facilitate communication between different fields and will spur development of the PCET field in multiple directions, such as those highlighted in the various parts of Section 1.3.

1.3 Insights and Emerging Areas of PCET Thermochemistry

In the above sections we have described the central tenets of PCET thermochemistry which underly all reactions. While these principles apply well to standard molecular systems, alternative solvent environments and materials systems represent frontiers where exploration is still needed. Here, we highlight the pioneering work that has already been done in these areas and suggest future directions.

1.3.1 Reactivity in Different Media

1.3.1.1 Solvent Dependence

In Table 1.2, we compile all reported substrates for which BDFEs and $E°$(V vs H_2) values are known in three or more solvents. When generating this list of compounds, all values from our previous review were double-checked to ensure that they met the more stringent criteria for inclusion used herein. Before application of this procedure there were many compounds whose BDFEs seemed to have a significant solvent dependence, but afterwards there was only one: 4-oxo-1-hydroxy-2,2,6,6-tetramethyl-piperidine (4-oxo-TEMPOH). The outlier BDFE for 4-oxo-TEMPOH was 61.2 kcal mol^{-1} in hexane, which was initially consistent with the intuition that a substrate

with polar substituents might show a solvent effect between MeCN and hexane. Nevertheless, we decided to double-check this value experimentally by performing an equilibration between TEMPOH (whose BDFE is reported as 63.4 kcal mol^{-1} in hexane) and 4-oxo-TEMPO. Interestingly, we find that the K_{eq} for this reaction is 3.9 ± 2.0, suggesting that 4-oxo-TEMPOH is less reducing than TEMPOH and should therefore have a higher BDFE (Appendix A). In fact, use of the corrected BDFE removes the effect of solvent on BDFE such that the average value for 4-oxo-TEMPOH across hexane, CCl_4, and MeCN is 65.6 ± 1.4 kcal mol^{-1}. With this correction in mind, for all substrates we know where data is available in three or more solvents, BDFEs are independent of solvent. This is a remarkable result because $E°$ and pK_a values often vary substantially with solvent, and yet the averages of BDFEs and $E°$(V vs H_2) values across a range of solvents have uncertainties similar to those of the individual values.

Table 1.2. Solvent dependence of PCET thermochemistry.[a]

Molecule	# of solvents	Avg. $E°$(V vs H_2)	Avg. $-\Delta G°/n$[b]	$\Delta\varepsilon$[c]
TEMPOH	4	0.558 ± 0.048	65.0 ± 1.3	34.8
4-oxo-TEMPOH[d]	3	0.595 ± 0.053	64.6 ± 1.4	34.8
2,4,6-^{t}Bu$_3$PhOH	6	1.003 ± 0.028	75.4 ± 0.8	77.9
4-MeO-2,6-^{t}Bu$_2$PhOH	3	0.864 ± 0.025	72.0 ± 0.6	34.4
1,4-hydroquinone	3	0.656 ± 0.011	67.4 ± 0.2	72.6
2,6-dimethyl-1,4-hydroquinone	5	0.560 ± 0.012	65.1 ± 0.4	72.6
$O_2 + 2H_2 \rightarrow 2H_2O$	4	1.242 ± 0.013	81.0 ± 0.4[e]	43.5
DPPH-H	3	0.929 ± 0.012	73.5 ± 0.4	34.4
$CO_{2(g)} + H_{2(g)} \rightarrow CO_{(g)} + H_2O$	4	−0.091 ± 0.016	50.3 ± 0.4	43.5
$CO_{2(g)} + 4H_{2(g)} \rightarrow CH_{4(g)} + 2H_2O$	3	0.176 ± 0.007	56.4 ± 0.3	43.5

[a] Averages and standard deviations were calculated for each molecule based on values for different solvent conditions listed in ref [77]. Values for $E°$(V vs H_2) are in V; $-eE°$ is the average free energy for $\frac{1}{2}H_{2(g)}$ addition. [b] These are averages of the average free energies to remove H• from the substrate. $-\Delta G°/n$ denotes the average free energy of PCET oxidation and is comparable to a BDFE. [c] Range of solvent dielectric constants for the values being averaged, with ε's taken from ref [78]. [d] Value in hexane redetermined by equilibration with TEMPOH. See Appendix A for full details. [e] Three solvents used to calculate the avg. of $-\Delta G°/n$.

The explanation of the solvent constancy or medium independence of ne^-/nH^+ transfer reactions can be described by a new square scheme (Scheme 1.4). The top and bottom of the Scheme are the equations for the BDFE of X–H, differing only in the solvent (S vs S′). The difference between the BDFEs in the two solvents is the difference in the transfer free energies of dissolved reagents.[72] The free energy of solvation ($\Delta G°_{solv}$) for H• is essentially constant across all solvents (Table 1.1), so all differences in BDFEs between solvents can be attributed to $\Delta G°_{solv}(XH) - \Delta G°_{solv}(X•)$. Both XH and X• are of similar size and polarity, differing only by one H-atom, so it is not surprising that these terms are usually similar and effectively cancel one another. One might expect significant differences because XH and X• have different capacities for hydrogen bonding, depending on the solvent, but this is not evident in the data. Even 1,4-hydroquinones, which are expected to have significantly different hydrogen

bonding characteristics as compared to their corresponding quinones, show very small solvent dependencies between protic and aprotic/H-bond accepting media (Table 1.2).

Scheme 1.4. Thermochemistry of BDFE medium dependence.

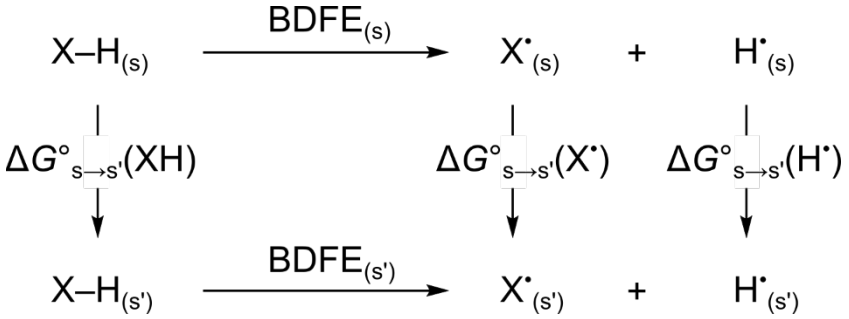

1.3.1.2 Phase Dependence

A scheme similar to Scheme 1.4 can be used to compare gas- and solution-phase X–H BDFEs and $E°$(V vs H_2) values. If the solvation of X• and XH cancel (including the entropy term for the change in standard state from 1 atm to 1 M for both reagents), the only difference between the solution- and gas-phase BDFEs is the $\Delta\Delta G°_f(H^•)$, which is 3-4 kcal mol^{-1} across many solvents (Table 1.1). Furthermore, under these assumptions there is no expected difference between values of $E°$(V vs H_2) across the solution- and gas-phase. In Table 1.3, we compare aqueous and gas-phase potentials of hydrogenation, as the difference between the two values describes whether X or XH_n is more favorably solubilized. For three simple alkyl and phenyl thiols there is no significant phase dependence of the potential of hydrogenation of RS• ($\Delta E°$(V vs H_2) = $E°_{(aq)} - E°_{(g)}$ = 0.01 ± 0.06 V), thereby demonstrating that the free energies of solvation of RSH and RS• are very similar. However, for three alkyl hydroperoxides $\Delta E°$(V vs H_2) = 0.32 ± 0.09 V. This indicates significantly more favorable solvation of ROOH versus ROO•. While it makes sense for ROOH to be preferentially stabilized by being a hydrogen bond donor, this effect is often small as evidenced by the phase independent PCET thermochemistry of PhOH and other hydrogen-bonding compounds. In general, a slight preferential solvation of XH_n over

X does seem to be common, although this trend shifts in a few rare cases including the reduction of H_2O_2 to $2H_2O$ and that of $Ph_2N^{\bullet} \rightarrow Ph_2NH$.

Table 1.3. Phase dependence of PCET thermochemistry.[a]

Reaction	$E°$(V vs H_2)$_{(g)}$	$E°$(V vs H_2)$_{(aq)}$	$\Delta E°$(V vs H_2)[b]
$PhO^{\bullet}/PhOH$	1.353	1.382	0.029
$HO^{\bullet}/HO–H$	2.690	2.730	0.040
$O/HO^{\bullet}$	1.997	2.134	0.137
$O^{\bullet-}/HO^{-}$	2.317	2.609	0.292
$HO_2^{\bullet}/H_2O_2$	1.242	1.46	0.218
$H_2O_2/2H_2O$	1.823	1.763	–0.06
$ROO^{\bullet}/ROOH$[c]	1.25(8)	1.57(9)	0.32(9)
$HN^{\bullet}NH–H/H_2NNH$-H	1.04	1.12	0.08
$PhNH^{\bullet}/PhNH_2$	1.428	1.437	0.009
4-$MePhNH^{\bullet}$/4-$MePhNH_2$	1.333	1.423	0.09
4-$CF_3PhNH^{\bullet}$/4-CF_3PhNH_2	1.389	1.564	0.175
$Ph_2N^{\bullet}/Ph_2NH$	1.320	1.225	–0.095
$HS^{\bullet}/HS–H$	1.49	1.56	0.07
$RS^{\bullet}/RS–H$[d]	1.33(1)	1.35(1)	0.02(1)
$PhS^{\bullet}/PhS–H$	1.16	1.08	–0.08
$O_{2(g)} + 2H_{2(g)} \rightarrow 2H_2O$	1.185	1.229	0.044
$O_{2(g)} + H_{2(g)} \rightarrow H_2O_2$	0.546	0.695	0.149
$O_{2(g)}/^{\bullet}OOH$	–0.15	–0.07	0.08
$CO_{2(g)} + H_{2(g)} \rightarrow HCOOH$	–0.225	–0.114	0.111
$CO_{2(g)} + H_{2(g)} \rightarrow CO_{(g)} + H_2O$	–0.148	–0.104	0.044
$CO_{2(g)} + 4H_{2(g)} \rightarrow CH_{4(g)} + 2H_2O$	0.145	0.169	0.024
$N_{2(g)} + 3H_{2(g)} \rightarrow 2NH_3$	0.057	0.092	0.035

[a] All values are from thermochemical tables in ref [77]. Values above the dotted line represent those where there is no phase change when converting from products to reactants for both the gas-phase and aqueous measurement, whereas that is not true for values below the line. This distinction is important as free energy contributions from changing standard state contribute to the phase dependence of values below the dotted line (see text). [b] $\Delta E°(V \text{ vs } H_2) = E°(V \text{ vs } H_2)_{(aq)} - E°(V \text{ vs } H_2)_{(g)}$. [c] Average of values for R = CH_3-, CH_3CH_2-, and $(CH_3)_3C$-. [d] Average of values for R = CH_3- and CH_3CH_2-.

Analyzing the phase dependences of reactions that involve more than X–H bond cleavages should be done with caution. For instance, the conversion of $N_{2(g)}$ + $3H_{2(g)}$ to $2NH_3$ involves the solvation of NH_3 and also the entropy term for the two ammonia molecules converting from 1 atm to 1 M standard state. Nevertheless, the potentials of hydrogenation for N_2 to NH_3 are roughly independent of phase. Similarly, the $\Delta E°$(V vs H_2) is <50 mV for several other complex reactions including the reduction of O_2 to H_2O, and the hydrogenations of CO_2 to both CO and CH_4.

These observations of phase-independent $E°$(V vs H_2) are not nearly as robust as the solvent-independence described in Table 1.2. Nevertheless, they demonstrate that in many cases the effect phase on PCET thermochemistry is minimal. Further study will be required to more clearly predict which compounds should be expected to demonstrate phase-dependent potentials of hydrogenation.

1.3.1.3 Mixed Solvent Systems

Non-traditional solvent systems, including mixed solvents and those without established pK_a scales, have been shown to be valuable for a variety of applications involving PCET reactivity. Investigators have employed various media to tune reagent activity, control reagent solubility, and separate reagents, in efforts to increase the selectivity and efficiency of their systems. The optimal medium for catalyzing PCET reactions must, amongst other properties, adequately solubilize the substrate and catalyst while maintaining a rapid rate of proton transfer. Organic solvents often excel at the former requirement, while aqueous solutions excel at the latter. In order to get the "best of both worlds", some authors have investigated the efficacy of mixed solvent systems. Below we discuss several examples and consider the challenges that PCET in mixed solvent systems poses to thermochemical measurements.

One example comes from the work of O'Hagan and co-workers who demonstrated that changes in the reaction medium—ionic liquids with varying mole fractions of H_2O—could engender faster rates of electrocatalytic hydrogen production

without increasing the overpotential.[74,75,79] A key to these studies was accurate measurements of overpotential and therefore of $E°'(H^+/H_2)$ in various solvents (Figure 1.2A), following the procedure of Roberts and Bullock discussed above.[66] With increasing water content, overpotentials remained relatively constant while catalytic currents increased by nearly two orders of magnitude. The rate increase correlated with the proton diffusion coefficient measured using pulsed-field-gradient NMR (Figure 1.2B).[75] Beyond changing water content, the rates were 3-5 orders of magnitude higher in the ionic liquid/water mixtures than in MeCN:H_2O mixtures. This effect was found to be related to the rate of boat/chair catalyst isomerization based on further studies which varied the chain length of substituents on the outskirts of the catalyst (Figure 1.2C,D).[79] Later work interrogated the melding of these effects with that of solvent viscosity, to design a state-of-the-art molecular electrocatalyst for hydrogen production.[80] These studies demonstrate that solvent engineering can play a valuable role in the development of advanced electrocatalysts for PCET processes.

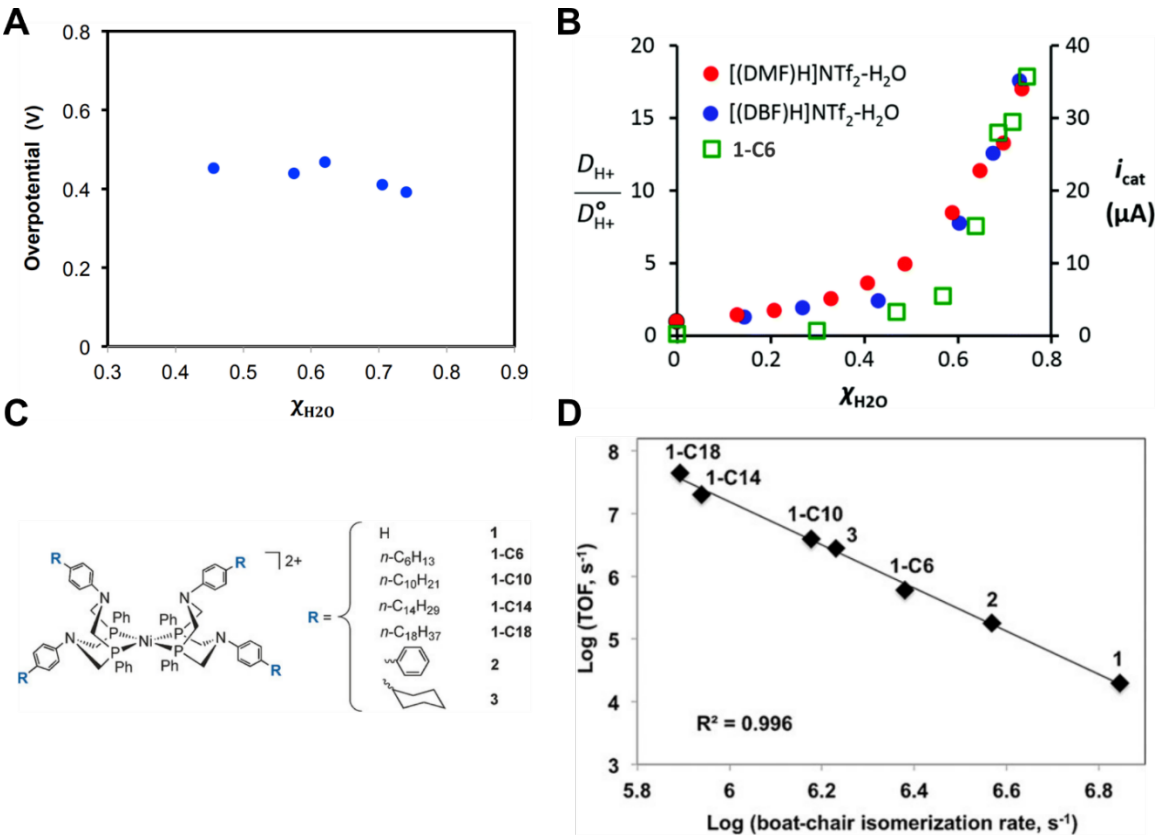

Figure 1.2. (A) Dependence of reaction overpotential on the mole fraction of H_2O in a [(DMF)H]NTf_2-H_2O ionic liquid, where overpotential is the difference between $E_{cat/2}$ and $E(H^+/H_2)$ under the reaction conditions. (B) The dependences of proton diffusion constant for two different ionic liquids (red or blue dots) and of catalytic current for 1-C6 in [(DBF)H]NTf_2-H_2O (green squares) on the mole fraction of H_2O. (C) Structures of the Nickel-catalysts used and their R-groups of varying steric bulk. (D) Relationship between the logarithms of boat-chair isomerization rate and turnover frequency. (A) and (B) are reprinted with permission from ref [75]. Copyright 2014 Royal Society of Chemistry. (C) and (D) are reprinted (adapted) with permission from ref [79]. Copyright 2016 WILEY.

Mixed-solvent systems and tailored microenvironments are of increasing interest. One high-profile study of CO_2 electroreduction with cationic iron porphyrins reported remarkable rates in DMF "in the presence of 3 M phenol".[81] This is roughly ¾ DMF and ¼ phenol in mole fraction. The authors estimated the standard potential for CO_2 to CO using the Henry's law constant for CO_2 and the pK_a of carbonic acid in pure DMF. Measurement of $E°'(H^+/H_2)$ in the CO_2-saturated, 0.1 M H_2O, mixed DMF/phenol solvent would allow for a more direct comparison of the catalytic response with the essentially solvent-independent $E°(CO_2/CO$ vs $H_2)$ (Table 1.3). These are important

considerations for reporting catalyst metrics that are comparable across conditions. Other recent work has used acetonitrile with ≥5M water (4/1 mole fraction MeCN/H_2O) for the electrochemical oxidations of cyclohexene and cyclic ketones.[82,83] As shown by the elegant O'Hagan studies above, OCP measurements of $E°(H^+/H_2)$ in such mixed solvent systems enables the determination of thermochemical parameters and comparisons with potentials of hydrogenation, since those are almost solvent-independent. We encourage researchers to use this approach, which offers simple access to accurate overpotentials, and enables quantitative analysis of effects of solvent identity on catalyst performance. Although the potentials are relatively insensitive to solvent identity (Table 1.2), rate constants may vary significantly. We also note that the overpotential for electrocatalysis can be different in the reaction-diffusion layer from that referenced to the bulk solution if the local environment at the electrode surface differs from the bulk solution.

More complex media with multiple liquid phases or regions are also of increasing importance. For example, a recent U.S. Department of Energy Basic Energy Sciences report recently identified the control of these "microenvironments" as a Priority Research Objective in solar fuels research.[84] One recent study used a two-phase 1-hexanol/water mixture to electrochemically generate hydrogen peroxide, with the 2,7-disulfonylanthraquinone electrocatalyst migrating between the aqueous and organic layers.[26] Selective electrochemical conversion of methane and O_2 to methanol under ambient conditions was enabled by a silicon nanowire electrode that created separate anoxic and oxic environments near the electrode interface.[85] In general, these studies and many related ones have not focused so much on the PCET thermochemistry, though it can play a key role.

1.3.2 Material Interfaces

An important emerging area in PCET thermochemistry is the measurement of hydrogen binding energies at solution/material interfaces. These may involve surface

X–H bonds, intercalation of H into the bulk, and perhaps cases in between. For hydrogen on surfaces, the main topic of the discussion below, the free energy of adsorption is commonly defined as the free energy of ½H_2 or H• addition. These values are equivalent to $E°$(V vs H_2) and BDFE, respectively.

Hydrogen is ubiquitous in and on materials. Intercalation of H into metals is known to cause embrittlement and other changes in properties.[86] Hydrogen ($H^+ + e^-$) is also an impurity in many semiconductor materials and is a common *n*-dopant in metal oxides.[87-89] Supercapacitance, for instance with RuO_2, is usually ascribed to surface and near-surface H binding.[90-93] Transfers of hydrogen are central in many areas of heterogeneous catalysis and electrocatalysis, from hydrogenations of organic molecules to the hydrogen evolution reaction. Such processes are often analyzed using "scaling-relationship" and "volcano plot" approaches that frequently utilize the hydrogen adsorption free energy (equivalent to $E°$(V vs H_2)) as a thermochemical predictor.[94-99] Given all of these applications, understanding the thermochemistry of H_2 adsorption on materials is, and will be, an important topic.

The thermochemistry of gas-phase H_2 addition to clean metal surfaces has been extensively examined by the surface science community. Studies using well-defined single crystals, epitaxially grown substrates, and nanoparticles under high-vacuum conditions have enabled measurements of surface–H bond enthalpies, with some measurements of free energies.[100-102] The PCET thermochemistry of noble or less active metals can also be amenable to study in solution using electrochemical techniques (Section 1.3.2.1). For other materials, however, experimental measurements of hydrogen adsorption energies at solution interfaces have largely been inaccessible. Instead, these materials have been examined primarily by computations, usually assuming ideal stoichiometries and crystalline structures.[95-97,103,104]

This section shows how the thermochemical approaches developed in Section 1.2 can be adapted to measure PCET energies for material interfaces. An excellent introduction to these connections was recently presented by Jackson and co-workers in Figure 1.3, as part of their studies of well-defined active sites on graphitic carbon electrodes (Section 1.3.2.3, Figure 1.3b).[105] The close relationship between BDFEs and $E°$(V vs H_2) emphasized above (eq 1.18) provides a close connection between the molecular picture (Figure 1.3a) and interfacial electrochemistry such as proton and electron addition to platinum (Figure 1.3c). The selected experimental studies described below illustrate these analogies, and reveal important differences between the PCET thermochemistry of molecular systems and that of material interfaces.

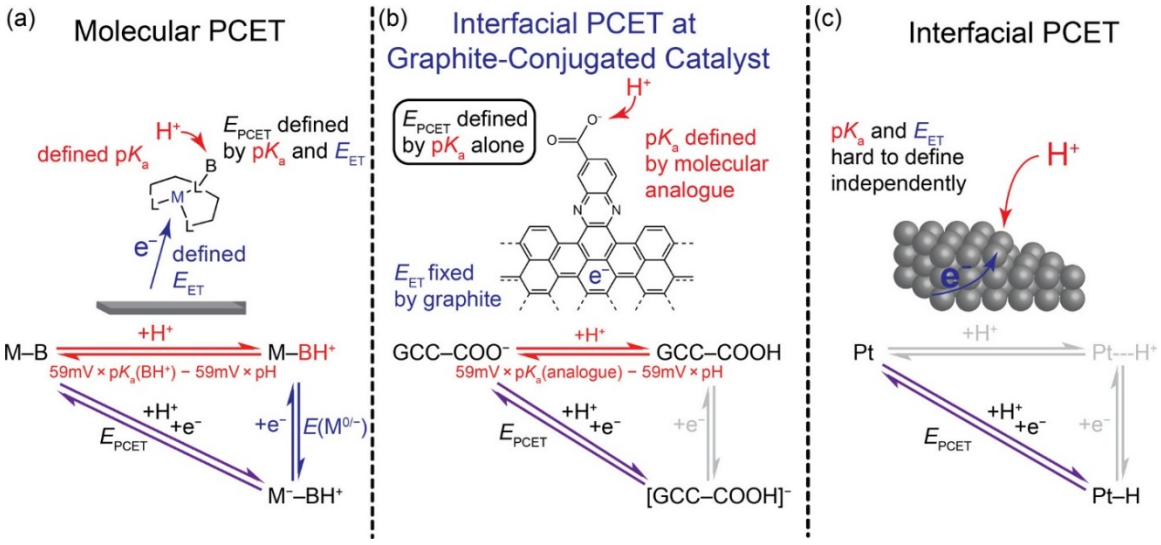

Figure 1.3. Square scheme representations of PCET thermochemistry for (a) a metal complex, (b) a graphite-conjugated catalyst (GCC) with a pendent carboxylate, and (c) a platinum electrode. Reprinted with permission from ref [105]. Copyright 2019 American Chemical Society.

1.3.2.1 The Volmer Reaction

The electrosorption of a proton to a surface is known as the Volmer reaction (Figure 1.3c).[106] This phenomenon has been well-studied on platinum surfaces, and in particular, the flat and symmetric (111) facet. Pt(111) single crystal surfaces in contact with non-interacting aqueous electrolytes show characteristic cyclic voltammograms between the onsets of hydrogen and oxygen evolution catalysis (Figure 1.4).[107,108] The

reversible Faradaic feature at more positive potentials corresponds to the formation of "underpotential deposited hydrogen" (H_{upd}), so called because this deposition occurs at potentials "under" (less reducing than) that needed to produce H_2 (RHE). Full coverage of H_{upd} on Pt(111) is commonly taken to be close to one H for every surface Pt atom.[109-111] These H_{upd} sites are distinct in both free energy and structure from the "overpotential deposited hydrogen" atoms that are active for the hydrogen evolution reaction.[99] The electrochemical response for H_{upd} on Pt(111) moves ~59 mV per unit pH change, exactly as expected for a molecular ne^-/nH^+ PCET reaction. This ~59 mV, or Nernstian, shift is important because it means that the potentials to deposit H_{upd} are constant versus $E°'(HA/H_2)$ (RHE in aqueous solutions, eq 1.19), and they can be extrapolated to give $E°$(V vs H_2) at standard state.

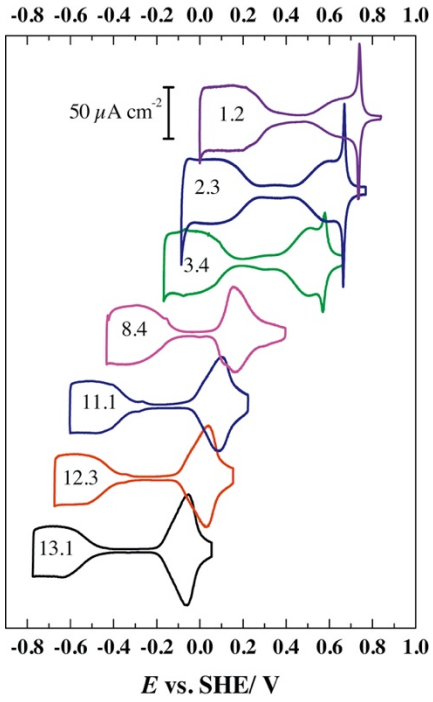

Figure 1.4. Cyclic voltammetry of a Pt(111) electrode at different solution pH's (scan rate: 50 mV s^{-1}). The wave for UPD hydrogen is the shape at the left in each CV, with the pH inscribed inside. Reprinted with permission from ref [108]. Copyright 2015 Elsevier.

The $E°$(V vs H_2) for the Volmer reaction can be converted to an average BDFE, or hydrogen adsorption free energy, using eq 1.18. Analyses of hydrogen electrosorption have previously explored the magnitude and distribution of surface adsorption free energies for polycrystalline and single-crystal noble metal electrodes.[112-116] For Pt(111), the midpoint of the H_{upd} wave of ~0.2 V vs RHE in aqueous media corresponds to an average BDFE of 57 kcal mol^{-1}. This value is slightly larger than the free energy to form $H^{\bullet}$ in water from H_2 gas (Table 1.1)—as it must be because it is *under*potential deposited. We will return to these data in Section 1.3.2.4, to analyze the width of the H_{upd} wave.

1.3.2.2 Pourbaix Diagrams for Metal Oxide Materials

The thermochemistry of bulk metal oxides and hydroxides has long been studied because of the importance of these materials and minerals. From our PCET

perspective, a landmark in these studies is the *Atlas of Electrochemical Equilibria in Aqueous Solutions* by Marcel Pourbaix, first published in 1963.[117] His diagrams, such as Figure 1.5, have proven to be a very valuable way to summarize a lot of thermochemical information. While Pourbaix's career was primarily in corrosion science, the motivation for his original diagram (1938) was catalysis.[118] The diagrams, known as p*E*/pH plots,[119] are now used in many fields including aqueous coordination chemistry and geochemistry, and have been conceptually extended to non-aqueous solvents.[120]

Pourbaix diagrams are *preponderance* diagrams, essentially a map of the most thermodynamically stable (preponderant) species in each *E*/pH region. One of the diagrams for copper from the *Atlas* is shown in Figure 1.5 (some Pourbaix diagrams have been updated since 1963, so readers should check the current literature). The four most important species are copper metal (Cu, at the bottom, the most stable copper species under reducing conditions), solid Cu_2O in the middle, and the top portion of the diagram divided between aqueous Cu^{2+} (in acidic, low pH conditions at the left and solid $Cu(OH)_2$ in the upper middle. [A separate but quite similar diagram in the *Atlas* involves CuO instead of $Cu(OH)_2$; for this discussion we ignore the soluble Cu^{II} species at high pH and the soluble Cu^{+}.] Each of the solid lines divides regions where different materials predominate. Lines (7) and (9) in the center of the diagram, for instance, separate Cu, Cu_2O and $Cu(OH)_2$, according to eqs 1.23 and 1.24. The slopes of these lines is –59 mV/pH, following the Nernst equation for these equations and the equal numbers of protons and electrons. These diagrams show pH-independent processes as horizontal lines, and non-redox protonation equilibria as vertical lines. Thus, these diagrams capture the full PCET thermochemistry of stable species as a function of pH and potential, including both materials and soluble species.

$$2Cu(OH)_2 + 2e^- + 2H^+ \rightarrow Cu_2O + 3H_2O \qquad \text{line (9)} \qquad (1.23)$$

$$Cu_2O + 2e^- + 2H^+ \rightarrow 2Cu + H_2O \qquad \text{line (7)} \qquad (1.24)$$

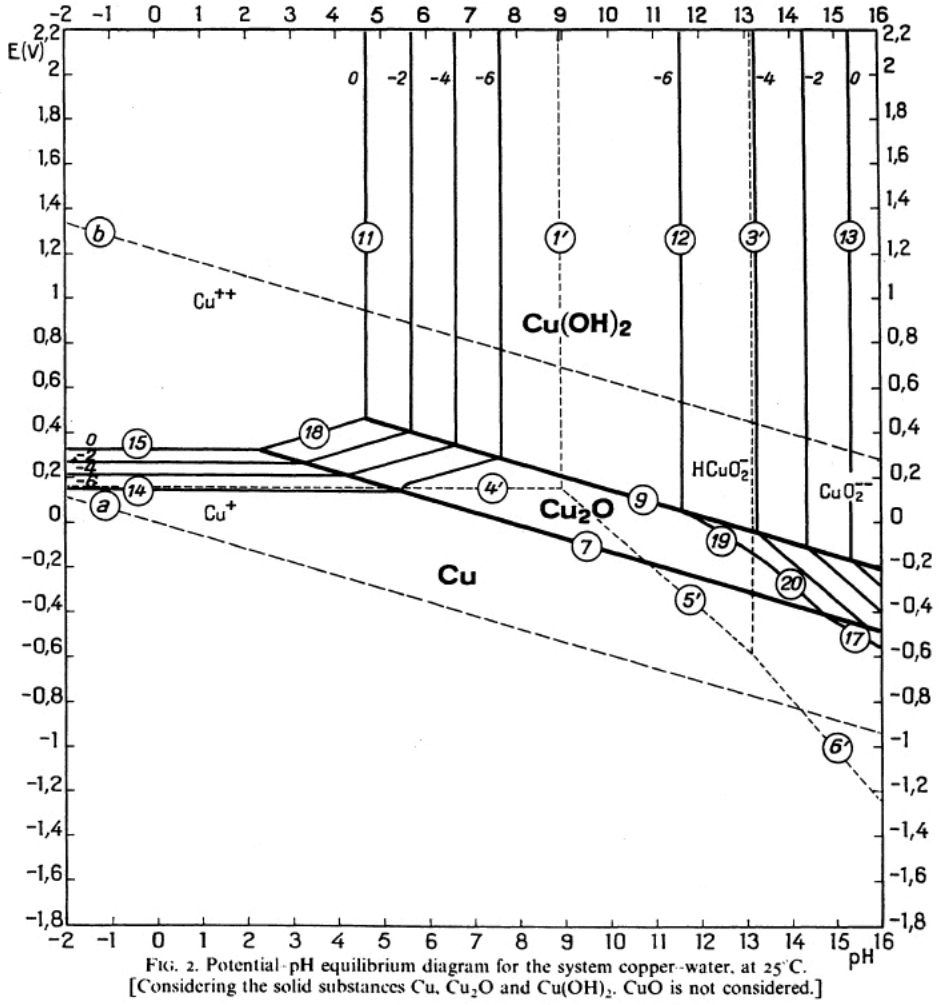

FIG. 2. Potential-pH equilibrium diagram for the system copper-water, at 25°C.
[Considering the solid substances Cu, Cu_2O and $Cu(OH)_2$. CuO is not considered.]

Figure 1.5. One of the Pourbaix (*E*/pH) diagrams for copper; reproduced from the *Atlas of Electrochemical Equilibria in Aqueous Solutions* by Marcel Pourbaix,[121] by permission of the National Association of Corrosion Engineers.

The encyclopedic detail of Pourbaix diagrams for bulk metal oxides has, so far, not been achievable for thin-film and nanoscale versions of the same minerals where material structures and stoichiometries are less well-defined. Nevertheless, electrochemical measurements of $1e^-/1H^+$ couples for semiconducting and conducting

metal oxide (nano)materials, similar to those shown in eqs 1.23 and 1.24, have been an important method for understanding their PCET thermochemistry.

Scheme 1.5. A) Electrochemical interconversion of $Ni^{III}OOH$ to $Ni^{II}(OH)_2$. B) Reversible PCET between a phenol/phenoxyl radical and $Ni^{III}OOH/Ni^{II}(OH)_2$.[122]

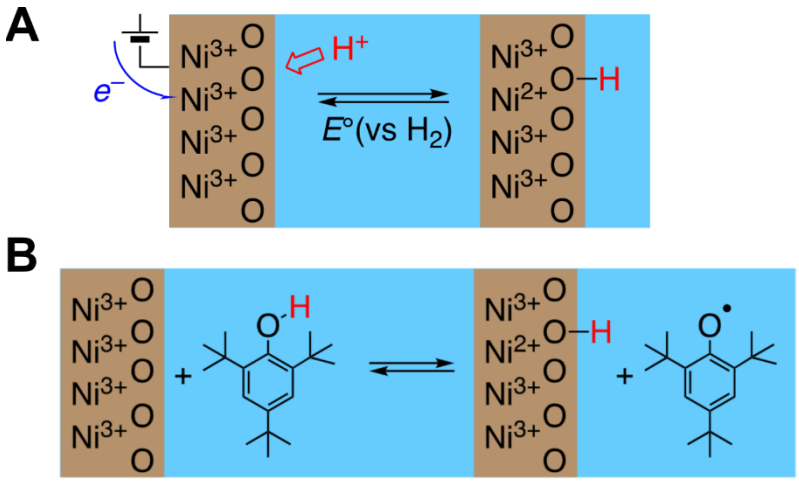

Nickel oxide is a widely used p-type semiconductor. Aqueous voltammetry of calcined NiO thin films typically show one or two well-defined Faradaic waves that have a Nernstian shift with pH (Figure 1.6A).[123,124] These waves are usually interpreted as the PCET oxidations of $Ni(OH)_2$, a hydrated form of nickel oxide at the surface (eqs 1.25 and 1.26; characterization of the "Ni^{IV}" material is a matter of some debate). Similar to H_{upd} on Pt(111), extrapolating the $E_{1/2}$ values of the CV waves to pH = 0 in Figure 1.6A should give good estimates of the $E°$(V vs H_2) and related BDFE values for these two processes. To test this analogy, electrodes were charged to the $Ni^{III}(O)(OH)$ and $Ni^{II}(OH)_2$ forms and separately reacted with sub-stoichiometric amounts of either 2,4,6-^{t}Bu$_3$PhOH or its corresponding phenoxyl radical (Scheme 1.5).[122] Reactions did not go to completion in either case, suggesting the formation of an equilibrium state. The BDFE of 2,4,6-^{t}Bu$_3$PhOH is 75.5 kcal mol^{-1}, very close to that determined electrochemically for $Ni^{II}(OH)_2$, thereby confirming that $E°$(V vs H_2) and the related BDFE can be determined for metal oxide materials that show Faradaic waves with Nernstian pH shifts.[122]

$$Ni^{III}(O)(OH) + e^- + H^+ \rightarrow Ni(OH)_2 \quad (1.25)$$

$$E°(V \text{ vs } H_2) = 0.99\pm0.03 \text{ V}; \text{ BDFE} = 75.6\pm1.0 \text{ kcal mol}^{-1}$$

$$\text{“}Ni^{IV}O_2\text{”} + e^- + H^+ \rightarrow Ni(O)(OH) \quad (1.26)$$

$$E°(V \text{ vs } H_2) = 1.36\pm0.02 \text{ V}; \text{ BDFE} = 84.2\pm1.0 \text{ kcal mol}^{-1}$$

Many other materials show Nernstian shifts of their potentials with pH.[125-129] One remarkable example is the demonstration by Lyon and Hupp that the conduction band of TiO_2 films shifts 64 mV per factor of ten in solution proton activity, over a range of more than 10^{25} (Figure 1.6B).[130] Hupp *et al.* concluded that, for TiO_2, SnO_2 and ZnO, proton uptake accompanied electron addition to the material. In other words, that these were PCET processes.[130,131] A similar ~60 mV shift per pH unit was observed for equilibration of colloidal TiO_2 nanoparticles with solution redox reagents,[132,133] which can be extrapolated to an $E°$(V vs H_2) of –0.16 ± 0.03 V (Figure 1.6C),[133] close to Lyons and Hupp's value for TiO_2 films. By analogy with the molecular thermochemistry in Section 1.2 and the NiO electrode study above, it seems likely that these $E°$(V vs H_2) potentials are best assigned as $1e^-/1H^+$ processes with a TiO–H BDFE of 49 kcal mol^{-1}.[133]

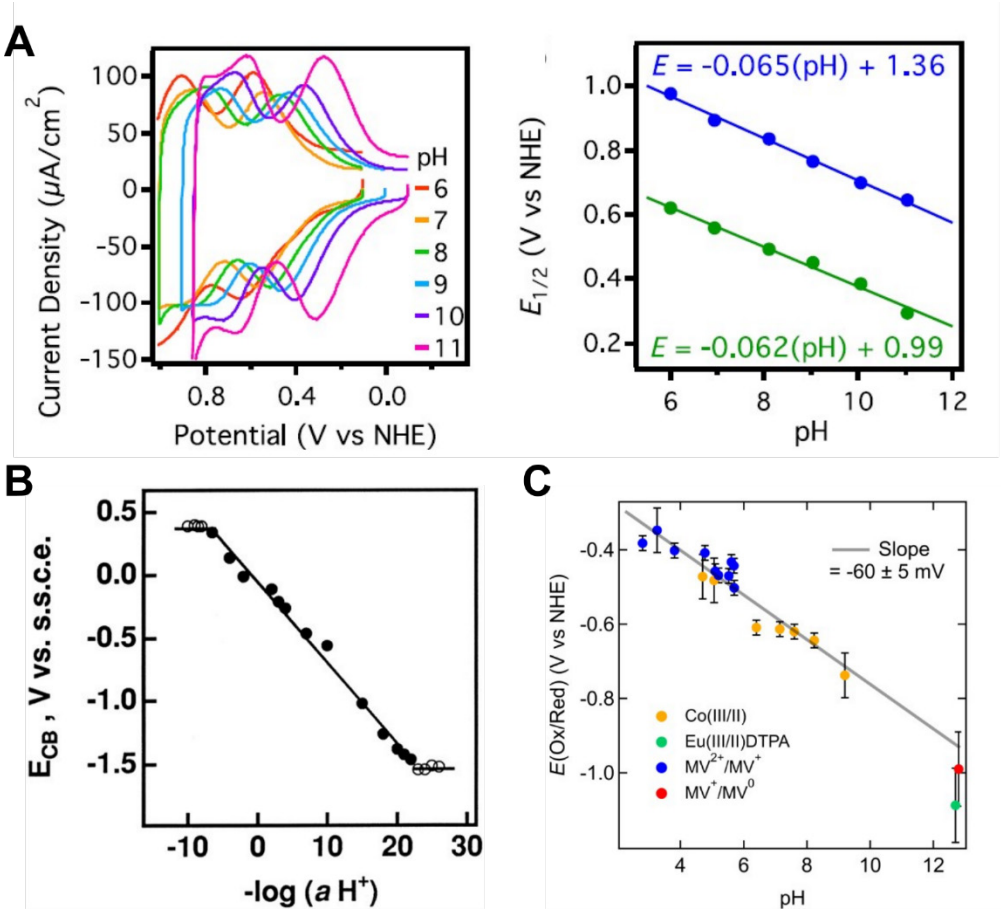

Figure 1.6. (A) NiO on FTO CVs of NiO|FTO collected in aqueous buffers and plot of $E_{1/2}$ vs pH for both redox features, showing Nernstian dependences. Reprinted with permission from ref [122]. Copyright 2019 American Chemical Society. (B) Dependence of reduction potential on log proton activity for a TiO_2 film, with a slope of 64 mV/log(aH^+).Reprinted with permission from ref [130]. Copyright 1999 American Chemical Society. (C) Reduction potentials of citrate-capped aqueous colloidal TiO_2 nanoparticles determined by titration with various solution ET reagents.[133] Reprinted with permission; copyright 2019 Dr. Jennifer L. Peper.

Overall, many materials at aqueous interfaces show a roughly 59 mV/pH unit dependence of their electrochemical response, including metals, oxides, chalcogenides and pnictides, at least in some forms and solution conditions.[134] In the context of this chapter, we suggest that all of these measurements can be used to determine $E°$(V vs H_2) and surface–H BDFE values.

1.3.2.3 Square Scheme Approach

The square scheme is a key tool for defining the PCET thermochemistry of molecules. This scheme describes the relationship between the proton and electron transfer free energies and that of the overall net hydrogen transfer reaction, Scheme 1.1. For molecules, the thermochemistry of the ET and PT steps can be simpler to measure than that of the overall reaction. However, in electrochemical measurements of many material interfaces this paradigm is flipped due to strongly coupled ET and the difficulty of structurally characterizing surface acid/base sites. Seminal work by White and co-workers utilized self-assembled monolayers on noble metal electrodes to create well-defined carboxylic acid sites. The deprotonation of these sites could be driven by the potentiostat and used to measure the p$K_{1/2}$ of these sites.[135] More recently, Jackson and co-workers have extended this concept to well-defined active sites on graphitic carbon electrodes, and defined a partial square scheme (Figure 1.7).[105]

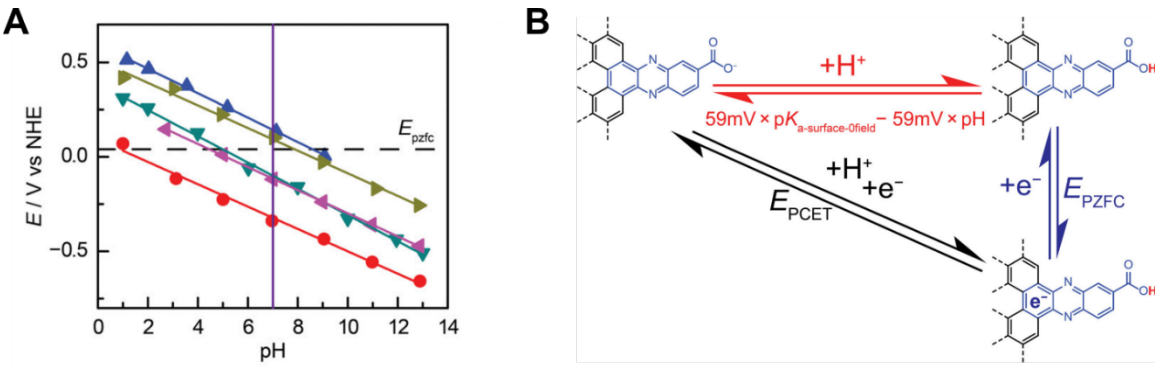

Figure 1.7. (A) Pourbaix diagram showing pH-dependence of interfacial proton-coupled electron-transfer (PCET) waves for GCC-phenazine (red), GCC-phen-NH_2 (purple), GCC-phen-COOH (dark green; structure shown in (b)), GCC-phen-*m*-OH (olive green), and GCC-phen-*o*-OH (blue). The dotted line shows the computed potential of zero free charge (E_{PZFC}). (B) Partial square scheme for interfacial PCET at GCC-phen-COOH, as an example reaction. The model reported partitions the potential for PCET (diagonal leg) into a horizontal leg, defined as the difference between the 0-field pK_a of the surface site and the pH of the solution, and a vertical leg, defined as the E_{PZFC}, of the electrode. Reprinted with permission from ref [105]. Copyright 2019 American Chemical Society.

The molecularly well-defined active sites, formed using conjugated aromatic pyrazine linkages with varying acid/base sites, were examined electrochemically as a function of pH (Figure 1.7A).[105] All of these graphite-conjugated catalysts (GCCs) exhibit a clear wave in their CVs and a Nernstian shift with pH. Based on these data and previous studies, the Faradaic features were ascribed to protonation/deprotonation of the acid/base group on the pyrazine linkage coupled to electron transfer from the external circuit, and $E°$(V vs H_2) and BDFE values were determined. This is perhaps surprising, because conductive electrodes typically do not show such well-defined waves, and because protonation of a carboxylate is not normally considered as coupled to electron transfer. We encourage interested readers to read the original papers which discuss the unique features of these systems.[105,136,137]

The CV waves of these GCCs surprisingly also show a Nernstian shift with the pK_a of the solution-phase pyrazine analogue.[105] These data revealed that the free energy for PT in the overall PCET step is well described by the pK_a of the surface acid/base group (the carboxylic acid/carboxylate in Figure 1.7B). With the free energies for the overall PCET reaction and proton transfer component in hand, the free energy for electron transfer could also be calculated. Jackson *et al.* suggested that this ET free energy is defined by the potential of zero free charge (E_{PZFC}), and can be used to complete a square scheme analogous to that those described molecules, Figure 1.7B. The E_{PZFC} is traditionally connected to the work function of a material and is generally considered to be extremely sensitive to surface structure.[138] The possibility of connections between work functions, PCET at materials, and square schemes for molecules are exciting and we look forward to future studies.

1.3.2.4 Surface Coverage, Heterogeneity, Adsorbate Interactions, and Isotherms

While the above sections have developed many analogies between the PCET thermochemistry of interfaces and molecular systems, there are a number of key differences. Among the most significant are the contributions of surface heterogeneity

and adsorbate interactions. In a molecular system, every molecule of a particular compound is by definition exactly the same, with the same BDFE. But surfaces essentially always have a distribution of sites and BDFEs. This is due to steps, edges, and other irregularities on a clean surface, and to the presence of impurity atoms or non-stoichiometry at the surface, in other words intrinsic and extrinsic defects. Even a perfectly well-ordered, clean surface has a range of BDFEs, because the adsorbates interact with each other. For example, the first H_{upd} atoms deposit on a clean Pt(111) surface at ca. +0.4 V vs RHE (Section 1.3.2.1) and they continue to deposit negative of RHE.[110,111,139] A normal Faradaic feature in the CV should be roughly Gaussian with a full-width half-maximum (FWHM) of 90.6 mV.[140,141] The >400 mV (or >9 kcal mol^{-1}) range of potentials to form a monolayer of H_{upd} is, therefore, indicative of interactions between surface–H species. Even after this monolayer has deposited, more hydrogen will still adsorb negative of RHE. This is known as *over*potential deposited hydrogen, or H_{opd}.[99] These hydrogen atoms are thought to deposit on the atop sites of the surface, as opposed to the three-fold sites where H_{upd} are generally thought to reside.[99,109,110,142] This example emphasizes the complexities of hydrogen adsorption even on a flat single-crystal surface.

The theory behind the range of BDFEs for Pt(111) is different from the PCET thermochemistry of molecular reagents in several important ways. In a molecular ensemble, every molecule is the same and the thermochemical ability of the ensemble to donate $H^{\bullet}$ depends only on the ratio of oxidized and reduced species. This relationship is described by a modified version of the Nernst equation (eq 1.27), and is analogous to the acidity of a buffer solution varying with the ratio of the components. Application of eq 1.27 to Pt(111) would predict a range in BDFEs of only 1.2 kcal mol^{-1} for deposition of a full monolayer; one eighth of the >9 kcal mol^{-1} range observed.

$$BDFE_{adj}(XH_n) = BDFE(XH_n) - \frac{1.364\ kcal\ mol^{-1}}{n}\log\left(\frac{[XH_n]}{[X]}\right) \qquad (1.27)$$

Unlike that for molecules, the theory of hydrogen adsorption to a surface must consider heterogeneity in the ensemble of active sites and interactions between adsorbates. In the limiting case of identical surface sites and no significant interaction between the surface H's, the free energy of binding will follow a Langmuir *isotherm*,[106] which simply reflects Le Chatelier's principle or the law of mass action. This isotherm is effectively equivalent to the Nernst equation, eq 1.27, and the BDFE° is defined at θ = 0.5 (eq 1.28). As discussed above, however, the Langmuir isotherm does not describe the very large range of BDFEs for Pt(111). These data can instead be fit by adding a linear correction term, $C\theta$, to eq 1.28 (eq 1.29).[139,142] This relationship is called a Frumkin isotherm, and it provides a first-order correction to interactions between surface adsorbates and/or surface heterogeneity which cause deviations from Langmuirian behavior.

$$BDFE = BDFE^o - 1.364 \times \log\left(\frac{\theta}{(1-\theta)}\right) \quad (1.28)$$

$$BDFE = BDFE^o - 1.364 \times \log\left(\frac{\theta}{1-\theta}\right) + C(\theta - 0.5) \quad (1.29)$$

As Pt(111) is one of the most studied surfaces in the materials literature, this depth of knowledge about the thermochemistry of a surface is quite unique. Nevertheless, these concepts are fairly universal. In Chapter 3, the thermochemistry of hydrogen adsorption to colloidal cerium oxide nanoparticles (nanoceria) is measured and shown to fit to a Frumkin isotherm. For nanoceria, the BDFE range is >13 kcal mol^{-1} or >0.5 V. In comparison to Pt(111), this is an even larger effect as the range of adsorbate coverages analyzed was limited. This study, and others,[143,144] suggest that significant deviations from Langmuirian behavior may be more commonplace on surfaces than previously thought. Implications of these deviations for both thermochemical and kinetic analyses are discussed in Chapter 3 and Chapter 4.

We hope that this section shows the power and the complexities of applying molecular PCET thermochemical approaches to the study of materials and solution/solid interfaces. As with molecules, the PCET thermochemistry of materials is a key property and predictive of reactivity. Furthermore, the descriptions and equivalence of the potential of hydrogenation and BDFE, derived in Section 1.2, are similarly applicable to materials and enable comparisons between electrochemical and thermochemical perspectives (1 eV = 23.06 kcal mol^{-1}; 1 kcal mol^{-1} = 43.36 meV). Unlike molecules, however, materials have complex surfaces that present a multitude of sites, either identical or different. We speculate, based on a few examples, that this multiplicity will often lead to a range of PCET thermochemistry for a single material surface. Such a range of thermochemistry may prove to be fundamental to many properties of the interface, including its catalytic proficiency.[145]

1.4 Conclusions

This chapter provides an introduction to PCET thermochemistry for both the layman and the expert. The foundational thermochemical cycles and experimental tools are discussed, along with novel insights to make these methodologies more accessible and better understood. This includes a focus on potentials of hydrogenation which are shown to be effectively equivalent to BDFEs and broadly applicable. The universality of $E°$(V vs H_2) and BDFEs is used to develop connections across a range of fields from PCET in ionic liquid and mixed solvents to surfaces and electrified interfaces. The interdisciplinary nature of this discussion emphasizes the critical importance and centrality of PCET thermochemistry to research across a range of fields.

1.5 References

1. Huynh, M. H. V.; Meyer, T. J., Proton-Coupled Electron Transfer. *Chem. Rev.* **2007,** *107* (11), 5004-5064.
2. Weinberg, D. R.; Gagliardi, C. J.; Hull, J. F.; Murphy, C. F.; Kent, C. A.; Westlake, B. C.; Paul, A.; Ess, D. H.; McCafferty, D. G.; Meyer, T. J., Proton-Coupled Electron Transfer. *Chem. Rev.* **2012,** *112* (7), 4016-4093.
3. Warren, J. J.; Tronic, T. A.; Mayer, J. M., Thermochemistry of Proton-Coupled Electron Transfer Reagents and Its Implications. *Chem. Rev.* **2010,** *110*, 6961-7001.
4. Hammes-Schiffer, S.; Stuchebrukhov, A. A., Theory of Coupled Electron and Proton Transfer Reactions. *Chem. Rev.* **2010,** *110* (12), 6939-6960.
5. Costentin, C.; Robert, M.; Savéant, J.-M., Update 1 of: Electrochemical Approach to the Mechanistic Study of Proton-Coupled Electron Transfer. *Chem. Rev.* **2010,** *110* (12), PR1-PR40.
6. Migliore, A.; Polizzi, N. F.; Therien, M. J.; Beratan, D. N., Biochemistry and Theory of Proton-Coupled Electron Transfer. *Chem. Rev.* **2014,** *114* (7), 3381-3465.
7. Pannwitz, A.; Wenger, O. S., Recent Advances in Bioinspired Proton-Coupled Electron Transfer. *Dalton Trans.* **2019,** *48* (18), 5861-5868.
8. Dempsey, J. L.; Winkler, J. R.; Gray, H. B., Proton-Coupled Electron Flow in Protein Redox Machines. *Chem. Rev.* **2010,** *110* (12), 7024-7039.
9. Stubbe, J.; Nocera, D. G.; Yee, C. S.; Chang, M. C. Y., Radical Initiation in the Class I Ribonucleotide Reductase: Long-Range Proton-Coupled Electron Transfer? *Chem. Rev.* **2003,** *103* (6), 2167-2202.
10. Gagliardi, C. J.; Westlake, B. C.; Kent, C. A.; Paul, J. J.; Papanikolas, J. M.; Meyer, T. J., Integrating Proton Coupled Electron Transfer (PCET) and Excited States. *Coord. Chem. Rev.* **2010,** *254* (21), 2459-2471.
11. Wenger, O. S., Proton-Coupled Electron Transfer with Photoexcited Ruthenium(II), Rhenium(I), and Iridium(III) Complexes. *Coord. Chem. Rev.* **2015,** *282-283*, 150-158.
12. Miller, D. C.; Tarantino, K. T.; Knowles, R. R., Proton-Coupled Electron Transfer in Organic Synthesis: Fundamentals, Applications, and Opportunities. *Top. Curr. Chem.* **2016,** *374* (3), 30.
13. Hoffmann, N., Proton-Coupled Electron Transfer in Photoredox Catalytic Reactions. *Eur. J. Org. Chem.* **2017,** *2017* (15), 1982-1992.
14. Wiedner, E. S.; Chambers, M. B.; Pitman, C. L.; Bullock, R. M.; Miller, A. J. M.; Appel, A. M., Thermodynamic Hydricity of Transition Metal Hydrides. *Chem. Rev.* **2016,** *116* (15), 8655-8692.
15. Brereton, K. R.; Smith, N. E.; Hazari, N.; Miller, A. J. M., Thermodynamic and Kinetic Hydricity of Transition Metal Hydrides. *Chem. Soc. Rev.* **2020,** *49* (22), 7929-7948.
16. Hammes-Schiffer, S., Introduction: Proton-Coupled Electron Transfer. *Chem. Rev.* **2010,** *110* (12), 6937-6938.
17. . Themed Collection Frontiers in Proton Coupled Electron Transfer (PCET) *Chem. Commun.* [Online], 2019. https://pubs.rsc.org/en/journals/articlecollectionlanding?sercode=cc&themeid=555a6d40-9f26-4f28-a334-fcc83195fa53.
18. Choi, G. J.; Zhu, Q.; Miller, D. C.; Gu, C. J.; Knowles, R. R., Catalytic Alkylation of Remote C-H Bonds Enabled by Proton-Coupled Electron Transfer. *Nature* **2016,** *539* (7628), 268-271.
19. Gentry, E. C.; Knowles, R. R., Synthetic Applications of Proton-Coupled Electron Transfer. *Acc. Chem. Res.* **2016,** *49* (8), 1546-1556.
20. Bruch, Q. J.; Connor, G. P.; Chen, C.-H.; Holland, P. L.; Mayer, J. M.; Hasanayn, F.; Miller, A. J. M., Dinitrogen Reduction to Ammonium at Rhenium Utilizing Light and Proton-Coupled Electron Transfer. *J. Am. Chem. Soc.* **2019,** *141* (51), 20198-20208.
21. Chalkley, M. J.; Peters, J. C., Relating N-H Bond Strengths to the Overpotential for Catalytic Nitrogen Fixation: Relating N-H Bond Strengths to the Overpotential for Catalytic Nitrogen Fixation. *Eur. J. Inorg. Chem.* **2020,** *2020* (15-16), 1353-1357.

22. Bezdek, M. J.; Pappas, I.; Chirik, P. J., Determining and Understanding N-H Bond Strengths in Synthetic Nitrogen Fixation Cycles. In *Nitrogen Fixation*, Nishibayashi, Y., Ed. Springer International Publishing: Cham, 2017; pp 1-21.
23. Bezdek, M. J.; Chirik, P. J., Thermodynamics of N–H Bond Formation in Bis(phosphine) Molybdenum(II) Diazenides and the Influence of the Trans Ligand. *Dalton Trans.* **2016,** *45* (40), 15922-15930.
24. Anson, C. W.; Stahl, S. S., Cooperative Electrocatalytic O2 Reduction Involving Co(salophen) with p-Hydroquinone as an Electron–Proton Transfer Mediator. *J. Am. Chem. Soc.* **2017,** *139* (51), 18472-18475.
25. Er, S.; Suh, C.; Marshak, M. P.; Aspuru-Guzik, A., Computational design of molecules for an all-quinone redox flow battery. *Chem. Sci.* **2015,** *6* (2), 885-893.
26. Murray, A. T.; Voskian, S.; Schreier, M.; Hatton, T. A.; Surendranath, Y., Electrosynthesis of Hydrogen Peroxide by Phase-Transfer Catalysis. *Joule* **2019,** *3* (12), 2942-2954.
27. Agarwal, R. G.; Wise, C. F.; Warren, J. J.; Mayer, J. M., Correction to Thermochemistry of Proton-Coupled Electron Transfer Reagents and its Implications. *Chem. Rev., submitted* **2021**.
28. Wise, C. F.; Agarwal, R. G.; Mayer, J. M., Determining Proton-Coupled Standard Potentials and X–H Bond Dissociation Free Energies in Nonaqueous Solvents Using Open-Circuit Potential Measurements. *J. Am. Chem. Soc.* **2020,** *142* (24), 10681-10691.
29. Bordwell, F. G.; Cheng, J., Substituent Effects on the Stabilities of Phenoxyl Radicals and the Acidities of Phenoxyl Radical Cations. *J. Am. Chem. Soc.* **1991,** *113* (5), 1736-1743.
30. Gerken, J. B.; Stahl, S. S., High-Potential Electrocatalytic O_2 Reduction with Nitroxyl/NO_x Mediators: Implications for Fuel Cells and Aerobic Oxidation Catalysis. *ACS Cent. Sci.* **2015,** *1* (5), 234-243.
31. Matsubara, Y., Unified Benchmarking of Electrocatalysts in Noninnocent Second Coordination Spheres for CO_2 Reduction. *ACS Energy Lett.* **2019,** *4* (8), 1999-2004.
32. Nagao, H.; Mizukawa, T.; Tanaka, K., Carbon-Carbon Bond Formation in the Electrochemical Reduction of Carbon Dioxide Catalyzed by a Ruthenium Complex. *Inorg. Chem.* **1994,** *33* (15), 3415-3420.
33. Luo, Y.-R., *Comprehensive Handbook of Chemical Bond Energies*. CRC Press: Boca Raton, 2007.
34. Internet Bond-Energy Databank (pK_a And BDE)—iBond Home Page. http://ibond.nankai.edu.cn (accessed Feb 15, 2021).
35. PCET thermochemistry can use a number of different standard states. Most experimental studies under typical laboratory conditions simply extrapolate solution concentrations to the common and accessible 1 M standard state. In principle, this should be more precisely defined as 'the properties of the solute at infinite dilution converted to a concentration of 1 M,' the typical definition of a unit activity coefficient. The latter definition requires additional information and calculations but has the advantage of avoiding non-idealities such as ion pairing or homoconjugation, which are often important at high concentrations of ions in organic solvents. Traditional thermochemical papers often use a standard state of 'unit mole fraction,' which is infinite dilution extrapolated to $\chi = 1$ (pure solute). For reagents that are gases at ambient temperatures, one finds both 1 atm and 1 M standard states. Species at 1 M are 24.5 times more concentrated than those at 1 atm at 298 K (1 mole per liter vs. 1 mole per 24.5 liters for an ideal gas). The concentration difference alone contributes an unfavorable $-T\Delta S°$ of $RT\ln(24.5) = 1.84$ kcal mol^{-1}. Readers are encouraged to specify their standard states and to give the units of equilibrium constants (e.g., atm^{-1} vs M^{-1} for $X + H_2 \rightleftarrows XH_2$ binding constants).
36. Lucarini, M.; Pedrielli, P.; Pedulli, G. F.; Cabiddu, S.; Fattuoni, C., Bond Dissociation Energies of O−H Bonds in Substituted Phenols from Equilibration Studies. *The Journal of Organic Chemistry* **1996,** *61* (26), 9259-9263.
37. Kreevoy, M. M.; Eichinger, B. E.; Stary, F. E.; Katz, E. A.; Sellstedt, J. H., The Effect of Structure on Mercaptan Dissociation Constants. *J. Org. Chem.* **1964,** *29* (6), 1641-1642.
38. Kreevoy, M. M.; Harper, E. T.; Duvall, R. E.; Wilgus, H. S.; Ditsch, L. T., Inductive Effects on the Acid Dissociation Constants of Mercaptans. *J. Am. Chem. Soc.* **1960,** *82* (18), 4899-4902.
39. Blanksby, S. J.; Ellison, G. B., Bond Dissociation Energies of Organic Molecules. *Acc. Chem. Res.* **2003,** *36* (4), 255-263.

40. Mader, E. A.; Manner, V. W.; Markle, T. F.; Wu, A.; Franz, J. A.; Mayer, J. M., Trends in Ground-State Entropies for Transition Metal Based Hydrogen Atom Transfer Reactions. *J. Am. Chem. Soc.* **2009,** *131* (12), 4335-4345.
41. Bordwell, F. G.; Cheng, J. P.; Harrelson, J. A., Homolytic Bond Dissociation Energies in Solution from Equilibrium Acidity and Electrochemical Data. *J. Am. Chem. Soc.* **1988,** *110* (4), 1229-1231.
42. Wayner, D. D. M.; Parker, V. D., Bond energies in solution from electrode potentials and thermochemical cycles. A simplified and general approach. *Acc. Chem. Res.* **1993,** *26* (5), 287-294.
43. Tilset, M., The Thermodynamics of Organometallic Systems Involving Electron-Transfer Paths. In *Electron Transfer In Chemistry*, Balzani, V., Ed. Wiley-VCH: Weinheim, Germany, 2001; pp 677-713.
44. Tilset, M., *Organometallic Electrochemistry: Thermodynamics of Metal–Ligand Bonding*. Elsevier: Amsterdam, 2007; Vol. 1.
45. Warren, J. J.; Mayer, J. M., Predicting Organic Hydrogen Atom Transfer Rate Constants Using the Marcus Cross Relation. *Proc. Natl. Acad. Sci. U. S. A.* **2010,** *107* (12), 5282-5287.
46. Mader, E. A.; Davidson, E. R.; Mayer, J. M., Large Ground-State Entropy Changes for Hydrogen Atom Transfer Reactions of Iron Complexes. *J. Am. Chem. Soc.* **2007,** *129* (16), 5153-5166.
47. Gritzner, G.; Kůta, J., Recommendations on Reporting Electrode Potentials in Nonaqueous Solvents. *Electrochim. Acta* **1984,** *29* (6), 869-873.
48. Noviandri, I.; Brown, K. N.; Fleming, D. S.; Gulyas, P. T.; Lay, P. A.; Masters, A. F.; Phillips, L., The Decamethylferrocenium/Decamethylferrocene Redox Couple: A Superior Redox Standard to the Ferrocenium/Ferrocene Redox Couple for Studying Solvent Effects on the Thermodynamics of Electron Transfer. *J. Phys. Chem. B* **1999,** *103* (32), 6713-6722.
49. Linstrom, P. J.; Mallard, W. G. NIST Chemistry Webbook, NIST Standard Database Number 69. http://webbook.nist.gov/chemistry/ (accessed February 8, 2021).
50. Roduner, E., Hydrophobic Solvation, Quantum Nature, and Diffusion of Atomic Hydrogen in Liquid Water. *Radiat. Phys. Chem.* **2005,** *72* (2), 201-206.
51. Serjeant, E. P.; Dempsey, B., *Ionisation Constants of Organic Acids in Aqueous Solution*. Permagon: Oxford, 1979.
52. Armstrong, D. A.; Huie, R. E.; Koppenol, W. H.; Lymar, S. V.; Merényi, G.; Neta, P.; Ruscic, B.; Stanbury, D. M.; Steenken, S.; Wardman, P., Standard Electrode Potentials Involving Radicals in Aqueous Solution: Inorganic Radicals (IUPAC Technical Report). *Pure Appl. Chem.* **2015,** *87* (11-12), 1139.
53. Parker, V. D., Homolytic Bond (H-A) Dissociation Free Energies in Solution. Applications of the Standard Potential of the (H^+/H•) Couple. *J. Am. Chem. Soc.* **1992,** *114* (19), 7458-7462.
54. Brunner, E., Solubility of hydrogen in 10 organic solvents at 298.15, 323.15, and 373.15 K. *J. Chem. Eng. Data* **1985,** *30* (3), 269-273.
55. Wilhelm, E.; Battino, R., Thermodynamic Functions of the Solubilities of Gases in Liquids at 25°. *Chem. Rev.* **1973,** *73* (1), 1-9.
56. Young, C. L., *Hydrogen and Deuterium*. 1st ed.; Pergamon Press: New York, 1981; Vol. 5/6, p 646.
57. Connelly, S. J.; Wiedner, E. S.; Appel, A. M., Predicting the reactivity of hydride donors in water: thermodynamic constants for hydrogen. *Dalton Trans.* **2015,** *44* (13), 5933-5938.
58. Wise, C. F.; Agarwal, R. G.; Mayer, J. M., Determining Proton-Coupled Standard Potentials and X–H Bond Dissociation Free Energies in Nonaqueous Solvents Using Open-Circuit Potential Measurements. *J. Am. Chem. Soc.* **2020,** *142* (24), 10681-10691.
59. Matsubara, Y., Standard Electrode Potentials for Electrochemical Hydrogen Production, Carbon Dioxide Reduction, and Oxygen Reduction Reactions in N,N-Dimethylacetamide. *Chem. Lett.* **2020,** *49* (8), 915-917.
60. Fourmond, V.; Jacques, P. A.; Fontecave, M.; Artero, V., H_2 Evolution and Molecular Electrocatalysts: Determination of Overpotentials and Effect of Homoconjugation. *Inorg. Chem.* **2010,** *49* (22), 10338-10347.

61. Kolthoff, I. M.; Chantooni, M. K., Critical Study Involving Water, Methanol, Acetonitrile, N,N-Dimethylformamide, and Dimethyl Sulfoxide of Medium Ion Activity Coefficients, ɣ, on the Basis of the $ɣ_{AsPh4}+ = ɣ_{PBh4}-$ Assumption. *J. Phys. Chem.* **1972,** *76* (14), 2024-2034.
62. Klug, C. M.; O'Hagan, M.; Bullock, R. M.; Appel, A. M.; Wiedner, E. S., Impact of Weak Agostic Interactions in Nickel Electrocatalysts for Hydrogen Oxidation. *Organometallics* **2017,** *36* (12), 2275-2284.
63. Quist, D. A.; Ehudin, M. A.; Schaefer, A. W.; Schneider, G. L.; Solomon, E. I.; Karlin, K. D., Ligand Identity-Induced Generation of Enhanced Oxidative Hydrogen Atom Transfer Reactivity for a CuII2(O2•–) Complex Driven by Formation of a CuII2(−OOH) Compound with a Strong O–H Bond. *J. Am. Chem. Soc.* **2019,** *141* (32), 12682-12696.
64. The value of *TS*°(H•) in THF used by Quist and co-workers was corrected to 6.43 kcal mol^{-1} to give *E*°(H^+/H_2) = –0.33 V. This value was averaged with those from the other cited references (–0.339 V and –0.361 V, respectively).
65. Garrido, G.; Koort, E.; Ràfols, C.; Bosch, E.; Rodima, T.; Leito, I.; Rosés, M., Acid−Base Equilibria in Nonpolar Media. Absolute pKa Scale of Bases in Tetrahydrofuran. *The Journal of Organic Chemistry* **2006,** *71* (24), 9062-9067.
66. Roberts, J. A. S.; Bullock, R. M., Direct Determination of Equilibrium Potentials for Hydrogen Oxidation/Production by Open Circuit Potential Measurements in Acetonitrile. *Inorg. Chem.* **2013,** *52* (7), 3823-3835.
67. Huynh, M. T.; Anson, C. W.; Cavell, A. C.; Stahl, S. S.; Hammes-Schiffer, S., Quinone $1e^–$ and $2e^–/2H^+$ Reduction Potentials: Identification and Analysis of Deviations from Systematic Scaling Relationships. *J. Am. Chem. Soc.* **2016,** *138* (49), 15903-15910.
68. Izutsu, K., *Electrochemistry in Nonaqueous Solutions, Second, Revised and Enlarged Edition*. Wiley-VCH: 2009.
69. Brozek, C. K.; Hartstein, K. H.; Gamelin, D. R., Potentiometric Titrations for Measuring the Capacitance of Colloidal Photodoped ZnO Nanocrystals. *J. Am. Chem. Soc.* **2016,** *138* (33), 10605-10610.
70. Dutton, P. L., Redox Potentiometry: Determination of Midpoint Potentials of Oxidation-Reduction Components of Biological Electron-Transfer Systems. In *Methods Enzymol.*, Academic Press: 1978; Vol. 54, pp 411-435.
71. Pitman, C. L.; Brereton, K. R.; Miller, A. J. M., Aqueous Hydricity of Late Metal Catalysts as a Continuum Tuned by Ligands and the Medium. *J. Am. Chem. Soc.* **2016,** *138* (7), 2252-2260.
72. Pegis, M. L.; Roberts, J. A. S.; Wasylenko, D. J.; Mader, E. A.; Appel, A. M.; Mayer, J. M., Standard Reduction Potentials for Oxygen and Carbon Dioxide Couples in Acetonitrile and N,N-Dimethylformamide. *Inorg. Chem.* **2015,** *54* (24), 11883-11888.
73. Matsubara, Y., Standard Electrode Potentials for the Reduction of CO_2 to CO in Acetonitrile–Water Mixtures Determined Using a Generalized Method for Proton-Coupled Electron-Transfer Reactions. *ACS Energy Lett.* **2017,** *2* (8), 1886-1891.
74. Pool, D. H.; Stewart, M. P.; O'Hagan, M.; Shaw, W. J.; Roberts, J. A. S.; Bullock, R. M.; DuBois, D. L., Acidic Ionic Liquid/Water Solution as Both Medium and Proton Source for Electrocatalytic H_2 Evolution by $[Ni(P_2N_2)_2]^{2+}$ Complexes. *Proc. Natl. Acad. Sci. U. S. A.* **2012,** *109* (39), 15634.
75. Hou, J.; Fang, M.; Cardenas, A. J. P.; Shaw, W. J.; Helm, M. L.; Bullock, R. M.; Roberts, J. A. S.; O'Hagan, M., Electrocatalytic H_2 Production with a Turnover Frequency $>10^7$ s^{-1}: The Medium Provides an Increase in Rate but Not Overpotential. *Energy Environ. Sci.* **2014,** *7* (12), 4013-4017.
76. Compton, R. G.; Banks, C. E., *Understanding Voltammetry*. Imperial College Press: London, 2007.
77. Agarwal, R. G.; Coste, S. C.; Groff, B. D.; Heuer, A. M.; Noh, H.; Parada, G. A.; Wise, C. F.; Nichols, E. M.; Warren, J. J.; Mayer, J. M., Free Energies of Proton-Coupled Electron Transfer Reagents and Their Applications. *Chem. Rev., accepted* **2021**.
78. Lide, D. R., *CRC Handbook of Chemistry and Physics*. 90 ed.; CRC Press: Boca Raton, FL, 2009.

79. Cardenas, A. J. P.; Ginovska, B.; Kumar, N.; Hou, J.; Raugei, S.; Helm, M. L.; Appel, A. M.; Bullock, R. M.; O'Hagan, M., Controlling Proton Delivery through Catalyst Structural Dynamics. *Angew. Chem. Int. Ed.* **2016,** *55* (43), 13509-13513.
80. Klug, C. M.; Cardenas, A. J. P.; Bullock, R. M.; O'Hagan, M.; Wiedner, E. S., Reversing the Tradeoff between Rate and Overpotential in Molecular Electrocatalysts for H_2 Production. *ACS Catal.* **2018,** *8* (4), 3286-3296.
81. Azcarate, I.; Costentin, C.; Robert, M.; Saveant, J. M., Through-Space Charge Interaction Substituent Effects in Molecular Catalysis Leading to the Design of the Most Efficient Catalyst of CO_2-to-CO Electrochemical Conversion. *J. Am. Chem. Soc.* **2016,** *138* (51), 16639-16644.
82. Jin, K.; Maalouf, J. H.; Lazouski, N.; Corbin, N.; Yang, D.; Manthiram, K., Epoxidation of Cyclooctene Using Water as the Oxygen Atom Source at Manganese Oxide Electrocatalysts. *J. Am. Chem. Soc.* **2019,** *141* (15), 6413-6418.
83. Maalouf, J. H.; Jin, K.; Yang, D.; Limaye, A. M.; Manthiram, K., Kinetic Analysis of Electrochemical Lactonization of Ketones Using Water as the Oxygen Atom Source. *ACS Catal.* **2020,** *10* (10), 5750-5756.
84. *Report of the Basic Energy Sciences Roundtable on Liquid Solar Fuels*; National Renewable Energy Lab. (NREL): United States, 2019.
85. Natinsky, B. S.; Lu, S.; Copeland, E. D.; Quintana, J. C.; Liu, C., Solution Catalytic Cycle of Incompatible Steps for Ambient Air Oxidation of Methane to Methanol. *ACS Cent. Sci.* **2019,** *5* (9), 1584-1590.
86. Kirchheim, R.; Pundt, A., 25 - Hydrogen in Metals. In *Physical Metallurgy (Fifth Edition)*, Laughlin, D. E.; Hono, K., Eds. Elsevier: Oxford, 2014; pp 2597-2705.
87. Janotti, A.; Van de Walle, C. G., Fundamentals of Zinc Oxide as a Semiconductor. *Rep. Prog. Phys.* **2009,** *72* (12), 126501.
88. Van de Walle, C. G.; Neugebauer, J., HYDROGEN IN SEMICONDUCTORS. *Annu. Rev. Mater. Res.* **2006,** *36* (1), 179-198.
89. Van de Walle, C. G.; Neugebauer, J., Universal alignment of hydrogen levels in semiconductors, insulators and solutions. *Nature* **2003,** *423* (6940), 626-628.
90. Conway, B. E., *Electrochemical Supercapacitors: Scientific Fundamentals and Technological Applications*. Springer Science & Business Media: New York, 1999.
91. Conway, B. E.; Gileadi, E., Kinetic Theory of Pseudo-Capacitance and Electrode Reactions at Appreciable Surface Coverage. *Trans. Faraday Soc.* **1962,** *58* (0), 2493-2509.
92. Fleischmann, S.; Mitchell, J. B.; Wang, R.; Zhan, C.; Jiang, D.-e.; Presser, V.; Augustyn, V., Pseudocapacitance: From Fundamental Understanding to High Power Energy Storage Materials. *Chem. Rev.* **2020,** *120* (14), 6738-6782.
93. Costentin, C.; Porter, T. R.; Saveant, J. M., How Do Pseudocapacitors Store Energy? Theoretical Analysis and Experimental Illustration. *ACS Appl. Mater. Interfaces* **2017,** *9* (10), 8649-8658.
94. Koper, M. T. M., Thermodynamic Theory of Multi-Electron Transfer Reactions: Implications for Electrocatalysis. *J. Electroanal. Chem.* **2011,** *660* (2), 254-260.
95. Seh, Z. W.; Kibsgaard, J.; Dickens, C. F.; Chorkendorff, I.; Nørskov, J. K.; Jaramillo, T. F., Combining theory and experiment in electrocatalysis: Insights into materials design. *Science* **2017,** *355* (6321), eaad4998.
96. Schmickler, W.; Trasatti, S., Comment on "Trends in the Exchange Current for Hydrogen Evolution" [J. Electrochem. Soc., 152, J23 (2005)]. *J. Electrochem. Soc.* **2006,** *153* (12), L31.
97. Nørskov, J. K.; Bligaard, T.; Logadottir, A.; Kitchin, J. R.; Chen, J. G.; Pandelov, S.; Stimming, U., Trends in the Exchange Current for Hydrogen Evolution. *J. Electrochem. Soc.* **2005,** *152* (3), J23.
98. Quaino, P.; Juarez, F.; Santos, E.; Schmickler, W., Volcano plots in hydrogen electrocatalysis – uses and abuses. *Beilstein Journal of Nanotechnology* **2014,** *5*, 846-854.
99. Lindgren, P.; Kastlunger, G.; Peterson, A. A., A Challenge to the $G \sim 0$ Interpretation of Hydrogen Evolution. *ACS Catal.* **2020,** *10* (1), 121-128.
100. Campbell, C. T.; Sellers, J. R. V., Enthalpies and Entropies of Adsorption on Well-Defined Oxide Surfaces: Experimental Measurements. *Chem. Rev.* **2013,** *113* (6), 4106-4135.
101. Silbaugh, T. L.; Campbell, C. T., Energies of Formation Reactions Measured for Adsorbates on Late Transition Metal Surfaces. *J. Phys. Chem. C* **2016,** *120* (44), 25161-25172.

102. García-Diéguez, M.; Hibbitts, D. D.; Iglesia, E., Hydrogen Chemisorption Isotherms on Platinum Particles at Catalytic Temperatures: Langmuir and Two-Dimensional Gas Models Revisited. *J. Phys. Chem. C* **2019,** *123* (13), 8447-8462.
103. Paier, J.; Penschke, C.; Sauer, J., Oxygen Defects and Surface Chemistry of Ceria: Quantum Chemical Studies Compared to Experiment. *Chem. Rev.* **2013,** *113* (6), 3949-3985.
104. Sauer, J., Molecular Models in *Ab Initio* Studies of Solids and Surfaces: From Ionic Crystals and Semiconductors to Catalysts. *Chem. Rev.* **1989,** *89* (1), 199-255.
105. Jackson, M. N.; Pegis, M. L.; Surendranath, Y., Graphite-Conjugated Acids Reveal a Molecular Framework for Proton-Coupled Electron Transfer at Electrode Surfaces. *ACS Cent. Sci.* **2019,** *5* (5), 831-841.
106. Gileadi, E., *Electrosorption*. Springer: Boston, MA, 1967.
107. Climent, V.; Feliu, J. M., Thirty years of platinum single crystal electrochemistry. *J. Solid State Electrochem.* **2011,** *15* (7), 1297.
108. Rizo, R.; Sitta, E.; Herrero, E.; Climent, V.; Feliu, J. M., Towards the Understanding of the Interfacial pH Scale at Pt(111) Electrodes. *Electrochim. Acta* **2015,** *162*, 138-145.
109. Fearon, J.; Watson, G. W., Hydrogen adsorption and diffusion on Pt {111} and PtSn {111}. *J. Mater. Chem.* **2006,** *16* (20), 1989-1996.
110. Karlberg, G. S.; Jaramillo, T. F.; Skúlason, E.; Rossmeisl, J.; Bligaard, T.; Nørskov, J. K., Cyclic Voltammograms for H on Pt(111) and Pt(100) from First Principles. *Phys. Rev. Lett.* **2007,** *99* (12), 126101.
111. Asiri, H. A.; Anderson, A. B., Using Gibbs Energies to Calculate the Pt(111) H_{upd} Cyclic Voltammogram. *J. Phys. Chem. C* **2013,** *117* (34), 17509-17513.
112. Jerkiewicz, G.; Zolfaghari, A., Determination of the Energy of the Metal−Underpotential-Deposited Hydrogen Bond for Rhodium Electrodes. *J. Phys. Chem.* **1996,** *100* (20), 8454-8461.
113. Jerkiewicz, G., Hydrogen Sorption At/In Electrodes. *Prog. Surf. Sci.* **1998,** *57* (2), 137-186.
114. Marković, N. M.; Schmidt, T. J.; Grgur, B. N.; Gasteiger, H. A.; Behm, R. J.; Ross, P. N., Effect of Temperature on Surface Processes at the Pt(111)−Liquid Interface: Hydrogen Adsorption, Oxide Formation, and CO Oxidation. *J. Phys. Chem. B* **1999,** *103* (40), 8568-8577.
115. Kowalczyk, P.; Savard, S.; Lasia, A., Determination of the adsorption energy distribution function of upd hydrogen on monocrystalline platinum. *J. Electroanal. Chem.* **2004,** *574* (1), 41-47.
116. Lasia, A., Modeling of Hydrogen Upd Isotherms. *J. Electroanal. Chem.* **2004,** *562* (1), 23-31.
117. Pourbaix, M., *Atlas D'équilibres Électrochimiques*. Gauthier-Villars: Paris, 1963; p 644.
118. Pourbaix, M., Thermodynamics and Corrosion. *Corros. Sci.* **1990,** *30* (10), 963-988.
119. Stumm, W.; Morgan, J. J., *Aquatic Chemistry: Chemical Equilibria and Rates in Natural Waters*. 3rd ed.; Wiley-Interscience: New York, 1995.
120. McCarthy, B. D.; Dempsey, J. L., Decoding Proton-Coupled Electron Transfer with Potential-pK_a Diagrams. *Inorg. Chem.* **2017,** *56* (3), 1225-1231.
121. Pourbaix, M., *Atlas of Electrochemical Equilibria in Aqueous Solutions*. National Association of Corrosion Engineers: Houston, Texas, 1974.
122. Wise, C. F.; Mayer, J. M., Electrochemically Determined O–H Bond Dissociation Free Energies of NiO Electrodes Predict Proton-Coupled Electron Transfer Reactivity. *J. Am. Chem. Soc.* **2019,** *141* (38), 14971-14975.
123. Boschloo, G.; Hagfeldt, A., Spectroelectrochemistry of Nanostructured NiO. *J. Phys. Chem. B* **2001,** *105* (15), 3039-3044.
124. Liu, Q.; Chen, Q.; Zhang, Q.; Xiao, Y.; Zhong, X.; Dong, G.; Delplancke-Ogletree, M.-P.; Terryn, H.; Baert, K.; Reniers, F.; Diao, X., In Situ Electrochromic Efficiency of a Nickel Oxide Thin Film: Origin of Electrochemical Process and Electrochromic Degradation. *J. Mater. Chem. C* **2018,** *6* (3), 646-653.
125. Manjakkal, L.; Szwagierczak, D.; Dahiya, R., Metal Oxides Based Electrochemical pH Sensors: Current Progress and Future Perspectives. *Prog. Mater Sci.* **2020,** *109*, 100635.
126. Brown, E. S.; Peczonczyk, S. L.; Wang, Z.; Maldonado, S., Photoelectrochemical Properties of CH_3-Terminated P-Type GaP(111)A. *J. Phys. Chem. C* **2014,** *118* (22), 11593-11600.

127. Finlayson, M. F.; Wheeler, B. L.; Kakuta, N.; Park, K. H.; Bard, A. J.; Campion, A.; Fox, M. A.; Webber, S. E.; White, J. M., Determination of Flat-Band Position of Cadmium Sulfide Crystals, Films, and Powders by Photocurrent and Impedance Techniques, Photoredox Reaction Mediated by Intragap States. *J. Phys. Chem.* **1985,** *89* (26), 5676-5681.
128. Stoerzinger, K. A.; Rao, R. R.; Wang, X. R.; Hong, W. T.; Rouleau, C. M.; Shao-Horn, Y., The Role of Ru Redox in pH-Dependent Oxygen Evolution on Rutile Ruthenium Dioxide Surfaces. *Chem* **2017,** *2* (5), 668-675.
129. Gambardella, A. A.; Bjorge, N. S.; Alspaugh, V. K.; Murray, R. W., Voltammetry of Diffusing 2 nm Iridium Oxide Nanoparticles. *The Journal of Physical Chemistry C* **2011,** *115* (44), 21659-21665.
130. Lyon, L. A.; Hupp, J. T., Energetics of the Nanocrystalline Titanium Dioxide/Aqueous Solution Interface: Approximate Conduction Band Edge Variations between H0 = −10 and H- = +26. *The Journal of Physical Chemistry B* **1999,** *103* (22), 4623-4628.
131. Lemon, B. I.; Hupp, J. T., Electrochemical Quartz Crystal Microbalance Studies of Electron Addition at Nanocrystalline Tin Oxide/Water and Zinc Oxide/Water Interfaces: Evidence for Band-Edge-Determining Proton Uptake. *J. Phys. Chem. B* **1997,** *101* (14), 2426-2429.
132. Koelle, U.; Moser, J.; Graetzel, M., Dynamics of Interfacial Charge-Transfer Reactions in Semiconductor Dispersions. Reduction of Cobaltoceniumdicarboxylate in Colloidal Titania. *Inorg. Chem.* **1985,** *24* (14), 2253-2258.
133. Peper, J. L. Studies of Titanium Dioxide Nanoparticles: Thermodynamics and Reactivity. Ph.D. Dissertation, Yale University, New Haven, CT, 2019.
134. Nozik, A. J., Photoelectrochemistry: Applications to Solar Energy Conversion. *Annu. Rev. Phys. Chem.* **1978,** *29* (1), 189-222.
135. White, H. S.; Peterson, J. D.; Cui, Q.; Stevenson, K. J., Voltammetric Measurement of Interfacial Acid/Base Reactions. *J. Phys. Chem. B* **1998,** *102* (16), 2930-2934. The p$K_{1/2}$ is defined in this paper as the pH at which half of the surface acid groups are deprotonated when the electrode potential is at the point of zero charge.
136. Warburton, R. E.; Hutchison, P.; Jackson, M. N.; Pegis, M. L.; Surendranath, Y.; Hammes-Schiffer, S., Interfacial Field-Driven Proton-Coupled Electron Transfer at Graphite-Conjugated Organic Acids. *J. Am. Chem. Soc.* **2020,** *142* (49), 20855-20864.
137. Jackson, M. N.; Surendranath, Y., Molecular Control of Heterogeneous Electrocatalysis through Graphite Conjugation. *Acc. Chem. Res.* **2019,** *52* (12), 3432-3441.
138. Koene, L.; Sluyters-Rehbach, M.; Sluyters, J. H., The Relation between Electrical Double Layer Data and Electronic Work Functions for Amalgams. *J. Electroanal. Chem.* **1995,** *396* (1), 569-581.
139. Strmcnik, D.; Tripkovic, D.; van der Vliet, D.; Stamenkovic, V.; Marković, N. M., Adsorption of hydrogen on Pt(111) and Pt(100) surfaces and its role in the HOR. *Electrochem. Commun.* **2008,** *10* (10), 1602-1605.
140. Bard, A. J.; Faulkner, L. R., *Electrochemical Methods: Fundamentals and Applications*. John Wiley & Sons: NY, 2nd edition, 2001, p 591 for the CV of an ideal Nernstian reaction following a Langmuir isotherm.
141. Eckermann, A. L.; Feld, D. J.; Shaw, J. A.; Meade, T. J., Electrochemistry of Redox-Active Self-Assembled Monolayers. *Coord. Chem. Rev.* **2010,** *254* (15), 1769-1802.
142. Kunimatsu, K.; Senzaki, T.; Samjeské, G.; Tsushima, M.; Osawa, M., Hydrogen adsorption and hydrogen evolution reaction on a polycrystalline Pt electrode studied by surface-enhanced infrared absorption spectroscopy. *Electrochim. Acta* **2007,** *52* (18), 5715-5724.
143. Delley, M. F.; Wu, Z.; Mundy, M. E.; Ung, D.; Cossairt, B. M.; Wang, H.; Mayer, J. M., Hydrogen on Cobalt Phosphide. *J. Am. Chem. Soc.* **2019,** *141* (38), 15390-15402.
144. Crandall, R. S.; Wojtowicz, P. J.; Faughnan, B. W., Theory and measurement of the change in chemical potential of hydrogen in amorphous H_xWO_3 as a function of the stoichiometric parameter x. *Solid State Commun.* **1976,** *18* (11), 1409-1411.
145. Agarwal, R. G.; Kim, H.-J.; Mayer, J. M., Nanoparticle O–H Bond Dissociation Free Energies from Equilibrium Measurements of Cerium Oxide Colloids. *J. Am. Chem. Soc.* **2021,** *143* (7), 2896-2907.

Chapter 2

Determining Proton-Coupled Standard Potentials and X–H Bond Dissociation Free Energies in Nonaqueous Solvents using Open-Circuit Potential Measurements

With contributions from Wise, C. W.; Agarwal, R. G.; Mayer, J. M. "Determining Proton-Coupled Standard Potentials and X–H Bond Dissociation Free Energies in Nonaqueous Solvents using Open-Circuit Potential Measurements." *J. Am. Chem. Soc.* **2020**, *142*, 10681-10691. CFW performed measurements on substrates in acetonitrile and wrote the bulk of the manuscript. RGA performed measurements on substrates in tetrahydrofuran and contributed to the structure, writing, and editing of the manuscript. CFW, RGA, and JMM performed the thermochemical analyses. The authors gratefully acknowledge helpful discussion from Dr. Aaron Appel, Dr. Eric Wiedner, and Dr. Morris Bullock.

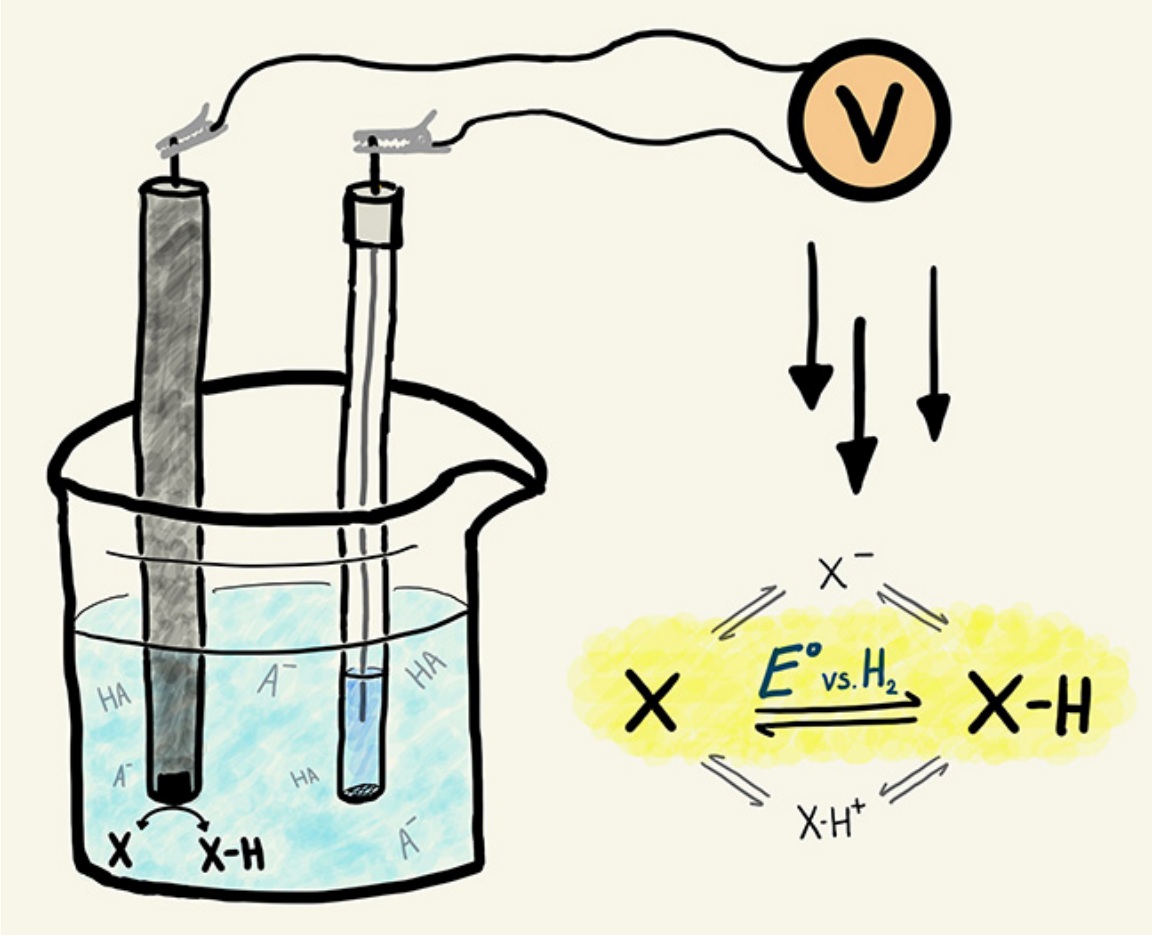

2.1 Introduction

Proton-coupled electron transfer (PCET) reactions are pervasive in biological systems, energy conversion, and catalysis. As a result, the PCET reactivity of organic small molecules, such as quinones, phenols, and hydroxylamines, is the subject of wide-ranging studies. For example, organic PCET reagents are increasingly being utilized as redox mediators in flow batteries,[1-6] electrocatalysis,[7,8] and aerobic oxidations.[9-11] Studies of N_2 reduction[12] and NH_3 oxidation[13-16] are beginning to use organic PCET reagents to add or remove hydrogen atom equivalents from M–N_xH_y species, and their mechanisms are increasingly being discussed as PCET. Understanding and optimizing the reactivity of PCET substrates and intermediates requires knowledge of their underlying thermochemistry. However, the standard potentials and corresponding bond dissociation free energies (BDFEs) of PCET reagents are often unavailable, particularly in nonaqueous solvents where many studies of PCET reactivity are performed.

The lack of thermochemical data for PCET reagents in organic solvents stems in part from the challenge of measuring these values directly. Nonaqueous X–H BDFEs can be obtained through several different methods since Gibbs free energy is a state function and therefore path-independent. Most commonly, these values are obtained by summing a 1e^- reduction potential and pK_a of the substrate (i.e., the "Bordwell" analysis).[17-19] However, this method is limited by its reliance on measurements of the thermodynamics of individual electron transfer (ET) and proton transfer (PT) steps for high-energy and often unstable intermediates, and by its requirement of a pK_a scale in the solvent of interest. Alternatively, in cases where the aqueous PCET standard potential of a reaction is known, the corresponding nonaqueous potential can be derived.[20,21] These conversions require the free energy to transfer the oxidized and reduced substrate between water and the organic solvent, which is generally not

known and can be challenging to measure for PCET reagents with low solubility and/or solvents with high miscibility. Finally, the relative nonaqueous thermochemistry of two PCET reagents can be obtained by measuring the equilibrium constant for the reaction between the oxidized form of one substrate and the reduced form of the other.[17] However, this method does not provide absolute thermodynamic values and is feasible only for substrates that are relatively close in potential, as a difference of 0.059 V/n (where n = number of e^-/H^+ equivalents) corresponds to an order of magnitude difference in equilibrium constant.

Given the limitations of these approaches, a direct method for measuring the standard potential and BDFE(s) of a PCET substrate in nonaqueous conditions would be valuable. In aqueous solutions, direct measurements of PCET potentials are possible using electrochemical methods such as cyclic voltammetry (CV). However, CV measurements of PCET substrates in nonaqueous conditions often show electrochemically irreversible responses for the ne^-/nH^+ process.[22-28] This electrochemical irreversibility typically results from complex hydrogen bonding interactions and/or slow kinetics of proton and electron transfers that prevent the substrate from equilibrating with the electrode on the CV time scale. Consequently, the measured CV midpoint potential does not necessarily indicate a thermodynamic potential. Circumventing these complications requires an electrochemical method that reaches equilibrium on longer time scales.

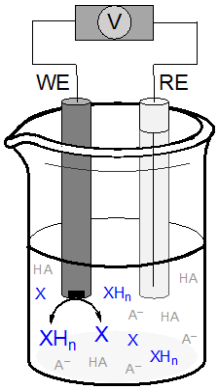

Figure 2.1. Schematic of open-circuit potential measurement for substrate (X/XH_n) in a buffered (HA/A^-) solution. The substrate equilibrates at the working electrode (WE), and the potential is measured relative to a reference electrode (RE).

To that end, we hypothesized that open-circuit potential (OCP) measurements could be used to obtain thermodynamic information about PCET substrates in nonaqueous conditions. The open-circuit potential of a solution is defined as the potential at which no current flows, or the equilibrium potential. In an OCP measurement, all electroactive solution species equilibrate at a working electrode, and the resulting potential is measured against a reference electrode; in essence, the potentiostat acts as a voltmeter (Figure 2.1). Therefore, the OCP is a purely thermodynamic measure of the solution potential, without complications from kinetic or mechanistic factors. This has been demonstrated for the H^+/H_2 couple in acetonitrile by Roberts and Bullock[29] and for electrochemically irreversible (but chemically reversible) redox processes of biological molecules[30] and metal complexes[31] in water.

Herein, we demonstrate that open-circuit potential measurements are a straightforward, robust, accurate, and accessible method for directly measuring ne^-/nH^+ standard potentials of PCET reagents in organic solvents. OCP measurements of 2,6-dimethyl-1,4-benzoquinone in acetonitrile serve as a case study to describe the theoretical and experimental aspects of the method and to provide strategies for obtaining accurate and reproducible results. We demonstrate the applicability of the method for various types of PCET substrates, and we report their standard potentials

and corresponding BDFEs in acetonitrile and tetrahydrofuran. Comparisons of the OCP method to other approaches for determining standard potentials and BDFEs highlight its scope, advantages, and limitations. The method is only applicable to X/XH_n couples whose interconversions are chemically reversible and give some sort of electrochemical response. Particularly valuable is its compatibility with any solvent or solvent mixture amenable to electrochemical measurements. These results and analyses further an understanding of PCET reaction thermochemistry in nonaqueous solvents and provide a tool that will be valuable for applications in catalysis, energy science, and beyond.

2.2 Results

2.2.1 General Experimental Considerations for Open-Circuit Potential Measurements

All OCP measurements were performed in an N_2-filled glovebox using a standard three-electrode setup, with a glassy carbon working electrode, Pt auxiliary electrode, and Ag wire pseudoreference electrode separated from the solution by a glass frit. The OCP was collected on solutions containing both the oxidized (X) and reduced (XH_n) form of the substrate of interest, in X/XH_n ratios ranging from 0.4:1 to 2.5:1. All solutions also contained 0.1 M $[Bu_4N][PF_6]$ electrolyte and a 1:1 acid/conjugate base buffer. Use of a 1:1 ratio of acid/conjugate base minimizes the effects of homoconjugation on the proton activity of the solution solution[29,32] (for substrates that undergo ne^-/nH^+ redox changes, see below). The buffer was present in at least 20-fold excess to the concentrations of X and XH_n, and the solutions were stirred during OCP measurements to promote faster equilibration of substrate. In general, the OCP was recorded every second for 5−10 min, or until the potential had stabilized such that it was changing less than ~1.5 mV over 5 min (~0.005 mV/s). The reported OCP values are averages of data collected in this plateau region. Measurements were performed in acetonitrile and tetrahydrofuran with a range of

substrates, and we note that the magnitude of drift can vary with solvent and substrate. Significant drift results in larger experimental uncertainties but does not preclude obtaining valuable results, unless it prevents observation of a Nernstian dependence on substrate ratio (vide infra). More experimental details are provided in Appendix B.

2.2.2 Case Study: Open-Circuit Potential Measurements and Validation Using 2,6-Dimethyl-1,4-benzoquinone (DMQ).

In this section, we use 2,6-dimethyl-1,4-benzoquinone (DMQ) as a case substrate to describe how to perform OCP measurements and to validate the method. Following the above procedure, the OCP was measured for a solution of equimolar DMQ and 2,6-dimethyl-1,4-hydroquinone (H_2DMQ) in acetonitrile (MeCN) containing an excess of 1:1 pyridinium tetrafluoroborate:pyridine ($pyrH^+$/pyr) buffer. In this case, the OCP reports on the equilibrium potential for the reaction in eq 2.1. As shown in Figure 2.2A, the OCP decreased by several mV in the first ~30 seconds of measurement and then reached a plateau, staying constant within <1 mV over 10 minutes. The stability of these measurements is indicated by the highly magnified y-axis scale, which spans only a 6 mV range. The small upward drift in potential is negligible, approximately 0.03 mV/min, making the total change over 10 minutes 0.3 mV, or less than 0.01 kcal mol^{-1}.

$$DMQ + 2e^- + 2pyrH^+ \rightleftharpoons H_2DMQ + 2pyr \qquad (2.1)$$

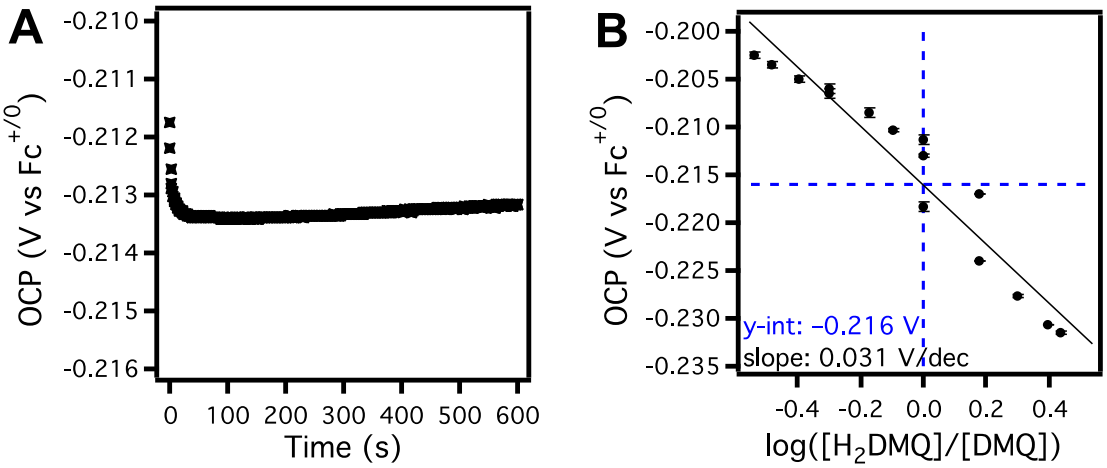

Figure 2.2. All measurements were performed in MeCN containing 0.05 M 1:1 pyrH$^+$/pyr buffer and 0.1 M [Bu$_4$N][PF$_6$] supporting electrolyte. (**A**) The open-circuit potential measured over 600 s for a solution of 1.0 mM DMQ and 1.0 mM H$_2$DMQ. Data was collected every second. (**B**) Open-circuit potentials measured at different ratios of DMQ:H$_2$DMQ and plotted against log([H$_2$DMQ]:[DMQ]), showing Nernstian dependence. Error bars represent one standard deviation in the measured potential over 600 s. The intersection of the dashed lines is the formal potential, $E^{\circ\prime}_{OCP}$ = –0.216 V vs Fc$^{+/0}$ (*vide infra*).

Several experimental considerations were developed to facilitate the OCP measurements and minimize potential sources of error. First, the DMQ:H$_2$DMQ ratio was kept close to 1:1, since we have found that large excesses in one direction or the other result in slow equilibrations and, as a result, less reliable data. As shown by Figure 2.2A, the equilibrated potential changes slowly over time, likely due to electroactive impurities or drift in the reference electrode over the long timescales of these experiments. The direction of the drift is consistent, so the DMQ:H$_2$DMQ ratio was varied in both directions to offset any error introduced by this effect. We have found that this strategy is particularly useful for cases where the magnitude of the drift is larger, and we recommend employing it for all substrates.

After the OCP measurements, ferrocene (Fc) was added to the DMQ/H$_2$DMQ solution, and a cyclic voltammogram was collected to obtain $E_{1/2}$(Fc$^+$/Fc) as a reference. Ferrocene cannot be present during the OCP measurements because it is electroactive and would skew the measured potential. The accuracy of $E_{1/2}$(Fc$^+$/Fc) is critical to ensure day-to-day reproducibility in the OCP measurements, since pseudo-

reference electrodes often drift slightly between experiments. However, collecting reliable CVs of Fc can be challenging in organic solvents that have low ion mobility and, as a result, high solution resistance. Thus, the internal resistance of the cell must be properly compensated such that the peak-to-peak separation of the $Fc^{+/0}$ couple is as close as possible to the theoretical 57.0 mV (at 25 °C).[33] If the $Fc^{+/0}$ couple overlaps with redox features of the substrate or is incompatible with the buffer,[34] another $1e^-$ redox agent can be used as an internal standard and its potential measured with respect to Fc in a separate solution under the same conditions.

The measured OCPs were validated as equilibrium potentials for the interconversion of DMQ and H_2DMQ by showing that they followed the Nernst equation. The Nernst equation to describe the reaction shown in eq 2.1 and similar PCET reactions is given in eq 2.2, where the more typical $[H^+]$ in the logarithm term has been substituted for the equilibrium expression $[H^+] = K_a[HA]/[A^-]$. Eq 2.2 predicts that an order of magnitude change in the ratio of oxidized to reduced substrate should be accompanied by a shift in the OCP of (0.0592/n) V, where n is the number of electrons passed. OCP measurements collected at varying ratios of H_2DMQ:DMQ in a 1:1 $pyrH^+$/pyr buffer solution in MeCN trended as predicted. A plot of the measured OCP vs. log([H_2DMQ]/[DMQ]) showed a –0.031(2) V/dec slope (Figure 2.2B), which is close to the theoretical slope of –0.0296 V/dec for a $2e^-/2H^+$ process such as this one (dec = decade, a 10-fold change in relative concentrations).

$$E = E^\circ - \frac{0.0592}{n}\log\frac{[\mathrm{XH}_n][\mathrm{A}^-]^n}{[\mathrm{X}][\mathrm{HA}]^n} - 0.0592\mathrm{p}K_\mathrm{a} \qquad (2.2)$$

To further validate the OCP method, the response of the measured potential to changes in buffer strength and buffer identity were examined. Per the Nernst equation, the OCP should not be affected by changing the buffer strength (the absolute concentration of the 1:1 HA and A^-). Consistent with this analysis, the OCP of an equimolar DMQ/H_2DMQ solution was constant within 1–2 mV at $pyrH^+$/pyr buffer

strengths from 2–50 mM (Figure 2.3A). The Nernst equation also predicts that changing the identity of the 1:1 buffer should change the OCP by –0.0592 V per pK_a unit. We probed this expected dependence by measuring the OCP of equimolar DMQ/H_2DMQ solutions in MeCN with 1:1 buffers of *N,N*-dimethylformamidium triflate/*N,N*-dimethylformamide (H^+-DMF/DMF, pK_a = 6.1),[35] pyrH^+/pyr (pK_a = 12.53),[36] lutidinium tetrafluoroborate/lutidine (lutH^+/lut, pK_a = 14.13),[36] and triethylammonium tetrafluoroborate/triethylamine (Et_3NH^+/Et_3N, pK_a = 18.82).[36] For each measurement, the buffer was in approximately 50-fold excess to substrate. A plot of OCP vs pK_a (Figure 2.3B) had a slope of –0.058 V/pK_a unit, in good agreement with the expected value. Observing the expected changes to the OCP with variations in buffer strength and identity indicates that the method gives accurate equilibrium thermodynamic measurements.

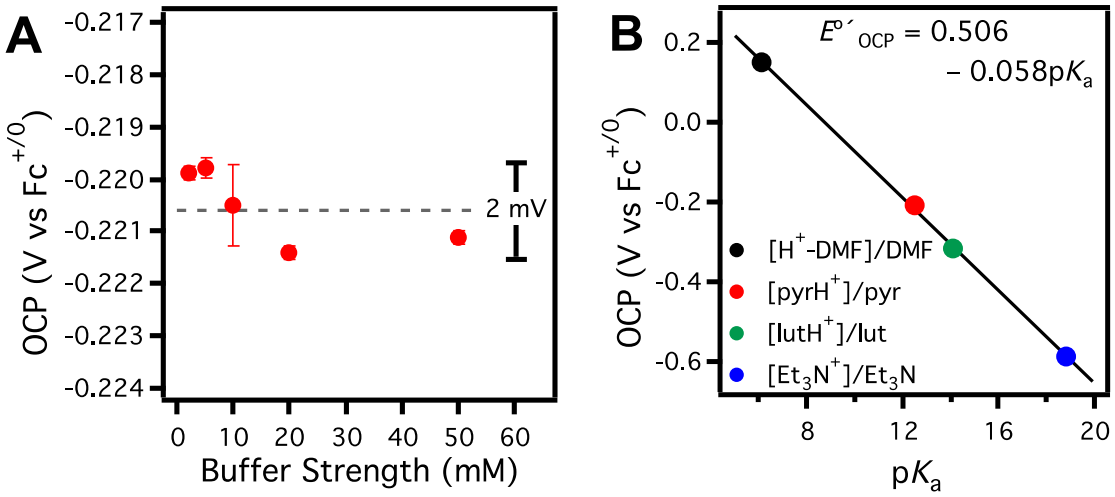

Figure 2.3. All measurements were performed in MeCN containing 0.1 M [Bu_4N][PF_6] supporting electrolyte. (**A**) Open-circuit potentials (vs $Fc^{+/0}$) for solutions of 0.56 mM DMQ and H_2DMQ with 2–50 mM 1:1 pyrH^+/pyr buffer. Gray dashed trace is the average OCP from all buffer strengths. Error bars represent one standard deviation in the measured potential over 600 s. (**B**) Open-circuit potentials measured for solutions of 1:1 DMQ:H_2DMQ with buffers of 0.05 M H^+-DMF/DMF (black), pyrH^+/pyr (red), lutH^+/lut (green) or Et_3NH^+/Et_3N (blue). Error bars (one standard deviation) are smaller than the data points.

The measured OCP at a 1:1 ratio of $X:XH_n$, gives the formal potential vs. $Fc^{+/0}$ ($E^{\circ\prime}_{OCP}$) under the experimental conditions.[37] For the DMQ/H_2DMQ redox couple with a

pyrH$^+$/pyr buffer in MeCN, $E^{\circ\prime}_{OCP}$ is the y-intercept at the center of the plot in Figure 2.2B: −0.216 V vs $Fc^{+/0}$. The formal potentials reported here are all defined at equal concentrations of oxidized and reduced substrate ([X] = [XH_n]) and in 1:1 buffers ([HA] = [A^-]). Because a proton is involved in the redox process, the formal potential of DMQ depends on the proton activity of the solution and therefore is only comparable to potentials of other PCET substrates measured under the same experimental conditions. We note that these formal potentials can be converted to the corresponding standard potential vs $Fc^{+/0}$ (E°_{OCP}) using the Nernst equation (eq 2.2). For a redox couple involving equal numbers of protons and electrons, E°_{OCP} is the formal potential plus 0.0592pK_a, or in other words, the formal potential extrapolated to standard state for proton activity. Measured values of the standard potential E°_{OCP} are equal regardless of the buffer condition in which the measurement was performed, as illustrated above by the near Nernstian slope of the data in Figure 2.3B.

2.2.3 Generality of the OCP Method

After establishing the validity of the OCP method with DMQ in MeCN as a case substrate, we explored the generality of the technique by performing measurements on a variety of substrates in MeCN and tetrahydrofuran (THF) using the same experimental set-up and procedure as described above. All substrates examined have stable, well-defined oxidized and reduced forms and undergo ne^-/nH^+ reactions. The substrate scope included compounds that contain O–H and N–H bonds and that undergo 1e^-/1H^+ as well as 2e^-/2H^+ redox transformations. The metal complex iron(II) tris(2,2′-bi-imidazoline)$^{2+}$ ($Fe^{II}H_2$bim), which is known to undergo multi-site PCET with electron transfer to the metal and proton transfer to the ligand,[38] was also measured. The substrates are shown in Figure B1 (Appendix B), with the relevant H atom(s) highlighted in red. Table 2.1 reports $E^{\circ\prime}_{OCP}(X/XH_n)$ with the associated buffer and solvent conditions. In all cases, the OCP was measured at different ratios of $X:XH_n$,

and the reported $E^{\circ\prime}_{OCP}$ is the y-intercept of the corresponding plot of OCP vs $\log([XH_n]/[X])$ (where $[XH_n] = [X]$) (see Appendix B).

As with the DMQ/H_2DMQ case, collecting OCP measurements at different $X:XH_n$ ratios for each substrate provided a means to internally validate the accuracy of the measured potentials. Specifically, we probed the expected Nernstian dependences of 59.2 or 29.6 mV/dec for substrates that undergo $1e^-/1H^+$ or $2e^-/2H^+$ redox processes, respectively. For the majority of the substrates, the OCP vs $\log([XH_n]/[X])$ plot showed a slope within 5 mV/dec of the expected value (Figures B2-B21). However, in some cases the slopes differed from the expected values by 10-15 mV/dec. We attribute these deviations to the occurrence of side reactions that form new electroactive species in solution (see Appendix B.3). In such situations, we recommend performing OCP measurements with several buffers to identify conditions that reduce undesired side reactivity and/or to obtain an average potential value. Even for the substrates that displayed significantly non-Nernstian behavior, we found that $E^{\circ}_{OCP}(X/XH_n)$ agrees within ~20 mV between buffer conditions, an improvement on standard literature methods for measuring PCET thermochemistry, which typically report values to $\pm$ 2 kcal mol^{-1} (~ 87 mV).[17]

Table 2.1. Measured formal potentials for PCET substrates in acetonitrile and tetrahydrofuran

	Acetonitrile [a]		Tetrahydrofuran [b]
Substrate	$E^{\circ\prime}_{OCP}$ (V vs $Fc^{+/0}$)	buffer	$E^{\circ\prime}_{OCP}$ (V vs $Fc^{+/0}$)
2,4,6-tri-*tert*-butylphenol	−0.15(1)	Et_3NH^+/Et_3N	−0.180(7)
1,1-diphenyl-2-picrylhydrazine	0.147(8)	$pyrH^+$/pyr	−0.216(7)
4-methoxy-2,6-di-*tert*-butylphenol	−0.274(1)	Et_3NH^+/Et_3N	−0.311(1)
$[Fe^{II}H_2bim]$ [c]	−0.429(3)	Et_3NH^+/Et_3N	nd [d]
1,4-hydroquinone	−0.106(2)	$pyrH^+$/pyr	−0.480(8)
TEMPOH [e]	−0.120(1)	$pyrH^+$/pyr	−0.560(8)
2,6-dimethyl-1,4-hydroquinone	−0.219(3)	$pyrH^+$/pyr	−0.588(7)
2,6-di-*tert*-butyl-1,4-hydroquinone	−0.295(6)	$pyrH^+$/pyr	nd
2,6-dimethoxy-1,4-hydroquinone	0.08(1)	DMF-H^+/DMF	nd
1,4-dihydroxynaphthalene	nd		−0.683(7)
2,7-di-*tert*-butyl-1,4-dihydroxynaphthalene	nd		−0.734(2)
1,2-diphenylhydrazine	−0.383(2)	$pyrH^+$/pyr	nd
5,10-dihydrophenazine	−0.479(1)	$pyrH^+$/pyr	nd
1,8-dichloro-9,10-dihydroxyanthracene	nd		−0.998(4)

[a] All measurements in MeCN contained 50 mM buffer and 0.1 M $[Bu_4N][PF_6]$ supporting electrolyte. Reported values are y-intercepts of plots of OCP vs log($[XH_n]/[X]$). The reported uncertainty is one standard deviation of multiple measurements (multiple y intercepts) in the same buffer condition with different stock solutions on different days. [b] All measurements in THF contained 20 mM Et_3NH^+/Et_3N buffer and 0.1 M $[Bu_4N][PF_6]$ supporting electrolyte. Reported values are y-intercepts of plots of OCP vs log($[XH_n]/[X]$). The reported uncertainty is one standard deviation from multiple measurements of 1:1 $X:XH_n$ mixtures. [c] Iron(II) tris(2,2′-bi-imidazoline)$^{2+}$. [d] not determined (so no buffer is listed). [e] 2,2,6,6-tetramethyl-1-hydroxypiperidine.

2.3 Discussion

2.3.1 Standard Potentials vs Hydrogen

We advocate in this report that nonaqueous PCET reduction potentials be referenced to the hydrogen potential in the solvent of interest (eq 2.3), similar to the use of NHE and RHE for aqueous solutions (see supporting information of [39]). While

ferrocene ($Fc^{+/0}$) is the typical standard for electrochemistry in organic solvents, changing to H^+/H_2 has a number of advantages for ne^-/nH^+ redox couples.

$$2H^+_{(solvent)} + 2e^- \rightleftharpoons H_{2(g)} \qquad (2.3)$$

By using hydrogen gas as a reference state, PCET potentials are largely independent of the solvent and solution conditions. From another perspective, potentials vs H_2 are not electrochemical reactions at all, but simply the free energy of hydrogenation of X to XH_n in the solvent of interest. We emphasize that these arguments and the thermochemical cycles developed below are for reactions involving equal numbers of protons and electrons, X/XH_n. Reactions with unequal numbers of protons and electrons, such as hydride transfers, have somewhat more complex thermochemistry.[40]

In acetonitrile, converting the formal potential vs $Fc^{+/0}$ to the standard potential vs H^+/H_2 (or potential of hydrogenation) is straight-forward, since the standard hydrogen potential vs $Fc^{+/0}$ (eq 2.6 in Scheme 2.1) has been reported. Roberts and Bullock determined $E°(H^+/H_2)$ = –0.028(4) V vs $Fc^{+/0}$ using a related OCP method.[29] Combining $E°'_{OCP}(X/XH_n)$, $pK_a(HA)$, and $E°(H^+/H_2)$ per Scheme 2.1 gives $E°(X/XH_n$, V vs H_2). These values are reported in Table 2.2. Each estimated uncertainty includes: one standard deviation from multiple $E°'_{OCP}(X/XH_n)$ measurements, the reported uncertainty in $E°(H^+/H_2)$, and the measured uncertainty in $E_{1/2}(Fc^+/Fc)$. The small overall uncertainties (<10 mV) reflect the stability of the OCP measurements and robustness of the method. See Appendix B.3 for a more detailed discussion of error analysis.

Scheme 2.1. Thermochemical Cycle for Converting OCP to Standard Potential vs H^+/H_2

$$X + nHA + ne^- \xrightarrow{E^{\circ\prime}_{OCP}(V \text{ vs } Fc^{+/0})} XH_n + nA^- \quad (2.4)$$

$$nH^+ + nA^- \xrightarrow{0.0592[pK_a(HA)]} nHA \quad (2.5)$$

$$^n/_2H_2\ (g) \xrightarrow{-E^\circ(H^+/H_2, \text{ vs. } Fc^{+/0})} nH^+ + ne^- \quad (2.6)$$

$$X + {}^n/_2H_2\ (g) \xrightarrow{E^\circ(X/XH_n, V \text{ vs } H_2)} XH_n \quad (2.7)$$

Scheme 2.1 requires a standard hydrogen potential vs $Fc^{+/0}$ and therefore cannot be applied to THF or any solvent mixture without an established pK_a scale. However, the net reaction at the bottom of Scheme 2.1 (eq 2.7) can be attained by an alternative thermochemical cycle that does not require either the pK_a of the buffer or the standard hydrogen potential in the solvent of interest. Scheme 2.2 also starts from the OCP measurement of the X/XH_n couple in an HA/A^- buffer but uses the H_2 potential *in the same buffer* ($E°'(H^+/H_2)$, eq 2.8) to obtain the standard reduction potential of the substrate ($E^\circ(X/XH_n)$). Measurements of $E°'(H^+/H_2)$ can be performed following the literature procedure[29] and involve a similar OCP approach to that described above (see Appendix B.4 for details).

Scheme 2.2. Thermochemical Cycle to Directly Convert OCP to Standard Potential vs H_2

$$X + nHA + ne^- \xrightarrow{E^{\circ\prime}_{OCP}(V \text{ vs } Fc^{+/0})} XH_n + nA^- \quad (2.4)$$

$$^n/_2H_2 + nA^- \xrightarrow{-E^\circ(H^+/H_2, \text{ vs. } Fc^{+/0})} nHA + ne^- \quad (2.8)$$

$$X + {}^n/_2H_2 \xrightarrow{E^\circ(V \text{ vs } H_2)} XH_n \quad (2.7)$$

This H_2 couple inherently contains thermochemical information about both the proton and the electron; thus, by following the cycle in Scheme 2.2, the buffer properties cancel, and $E^\circ(X/XH_n)$ is simply the sum of $E^{\circ\prime}_{OCP}(X/XH_n)$ and $E^{\circ\prime}(H^+/H_2)$. Values of $E^\circ(X/XH_n)$ for substrates measured in THF are reported in Table 2.2, and the

uncertainty reflects one standard deviation from multiple $E°'_{OCP}(X/XH_n)$ measurements as well as the measured uncertainty in $E°'(H^+/H_2)$. Scheme 2.2 can be applied to any solvent, mixed solvent, or electrolyte condition amenable to electrochemical measurements, and use of this cycle removes any error or uncertainty associated with reported pK_a values. These features of the OCP method are potentially very valuable because accurate pK_a scales and extensive tables of pK_a values exist only for a few organic solvents.

Table 2.2. Standard potentials and BDFEs for PCET substrates in acetonitrile and tetrahydrofuran

	Acetonitrile		Tetrahydrofuran	
Substrate	$E°$(V vs H_2)[a]	BDFE (kcal mol^{-1})[b]	$E°$(V vs H_2)[c]	BDFE (kcal mol^{-1})[b]
2,4,6-tri-*tert*-butylphenol	0.99(1)	74.8	0.97(1)	74.4
1,1-diphenyl-2-picrylhydrazine	0.917(9)	73.1	0.93(1)	73.5
4-methoxy-2,6-di-*tert*-butylphenol	0.868(4)	72.0	0.837(7)	71.3
[$Fe^{II}H_2$bim][d]	0.713(5)	68.4	nd[e]	nd
1,4-hydroquinone	0.664(4)	67.3	0.66(1)	67.4
TEMPOH[f]	0.60(6)	66	0.58(1)	65.5
2,6-dimethyl-1,4-hydroquinone	0.550(7)	64.6	0.56(1)	64.9
2,6-di-*tert*-butyl-1,4-hydroquinone	0.475(8)	62.9	nd	nd
2,6-dimethoxy-1,4-hydroquinone	0.469(7)	62.8	nd	nd
1,4-dihydroxynaphthalene	nd	nd	0.46(1)	62.7
2,7-di-*tert*-butyl-1,4-dihydroxynaphthalene	nd	nd	0.414(7)	61.5
1,2-diphenylhydrazine	0.387(4)	60.9	nd	nd
5,10-dihydrophenazine	0.291(4)	58.7	nd	nd
1,8-dichloro-9,10-dihydroxyanthracene	nd	nd	0.150(8)	55.4

[a] Calculated following Scheme 2.1, using $E°(H^+/H_2)$ = −0.028(4) V vs $Fc^{+/0}$ and the appropriate buffer pK_a. The reported uncertainty is one standard deviation from multiple measurements (in the same or different buffer conditions) propagated with the uncertainties in $E°(H^+/H_2)$ and $E_{1/2}(Fc^{+/}Fc)$. [b] Calculated as BDFE(X–H) = $23.06E°(X/XH_n)$ + $\Delta G°(½H_2(g)/H^{\bullet}{}_{1M})$ (eq 2.13), where $\Delta G°(½H_2\ (g)/H^{\bullet}{}_{1\,M})$ = 52.0 kcal mol^{-1} for both MeCN and THF (Table 2.3). Relative uncertainties can be converted from the uncertainties in $E°(X/XH_n)$ and are < 0.3 kcal mol^{-1} for most substrates. Absolute uncertainties are about ± 1 kcal mol^{-1} taking into account the uncertainty in approximating the solvation of H• as H_2, which is discussed in more detail in Appendix B.3.1.5 and ref. [41]. [c] Calculated using $E°'(H^+/H_2)$ = −1.148(7) V vs $Fc^{+/0}$ in a Et_3NH^+/Et_3N buffer (Appendix B.4.1), following Scheme 2.2. The reported uncertainty is one standard deviation from multiple measurements of 1:1 mixtures of $X:XH_n$ propagated with the uncertainty in $E°'(H^+/H_2)$. [d] Iron(II) tris(2,2′-bi-imidazoline)$^{2+}$. [e] not determined. [f] 2,2,6,6-tetramethyl-1-hydroxypiperidine.

2.3.2 BDFEs from PCET Standard Potentials vs H_2

The standard potential vs H_2 for a PCET reagent is closely related to its average X–H BDFE, as shown in Scheme 2.3. Eq 2.9 converts the standard potential to the free energy to remove $H_{2(g)}$. By definition, a solution BDFE is the free energy for the homolysis of a *single* X–H bond to form solvated X$^\bullet$ and H$^\bullet$. Thus, the sum of the X–H BDFEs in XH_2, for example, is the sum of: (*i*) the energy to remove H_2 (eq 2.9), (*ii*) the free energy of homolysis of $½H_{2(g)}$ into $2H^\bullet_{(g)}$ (eq 2.10), and (*iii*) the free energy to transfer the two H$^\bullet$ from the gas phase to solution (eq 2.11).

Scheme 2.3. Thermochemical Cycle for Converting Standard Potential to BDFE

$$XH_n\ (solv) \xrightarrow{\Delta G^\circ = nFE^\circ(X/XH_n)} X\ (solv) + (^n/_2)H_2\ (g) \qquad (2.9)$$

$$(^n/_2)H_2\ (g) \xrightarrow{n\Delta G^\circ(^1/_2H_2/H^\bullet)} nH^\bullet\ (g,\ 1\ atm) \qquad (2.10)$$

$$nH^\bullet\ (g,\ 1\ atm) \xrightarrow{n\Delta G^\circ(H^\bullet(g)/H^\bullet(solv))} nH^\bullet\ (solv,\ 1M) \qquad (2.11)$$

$$XH_n\ (solv) \xrightarrow{\Delta G^\circ = n(BDFE)} X\ (solv) + nH\bullet\ (solv,\ 1M) \qquad (2.12)$$

Equations 2.10 and 2.11 in Scheme 2.3 involve only hydrogen and not the PCET reagent of interest. The gas-phase BDFE of $½H_{2(g)}$ to $H^\bullet_{(g)}$ (eq 2.10) is solvent-independent and is very accurately known to be 48.6 kcal mol^{-1} from literature enthalpies and entropies of formation.[42] Eq 2.11 is a solvent-dependent term for the free energy of solvation for H$^\bullet$, from the gas-phase standard state of 1 atm to the solution-phase standard state of 1 M. This term has been much discussed, with the consensus that it is well approximated as being the same as that of H_2 in a number of organic solvents.[37,43,44] The derivation of $\Delta G^\circ(½\ H_{2(g)}/H^\bullet_{1M})$ from these data is discussed in Appendix B.5, and the values are reported in Table 2.3 below.

Table 2.3. Free Energy to Convert ½ H_2 (g) to $H^{\bullet}_{1M}$ in Organic Solvents [a]

Solvent	$\Delta G^{\circ}(\frac{1}{2}H_{2(g)} / H^{\bullet}_{1M})$
acetonitrile	52.0
N,N-dimethylformamide	52.3
1,4-dioxane	52.2
acetone	51.9
tetrahydrofuran	52.0
toluene	52.0
n-hexane	51.7

[a] Calculated using data from references [42] and [43], values in kcal mol^{-1} at 298 K, see Appendix B.5 for details. The uncertainty in these values is dominated by the uncertainty in the assumption that the solvation of $H^{\bullet}$ can be approximated with that of H_2. The validity of this assumption has been rigorously examined in water with a reported uncertainty of $\pm$ 0.03 V, or ~0.7 kcal mol^{-1}. We therefore conservatively apply an uncertainty of $\pm$ 1 kcal mol^{-1} to these free energies.

The $E^{\circ}(X/XH_n)$ values in Table 2.2 can be combined with the appropriate $\Delta G^{\circ}(\frac{1}{2}H_2$ (g)/$H^{\bullet}_{1M}$) from Table 2.3 to yield $BDFE_{avg}(XH_n)$, also reported in Table 2.2 (eq 2.13). As discussed in Section 2.3.3 below, BDFEs should be relatively solvent independent. Consistent with this analysis, the calculated BDFEs for the six substrates measured in both MeCN and THF differed by less than 0.6 kcal mol^{-1}. External validation of the OCP method by comparing our results to literature BDFEs was more challenging, since most of the BDFE values presented in Table 2.3 have never previously been measured. However, the few reports of BDFEs in MeCN agree well with our OCP measurements (all values in kcal mol^{-1}): BDFE(TEMPOH) = 66 $\pm$ 1 (here) and 64.2 $\pm$ 2 (adjusted lit.); BDFE(2,4,6-^{t}Bu$_3$PhOH) = 74.7 $\pm$ 0.3 (here) and 74.8 $\pm$ 2 (adjusted lit.), and BDFE($Fe^{II}H_2$bim) = 68.3 $\pm$ 0.1 (here) and 69.4 $\pm$ 2 (adjusted lit.) (the adjusted literature values have been recalculated from the prior report[17,45] using the corrected C_G for MeCN reported in Section 2.3.4 below). As the OCP method *directly* measures the PCET potential of the substrate, it should yield more accurate BDFE values than other methods.

$$BDFE_{avg}(X–H) = 23.06E^{\circ}(X/XH_n) + \Delta G^{\circ}(\tfrac{1}{2}H_{2(g)} / H^{\bullet}_{1M}) \qquad (2.13)$$

2.3.3 Solvent Dependence of Standard Potentials vs. H_2 and BDFEs

The standard potential for X to XH_n referenced to H^+/H_2 is simply the free energy of hydrogenation in that solvent ($E° = -\Delta G°/nF$), as noted in Section 2.3.1 above. This implies that the value of $E°$ in different solvents should differ only by the changes in the free energies of solvation for X and XH_n between solvents. Neutral organic molecules of similar size tend to have similar solvation free energies in organic solvents, and these $\Delta G°_{solv}$ typically have small magnitudes. The primary difference in solvation of XH_n and X is the formation of XH_n-solvent hydrogen bonds, but the strength of those hydrogen bonds vary only slightly between H-bond accepting solvents like MeCN and THF.[17,46,47] Therefore, OCP measurements of $E°$ values vs. H_2 can be directly compared and should vary only a small amount between solvents. The average BDFEs should also be similar in different solvents, since the free energy to convert $½H_{2(g)}$ to $H^{\bullet}_{solv}$ differs only slightly between solvents ($\pm$ 0.5 kcal mol^{-1}, Table 2.3). For comparisons of both $E°$ and BDFE values, the largest differences will be observed between solvents with very different hydrogen bonding properties, as discussed elsewhere.[17,48-50]

As an example, Table 2.4 compares $E°$ and BDFE values for the DMQ/H_2DMQ couple in in acetonitrile, THF, DMF, isopropanol, and water. The values in organic solvents are from OCP measurements (Table 2.2**,** and Appendix B.2.3 & B.2.4); the aqueous experimental value is from cyclic voltammetry studies in reference [51]. All $E°$ values are the same within 30 mV, despite the very large differences in polarity and hydrogen bonding over this series of solvents. Similarly, the BDFEs vary by only 1.3 kcal mol^{-1}. Table 2.4 also includes a computed aqueous $E°$ value for this quinone, from DFT calculations,[51] which is in excellent agreement as well. Similar comparisons between solvents and with computations for other substrates are presented in Table B3. The close agreement between these various values provides further validation of the OCP method presented here. The conclusion that $E°$ values vs. H_2 and BDFEs vary

little with solvent should be of broad value and reinforces our encouragement to report *E*° for PCET couples versus the hydrogen reference electrode.

Table 2.4. Solvent dependence of standard potentials and BDFEs for 2,6-dimethyl-1,4-hydroquinone and comparison with computation.

Solvent	$E°$(V vs H_2)[a]	BDFE (kcal mol^{-1})[b]
MeCN	0.550(7)	64.6
THF	0.56(1)	64.9
DMF	0.578(2)	65.6
IPA	0.566(5)	nd[c]
H_2O (expt.)	0.5475	65.9
H_2O (DFT)	0.553	66.1

[a] Experimental *E*° in organic solvents from OCP measurements (Table 2.2 and Table B3). Experimental and computational *E*° in H_2O taken from reference [51]. [b] BDFE values from Table 2.2 or eq 2.13, where $\Delta G°(½H_{2(g)} / H^{\bullet}_{1M})$ = 52.3 kcal mol^{-1} for DMF from Table 2.3 and 53.3 kcal mol^{-1} for H_2O from ref. [39]. [c] Not determined.

2.3.4 Comparing the OCP Method to Standard Methods for Determining Solution BDFEs

Solution BDFEs are most commonly determined using eq 2.14 or its variant with pK_a(XH^+) and $E°(XH^{+/0})$.[17] This approach, developed by Bordwell,[18,19] requires thermodynamic parameters for high-energy intermediates and having a pK_a scale in the solvent of interest. In addition, accurate BDFE calculations require that the thermodynamic measurements be performed under identical conditions, while literature pK_a values are rarely measured in the presence of the electrolyte used for *E*° measurements. pK_a values and electrochemical potentials often vary substantially with solvent because the solvation of ions is exoergic and strongly dependent on the properties of the solvent. In some solvents, such as THF, ion pairing effects must also be taken into account, both when deriving a pK_a scale (as done in ref [52]) and when determining the proton activity of THF solutions. For instance, the proton activity will typically depend on the absolute concentrations of acid/base and on the nature of the counter ion in the $[BH^+][Y^-]$/B or AH/$[A^-][Z^+]$ buffer. The OCP method avoids many of

these complications by providing direct measurements of the proton-coupled potential and the hydrogen potential under the exact conditions of interest. Using the same solution conditions to collect thermodynamic data for the substrate and the e^-/H^+ equivalents (eqs 2.4 and 2.8 in Scheme 2.2) minimizes the effects of ion pairing and solvation on the accuracy of the data.

$$\mathrm{BDFE_{sol}(X{-}H)} = 1.37\mathrm{p}K_a(\mathrm{XH}) + 23.06E°(\mathrm{X^{0/-}}) + C_{\mathrm{G,sol}} \qquad (2.14)$$

There are cases, however, where the OCP method cannot be used to directly obtain a BDFE. In an overall $2e^-/2H^+$ redox process, for instance, it does not provide the individual BDFEs (for HX–H and $^{\bullet}$X–H). These individual BDFEs often differ substantially from the average BDFE calculated from OCP measurements, with the first BDFE usually being much stronger. While average BDFEs are often better thermodynamic predictors of overall reactivity, knowledge of individual BDFEs can be valuable for kinetic studies.[17] Calculation of the component BDFEs of HX–H and $^{\bullet}$X–H can sometimes be accomplished using a Bordwell analysis (eq 2.14), barring any of the aforementioned limitations of this approach. However, due to the instability of the various intermediates, calculation of both component BDFEs in this manner is rarely possible.[17] As a result, we propose the complementary use of the Bordwell analysis and OCP measurements as an alternative strategy for the experimental determination of thermochemical values across the various sections of a square scheme. Knowing the average BDFE from OCP measurements and one component BDFE from the Bordwell approach allows facile calculation of the second component BDFE.

As another example, when the proton and electron come from different sources, eq 2.14 is used to calculate the *effective* BDFE of the hydrogen atom equivalent.[17] In these situations, OCP measurements can provide a measurement of the C_G term, defined as $-FE°(H^{+/\bullet})$, though we note that this approach is only feasible for solvents with a pK_a scale. As an example, we derive here the C_G in THF. To our knowledge, the

only reported C_G(THF) comes from converting the corresponding C_H term, which gives a value of 61 kcal mol^{-1}.[53] Using our measured OCP for $E°'(H^+/H_2)$ with 1:1 $[Et_3NH][BF_4]/Et_3N$ buffer and 0.1 M $[NBu_4][PF_6]$ electrolyte in THF and p$K_a(Et_3NH^+)$ = 13.66 ± 0.05 (from ref. [52]) yields $E°(H^+/H_2)$ = –0.339(8) V vs $Fc^{+/0}$. Addition of this $E°(H^+/H_2)$ to $\Delta G°(½H_{2(g)}$ / $H^•_{1M})$ for THF gives C_G(THF) = 59.8 kcal mol^{-1}. However, these thermochemical values appear to have a significant dependence on solution conditions, likely due to the strong ion-pairing effects mentioned above. For instance, a reported $E°'(H^+/H_2)$ in THF measured with the same OCP method and buffer but with $[NBu_4][B(C_6F_5)_4]$ electrolyte[54] differs from our measurement by 20 mV and yields $E°(H^+/H_2)$ = –0.361 V vs $Fc^{+/0}$ and C_G(THF) = 60.3 kcal mol^{-1}. Additionally, using the CV midpoint potential of $HClO_4$ in THF containing $[NBu_4][ClO_4]$ electrolyte, another report determined $E°(H^+/H_2)$ = –0.44 V vs $Fc^{+/0}$,[55] which would give C_G(THF) = 62.1 kcal mol^{-1}, although this value carries a greater uncertainty as has been discussed elsewhere.[56] We recommend that investigators use C_G(THF) = 60.4 ± 2 kcal mol^{-1}, an average of the value derived from C_H and those determined using an OCP approach, with a conservative uncertainty to account for the potentially large effects of ion pairing under different electrolyte/buffer conditions. These results also highlight the value in studying PCET reactions under the same solution conditions as those used for thermochemical measurements, a stipulation that is more easily met when using the OCP method to directly measure PCET thermodynamics.

We note that previously reported C_G terms for MeCN and DMF[17,38] should be corrected for a sign error in their derivations. Summing $\Delta G°(½H_{2(g)}$ / $H^•_{1M})$ values from Table 2.3 and literature values of $E°(H^+/H_2)$[20,29] gives the C_G terms for MeCN and DMF as 52.6 kcal mol^{-1} and 67.6 kcal mol^{-1}, respectively. See Appendix B.6 for details.

2.3.5 Scope, Advantages, and Limitations of OCP Measurements

The above discussion demonstrates that OCP measurements are a powerful method for obtaining accurate standard potentials and BDFEs for a wide variety of

PCET reagents in a number of solvents. In this section, we summarize the scope of the method and its requirements, and we discuss some advantages and limitations in the context of alternative approaches to measuring nonaqueous PCET thermodynamics.

To obtain accurate measurements with the OCP method, a few simple requirements must be met. The solvent should be able to solubilize ≥ 0.1 M electrolyte and ≥ 0.02 M acid/base buffer to achieve sufficient ionic conductivity and facilitate proton transfer. Both the oxidized (X) and reduced (XH_n) forms of the substrate should have appreciable solubility (≥ ~1 mM concentrations) in the solvent and electrolyte of interest and be stable over the course of the experiment. If these conditions are not met the redox potential of interest may not be the dominant one in solution, and the measured OCP may be skewed by the occurrence of side reactions and/or the presence of redox-active impurities. Additionally, an inherent limitation of the OCP method is its inability to provide thermochemical information for reactions involving transient species; other methods are needed for such cases.[49,57-59] We have observed faster equilibration times when the concentrations of X and XH_n are within a factor of 2 of each other, and we generally avoided measurements with concentrations that differed by more than a factor of 5. All of our successful measurements involved substrates that are electroactive within the solvent window, as determined experimentally by cyclic voltammetry (CV). Overall, the observation of PCET redox features in a CV, regardless of electrochemical reversibility, is a good indication that the substrate and system will be amenable to OCP measurements. Nonetheless, we encourage readers to use experimental checks – such as probing the dependence of the OCP on $\log([XH_n]/[X])$ and buffer pK_a – to determine whether their measurements are thermodynamically relevant.

However, some substrates that appeared to meet these requirements showed inconsistent behavior. One example is 2,4,6-tri-*tert*-butylphenol in MeCN, which showed noticeable day-to-day deviations in the measured potential at a given

substrate ratio. To compensate for these errors, we varied the substrate ratio in both directions and averaged data collected under multiple buffer conditions. See Appendix B.2.5 for details. Another example is the phenazine/dihydrophenazine couple, which was measurable in MeCN but showed a large drift in the OCP when measured in THF. A plot of OCP vs log([XH_n]/[X]) had a slope that exceeded 120 mV/dec, a large deviation from the expected 29.6 mV/dec for a $2e^-/2H^+$ redox processes. The source of this instability could not be identified or remedied, and as a result, we chose not to report values for phenazine/dihydrophenazine in THF. In general, we caution against extracting standard potentials or BDFEs from data that severely deviates from Nernstian behavior.

The tables above demonstrate that the OCP method can be used to determine valuable thermodynamic parameters for many classes of PCET substrates. Potentials are reported for substrates that contain O–H or N–H bonds, substrates that undergo single ($1e^-/1H^+$) or multiple ($2e^-/2H^+$) PCET events, and substrates that involve PCET to a single site (i.e. hydrogen atom transfer) or multiple sites (in our example, ET to a metal center and PT to a ligand). All of the cases examined here involve PCET reactions with equal numbers of electrons and protons, ne^-/nH^+ couples. As laid out in the thermochemical cycles in Schemes 2.1–2.3, it is straightforward to convert OCP measurements on such ne^-/nH^+ couples to standard potentials and BDFEs. While beyond the scope of the current study, we expect that OCP measurements could also be useful for PCET couples with unequal proton/electron stoichiometries, especially when the buffer pK_a is well known. Hydride transfers are the best studied examples, and their thermochemistry has been developed in a recent review.[40] A recent paper on standard potentials for N_2 reduction to NH_3 or NH_4^+ in organic solvents examines some of the issues of uneven proton/electron stoichiometry (these potentials were determined from aqueous values, not from OCP measurements).[21]

In our hands, a primary constraint on the scope of this method is that only substrates undergoing PCET at polar X–H bonds are amenable to OCP measurements (O–H or N–H bonds). Several attempts to measure PCET potentials for reactions of C–H bonds were unsuccessful. The OCP of MeCN or THF solutions containing varying concentrations of anthracene and dihydroanthracene took ~40 minutes to equilibrate and did not trend with the $X:XH_n$ ratio according to the Nernst equation, suggesting that the measured potential was not the thermodynamic value for this substrate. No equilibration of the OCP was observed over >1 hour for other C–H bond-containing substrates, such as isopropanol/acetone. Similarly, THF is an inert solvent for OCP measurements despite its ability to be oxidized to dihydrofuran and furan. We hypothesize that the inability to measure redox processes involving C–H bonds using the OCP method can be attributed to slow PCET kinetics at the glassy carbon working electrode. The much slower PCET reactivity of C–H vs O–H and N–H bonds has been documented elsewhere.[60] The very slow PCET (H-atom) self-exchange rate constants for C–H substrates are evident in the reported value of 8×10^{-5} M^{-1} s^{-1} for benzyl radical/toluene, dramatically slower than those for substrates with polar X–H bonds (5 to $>10^6$ M^{-1} s^{-1}).[47] For such substrates, alternative methods for obtaining nonaqueous PCET thermodynamics could be more viable, including spectroscopic equilibrations, reduction potential-pK_a measurements, or conversions from aqueous potentials.[17,38,61-63]

Finally, we emphasize that cyclic voltammetry (CV) is generally not an appropriate technique for directly obtaining standard potentials of PCET reagents in nonaqueous conditions. While CV is a very common method for measuring PCET thermodynamics in water and ET thermodynamics in organic solvents, proton-coupled electrochemical reactions are almost always electrochemically irreversible in organic solutions (likely due to the slower PT kinetics than in water). Several experimental results indicated that such electrochemically irreversible CVs cannot be used to

estimate standard potentials. For example, the midpoint potentials of CVs collected in buffered MeCN suggested that 2,6-di-*tert*-butyl-1,4-benzoquinone (DTQ) is 15 mV more *oxidizing* than 2,6-dimethyl-1,4-benzoquinone (DMQ) (Figure B27A). However, OCP measurements of the same solutions demonstrated that DTQ is more *reducing* than DMQ by 95 mV (Figure B27B), consistent with experimental and computed aqueous potentials of the two substrates[51] and with the equilibrium between DMQ and H_2DTQ measured by ^{1}H NMR spectroscopy in MeCN (Figure B28). In another experiment, the midpoint potentials of CVs of a buffered DMQ/H_2DMQ solution collected at glassy carbon, gold, and boron-doped diamond working electrodes spanned a 50 mV range. In contrast, OCP measurements of the same solution at the same three electrodes agreed within 6 mV (Figure B29, Table B4). While prior studies have suggested that electrode material and pre-treatment can influence potential measurements under certain conditions,[64,65] these results indicate that the nature of the electrode material does not influence the thermodynamic equilibrium between the substrate and electrode in this case. Overall, these data show that the slow electrochemical kinetics complicating CV measurements of PCET processes have much less effect on OCP measurements, likely due to the longer experimental timescale of the OCP method.

2.4 Conclusions

The results and analyses reported here show that open-circuit potential (OCP) measurements are a straightforward and accessible method for obtaining standard potentials and bond dissociation free energies for PCET reagents in nonaqueous solvents. The procedures for performing these measurements are described, including experimental considerations for collecting accurate and reproducible data. Formal potentials, standard potentials vs the H^+/H_2 reference, and BDFEs are reported for a variety of PCET reagents in acetonitrile and tetrahydrofuran. Comparisons to additional

measurements in *N,N*-dimethylformamide and isopropyl alcohol and literature values in water show that *E*° values vs H^+/H_2 and BDFEs are remarkably constant across different solvents for X/XH_n PCET couples. For this and other reasons, we recommend that the H^+/H_2 reference scale be used for PCET reduction potentials.

2.5 References

1. Er, S.; Suh, C.; Marshak, M. P.; Aspuru-Guzik, A., Computational design of molecules for an all-quinone redox flow battery. *Chem. Sci.* **2015,** *6* (2), 885-893.
2. Huskinson, B.; Marshak, M. P.; Suh, C.; Er, S.; Gerhardt, M. R.; Galvin, C. J.; Chen, X.; Aspuru-Guzik, A.; Gordon, R. G.; Aziz, M. J., A metal-free organic-inorganic aqueous flow battery. *Nature* **2014,** *505* (7482), 195-198.
3. Wei, X.; Pan, W.; Duan, W.; Hollas, A.; Yang, Z.; Li, B.; Nie, Z.; Liu, J.; Reed, D.; Wang, W.; Sprenkle, V., Materials and Systems for Organic Redox Flow Batteries: Status and Challenges. *ACS Energy Lett.* **2017,** *2* (9), 2187-2204.
4. Shin, S.-H.; Yun, S.-H.; Moon, S.-H., A review of current developments in non-aqueous redox flow batteries: characterization of their membranes for design perspective. *RSC Advances* **2013,** *3* (24), 9095-9116.
5. Park, S.-K.; Shim, J.; Yang, J.; Shin, K.-H.; Jin, C.-S.; Lee, B. S.; Lee, Y.-S.; Jeon, J.-D., Electrochemical properties of a non-aqueous redox battery with all-organic redox couples. *Electrochem. Commun.* **2015,** *59*, 68-71.
6. Luo, J.; Hu, B.; Hu, M.; Zhao, Y.; Liu, T. L., Status and Prospects of Organic Redox Flow Batteries toward Sustainable Energy Storage. *ACS Energy Lett.* **2019,** *4* (9), 2220-2240.
7. Anson, C. W.; Stahl, S. S., Cooperative Electrocatalytic O2 Reduction Involving Co(salophen) with p-Hydroquinone as an Electron–Proton Transfer Mediator. *J. Am. Chem. Soc.* **2017,** *139* (51), 18472-18475.
8. Amatore, C.; Cammoun, C.; Jutand, A., Palladium/Benzoquinone-Catalyzed Electrochemical Oxidation of Alcohols Under Anaerobic Conditions. *Synlett* **2007,** *2007* (14), 2173-2178.
9. Piera, J.; Bäckvall, J.-E., Catalytic Oxidation of Organic Substrates by Molecular Oxygen and Hydrogen Peroxide by Multistep Electron Transfer—A Biomimetic Approach. *Angew. Chem. Int. Ed.* **2008,** *47* (19), 3506-3523.
10. Wendlandt, A. E.; Stahl, S. S., Quinone-Catalyzed Selective Oxidation of Organic Molecules. *Angew. Chem. Int. Ed.* **2015,** *54* (49), 14638-14658.
11. Wendlandt, A. E.; Stahl, S. S., Quinones in Hydrogen Peroxide Synthesis and Catalytic Aerobic Oxidation Reactions. In *Liquid Phase Aerobic Oxidation Catalysis: Industrial Applications and Academic Perspectives*, Wiley-VCH Verlag GmbH & Co. KGaA: 2016; pp 219-237.
12. Bezdek, M. J.; Pappas, I.; Chirik, P. J., Determining and Understanding N-H Bond Strengths in Synthetic Nitrogen Fixation Cycles. In *Nitrogen Fixation*, Nishibayashi, Y., Ed. Springer International Publishing: Cham, 2017; pp 1-21.
13. Bezdek, M. J.; Guo, S.; Chirik, P. J., Coordination-induced weakening of ammonia, water, and hydrazine X–H bonds in a molybdenum complex. *Science* **2016,** *354* (6313), 730.
14. Bhattacharya, P.; Heiden, Z. M.; Chambers, G. M.; Johnson, S. I.; Bullock, R. M.; Mock, M. T., Catalytic Ammonia Oxidation to Dinitrogen by Hydrogen Atom Abstraction. *Angew. Chem. Int. Ed.* **2019,** *58* (34), 11618-11624.
15. Johnson, S. I.; Heins, S. P.; Klug, C. M.; Wiedner, E. S.; Bullock, R. M.; Raugei, S., Design and reactivity of pentapyridyl metal complexes for ammonia oxidation. *Chem. Commun.* **2019,** *55* (35), 5083-5086.
16. Bhattacharya, P.; Heiden, Z. M.; Wiedner, E. S.; Raugei, S.; Piro, N. A.; Kassel, W. S.; Bullock, R. M.; Mock, M. T., Ammonia Oxidation by Abstraction of Three Hydrogen Atoms from a Mo–NH3 Complex. *J. Am. Chem. Soc.* **2017,** *139* (8), 2916-2919.
17. Warren, J. J.; Tronic, T. A.; Mayer, J. M., Thermochemistry of Proton-Coupled Electron Transfer Reagents and Its Implications. *Chem. Rev.* **2010,** *110*, 6961-7001.
18. (a) Bordwell, F.G.; Cheng, J-P.; Harrelson, J.A. Homolytic Bond Dissociation Energies in Solution from Equilibrium Acidity and Electrochemical Data. J. Am. Chem. Soc. 1988, 110, 1229-1231.

(b) Bordwell, F.G.; Cheng, J-P.; Ji, G-Z.; Satish, A.V.; Zhang, X. Bond Dissociation Energies in DMSO Related to the Gas Phase. J. Am. Chem. Soc. 1991, 113, 9790-9795.
19. The Bordwell approach has some antecedents, including: (a) Wiberg, K.B. Foster, G. The Stereochemistry of the Chromic Acid Oxidation of Tertiary Hydrogens. J. Am. Chem. Soc. 1961,

83, 423-429. (b) Breslow, R.; Balasubramanian, K. pKa of triphenylcyclopropene. Electrochemical determination of an inaccessible equilibrium constant. J. Am. Chem. Soc. 1969, 91, 5182-5183. (c) Halpern, J. Homogeneous Catalytic Activation of Molecular Hydrogen by Metal Ions. In Advances in Catalysis, Farkas, A., Ed. Academic Press: 1957; Vol. 9, pp 302-311.
20. Pegis, M. L.; Roberts, J. A. S.; Wasylenko, D. J.; Mader, E. A.; Appel, A. M.; Mayer, J. M., Standard Reduction Potentials for Oxygen and Carbon Dioxide Couples in Acetonitrile and N,N-Dimethylformamide. *Inorg. Chem.* **2015,** *54* (24), 11883-11888.
21. Lindley, B. M.; Appel, A. M.; Krogh-Jespersen, K.; Mayer, J. M.; Miller, A. J. M., Evaluating the Thermodynamics of Electrocatalytic N2 Reduction in Acetonitrile. *ACS Energy Lett.* **2016,** *1* (4), 698-704.
22. Costentin, C.; Robert, M.; Savéant, J.-M., Update 1 of: Electrochemical Approach to the Mechanistic Study of Proton-Coupled Electron Transfer. *Chem. Rev.* **2010,** *110* (12), PR1-PR40.
23. Alligrant, T. M.; Hackett, J. C.; Alvarez, J. C., Acid/base and hydrogen bonding effects on the proton-coupled electron transfer of quinones and hydroquinones in acetonitrile: Mechanistic investigation by voltammetry, 1H NMR and computation. *Electrochim. Acta* **2010,** *55* (22), 6507-6516.
24. Tessensohn, M. E.; Hirao, H.; Webster, R. D., Electrochemical Properties of Phenols and Quinones in Organic Solvents are Strongly Influenced by Hydrogen-Bonding with Water. *The Journal of Physical Chemistry C* **2013,** *117* (2), 1081-1090.
25. Staley, P. A.; Newell, C. M.; Pullman, D. P.; Smith, D. K., The Effect of Glassy Carbon Surface Oxides in Non-Aqueous Voltammetry: The Case of Quinones in Acetonitrile. *Anal. Chem.* **2014,** *86* (21), 10917-10924.
26. Chambers, J. Q., Electrochemistry of quinones. In *The Quinonoid Compounds: Volume 1*, Patai, S.; Rappoport, Z., Eds. 1988; pp 719-757.
27. Gupta, N.; Linschitz, H., Hydrogen-Bonding and Protonation Effects in Electrochemistry of Quinones in Aprotic Solvents. *J. Am. Chem. Soc.* **1997,** *119* (27), 6384-6391.
28. Clare, L. A.; Pham, A. T.; Magdaleno, F.; Acosta, J.; Woods, J. E.; Cooksy, A. L.; Smith, D. K., Electrochemical Evidence for Intermolecular Proton-Coupled Electron Transfer through a Hydrogen Bond Complex in a p-Phenylenediamine-Based Urea. Introduction of the “Wedge Scheme” as a Useful Means To Describe Reactions of This Type. *J. Am. Chem. Soc.* **2013,** *135* (50), 18930-18941.
29. Roberts, J. A. S.; Bullock, R. M., Direct Determination of Equilibrium Potentials for Hydrogen Oxidation/Production by Open Circuit Potential Measurements in Acetonitrile. *Inorg. Chem.* **2013,** *52* (7), 3823-3835.
30. Dutton, P. L., Redox Potentiometry: Determination of Midpoint Potentials of Oxidation-Reduction Components of Biological Electron-Transfer Systems. In *Methods Enzymol.*, Academic Press: 1978; Vol. 54, pp 411-435.
31. Pitman, C. L.; Brereton, K. R.; Miller, A. J. M., Aqueous Hydricity of Late Metal Catalysts as a Continuum Tuned by Ligands and the Medium. *J. Am. Chem. Soc.* **2016,** *138* (7), 2252-2260.
32. Appel, A. M.; Helm, M. L., Determining the Overpotential for a Molecular Electrocatalyst. *ACS Catal.* **2014,** *4*, 630-633.
33. Savéant, J. M., Single Electron Transfer at an Electrode. In *Elements of Molecular and Biomolecular Electrochemistry*, John Wiley & Sons, Inc.: 2006; pp 1-77.
34. Prins, R.; Korswagen, A. R.; Kortbeek, A. G. T. G., Decomposition of the ferricenium cation by nucleophilic reagents. *J. Organomet. Chem.* **1972,** *39* (2), 335-344.
35. Izutsu, K., *Acid-Base Dissociation Constants in Dipolar Aprotic Solvent; IUPAC Chemical Data Series*. Blackwell Science: Oxford, UK 1990.
36. Kaljurand, I.; Kütt, A.; Sooväli, L.; Rodima, T.; Mäemets, V.; Leito, I.; Koppel, I. A., Extension of the Self-Consistent Spectrophotometric Basicity Scale in Acetonitrile to a Full Span of 28 pKa Units: Unification of Different Basicity Scales. *The Journal of Organic Chemistry* **2005,** *70* (3), 1019-1028.
37. The prime (‘) in E°’OCP distinguishes the formal potential from a standard potential, as described in Bard, A. J.; Faulkner, L. R. Electrochemical methods: fundamentals and applications. 2nd ed.; Wiley: New York, 2001; pp 52-53.

38. Mader, E. A.; Davidson, E. R.; Mayer, J. M., Large Ground-State Entropy Changes for Hydrogen Atom Transfer Reactions of Iron Complexes. *J. Am. Chem. Soc.* **2007,** *129* (16), 5153-5166.
39. Connelly, S. J.; Wiedner, E. S.; Appel, A. M., Predicting the reactivity of hydride donors in water: thermodynamic constants for hydrogen. *Dalton Trans.* **2015,** *44* (13), 5933-5938.
40. Wiedner, E. S.; Chambers, M. B.; Pitman, C. L.; Bullock, R. M.; Miller, A. J. M.; Appel, A. M., Thermodynamic Hydricity of Transition Metal Hydrides. *Chem. Rev.* **2016,** *116* (15), 8655-8692.
41. Armstrong, D. A.; Huie, R. E.; Koppenol, W. H.; Lymar, S. V.; Merényi, G.; Neta, P.; Ruscic, B.; Stanbury, D. M.; Steenken, S.; Wardman, P., Standard electrode potentials involving radicals in aqueous solution: inorganic radicals (IUPAC Technical Report). *Pure Appl. Chem.* **2015,** *87* (11-12), 1139-1150.
42. Linstrom, P. J.; Mallard, W. G., NIST Chemistry WebBook, NIST Standard Reference Database Number 69. National Institute of Standards and Technology Gaithersburg, MD 20899.
43. Brunner, E., Solubility of hydrogen in 10 organic solvents at 298.15, 323.15, and 373.15 K. *J. Chem. Eng. Data* **1985,** *30* (3), 269-273.
44. Roduner, E.; Bartels, D. M., Solvent and isotope effects on addition of atomic hydrogen to benzene in aqueous solution. *Berichte der Bunsengesellschaft für physikalische Chemie* **1992,** *96* (8), 1037-1042.
45. Jerkiewicz, G.; Zolfaghari, A., Determination of the Energy of the Metal−Underpotential-Deposited Hydrogen Bond for Rhodium Electrodes. *J. Phys. Chem.* **1996,** *100* (20), 8454-8461.
46. Abraham, M. H., Scales of solute hydrogen-bonding: their construction and application to physicochemical and biochemical processes. *Chem. Soc. Rev.* **1993,** *22* (2), 73-83.
47. Warren, J. J.; Mayer, J. M., Predicting organic hydrogen atom transfer rate constants using the Marcus cross relation. *Proceedings of the National Academy of Sciences* **2010,** *107* (12), 5282.
48. Lucarini, M.; Mugnaini, V.; Pedulli, G. F.; Guerra, M., Hydrogen-Bonding Effects on the Properties of Phenoxyl Radicals. An EPR, Kinetic, and Computational Study. *J. Am. Chem. Soc.* **2003,** *125* (27), 8318-8329.
49. Mulder, P.; Korth, H.-G.; Pratt, D. A.; DiLabio, G. A.; Valgimigli, L.; Pedulli, G. F.; Ingold, K. U., Critical Re-evaluation of the O−H Bond Dissociation Enthalpy in Phenol. *The Journal of Physical Chemistry A* **2005,** *109* (11), 2647-2655.
50. Litwinienko, G.; Ingold, K. U., Solvent Effects on the Rates and Mechanisms of Reaction of Phenols with Free Radicals. *Acc. Chem. Res.* **2007,** *40* (3), 222-230.
51. Huynh, M. T.; Anson, C. W.; Cavell, A. C.; Stahl, S. S.; Hammes-Schiffer, S., Quinone $1e^-$ and $2e^-/2H^+$ Reduction Potentials: Identification and Analysis of Deviations from Systematic Scaling Relationships. *J. Am. Chem. Soc.* **2016,** *138* (49), 15903-15910.
52. Garrido, G.; Koort, E.; Ràfols, C.; Bosch, E.; Rodima, T.; Leito, I.; Rosés, M., Acid−Base Equilibria in Nonpolar Media. Absolute pKa Scale of Bases in Tetrahydrofuran. *The Journal of Organic Chemistry* **2006,** *71* (24), 9062-9067.
53. Quist, D. A.; Ehudin, M. A.; Schaefer, A. W.; Schneider, G. L.; Solomon, E. I.; Karlin, K. D., Ligand Identity-Induced Generation of Enhanced Oxidative Hydrogen Atom Transfer Reactivity for a CuII2(O2•–) Complex Driven by Formation of a CuII2(−OOH) Compound with a Strong O–H Bond. *J. Am. Chem. Soc.* **2019,** *141* (32), 12682-12696.
54. Klug, C. M.; O'Hagan, M.; Bullock, R. M.; Appel, A. M.; Wiedner, E. S., Impact of Weak Agostic Interactions in Nickel Electrocatalysts for Hydrogen Oxidation. *Organometallics* **2017,** *36* (12), 2275-2284.
55. Daniele, S.; Ugo, P.; Mazzocchin, G.-A.; Bontempelli, G., Acid-base equilibria in organic solvents: Part 1. Evaluation of solvent basicity by cyclic voltammetry. *Anal. Chim. Acta* **1985,** *173*, 141-148.
56. Fourmond, V.; Jacques, P.-A.; Fontecave, M.; Artero, V., H_2 Evolution and Molecular Electrocatalysts: Determination of Overpotentials and Effect of Homoconjugation. *Inorg. Chem.* **2010,** *49* (22), 10338-10347.
57. Lucarini, M.; Pedrielli, P.; Pedulli, G. F.; Cabiddu, S.; Fattuoni, C., Bond Dissociation Energies of O−H Bonds in Substituted Phenols from Equilibration Studies. *The Journal of Organic Chemistry* **1996,** *61* (26), 9259-9263.

58. Rodgers, M. A. J., Nanosecond pulse radiolysis of acetone. Kinetic and thermodynamic properties of some aromatic radical cations. *J. Chem. Soc., Faraday Trans. 1* **1972,** *68* (0), 1278-1286.
59. Wayner, D. D. M.; McPhee, D. J.; Griller, D., Oxidation and reduction potentials of transient free radicals. *J. Am. Chem. Soc.* **1988,** *110* (1), 132-137.
60. Mayer, J. M., Understanding Hydrogen Atom Transfer: From Bond Strengths to Marcus Theory. *Acc. Chem. Res.* **2011,** *44* (1), 36-46.
61. Tilset, M.; Parker, V. D., Solution homolytic bond dissociation energies of organotransition-metal hydrides. *J. Am. Chem. Soc.* **1989,** *111* (17), 6711-6717.
62. Parker, V. D.; Handoo, K. L.; Roness, F.; Tilset, M., Electrode potentials and the thermodynamics of isodesmic reactions. *J. Am. Chem. Soc.* **1991,** *113* (20), 7493-7498.
63. Wayner, D. D. M.; Parker, V. D., Bond energies in solution from electrode potentials and thermochemical cycles. A simplified and general approach. *Acc. Chem. Res.* **1993,** *26* (5), 287-294.
64. Redepenning, J.; Tunison, H. M.; Finklea, H. O., Influence of Donnan potentials on apparent formal potentials measured for organized thiol monolayers with attached pentaamminepyridineruthenium redox centers. *Langmuir* **1993,** *9* (5), 1404-1407.
65. Park, J. H.; Zhou, H.; Percival, S. J.; Zhang, B.; Fan, F.-R. F.; Bard, A. J., Open Circuit (Mixed) Potential Changes Upon Contact Between Different Inert Electrodes–Size and Kinetic Effects. *Anal. Chem.* **2013,** *85* (2), 964-970.

Chapter 3

Nanoparticle O–H Bond Dissociation Free Energies from Equilibrium Measurements of Cerium Oxide Colloids

With contributions from Agarwal, R. G.; Kim, H. J.; Mayer, J. M. "Nanoparticle O–H Bond Dissociation Free Energies from Equilibrium Measurements of Cerium Oxide Colloids." *J. Am. Chem. Soc.* **2021**, *143*, 2896-2907. RGA performed measurements with the ~2 nm diameter batches of cerium oxide nanoparticles and wrote the manuscript. HJK performed measurements with the 4 nm batch of nanoparticles. The authors gratefully acknowledge Dr. Eric Paulson (Yale Chemical and Biophysical Instrumentation Center) for assistance with quantitative ^{1}H NMR studies and Dr. Tianpin Wu (Argonne National Laboratory Advanced Photon Source) for assistance with XANES.

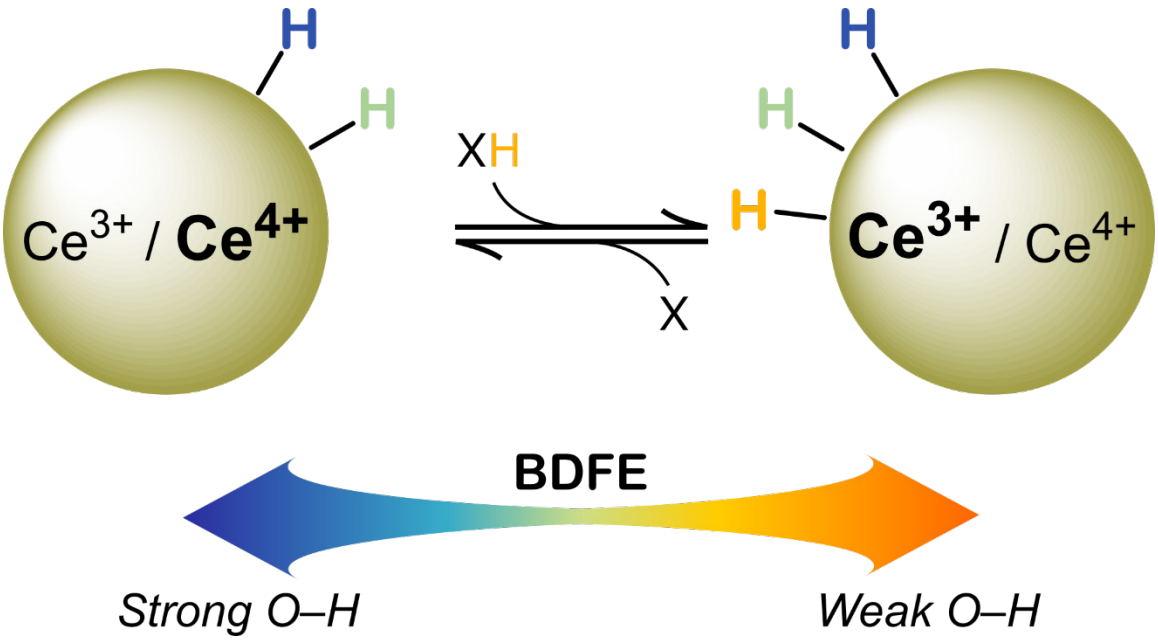

3.1 Introduction

Redox-active metal oxide materials and nanomaterials are important technologically and in the environment.[1-6] Many of the redox transformations they perform involve the transfer of hydrogen atoms (protons and electrons).[7-11] As a result, free energies of hydrogen atom transfer to and from these materials are fundamental thermochemical values of great importance. This report's emphasis on nanoparticle bond strength thermochemistry follows the longstanding interest in surface–H and

surface–X adsorption energies in surface science,[12,13] and the use of such energies as descriptors in the popular 'scaling relationship' and 'volcano plot' analyses of heterogeneous catalysis and electrocatalysis.[14-17] Despite wide interest, measurements of surface–H adsorption energies have almost entirely been restricted to single crystal metals and ultrahigh-vacuum conditions.[13,18] Computed adsorption energies are more widely reported. However, especially for binary materials such as redox-active oxides, they often rely on assumptions about the stoichiometry and structure of the material's surface and little data exists for their validation.[13,19,20] As a result, there is a need for more methods to measure adsorption energies for chemically reactive materials under solution conditions. Here we report the first free energy measurements of the bond strength between hydrogen and a metal oxide nanomaterial, and explore how those bond strengths change with the hydrogen stoichiometry of the oxide. This advance is enabled by a novel equilibrium method which is applied to reactions between cerium oxide nanoparticle colloids and molecular reagents (Scheme 3.1).

Scheme 3.1. Equilibrium between cerium oxide nanoparticles and a substituted 1,4-hydroquinone.

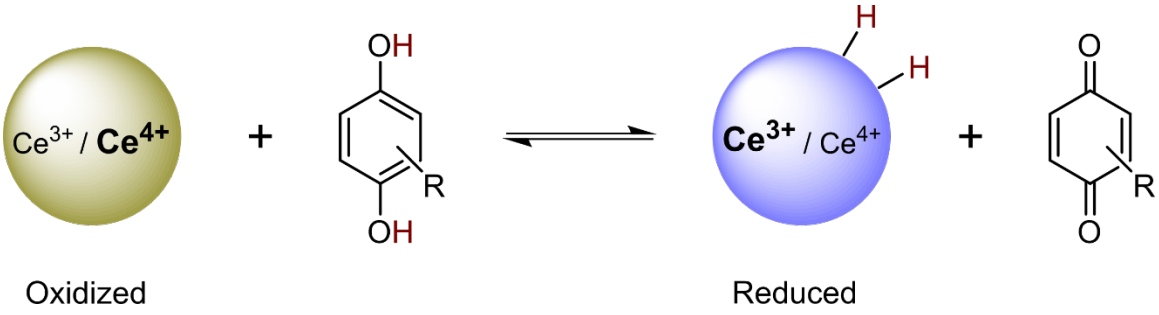

Cerium oxide (ceria) is a prototypical mixed-valence oxide, typically containing both Ce^{4+} and Ce^{3+} ions, which can vary its stoichiometry and average redox state (%Ce^{3+}) in redox reactions. This phenomenon has been the subject of significant study, and is especially pronounced at the nanoscale (nanoceria).[21-28] In nanoceria, the extent to which the %Ce^{3+} can be varied is enhanced by greater surface-to-bulk

ratios, which stabilize Ce^{3+} sites. This wide range of accessible redox states is important to ceria's applications as a catalyst, co-catalyst, and reducible oxide support. In modern 'three-way' automotive catalytic converters, for example, ceria acts as a source and sink for redox equivalents to facilitate both the reduction of nitric oxide and the oxidation of carbon monoxide.[23] Ceria also catalyzes the methanation of CO_2, the hydrogenation of various alkynes, and other reactions.[19,29-34] Furthermore, aqueous suspensions of nanoceria are being explored to treat ailments caused by reactive oxygen species.[24,25,35-37] All of these applications depend on variations in the $\%Ce^{3+}$ of the ceria.

Redox reactions of ceria typically occur by the transfer of either hydrogen or oxygen atoms, and therefore the thermochemistry of these atom-transfer reactions is central to understanding ceria's reactivity. Under high-temperature conditions, the Ce^{3+}/Ce^{4+} mixed valency is most commonly balanced by oxygen vacancies in the fluorite lattice, and the material is written as CeO_{2-x}.[38] The thermochemistry of oxygen loss at bulk ceria is known to be modulated by the material's average redox state.[26,27,39,40] At closer to ambient temperatures, or in colloidal suspensions, charge balance can instead be maintained by hydrogen atom binding (because loss of H_2O is less favorable, see below).[26,33] As with many reducible metal oxides,[10,41,42] hydrogen atom addition ($H^\bullet \equiv e^- + H^+$) to ceria is most commonly thought to result in the reduction of one Ce^{4+} to Ce^{3+}, with protonation of one oxide to hydroxide ($CeO_x(OH)_y$).[43] The thermochemistry for binding hydrogen to materials is typically described as the hydrogen adsorption energy. This is the free energy or enthalpy of dissociative H_2 chemisorption to form surface–H. For ceria these values have only been accessible by computation, and reported $CeO_2(111)$ surface O–H bond strengths vary significantly between studies.[29,44,45] These papers, like most that compute H adsorption on binary materials, report single values for the hydrogen adsorption energy. However, a recent computational study of Ce_nO_{2n} nanoclusters described significant

heterogeneity in the hydrogen adsorption energy between different surface sites.[46] Experimental measurements of the low-temperature thermochemistry of ceria–and other metal oxides–are needed as benchmarks and to clarify whether the single bond strength model is appropriate for these complex surfaces.

The preferred thermochemical descriptor for hydrogen binding in *solution* reactions is the standard free energy of bond homolysis, called the bond dissociation free energy (BDFE), eq 3.1.[47,48]

$$X–H \rightarrow X^{\bullet} + H^{\bullet} \qquad \Delta G° = \text{bond dissociation free energy, BDFE} \qquad (3.1)$$

We use BDFEs in this paper because they have been reported for a wide variety of molecules in solution and this parameter has been shown to be robust descriptor of hydrogen atom transfer (HAT) and proton-coupled electron transfer (PCET) reactivity.[47,49-53] Furthermore, the utility of BDFEs as a descriptor of material bond strengths has already been demonstrated by our group in a recent study of $Ni(OH)_2$ electrodes.[54] Use of these values allows connections to the surface science literature as BDFEs are directly related to the hydrogen adsorption free energies by combination with the free energy of H_2 homolysis.[48,55]

Herein, we report measurements of equilibria between colloidal ceria nanoparticles and various PCET reagents, as a new method, to provide the first experimentally determined BDFEs for surface O–H bonds in colloidal nanoceria, or any colloidal metal oxide nanoparticle. While there have been many studies of the reaction chemistry of metal oxide nanoparticle suspensions,[56-65] it is only recently that PCET reactions have been emphasized.[9,66,67] Our previous study demonstrated that nanoceria colloids react with a wide range of PCET reagents.[68] We show here that reactions between nanoceria and a PCET reagent can reach an equilibrium state where the thermodynamic affinity for a hydrogen atom, or BDFE, is equal between the two species. Interestingly, we observe that these BDFEs are significantly tuned by the

redox state of the nanoceria. The implications of this relationship and these values for the rational design of nanoceria catalysts are discussed. More generally, this work opens the door to many more experimental studies of hydrogen adsorption free energies at oxide solid/solution interfaces, which are important in fields including catalysis, electrocatalysis, reaction chemistry, corrosion, geochemistry, nanomedicine, and as benchmarks for computational studies.

3.2 Results

This study demonstrates a novel and general method for determining the bond strengths between hydrogen and metal oxide nanoparticles using oleate-capped cerium oxide nanoparticle colloids (OLE-Ce) in low-polarity organic solvents (Appendix C). The majority of experiments were performed in tetrahydrofuran (THF) with an OLE-Ce batch designated **Ce-1**, in which nanoparticles had an average diameter (*d*) of 1.8 ± 0.2 nm by transmission electron microscopy (TEM) (Appendix C.2). Comparative studies were done with a second batch of OLE-Ce prepared in the same fashion (**Ce-2**, *d* = 1.9 ± 0.3 nm), and on a larger OLE-Ce colloid (**Ce-L**, *d* = 4.0 ± 0.4 nm). Experiments involved chemical reactions of these OLE-Ce colloids with soluble small molecules that can donate or accept hydrogen atoms – mostly 1,4-hydroquinones and their corresponding quinones. These PCET reagents were chosen because they have a variety of average O–H BDFEs and they are poor ligands for nanoceria.[55,68] Reactions were done in mixtures of THF-d_8 and proteo-THF over a period of days at room temperature, and organic products were quantified by integration of peaks in the solvent-suppressed ^{1}H NMR spectra using 1,3,5-trimethoxybenzene (TMB) as an internal standard (Appendix C.1.4 & C.6.1). Solutions were also analyzed in air-free quartz capillaries by X-ray absorbance near edge spectroscopy (XANES) at the Ce L_{III}-edge before and after reactions, to obtain the ratio of Ce^{3+} to Ce^{4+} ions in the material (Appendix C.3). For as-prepared **Ce-1**, the %Ce^{3+} is 29.5% by XANES.

Throughout this work, BDFE values are used as thermochemical metrics of hydrogen atom affinity, where larger values indicate stronger bonds. All of the values used for organic substrates (XH_n) were determined recently by our laboratory, in THF, using open-circuit potential measurements.[55] For reagents where $n > 1$ the reported BDFEs refer to the average of the component BDFEs.

3.2.1 Equilibrium Case Study: OLE-Ce and 2,6-dimethyl-1,4-hydroquinone (H_2DMQ)

This section describes detailed ^{1}H NMR and XANES studies of the reaction between **Ce-1** and 2,6-dimethyl-1,4-hydroquinone (H_2DMQ, BDFE = 64.9 kcal mol^{-1})[55] in THF as a case study for the equilibration strategy (Scheme 3.1). Reaction progress was monitored with ^{1}H NMR spectroscopy by quantifying the production of the organic product, in this case 2,6-dimethyl-1,4-benzoquinone (DMQ). Quantification of the product provides a direct measure of the change in $\%Ce^{3+}$ ($\Delta\%Ce^{3+}$) during the reaction, because, as demonstrated below, a general stoichiometric relationship holds (eq 3.2). Reported values of $\Delta\%Ce^{3+}$ are always relative to the $\%Ce^{3+}$ of the as-prepared sample of OLE-Ce, even if multiple reactions are done in sequence.

$$CeO_xH_y + aXH_n \rightleftharpoons CeO_xH_{(y+an)} + aX \qquad (3.2)$$

The oxidation of H_2DMQ by as-prepared **Ce-1** was explored in the presence of excess reducing equivalents (two per molecule of H_2DMQ) as compared to potential oxidizing equivalents (the number of Ce atoms). Although the concentration of cerium atoms ([Ce]) should be limiting in the reaction with H_2DMQ, reduction of **Ce-1** was observed to plateau at $\Delta\%Ce^{3+} \approx 33\%$, after roughly 3 days (Figure 3.1A). This value is well below the $\Delta\%Ce^{3+}$ expected for a stoichiometric reaction (see below), and therefore suggested that an equilibrium state was reached. To test this hypothesis, **Ce-1** was first reduced to $\Delta\%Ce^{3+} \approx 36\%$ by using a sub-stoichiometric amount of the more reducing 1,8-dichloro-9,10-dihydroanthraquinone (H_2DCAQ, BDFE = 55.4 kcal

mol^{-1})[55]. In this reaction H_2DCAQ is quantitatively oxidized to the quinone. The reduced colloid was then exposed to excess DMQ (Scheme 3.1 in the reverse direction). Reduction of DMQ to H_2DMQ was observed in initial time points, but then plateaued at $\Delta\%Ce^{3+} \approx 28\%$. The observation of reactions in both directions supports the initial conclusion of achieving equilibrium states. The plateau value of $\Delta\%Ce^{3+}$ was somewhat higher in the oxidation of H_2DMQ than in the reduction of DMQ (Figure 3.1A), as discussed below.

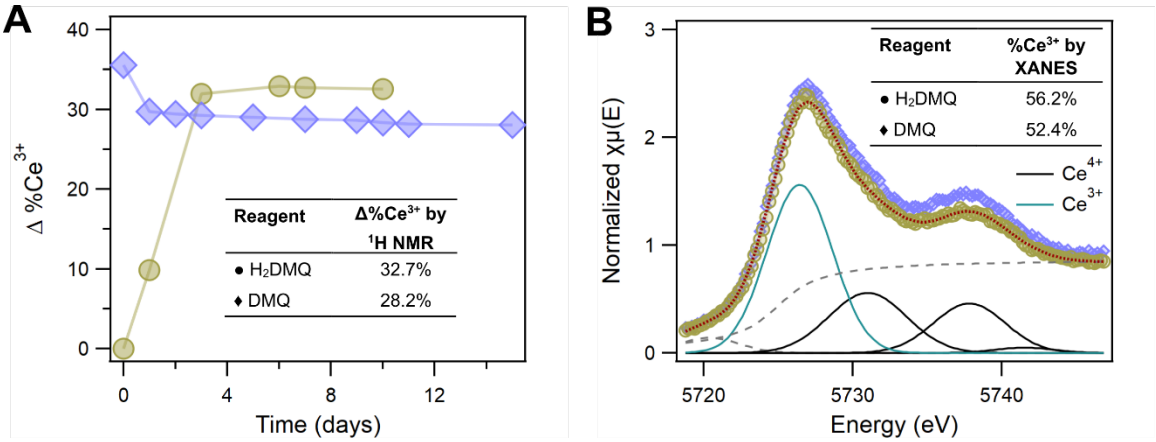

Figure 3.1. (**A**) $\Delta\%Ce^{3+}$ values plotted as a function of reaction time, determined by quantitation of the organic products by ^{1}H NMR spectroscopy. The oxidation of H_2DMQ (gold) by **Ce-1** and the reduction of DMQ by pre-reduced **Ce-1** (purple) are shown. Uncertainties in the $\Delta\%Ce^{3+}$ values are roughly the vertical size of the symbols. Values in the table (±2%) are the averages of all $\Delta\%Ce^{3+}$ values in the plateau region. $\Delta\%Ce^{3+}$ values were corroborated by (**B**) XANES data of the equilibrated suspensions in THF (same color scheme as Figure 3.1A). A fit for the spectrum of **Ce-1**/H_2DMQ (red, dotted) is included, together with contributions from Ce^{3+} (teal), Ce^{4+} (black), and background / pre-edge contributions (gray, dashed). For the oxidation of H_2DMQ by **Ce-1,** [Ce] = 9.0 mM, [H_2DMQ] = 6.3 mM, and [TMB] = 7.5 mM. For the reduction of DMQ, **Ce-1** was first reduced by adding a sub-stoichiometric amount of H_2DCAQ and waiting until it had all been consumed before adding DMQ; [Ce] = 9.1 mM, [DMQ] = 4.3 mM, and [TMB] = 7.4 mM. As in (**A**), the estimated uncertainties are ≤ ±2% in $\%Ce^{3+}$.

XANES data collected for these colloidal samples at the Ce L_{III}-edge provided a direct measure of the absolute $\%Ce^{3+}$ (rather than the change, $\Delta\%Ce^{3+}$, from ^{1}H NMR data and eq 3.2). As reported previously, XANES spectra were fit to multiple transitions originating from either Ce^{3+} or Ce^{4+}.[68] In short, absorbance at the rising edge is primarily attributed to a transition from the Ce^{3+} state, while absorbance at higher energies is assigned to multiple transitions from Ce^{4+} states.[69-71] Deconvolution of contributions from Ce^{3+} and Ce^{4+} states in XANES spectra provide a quantitative measure of the absolute $\%Ce^{3+}$ of OLE-Ce (Appendix C.3). These experiments again showed that reactions of H_2DMQ and DMQ with **Ce-1** and pre-reduced **Ce-1**, respectively, gave fairly similar $\%Ce^{3+}$ values (Figure 3.1B). In both cases, the $\%Ce^{3+}$ values were significantly higher than that measured for as-prepared **Ce-1**, $\%Ce^{3+}$ = 29.5%.

The final $\%Ce^{3+}$ values for reactions between **Ce-1** and either H_2DMQ or DMQ (starting at opposite sides of Scheme 3.1) show a consistent difference by both XANES and ^{1}H NMR. By both measures the reaction with H_2DMQ gives a higher $\%Ce^{3+}$ than the reaction with excess DMQ. This discrepancy falls outside of the uncertainties, which we estimate to be ≤ ±2% in $\%Ce^{3+}$ for both ^{1}H NMR and XANES. Such a discrepancy is actually *expected* for an equilibrium state, because of the excess of the organic reagent that was used in each case. The law of mass action (Le Chatelier's principle) dictates that **Ce-1** will be more reduced when an excess of the H_2DMQ reductant was used, and more oxidized in the presence of an excess of the DMQ oxidant. This is what is observed by both ^{1}H NMR and XANES (Figure 3.1). Together, these data show that the $2e^-/2H^+$ transfer between **Ce-1** and the H_2DMQ/DMQ redox couple reaches equilibrium.

At equilibrium the overall PCET reaction is isoergic by definition, and therefore the BDFE of **Ce-1** ($BDFE_{Ce}$) must be equal to the "concentration-adjusted BDFE" ($BDFE_{adj}$) of H_2DMQ. The $BDFE_{adj}$ is used because the concentrations of H_2DMQ and DMQ in solution modulate their hydrogen atom affinity, per Le Chatelier's principle. Just as the thermodynamic proton-donor ability of a protic acid depends on the $[HA]/[A^-]$ ratio, the ability of the H_2DMQ to donate hydrogen atoms depends on the $[H_2DMQ]/[DMQ]$ ratio. This change in driving force will necessarily shift the position of the equilibrium measured. The $BDFE_{adj}$ is given quantitatively by a version of the Nernst equation (eq 3.3), where the constant is $2.303RT$ at 298 K in kcal mol^{-1}.[55]

$$BDFE_{adj}(XH_n) = BDFE(XH_n) - \frac{1.364\ kcal\ mol^{-1}}{n}\log\left(\frac{[XH_n]}{[X]}\right) \qquad (3.3)$$

Application of eq 3.3 for the equilibria established between H_2DMQ/DMQ and **Ce-1** gives $BDFE_{Ce}$ = 64.6 kcal mol^{-1} when $\Delta\%Ce^{3+}$ = 32.7% and 65.6 kcal mol^{-1} when $\Delta\%Ce^{3+}$ = 28.2%. We estimate the uncertainty between $BDFE_{Ce}$ values to be ±0.3 kcal mol^{-1} based on the accuracy of equilibrium positions from the NMR quantitation. The

difference in BDFEs for the two equilibrated samples falls outside of the relative uncertainties, thereby confirming the expectation that more reduced ceria nanoparticles form a weaker bond to hydrogen (lower BDFE).

3.2.2 Expansion of Equilibrium Method to Other PCET Reagents

The equilibrium method described above was expanded to 1,1-diphenyl-2-picrylhydrazine (DPPH-H, BDFE = 73.5 kcal mol^{-1}), 1,4-hydroquinone (H_2BQ, BDFE = 67.4 kcal mol^{-1}), 1,4-dihydroxynaphthalene (H_2NQ, BDFE = 62.7 kcal mol^{-1}), and 2,7-di-*tert*-butyl-1,4-dihydroxynaphthalene (H_2DTNQ, BDFE = 61.5 kcal mol^{-1}).[55] The BDFEs of these substrates span 12.0 kcal mol^{-1} (Scheme 3.2).[55] In all cases mass balance of organic products and reagents was maintained during ^1H NMR time courses (Figure C24D), and equilibrium states were reached with **Ce-1** when approached through reaction with either the oxidized or reduced form of the PCET reagent (Appendix C.6). Further generalization of these studies to **Ce-2** and **Ce-L** demonstrated the formation of equilibrium states with the same PCET reagents (Table 3.1). All of the values in Table 3.1 include the Nernstian corrections for the $[XH_n]/[X]$ ratios, eq 3.3. For all substrates, the results of each repeated experiment are given (instead of averaged) because each equilibrium state is slightly different due to differing reagent concentrations (Table C5).

Scheme 3.2. PCET Reagent Structures and Avg. X-H BDFEs in kcal mol^{-1}.[55]

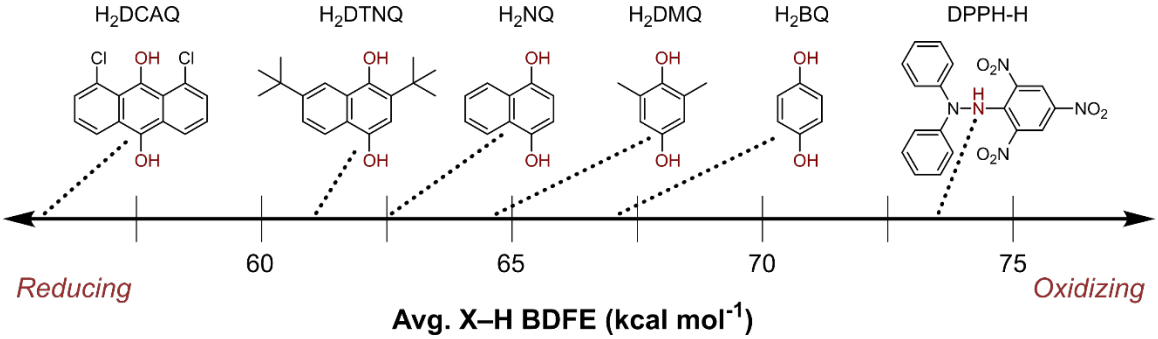

Since the mass balance and reversibility of eq 3.2 are followed in these reactions (see below), the $\Delta\%Ce^{3+}$ values determined by ^1H NMR can be made absolute

by using a XANES $\%Ce^{3+}$ value as a reference point. The XANES value for the **Ce-1**/H_2DMQ equilibrated sample was chosen as the reference since the reaction shows facile kinetics, the same sample has been measured by both XANES and ^{1}H NMR, and the equilibrium $\%Ce^{3+}$ value lies close to the center of the range explored in these studies. This final reason is important because, while XANES is a direct measure of the $\%Ce^{3+}$, the spectral fitting procedure assumes that the peaks shapes for the Ce^{3+} and Ce^{4+} contributions to the spectrum remain constant over the entire range of $\%Ce^{3+}$. A generalized $\%Ce^{3+}$ anchor of 23.5% for as-prepared **Ce-1** was determined from the $\%Ce^{3+}$ reference point measured by XANES and $\Delta\%Ce^{3+}$ by ^{1}H NMR for **Ce-1**/H_2DMQ (Figure 3.1). Similar procedures were also applied to give anchor values for as-prepared **Ce-2** (24.8%) and **Ce-L** (10.8%). For the remainder of this report, all quoted $\%Ce^{3+}$ values were determined by ^{1}H NMR using these anchor values unless otherwise stated.

Table 3.1. OLE-Ce Colloid Equilibrium States and BDFEs.[a]

Reagent	%Ce^{3+}	$BDFE_{Ce}$	Reagent	%Ce^{3+}	$BDFE_{Ce}$
DTNQ [b]	72.6	62.3	H_2DTNQ [d]	64.2	61.4
H_2DTNQ [c]	72.2	61.3	H_2NQ [d]	59.8	62.5
H_2DTNQ [c]	72.2	61.5	H_2NQ [d]	59.3	62.5
DTNQ [b]	70.3	62.6	H_2NQ [d]	59.1	62.5
DTNQ [b]	66.8	62.2	H_2DMQ [d]	53.4	64.6
NQ [b]	63.6	63.4	H_2DMQ [d]	52.9	64.6
H_2NQ [c]	62.2	62.5	H_2DMQ [d]	52.6	64.6
H_2NQ [c]	61.5	62.7	H_2BQ [d]	44.2	67.0
NQ [b]	60.1	63.6	H_2BQ [d]	44.1	67.0
NQ [b]	59.7	63.6	DPPH [d]	15.1	72.5
H_2DMQ [c]	56.2	64.6	DPPH [d]	14.1	73.1
H_2DMQ [c]	53.2	64.6	H_2DTNQ [e]	20.6	60.7
DMQ [b]	52.6	65.5	H_2NQ [e]	20.1	61.9
DMQ [b]	51.7	65.6	H_2DTNQ [e]	20.0	60.8
H_2BQ [c]	43.6	66.9	DTNQ [f]	19.4	61.9
H_2BQ [c]	42.7	66.9	H_2NQ [e]	18.5	61.9
BQ [b]	36.1	68.0	H_2DMQ [e]	17.6	64.0
BQ [b]	36.0	68.2	H_2DMQ [e]	16.6	64.0
DPPH [c]	18.0	74.2	H_2BQ [e]	14.6	66.3
DPPH [c]	17.5	74.3	H_2BQ [e]	14.1	66.3
H_2DTNQ [d]	65.6	61.4	DPPH [e]	8.4	73.4

[a] %Ce^{3+} from ^{1}H NMR data benchmarked to XAS results for OLE-Ce/H_2DMQ. $BDFE_{Ce}$ is equal to the $BDFE_{adj}$ from eq 3.3. BDFEs in kcal mol^{-1} with relative uncertainties of ±0.3 kcal mol^{-1}. [b] Reacted with **Ce-1** that was first reduced with H_2DCAQ. [c] Reacted with **Ce-1**. [d] Reacted with **Ce-2**. [e] Reacted with **Ce-L** with equilibrium plateau at ≥24 days. [f] Reacted with **Ce-L** that was first reduced with H_2DCAQ.

Successful equilibrium studies required PCET reagents to show mass balance in terms of reagent consumed and product formed (eq 3.2), and to have a small enough kinetic barrier for the reaction with OLE-Ce to allow for quantification of reaction progress. Substrates which were explored but did not meet these criteria include 2,2,6,6-tetramethylpiperidin-1-yl)oxyl (TEMPO) and 2,6-di-tert-butyl-4-methoxy phenoxyl radical, both of which reacted on timescales too slow for reasonable measurement (no reaction completion after >1 month). Additionally, reactions

between *meta*-chloroperbenzoic acid (*m*CPBA) and OLE-Ce were facile but did not show mass balance (Appendix C.4).

Equilibria between OLE-Ce and hydroquinones were also studied under alternative solvent conditions (Appendix C.8). In a THF solution containing 0.1 M tetrabutylammonium hexafluorophosphate electrolyte, the equilibrium position measured for the H_2BQ/**Ce-1** reaction was nearly unchanged from that in pure THF. Additionally, changing the solvent from THF to lower polarity solvents, such as toluene-d_8, led to greater reduction of OLE-Ce in reactions with H_2DMQ. These results indicate that the reactions do not involve any significant change in the charge of the nanoparticles, as is discussed further below.

We also explored potential perturbations of the H_2DMQ/**Ce-1** equilibrium by excess cerium(III) oleate ($Ce(OLE)_3$), oleic acid, tetrabutylammonium oleate (TBA^+OLE^-), and H_2O. Addition of H_2O and $Ce(OLE)_3$ had no effect on the equilibrium position (Table C.7). Addition of TBA^+OLE^- lead to a loss in H_2DMQ mass balance over time, deprotonation of H_2DMQ, and halted oxidation to DMQ. Finally, addition of oleic acid led to greater oxidation of H_2DMQ, as well as the production of $Ce(OLE)_3$ (Figure C29). Analyses of these equilibrium shifts are presented below.

3.2.3 Validation of Mass Balance (Eq 3.2) Across the Full Range of Accessible $\%Ce^{3+}$

Previous XANES studies in our group have demonstrated that a single batch of similarly prepared oleate-capped cerium oxide nanoparticles accessed a wide range of $\%Ce^{3+}$, from ca. 18% to 67%.[68] The range of $\%Ce^{3+}$ accessed in reactions with PCET reagents is valuable as it provides a lower limit for the average number of redox-active sites per OLE-Ce nanoparticle. For **Ce-1** the range was measured through reactions with well-behaved highly-oxidizing and highly-reducing organic PCET reagents. The strongest reductant used in these studies was H_2DCAQ, while the strongest well-

behaved oxidant used was 2,2-diphenyl-1-picrylhydrazyl (DPPH), which reduces to DPPH-H.

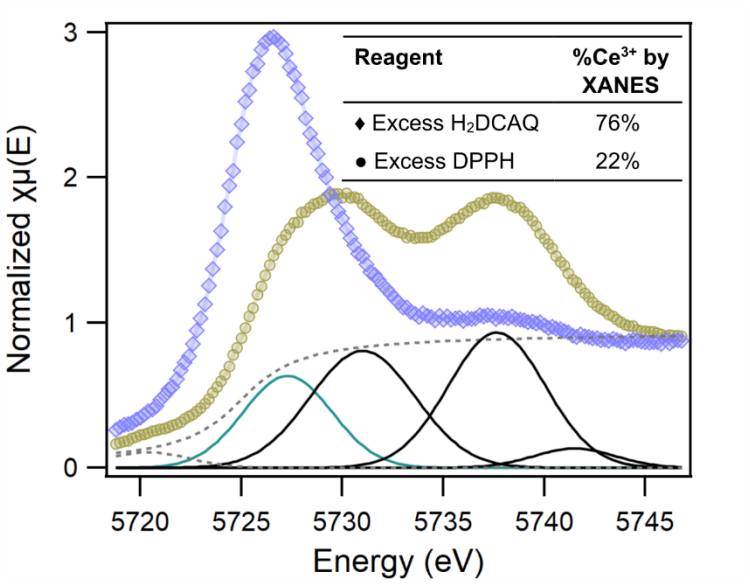

Figure 3.2. XANES spectra of reactions of **Ce-1** with either excess H_2DCAQ (purple, diamonds) or excess DPPH (gold, circles) in THF. Fits for the spectrum of **Ce-1** / DPPH are included with contributions from Ce^{3+} (teal), Ce^{4+} (black), and background / pre-edge contributions (gray, dashed).

In reactions with excess H_2DCAQ or with excess DPPH, XANES measurements of the $\%Ce^{3+}$ of **Ce-1** vary from 22 – 76% (Figure 3.2), a range of 54%. This range is consistent with the range in $\%Ce^{3+}$ observed by ^{1}H NMR ($\Delta\%Ce^{3+}$ = 58 ± 2%). The NMR value has greater uncertainty due to side reactions which occur between highly reduced **Ce-1** and H_2DCAQ (Appendix C.4.1). The reversibility of these redox transformations was also tested by subjecting **Ce-1** to repeated oxidation and reduction cycles with DPPH and H_2DCAQ. These experiments show a nearly identical relationship between expected and measured $\%Ce^{3+}$, demonstrating that these redox reactions are quantitative and highly reversible (Figure 3.3). This assertion is further supported by ^{1}H NMR studies of the **Ce-1** ligand sphere, which showed reversible changes in the NMR integrals for bound oleate and H_2O upon reduction and re-oxidation (Appendix C.4). Dynamic light scattering (DLS) studies of **Ce-2** also indicate

that the size and dispersity of the colloid remain constant with reduction (Figure C8). These investigations confirm the reversibility of redox reactions at OLE-Ce colloids and the validity of eq 3.2 across the full range of $\%Ce^{3+}$ accessed in these studies.

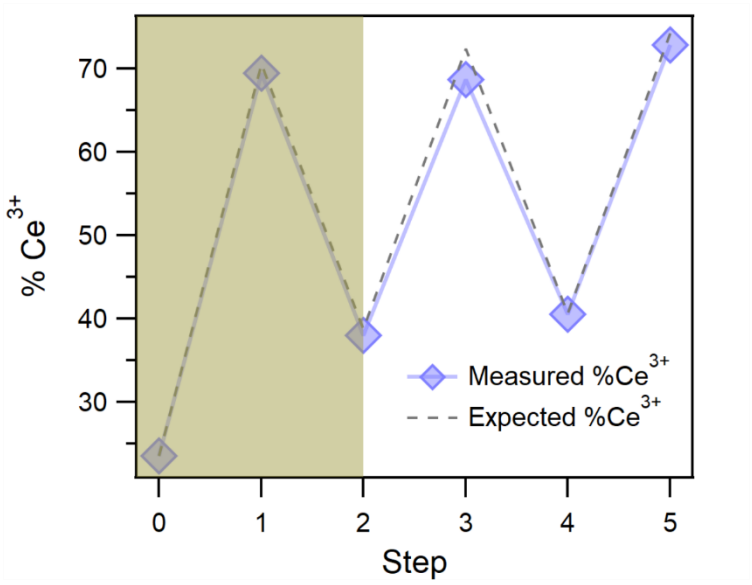

Figure 3.3. Redox cycling of **Ce-1** using H_2DCAQ as the reductant and DPPH as the oxidant. NMR samples were prepared using stock solutions of H_2DCAQ and DPPH in THF-d_8. The traces for the observed (purple) and expected (gray) changes in $\%Ce^{3+}$ are shown. Expected $\%Ce^{3+}$ was determined by quantifying organic products produced (and therefore $\Delta\%Ce^{3+}$) for the first additions of H_2DCAQ and DPPH stock solutions shown in the shaded region (gold) of the graph. Uncertainties are similar to the size of the symbols.

3.3 Discussion

3.3.1 OLE-Ce BDFE Trends

Equilibrium states are reached between OLE-Ce and a variety of PCET reagents, providing a direct measure of the hydrogen atom affinity of the ceria nanoparticles, the $BDFE_{Ce}$, at various values of $\%Ce^{3+}$ (Table 3.1). A plot of these data shows a roughly linear inverse correlation for the **Ce-1** and **Ce-2** samples (Figure 3.4, blue circles and green stars), where more reduced ceria nanocrystals – higher $\%Ce^{3+}$ – have weaker bonds to hydrogen – lower $BDFE_{Ce}$. The larger **Ce-L** nanocrystals also show an inverse linear correlation (Figure 3.4, orange triangles), but the correlation for **Ce-L** is steeper and shifted to lower values of $\%Ce^{3+}$. These negative correlations

match the general chemical intuition that reducing OLE-Ce colloids should weaken their ceria–H bonds. The observation of similar relationships for all three batches of nanoceria, despite their differences in size, highlights the generality of this result. We also note that these plots of $BDFE_{Ce}$ vs. $\%Ce^{3+}$ are significantly less linear without the Nernstian correction for the concentrations of the PCET reagents (Figure C26).

Remarkably, the $BDFE_{Ce}$ of **Ce-1** is tuned over 13.0 kcal mol^{-1} (0.56 eV) with changes in the $\%Ce^{3+}$. Similar ranges in $BDFE_{Ce}$ are observed for **Ce-2** and **Ce-L** (Table C5). For **Ce-1**, this enormous range in $BDFE_{Ce}$ occurs over a change in $\%Ce^{3+}$ from 17.5% to 72.2%. This variation in $BDFE_{Ce}$ with $\%Ce^{3+}$ is too large to be explained solely by a Le Chatelier or mass-action effect, which would predict a change of only 0.6 kcal mol^{-1} for this change in $\%Ce^{3+}$.[72] This effect is even more pronounced for the larger **Ce-L** colloid, where the same variation in $BDFE_{Ce}$ occurs over a change in $\%Ce^{3+}$ of only 12%. The difference in the slopes of these correlations is discussed below.

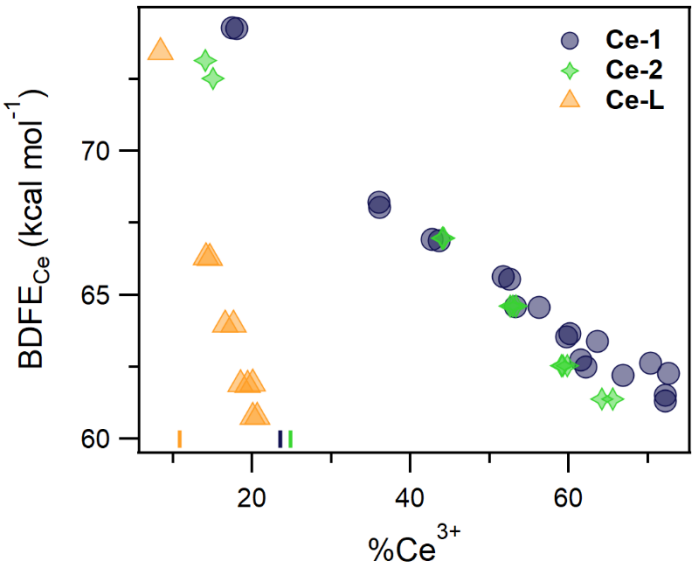

Figure 3.4. Plot of $BDFE_{Ce}$ vs. the $\%Ce^{3+}$ of various OLE-Ce colloids at equilibrium with different organic reagents. The data (from Table 3.1) are for **Ce-1** (blue circles), **Ce-2** (green stars), and **Ce-L** (orange triangles) equilibrium states. Colored tick marks on the x-axis denote the anchor $\%Ce^{3+}$ values of as-prepared OLE-Ce colloids.

3.3.2 OLE-Ce Active Site Location and Structure

The data presented above demonstrate that OLE-Ce can reversibly store and release a large number of hydrogen atom equivalents, but they do not reveal the location and structure of the added H• – the relevant active site(s). A detailed description of the structure of these oleate-capped and very small nanocrystals (ca. 4 unit cells across) is beyond the scope of this study. However, the results do provide insight into the specific questions of what kinds of bonds are formed and whether reduction occurs primarily at surface sites or throughout the bulk of the nanocrystal.

The issue of surface vs. bulk reduction was investigated by examining how the maximum loading of hydrogen atoms was affected by nanoparticle size. By XANES, the smaller **Ce-1** particles (d = 1.8 nm) could be reduced as far as 76% in $\%Ce^{3+}$, while the larger **Ce-L** (d = 4.0 nm) could be reduced to only 30% (Table C4). This suggests a surface-confined process, because the larger particles have a smaller fraction of surface cerium ions (Table C1). To quantitatively probe the hypothesis that reduction occurs primarily at the surface, the number of surface cerium sites was

estimated by two methods. In the first, the nanoparticle was treated as a sphere and its surface as a shell, while in the second the number of surface cerium atoms was estimated based on the reported faceting of uncapped 3 – 10 nm cerium oxide nanoparticles.[73] The sphere method estimates that the proportion of surface cerium atoms for **Ce-1** and **Ce-L** are 80-89% and 47-55% respectively, while the facet method estimates 76 – 95% and 35 – 42%, based on the size distributions determined from TEM images (Appendix C.2). While both of these methods require significant assumptions, the differences in proportions of surface cerium atoms between the two sizes of OLE-Ce are larger than the uncertainties. These estimates indicate a surface-confined process, which is consistent with the literature on H_2 reduction of ceria.[26,29,45,74] They imply that a large fraction of surface cerium ions can be reduced in these reactions, while the cerium ions in the core of the nanocrystals are much more resistant to reduction.

Scheme 3.3. Possible PCET Reactions at Nanoceria Surfaces.

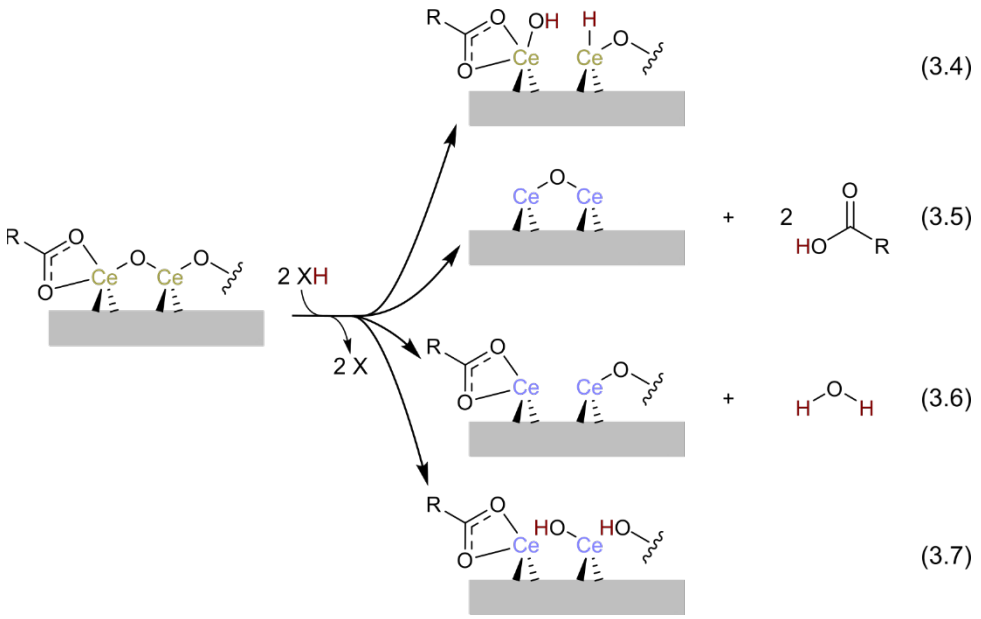

Transfer of hydrogen atoms from the organic reagents to the ceria surface could in principle form water, form oleic acid from surface oleate groups, form surface

hydroxides, or form cerium hydrides (Scheme 3.3). The formation of cerium hydrides has recently been proposed in gas-solid hydrogenation reactions, at high temperatures or with heat-treated ceria, and in reactions with borane reagents.[75-78] However, our observation of $\%Ce^{3+}$ increasing upon addition of hydrogen atom donors is incompatible with the proposed mechanisms of Ce–H formation given the BDFEs of the reductants used in these studies (eq 3.4). Nanoceria mechanisms involving the formation of either oleate/oleic acid or H_2O (eqs 3.5 & 3.6) can also be ruled out (Appendix C.8). Addition of 3Å sieves, which should remove free H_2O in THF, does not affect the ability to reversibly change the $\%Ce^{3+}$ of **Ce-1** (Figure C12), and the measured changes in oleic acid concentrations during the reactions are not consistent with the stoichiometric relationship in eq 3.5. Addition of excess oleic acid leads to greater oxidation of H_2DMQ by **Ce-1**, and addition of TBA^+OLE^- shuts down reactivity. These observations are contradictory to the mechanism shown in eq 3.5. The increased reactivity of **Ce-1** in the presence of oleic acid occurs concomitantly with the appearance of $Ce(OLE)_3$ in the ^{1}H NMR spectrum. $Ce(OLE)_3$ does not grow in the ^{1}H NMR spectrum if oleic acid is not added in excess, and addition of only $Ce(OLE)_3$ does not perturb the equilibrium position of H_2DMQ/**Ce-1** (Figure C29). In light of these results, we propose that oleic acid protonates surface Ce^{3+} ions to form solution-phase $Ce(OLE)_3$, thereby generating more active ceria surface and boosting apparent reactivity.

By process of elimination, it is most likely that OLE-Ce colloids react to form hydroxyl groups (eq 3.7). Although we were unable to directly verify this structure for OLE-Ce, other reports have observed or predicted surface hydroxyl groups on ceria under other conditions.[26,29,44,79-83] Because the redox chemistry occurs primarily at the surface cerium ions (see above), and the conversion of oxide to hydroxide provides the local charge balance for the reduction to Ce^{3+}, it is most likely that the hydroxide groups formed are also at the surface. As a result, we conclude that the relevant

thermodynamic predictor of PCET reactivity at OLE-Ce is the BDFE of its surface O–H bonds.

We now revisit the correlation of $BDFE_{Ce}$ with $\%Ce^{3+}$, in light of the conclusions that the transfer of hydrogen atoms to the ceria nanocrystals forms surface Ce^{3+} and hydroxide ions. By using the $\%Ce^{3+}$ metric, Figure 3.4 implicitly assumes that all cerium atoms in OLE-Ce are active. Since the majority of redox activity comes from surface cerium atoms, a more appropriate analysis would only use the fraction of cerium atoms at the nanocrystal surface. To estimate this fraction, we use the facet method described above with the average diameters from TEM measurements. These indicate that roughly 85% of the cerium atoms are at the surface for **Ce-1**, 80% for **Ce-2** and 39% for **Ce-L** (Appendix C.2.2). With the assumption that the measured changes in $\%Ce^{3+}$ occur only at surface sites, these values provide estimates of the percentage of surface cerium atoms that are Ce^{3+} (%Surface-Ce^{3+}). Replotting the data as $BDFE_{Ce}$ vs. %Surface-Ce^{3+} significantly coalesces the relationships observed for the three OLE-Ce batches (Figure 3.5). The shaded regions in Figure 3.5 are estimates of the uncertainties in %Surface-Ce^{3+} calculated from 1σ variance in the average diameters by TEM. When accounting for these uncertainties, the data for **Ce-L** remains distinct from that for **Ce-1** and **Ce-2**, an observation that future work will need to examine. Still, the closer agreement between the large and small OLE-Ce batches supports the conclusion that redox reactivity occurs primarily at surface sites, as is commonly found for nanoceria.[84,85]

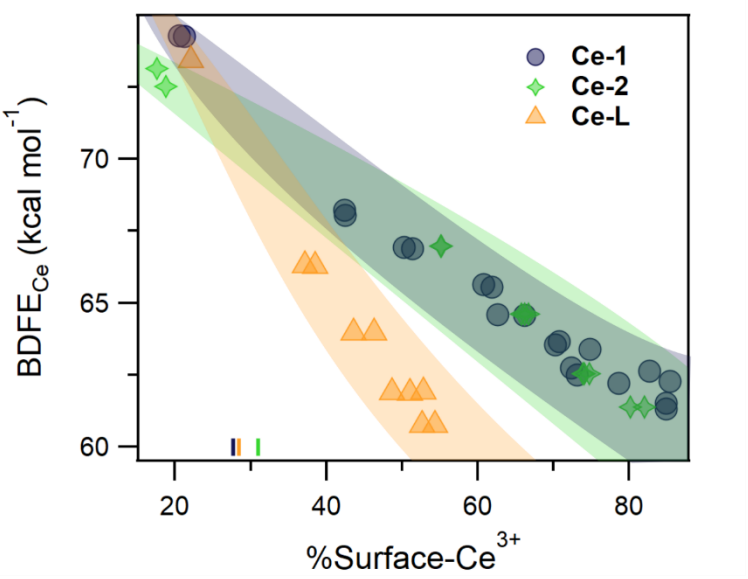

Figure 3.5. Plot of $BDFE_{Ce}$ (the same data as Figure 3.4; Table 3.1) vs. the %Surface-Ce^{3+} for **Ce-1** (blue circles), **Ce-2** (green stars), and **Ce-L** (orange triangles). The %Surface-Ce^{3+} were estimated from the average nanoparticle diameters (*d*) from TEM images, and the shaded regions estimate the uncertainties resulting from the 1σ variance in *d*. Colored tick marks on the x-axis denote the anchor %Surface-Ce^{3+} values of as-prepared OLE-Ce colloids.

3.3.3 Physical Models of the $BDFE_{Ce}$ vs. %Surface-Ce^{3+} Relationship and their Implications

The large variation in $BDFE_{Ce}$ with changes in the average redox state of the ceria nanocrystals was unexpected. This section explores plausible physical models of interfacial energetics that could shed light on this variation.

In principle, the linear relationship between $BDFE_{Ce}$ and the "charge added", or %Surface-Ce^{3+}, could be described by a capacitive model, similar to previous studies of ZnO nanoparticles.[86] However, invoking this model is inconsistent with a basic property of capacitive systems: a buildup of electric charge.[87] The equilibrations above involve the movement of chemical redox equivalents, but as neutral hydrogen atoms. The lack of charge buildup in these reactions is confirmed by the insensitivity of OLE-Ce reduction to the addition of electrolyte or lowering of the solvent dielectric constant (Appendix C.8). As a result, a traditional capacitive model can be ruled out for the data presented above.

A more attractive model comes from surface science where the relationship between hydrogen adsorption energy and surface coverage (θ) has been studied in detail for well-defined metal surfaces using *isotherms*. The simplest of these models is the Langmuir isotherm which describes surface adsorbates as an ideal 2D gas, such that the adsorption energy is independent of θ. This treatment is highly analogous to a Nernstian electrochemical dependence. As noted above, the $BDFE_{Ce}$ vs. %Surface-Ce^{3+} in Figure 3.5 cannot be fit with Langmuirian or Nernstian treatments, which would predict a 20-fold smaller variation in $BDFE_{Ce}$. However, deviations from Langmuirian behavior are well known, and in such cases data are often modeled with the Frumkin isotherm.[88] This applies a linear correction to the Langmuir isotherm, such that the hydrogen adsorption energy at $\theta = 0.5$ is $\mu + 0.5C$ where C designates the magnitude of the linear correction in kcal mol^{-1} (eq 3.8). Application of a Frumkin isotherm to the data in Figure 3.5 leads to good fits (Figure C27). In fits to eq 3.8, the dependence on θ is dominated by the correction term; for instance, $C \cong 16$ kcal mol^{-1} for **Ce-1** and **Ce-2**.

$$BDFE_{Ce} = \mu - 1.364 \times \log\left(\frac{\theta}{1-\theta}\right) + C \times \theta \qquad (3.8)$$

At present, we have limited insight into the physical basis for the large Frumkin correction required to fit the $BDFE_{Ce}$ vs. Surface-%Ce^{3+} data for OLE-Ce. Frumkin corrections are commonly associated with either interactions between adsorbates or with a distribution of chemically distinct adsorption sites. Either explanation could apply to these ceria nanoparticles based on prior studies. In support of a distribution of chemically distinct active sites, crystallographic analyses of atomically-precise nanoceria clusters demonstrate local distortions in Ce–O bond lengths near Ce^{3+} sites, suggest that Ce^{4+} and Ce^{3+} ions have different ligand preferences, and provide evidence for a localized, or mixed-valence, description of nanoceria electronic structure.[89] Ligand effects are also known for aqueous Ce^{4+} cations, where anion

identity is known to have a significant effect on the reduction potential.[90] Furthermore, a computational study of Ce_nO_{2n} nanoclusters, where n = 12 and n = 14, has shown that the hydrogen adsorption energy can vary by as much as 0.3 eV depending on the adsorption site.[46] However, the continuous linearity of the $BDFE_{Ce}$ vs. %Surface-Ce^{3+} relationship could be suggestive of an adsorbate-interaction model. This is further supported by an *ab initio* study which calls into question the mixed valence description of ceria, and instead suggests greater covalency in the lattice.[91] Additionally, adsorbate interactions have already been invoked to explain the well-studied relationship between ceria nanoparticle size and lattice parameter.[92] Parsing these effects is complex as localized states can also induce adsorbate interactions through lattice strain, an effect that is further heightened for small nanoparticles such as the ones used in these studies. From this perspective, these two models may not be so distinct given that each OLE-Ce colloid has distribution of nanoparticles sizes, a high concentration of edge and corner sites, and a complex distribution of capping ligands.

The *non*-Langmuirian behavior of ceria observed here may be important for improving and understanding its efficacy in applications as a catalyst and catalyst support. A recent report showed that even small changes in %Ce^{3+} (<10%) of a ceria support can induce significant changes in the oxidation state of platinum single-atom catalysts and influence their oxidation activities.[93] Furthermore, the %Ce^{3+} of aqueous nanoceria colloids has been shown to modulate its activity for scavenging reactive oxygen species.[24,25] Related effects are likely relevant to the high temperature (>600 K) oxygen-atom transfer reactivity of ceria, where relationships between oxygen vacancy concentration and oxygen chemical potential are known.[27,40,94,95] The chemical potentials of oxygen (μ_O) and hydrogen ($BDFE_{Ce}$) in ceria are simply related by the addition of water to an oxygen vacancy (Scheme 3.4);[42] this is the basis of solar-thermal water splitting by CeO_2 and other oxides.[96-98] At the suggestion of a reviewer, we include a plot of our $BDFE_{Ce}$ values measured at room temperature *vs.* the μ_O of

bulk ceria at 1,000 °C for the same ratio of reduced active sites (Figure C28).[27,40] Interestingly, a strong negative correlation is observed, consistent with the chemical intuition implied by Scheme 3.4. While the conditions are very different between these two measurements, this plot demonstrates a clear connection between the low and high temperature reactivity of ceria.

Scheme 3.4. Relating Oxygen Vacancies and Surface Hydrogen.

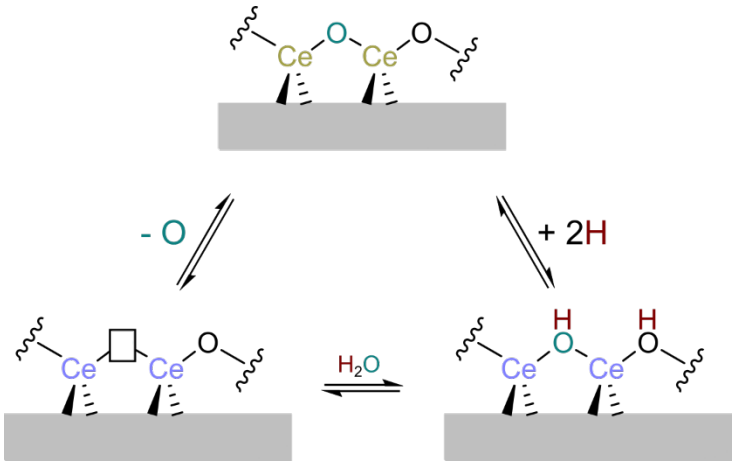

The relationship between $BDFE_{Ce}$ and $\%Ce^{3+}$ also has implications for *in silico* studies of hydrogen adsorption at materials which, for the most part, report single values for the hydrogen adsorption energy. In the context of ceria, reported $CeO_2(111)$ surface O–H bond strengths are in the same range as reported here, 62 to 82 kcal mol^{-1}, but they vary between different *in silico* studies. Furthermore, the effect of ceria redox state has not been significantly explored.[29,44,45] Experimental investigations of materials other than ceria have also suggested *ranges* of hydrogen adsorption energies. For example, a similar relationship between hydrogen atom affinity and redox state has been observed for tungsten trioxide,[99] and a recent study of cobalt phosphide from our group also suggests a distribution of BDFEs.[100] Consideration of these ranges in bond strengths will likely have implications for 'volcano plot' analyses that often use a single hydrogen binding energy as the descriptor. Due to the general importance of MO–H bond strengths, we hope that this study will stimulate new

computational approaches to understand the relationship between material redox state and bond strength thermochemistry.[101]

3.4 Conclusions

We present a novel equilibrium strategy for determining the hydrogen atom affinity of colloidal metal oxide nanoparticles through solution-phase reactivity studies of organic PCET reagents and oleate-capped cerium oxide nanoparticles. On average, nearly 60% of cerium atoms in a 2 nm diameter nanoparticle were shown to be redox active in these PCET reactions. Redox changes across this wide range of $\%Ce^{3+}$ were demonstrated to be reversible through an in-depth accounting of reaction stoichiometries and parallel characterizations of the colloids by ^{1}H NMR and XANES. The observed reversibility, and other data, show that in these reactions OLE-Ce colloids reach equilibrium states with many of the organic reagents used. Studies of how nanoparticle size affects the position of the equilibrium state demonstrated that the relevant bond on OLE-Ce is surface-confined, and further investigations indicated that the bond is a surface O–H group. On the basis of these findings, we have measured surface O–H BDFEs for colloidal nanoceria, and the first experimental BDFEs for any nanoscale metal oxide. This work demonstrates that the concepts of molecular bond strength thermochemistry can be applied to nanoscale materials to measure their hydrogen atom affinities.

Remarkably, the measured CeO–H BDFEs span 13 kcal mol^{-1} (0.56 eV) and show a linear dependence on the $\%Ce^{3+}$ of the nanocrystals. This broad relationship, which was not previously recognized, can be well described by a Frumkin isotherm that deviates substantially from Langmuirian behavior. The range of BDFEs measured provide important experimental benchmarks for future *in silico* studies and highlight the importance of considering the compositional complexities of nanoceria and many other catalytic and electrocatalytic metal oxide surfaces. Along these lines, we propose

that the tunability of $BDFE_{Ce}$ is important to the widespread use of ceria as a catalyst support. These findings should further the design and understanding of ceria-based catalysts and beyond.

3.5 References

1. Jackson, S. D.; Hargreaves, J. S. J., *Metal Oxide Catalysis*. 1 ed.; Wiley: 2008.
2. Fierro, J. L. G., *Metal Oxides: Chemistry and Applications*. 0 ed.; CRC Press: 2005.
3. Védrine, J. C., *Metal Oxides in Heterogeneous Catalysis*. Elsevier: 2018.
4. Pourbaix, M., *Atlas of Electrochemical Equilibria in Aqueous Solutions*. National Association of Corrosion Engineers: Houston, Texas, 1974.
5. Stumm, W.; Morgan, J. J., *Aquatic Chemistry: Chemical Equilibria and Rates in Natural Waters*. 3rd ed.; Wiley-Interscience: New York, 1995.
6. Rodríguez, J. A.; Fernández-García, M., *Synthesis, Properties, and Applications of Oxide Nanomaterials*. John Wiley & Sons, Inc.: 2006.
7. Bard, A. J., Inner-Sphere Heterogeneous Electrode Reactions. Electrocatalysis and Photocatalysis: The Challenge. *J. Am. Chem. Soc.* **2010,** *132* (22), 7559-7567.
8. Wöll, C., Hydrogen adsorption on metal oxide surfaces: a reinvestigation using He-atom scattering. *J. Phys.: Condens. Matter* **2004,** *16* (29), S2981-S2994.
9. Schrauben Joel, N.; Hayoun, R.; Valdez Carolyn, N.; Braten, M.; Fridley, L.; Mayer James, M., Titanium and Zinc Oxide Nanoparticles Are Proton-Coupled Electron Transfer Agents. *Science* **2012,** *336* (6086), 1298-1301.
10. Van de Walle, C. G.; Neugebauer, J., HYDROGEN IN SEMICONDUCTORS. *Annu. Rev. Mater. Res.* **2006,** *36* (1), 179-198.
11. Fung, V.; Hu, G.; Wu, Z.; Jiang, D.-e., Hydrogen in Nanocatalysis. *The Journal of Physical Chemistry Letters* **2020,** *11* (17), 7049-7057.
12. Campbell, C. T.; Mao, Z., Chemical Potential of Metal Atoms in Supported Nanoparticles: Dependence upon Particle Size and Support. *ACS Catal.* **2017,** *7* (12), 8460-8466.
13. Campbell, C. T.; Sellers, J. R. V., Enthalpies and Entropies of Adsorption on Well-Defined Oxide Surfaces: Experimental Measurements. *Chem. Rev.* **2013,** *113* (6), 4106-4135.
14. Seh, Z. W.; Kibsgaard, J.; Dickens, C. F.; Chorkendorff, I.; Nørskov, J. K.; Jaramillo, T. F., Combining theory and experiment in electrocatalysis: Insights into materials design. *Science* **2017,** *355* (6321), eaad4998.
15. Quaino, P.; Juarez, F.; Santos, E.; Schmickler, W., Volcano plots in hydrogen electrocatalysis – uses and abuses. *Beilstein Journal of Nanotechnology* **2014,** *5*, 846-854.
16. Nørskov, J. K.; Bligaard, T.; Logadottir, A.; Kitchin, J. R.; Chen, J. G.; Pandelov, S.; Stimming, U., Trends in the Exchange Current for Hydrogen Evolution. *J. Electrochem. Soc.* **2005,** *152* (3), J23.
17. Schmickler, W.; Trasatti, S., Comment on “Trends in the Exchange Current for Hydrogen Evolution” [J. Electrochem. Soc., 152, J23 (2005)]. *J. Electrochem. Soc.* **2006,** *153* (12), L31.
18. Samorjai, G. A.; Li, Y., Thermodynamics of Adsorbed Monolayers. In *Introduction to Surface Chemistry and Catalysis*, 2nd ed.; John Wiley & Sons, Inc.: New York, 2010; pp 313-323.
19. Ganduglia-Pirovano, M. V., The non-innocent role of cerium oxide in heterogeneous catalysis: A theoretical perspective. *Catal. Today* **2015,** *253*, 20-32.
20. Kibsgaard, J.; Tsai, C.; Chan, K.; Benck, J. D.; Nørskov, J. K.; Abild-Pedersen, F.; Jaramillo, T. F., Designing an improved transition metal phosphide catalyst for hydrogen evolution using experimental and theoretical trends. *Energy Environ. Sci.* **2015,** *8* (10), 3022-3029.
21. Esch, F.; Fabris, S.; Zhou, L.; Montini, T.; Africh, C.; Fornasiero, P.; Comelli, G.; Rosei, R., Electron Localization Determines Defect Formation on Ceria Substrates. *Science* **2005,** *309* (5735), 752-755.
22. Skorodumova, N. V.; Simak, S. I.; Lundqvist, B. I.; Abrikosov, I. A.; Johansson, B., Quantum Origin of the Oxygen Storage Capability of Ceria. *Phys. Rev. Lett.* **2002,** *89* (16), 166601.
23. Sayle, T. X. T.; Caddeo, F.; Zhang, X.; Sakthivel, T.; Das, S.; Seal, S.; Ptasinska, S.; Sayle, D. C., Structure-Activity Map of Ceria Nanoparticles, Nanocubes, and Mesoporous Architectures. *Chem. Mater.* **2016,** *28* (20), 7287-7295.
24. Pirmohamed, T.; Dowding, J. M.; Singh, S.; Wasserman, B.; Heckert, E.; Karakoti, A. S.; King, J. E. S.; Seal, S.; Self, W. T., Nanoceria exhibit redox state-dependent catalase mimetic activity. *Chem. Commun.* **2010,** *46* (16), 2736-2738.

25. Baldim, V.; Bedioui, F.; Mignet, N.; Margaill, I.; Berret, J.-F., The enzyme-like catalytic activity of cerium oxide nanoparticles and its dependency on Ce^{3+} surface area concentration. *Nanoscale* **2018,** *10* (15), 6971-6980.
26. Bernal, S.; Calvino, J. J.; Cifredo, G. A.; Gatica, J. M.; Omil, J. A. P.; Pintado, J. M., Hydrogen chemisorption on ceria: influence of the oxide surface area and degree of reduction. *J. Chem. Soc., Faraday Trans.* **1993,** *89* (18), 3499-3505.
27. Bulfin, B.; Lowe, A. J.; Keogh, K. A.; Murphy, B. E.; Lübben, O.; Krasnikov, S. A.; Shvets, I. V., Analytical Model of CeO2 Oxidation and Reduction. *The Journal of Physical Chemistry C* **2013,** *117* (46), 24129-24137.
28. Pettinger, N. W.; Empey, J. M.; Fröbel, S.; Kohler, B., Photoreductive dissolution of cerium oxide nanoparticles and their size-dependent absorption properties. *PCCP* **2020,** *22* (10), 5756-5764.
29. Werner, K.; Weng, X.; Calaza, F.; Sterrer, M.; Kropp, T.; Paier, J.; Sauer, J.; Wilde, M.; Fukutani, K.; Shaikhutdinov, S.; Freund, H.-J., Toward an Understanding of Selective Alkyne Hydrogenation on Ceria: On the Impact of O Vacancies on H2 Interaction with CeO2(111). *J. Am. Chem. Soc.* **2017,** *139* (48), 17608-17616.
30. Vilé, G.; Bridier, B.; Wichert, J.; Pérez-Ramírez, J., Ceria in Hydrogenation Catalysis: High Selectivity in the Conversion of Alkynes to Olefins. *Angew. Chem. Int. Ed.* **2012,** *51* (34), 8620-8623.
31. García-Melchor, M.; Bellarosa, L.; López, N., Unique Reaction Path in Heterogeneous Catalysis: The Concerted Semi-Hydrogenation of Propyne to Propene on CeO_2. *ACS Catal.* **2014,** *4* (11), 4015-4020.
32. Chang, K.; Zhang, H.; Cheng, M.-j.; Lu, Q., Application of Ceria in CO_2 Conversion Catalysis. *ACS Catal.* **2020,** *10* (1), 613-631.
33. Sohlberg, K.; Pantelides, S. T.; Pennycook, S. J., Interactions of Hydrogen with CeO_2. *J. Am. Chem. Soc.* **2001,** *123* (27), 6609-6611.
34. Luo, M.; Wang, Z.; Li, Y. C.; Li, J.; Li, F.; Lum, Y.; Nam, D.-H.; Chen, B.; Wicks, J.; Xu, A.; Zhuang, T.; Leow, W. R.; Wang, X.; Dinh, C.-T.; Wang, Y.; Wang, Y.; Sinton, D.; Sargent, E. H., Hydroxide promotes carbon dioxide electroreduction to ethanol on copper via tuning of adsorbed hydrogen. *Nature Communications* **2019,** *10* (1), 1-7.
35. Lu, M.; Zhang, Y.; Wang, Y.; Jiang, M.; Yao, X., Insight into Several Factors that Affect the Conversion between Antioxidant and Oxidant Activities of Nanoceria. *ACS Appl. Mater. Interfaces* **2016,** *8* (36), 23580-23590.
36. Nelson, B. C.; Johnson, M. E.; Walker, M. L.; Riley, K. R.; Sims, C. M., Antioxidant Cerium Oxide Nanoparticles in Biology and Medicine. *Antioxidants* **2016,** *5* (2).
37. Andreescu, D.; Bulbul, G.; Özel, R. E.; Hayat, A.; Sardesai, N.; Andreescu, S., Applications and implications of nanoceria reactivity: measurement tools and environmental impact. *Environ. Sci.: Nano* **2014,** *1* (5), 445-458.
38. Trovarelli, A.; Fornasiero, P., *Catalysis by Ceria and Related Materials*. Imperial College Press: 2013.
39. Zhang, C.; Yu, Y.; Grass, M. E.; Dejoie, C.; Ding, W.; Gaskell, K.; Jabeen, N.; Hong, Y. P.; Shavorskiy, A.; Bluhm, H.; Li, W.-X.; Jackson, G. S.; Hussain, Z.; Liu, Z.; Eichhorn, B. W., Mechanistic Studies of Water Electrolysis and Hydrogen Electro-Oxidation on High Temperature Ceria-Based Solid Oxide Electrochemical Cells. *J. Am. Chem. Soc.* **2013,** *135* (31), 11572-11579.
40. Bevan, D. J. M.; Kordis, J., Mixed oxides of the type MO_2 (fluorite)—M_2O_3—I oxygen dissociation pressures and phase relationships in the system CeO_2□Ce_2O_3 at high temperatures. *J. Inorg. Nucl. Chem.* **1964,** *26* (9), 1509-1523.
41. Van de Walle, C. G.; Neugebauer, J., Universal alignment of hydrogen levels in semiconductors, insulators and solutions. *Nature* **2003,** *423* (6940), 626-628.
42. Norby, T.; Widerøe, M.; Glöckner, R.; Larring, Y., Hydrogen in oxides. *Dalton Trans.* **2004,** (19), 3012-3018.
43. Shahed, S. M. F.; Hasegawa, T.; Sainoo, Y.; Watanabe, Y.; Isomura, N.; Beniya, A.; Hirata, H.; Komeda, T., STM and XPS study of CeO_2(111) reduction by atomic hydrogen. *Surf. Sci.* **2014,** *628*, 30-35.

44. Vicario, G.; Balducci, G.; Fabris, S.; de Gironcoli, S.; Baroni, S., Interaction of Hydrogen with Cerium Oxide Surfaces: a Quantum Mechanical Computational Study. *The Journal of Physical Chemistry B* **2006,** *110* (39), 19380-19385.
45. Paier, J.; Penschke, C.; Sauer, J., Oxygen Defects and Surface Chemistry of Ceria: Quantum Chemical Studies Compared to Experiment. *Chem. Rev.* **2013,** *113* (6), 3949-3985.
46. Zhou, C.; Zhang, B.; Hu, P.; Wang, H., An effective structural descriptor to quantify the reactivity of lattice oxygen in CeO_2 subnano-clusters. *PCCP* **2020**, 10.1039.C9CP05805B.
47. Warren, J. J.; Tronic, T. A.; Mayer, J. M., Thermochemistry of Proton-Coupled Electron Transfer Reagents and Its Implications. *Chem. Rev.* **2010,** *110*, 6961-7001.
48. Agarwal, R. G.; Coste, S. C.; Groff, B. D.; Heuer, A. M.; Noh, H.; Parada, G. A.; Wise, C. F.; Nichols, E. M.; Warren, J. J.; Mayer, J. M., Free Energies of Proton-Coupled Electron Transfer Reagents and Their Applications. *Chem. Rev., accepted* **2021**.
49. Bezdek, M. J.; Pappas, I.; Chirik, P. J., Determining and Understanding N-H Bond Strengths in Synthetic Nitrogen Fixation Cycles. In *Nitrogen Fixation*, Nishibayashi, Y., Ed. Springer International Publishing: Cham, 2017; pp 1-21.
50. Gentry, E. C.; Knowles, R. R., Synthetic Applications of Proton-Coupled Electron Transfer. *Acc. Chem. Res.* **2016,** *49* (8), 1546-1556.
51. Chalkley, M. J.; Peters, J. C., Relating N-H Bond Strengths to the Overpotential for Catalytic Nitrogen Fixation: Relating N-H Bond Strengths to the Overpotential for Catalytic Nitrogen Fixation. *Eur. J. Inorg. Chem.* **2020,** *2020* (15-16), 1353-1357.
52. Darcy, J. W.; Koronkiewicz, B.; Parada, G. A.; Mayer, J. M., A Continuum of Proton-Coupled Electron Transfer Reactivity. *Acc. Chem. Res.* **2018,** *51* (10), 2391-2399.
53. Roth, J. P., Application of the Marcus Cross Relation to Hydrogen Atom Transfer Reactions. *Science* **2001,** *294* (5551), 2524-2526.
54. Wise, C. F.; Mayer, J. M., Electrochemically Determined O–H Bond Dissociation Free Energies of NiO Electrodes Predict Proton-Coupled Electron Transfer Reactivity. *J. Am. Chem. Soc.* **2019,** *141* (38), 14971-14975.
55. Wise, C. F.; Agarwal, R. G.; Mayer, J. M., Determining Proton-Coupled Standard Potentials and X–H Bond Dissociation Free Energies in Nonaqueous Solvents Using Open-Circuit Potential Measurements. *J. Am. Chem. Soc.* **2020,** *142* (24), 10681-10691.
56. Coppel, Y.; Spataro, G.; Pagès, C.; Chaudret, B.; Maisonnat, A.; Kahn, M. L., Full Characterization of Colloidal Solutions of Long-Alkyl-Chain-Amine-Stabilized ZnO Nanoparticles by NMR Spectroscopy: Surface State, Equilibria, and Affinity. *Chemistry - A European Journal* **2012,** *18* (17), 5384-5393.
57. Shim, M.; Guyot-Sionnest, P., n-type colloidal semiconductor nanocrystals. *Nature* **2000,** *407* (6807), 981-983.
58. Kölle, U.; Grützel, M., Organometallic Rhodium(III) Complexes as Catalysts for the Photoreduction of Protons to Hydrogen on Colloidal TiO_2. *Angewandte Chemie International Edition in English* **1987,** *26* (6), 567-570.
59. Wang, C.-y.; Pagel, R.; Bahnemann, D. W.; Dohrmann, J. K., Quantum Yield of Formaldehyde Formation in the Presence of Colloidal TiO_2-Based Photocatalysts: Effect of Intermittent Illumination, Platinization, and Deoxygenation. *The Journal of Physical Chemistry B* **2004,** *108* (37), 14082-14092.
60. Buonsanti, R.; Llordes, A.; Aloni, S.; Helms, B. A.; Milliron, D. J., Tunable Infrared Absorption and Visible Transparency of Colloidal Aluminum-Doped Zinc Oxide Nanocrystals. *Nano Lett.* **2011,** *11* (11), 4706-4710.
61. Cohn, A. W.; Kittilstved, K. R.; Gamelin, D. R., Tuning the Potentials of “Extra” Electrons in Colloidal *n*-Type ZnO Nanocrystals via Mg^{2+} Substitution. *J. Am. Chem. Soc.* **2012,** *134* (18), 7937-7943.
62. Ribot, F.; Escax, V.; Roiland, C.; Sanchez, C.; Martins, J. C.; Biesemans, M.; Verbruggen, I.; Willem, R., *In situ* evaluation of interfacial affinity in CeO_2 based hybrid nanoparticles by pulsed field gradient NMR. *Chem. Commun.* **2005,** (8), 1019.
63. Schneider, J.; Matsuoka, M.; Takeuchi, M.; Zhang, J.; Horiuchi, Y.; Anpo, M.; Bahnemann, D. W., Understanding TiO_2 Photocatalysis: Mechanisms and Materials. *Chem. Rev.* **2014,** *114* (19), 9919-9986.

64. Cohn, A. W.; Janßen, N.; Mayer, J. M.; Gamelin, D. R., Photocharging ZnO Nanocrystals: Picosecond Hole Capture, Electron Accumulation, and Auger Recombination. *The Journal of Physical Chemistry C* **2012,** *116* (38), 20633-20642.
65. Grauer, D. C.; Alivisatos, A. P., Ligand Dissociation Mediated Charge Transfer Observed at Colloidal $W_{18}O_{49}$ Nanoparticle Interfaces. *Langmuir* **2014,** *30* (9), 2325-2328.
66. Gambardella, A. A.; Bjorge, N. S.; Alspaugh, V. K.; Murray, R. W., Voltammetry of Diffusing 2 nm Iridium Oxide Nanoparticles. *The Journal of Physical Chemistry C* **2011,** *115* (44), 21659-21665.
67. Brozek, C. K.; Hartstein, K. H.; Gamelin, D. R., Potentiometric Titrations for Measuring the Capacitance of Colloidal Photodoped ZnO Nanocrystals. *J. Am. Chem. Soc.* **2016,** *138* (33), 10605-10610.
68. Damatov, D.; Laga, S. M.; Mader, E. A.; Peng, J.; Agarwal, R. G.; Mayer, J. M., Redox Reactivity of Colloidal Nanoceria and Use of Optical Spectra as an In Situ Monitor of Ce Oxidation States. *Inorg. Chem.* **2018,** *57* (22), 14401-14408.
69. Nachimuthu, P.; Shih, W.-C.; Liu, R.-S.; Jang, L.-Y.; Chen, J.-M., The Study of Nanocrystalline Cerium Oxide by X-Ray Absorption Spectroscopy. *J. Solid State Chem.* **2000,** *149* (2), 408-413.
70. Cafun, J.-D.; Kvashnina, K. O.; Casals, E.; Puntes, V. F.; Glatzel, P., Absence of Ce^{3+} Sites in Chemically Active Colloidal Ceria Nanoparticles. *ACS Nano* **2013,** *7* (12), 10726-10732.
71. Zhang, J.; Wu, Z.; Liu, T.; Hu, T.; Wu, Z.; Ju, X., XANES study on the valence transitions in cerium oxide nanoparticles. *Journal of Synchrotron Radiation* **2001,** *8* (2), 531-532.
72. A Nernstian relationship where the BDFEs vary according to –RT[log(%Ce^{3+}/%Ce^{4+})] would predict a variation of 0.64 kcal mol^(-1) for a change of %Ce^{3+} from 17.5% to 72.2%:

$-0.001987(298)[\log(17.5/(100-17.5)) - \log(72.2/(100-72.2))] = 0.64$ kcal mol^{-1}.
73. Wang, Z. L.; Feng, X., Polyhedral Shapes of CeO_2 Nanoparticles. *The Journal of Physical Chemistry B* **2003,** *107* (49), 13563-13566.
74. Perrichon, V.; Laachir, A.; Bergeret, G.; Fréty, R.; Tournayan, L.; Touret, O., Reduction of cerias with different textures by hydrogen and their reoxidation by oxygen. *J. Chem. Soc., Faraday Trans.* **1994,** *90* (5), 773-781.
75. Wu, Z.; Cheng, Y.; Tao, F.; Daemen, L.; Foo, G. S.; Nguyen, L.; Zhang, X.; Beste, A.; Ramirez-Cuesta, A. J., Direct Neutron Spectroscopy Observation of Cerium Hydride Species on a Cerium Oxide Catalyst. *J. Am. Chem. Soc.* **2017,** *139* (28), 9721-9727.
76. Li, Z.; Werner, K.; Qian, K.; You, R.; Płucienik, A.; Jia, A.; Wu, L.; Zhang, L.; Pan, H.; Kuhlenbeck, H.; Shaikhutdinov, S.; Huang, W.; Freund, H.-J., Oxidation of Reduced Ceria by Incorporation of Hydrogen. *Angew. Chem. Int. Ed.* **2019,** *58*, 2-10.
77. Ji, P.; Sawano, T.; Lin, Z.; Urban, A.; Boures, D.; Lin, W., Cerium-Hydride Secondary Building Units in a Porous Metal–Organic Framework for Catalytic Hydroboration and Hydrophosphination. *J. Am. Chem. Soc.* **2016,** *138* (45), 14860-14863.
78. Moon, J.; Cheng, Y.; Daemen, L. L.; Li, M.; Polo-Garzon, F.; Ramirez-Cuesta, A. J.; Wu, Z., Discriminating the Role of Surface Hydride and Hydroxyl for Acetylene Semihydrogenation over Ceria through *In Situ* Neutron and Infrared Spectroscopy. *ACS Catal.* **2020**, 5278-5287.
79. García-Melchor, M.; López, N., Homolytic Products from Heterolytic Paths in H_2 Dissociation on Metal Oxides: The Example of CeO_2. *The Journal of Physical Chemistry C* **2014,** *118* (20), 10921-10926.
80. Copéret, C.; Estes, D. P.; Larmier, K.; Searles, K., Isolated Surface Hydrides: Formation, Structure, and Reactivity. *Chem. Rev.* **2016,** *116* (15), 8463-8505.
81. Gill, L.; Beste, A.; Chen, B.; Li, M.; Mann, A. K. P.; Overbury, S. H.; Hagaman, E. W., Fast MAS ^{1}H NMR Study of Water Adsorption and Dissociation on the (100) Surface of Ceria Nanocubes: A Fully Hydroxylated, Hydrophobic Ceria Surface. *The Journal of Physical Chemistry C* **2017,** *121* (13), 7450-7465.
82. Chen, J.; Hope, M. A.; Lin, Z.; Wang, M.; Liu, T.; Halat, D. M.; Wen, Y.; Chen, T.; Ke, X.; Magusin, P. C. M. M.; Ding, W.; Xia, X.; Wu, X.-P.; Gong, X.-Q.; Grey, C. P.; Peng, L., Interactions of Oxide Surfaces with Water Revealed with Solid-State NMR Spectroscopy. *J. Am. Chem. Soc.* **2020**, jacs.0c03760.

83. Chen, B.; Ma, Y.; Ding, L.; Xu, L.; Wu, Z.; Yuan, Q.; Huang, W., Reactivity of Hydroxyls and Water on a CeO_2 (111) Thin Film Surface: The Role of Oxygen Vacancy. *The Journal of Physical Chemistry C* **2013,** *117* (11), 5800-5810.
84. Goris, B.; Turner, S.; Bals, S.; Van Tendeloo, G., Three-Dimensional Valency Mapping in Ceria Nanocrystals. *ACS Nano* **2014,** *8* (10), 10878-10884.
85. Spadaro, M. C.; Luches, P.; Bertoni, G.; Grillo, V.; Turner, S.; Van Tendeloo, G.; Valeri, S.; D'Addato, S., Influence of defect distribution on the reducibility of CeO_{2-x} nanoparticles. *Nanotechnology* **2016,** *27* (42), 425705.
86. Liu, H.; Brozek, C. K.; Sun, S.; Lingerfelt, D. B.; Gamelin, D. R.; Li, X., A Hybrid Quantum-Classical Model of Electrostatics in Multiply Charged Quantum Dots. *The Journal of Physical Chemistry C* **2017,** *121* (46), 26086-26095.
87. An areal capacitance can be estimated from the ca. 77 Ce atoms per 1.8 nm diameter nanoparticle for **Ce-1** and from the $\Delta\%Ce^{3+}$ being 54.7% between states spanning 13.0 kcal mol^{-1} (or 564 mV) in BDFE:

Areal Capacitance = $q/\Delta EA$, where q in Coulombs = $(77*0.564*1/(6.24*10^{18}))$ C, ΔE = 0.546 V, and the area of a sphere of radius 0.9 nm is $(4\pi*(0.9*10^{-7})^2)$ cm^2, yielding areal capacitance = 125 μF cm^{-2}.
88. Gómez, R.; Orts, J. M.; Álvarez-Ruiz, B.; Feliu, J. M., Effect of Temperature on Hydrogen Adsorption on Pt(111), Pt(110), and Pt(100) Electrodes in 0.1 M $HClO_4$. *The Journal of Physical Chemistry B* **2004,** *108* (1), 228-238.
89. Mitchell, K. J.; Abboud, K. A.; Christou, G., Atomically-precise colloidal nanoparticles of cerium dioxide. *Nature Communications* **2017,** *8* (1), 1445.
90. Buchanan, C. A.; Ko, E.; Cira, S.; Balasubramanian, M.; Goldsmith, B. R.; Singh, N., Structures and Free Energies of Cerium Ions in Acidic Electrolytes. *Inorg. Chem.* **2020,** *59* (17), 12552-12563.
91. Duchoň, T.; Aulická, M.; Schwier, E. F.; Iwasawa, H.; Zhao, C.; Xu, Y.; Veltruská, K.; Shimada, K.; Matolín, V., Covalent versus localized nature of 4f electrons in ceria: Resonant angle-resolved photoemission spectroscopy and density functional theory. *Physical Review B* **2017,** *95* (16), 165124.
92. Prieur, D.; Bonani, W.; Popa, K.; Walter, O.; Kriegsman, K. W.; Engelhard, M. H.; Guo, X.; Eloirdi, R.; Gouder, T.; Beck, A.; Vitova, T.; Scheinost, A. C.; Kvashnina, K.; Martin, P., Size Dependence of Lattice Parameter and Electronic Structure in CeO_2 Nanoparticles. *Inorg. Chem.* **2020,** *59* (8), 5760-5767.
93. Jeong, H.; Shin, D.; Kim, B. S.; Bae, J.; Shin, S.; Choe, C.; Han, J. W.; Lee, H., Controlling the Oxidation State of Pt Single Atoms for Maximizing Catalytic Activity. *Angew. Chem. Int. Ed.* **2020**, anie.202009776.
94. Dejoie, C.; Yu, Y.; Bernardi, F.; Tamura, N.; Kunz, M.; Marcus, M. A.; Huang, Y.-L.; Zhang, C.; Eichhorn, B. W.; Liu, Z., Potential Control of Oxygen Non-Stoichiometry in Cerium Oxide and Phase Transition Away from Equilibrium. *ACS Appl. Mater. Interfaces* **2020,** *12* (28), 31514-31521.
95. Hillert, M.; Jansson, B., Thermodynamic Model for Nonstoichiometric Ionic Phases - Application to CeO_{2-x}. *J. Am. Ceram. Soc.* **1986,** *69* (10), 732-734.
96. Chueh, W. C.; Falter, C.; Abbott, M.; Scipio, D.; Furler, P.; Haile, S. M.; Steinfeld, A., High-Flux Solar-Driven Thermochemical Dissociation of CO_2 and H_2O Using Nonstoichiometric Ceria. *Science* **2010,** *330* (6012), 1797-1801.
97. Abanades, S.; Legal, A.; Cordier, A.; Peraudeau, G.; Flamant, G.; Julbe, A., Investigation of reactive cerium-based oxides for H_2 production by thermochemical two-step water-splitting. *Journal of Materials Science* **2010,** *45* (15), 4163-4173.
98. Rao, C. N. R.; Dey, S., Solar thermochemical splitting of water to generate hydrogen. *Proceedings of the National Academy of Sciences* **2017,** *114* (51), 13385-13393.
99. Crandall, R. S.; Wojtowicz, P. J.; Faughnan, B. W., Theory and measurement of the change in chemical potential of hydrogen in amorphous H_xWO_3 as a function of the stoichiometric parameter x. *Solid State Commun.* **1976,** *18* (11), 1409-1411.
100. Delley, M. F.; Wu, Z.; Mundy, M. E.; Ung, D.; Cossairt, B. M.; Wang, H.; Mayer, J. M., Hydrogen on Cobalt Phosphide. *J. Am. Chem. Soc.* **2019,** *141* (38), 15390-15402.

101. Zakaryan, H. A.; Kvashnin, A. G.; Oganov, A. R., Stable reconstruction of the (110) surface and its role in pseudocapacitance of rutile-like RuO_2. *Scientific Reports* **2017,** *7* (1), 10357.

Chapter 4

CeO-H Bond Strength Modulated Brønsted-Evans Polanyi Relationships for Cerium Oxide Nanoparticle Colloids

With contributions from Agarwal, R. G.; Mayer, J. M. "CeO-H Bond Strength Modulated Brønsted-Evans Polanyi Relationships for Cerium Oxide Nanoparticle Colloids." *Manuscript in Preparation*. I gratefully acknowledge Dr. Anna Brezny for her help with experimental design and kinetic analysis for this project.

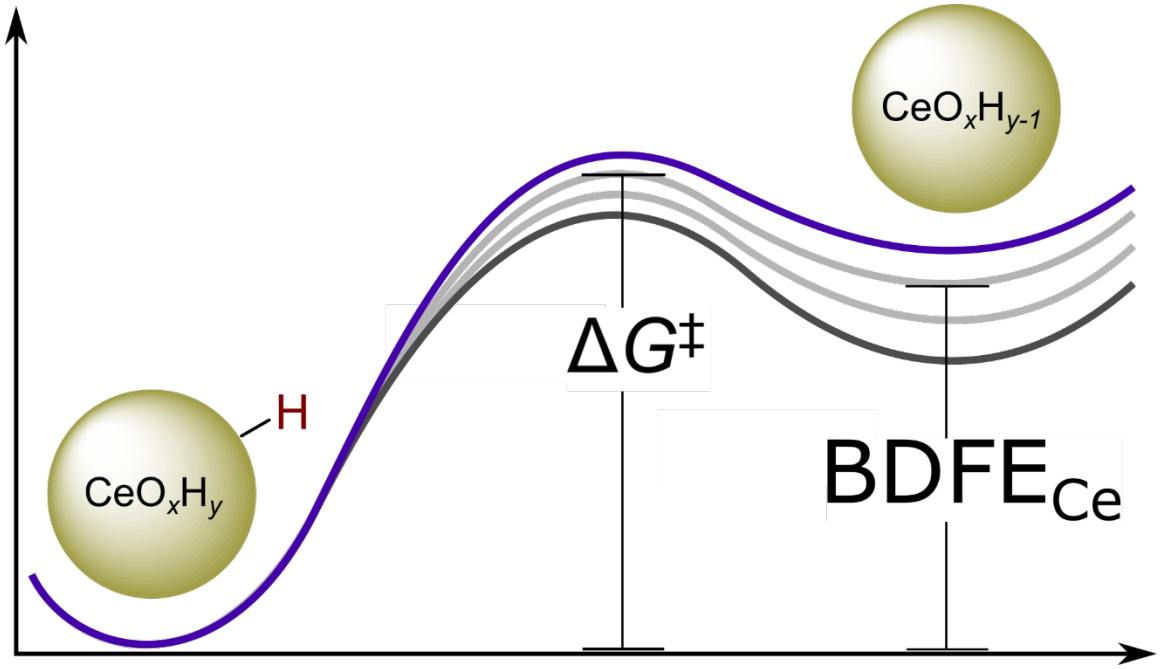

4.1 Introduction

The free energy of hydrogen adsorption ($\Delta G°_H$) at an interface is an important predictor of heterogeneous catalyst or electrocatalyst performance for a variety of chemical processes, including those at both sides of a water electrolysis cell.[1] More generally, this type of study is part of family where some thermochemical property is used as a descriptor for the kinetic properties of a set of reactions. These predictions are commonly derived using a "volcano plot" or similar analysis in which a computed $\Delta G°$ is plotted against an experimental metric of their kinetic prowess, such as exchange current density or reaction rate.[1-4] These analyses have proven powerful in

the search for new catalysts,[5-7] although, this approach has also been questioned.[3,8,9] The volcano plot or 'scaling relationship' analysis implies theoretical limits on the rate and efficiency of catalysis, so significant work has been done to circumvent them.[10-12]

One key theoretical basis for such analyses is the longstanding empirical Brønsted-Evans Polanyi (BEP) linear relationships between the free energy of activation and free energy of the reaction, or equivalently, between the logarithms of the rate and equilibrium constant (eqs 4.4.1a and b).[5,13-17] These two equations have the same constant, the Brønsted α, which is typically between 0 and 1.[18-22] The values of α can in some cases be related to the position of the transition state along the reaction coordinate, with 1 being closest to products.[18-22]

$$\Delta G^{\ddagger} = \alpha \Delta G° + c \qquad (4.4.1a)$$

$$\log(k) = \alpha \log(K_{eq}) + d \qquad (4.4.1b)$$

The BEP relation was developed for a single elementary reaction step in homogeneous media (gas or solution), with the $\Delta G^{\ddagger}$ and $\Delta G°$ referring specifically to that one step.[23,24] However, similar relationships, also denoted as BEP relations, are often applied to surfaces, and other systems where the mechanism is not completely known. The application of BEP models to multistep catalytic reactions on different materials surfaces is common but often requires that the energies of different intermediates and transition states linearly correlate with each other and with the descriptor, and that the Brønsted α's do not vary substantially from one reaction to another.[1,6,25] It is this use of linear correlations, well supported by computational studies,[5,26,27] that gave rise to the term 'scaling relationships' to describe this approach. More detailed models are also being developed, including those with microkinetic modeling and methodologies such as the Degree of Rate Control.[8,28-32]

Another key assumption in the common use of BEP relations for surface reactions is that the dependence of the thermodynamic and kinetic parameters on

surface coverage is small and constant across different materials. Analyses of solution and gas phase reactions can assume a priori that all the molecules are the same over a wide range of concentration or partial pressure (though there are non-idealities at high concentrations or pressures). On a surface, however, there are often interactions among adsorbates that shift the adsorbate properties as a function of coverage.[33-36] The effect of adsorbate interactions on BEP analyses has received considerably less consideration, and coverage effects are not generally considered in 'big picture' volcano plot analyses. However, they can be quite significant. For hydrogen adsorption to Pt(111), a model reaction, the underpotential deposition of hydrogen varies with Pt–H coverage over a range of 0.5 eV or ~12 kcal mol^{-1}.[37] This is nearly half the width of a traditional volcano plot for the hydrogen evolution reaction.[38] This range is six-times greater than what would be expected for an ideal, Langmuirian, surface adsorption process (~2 kcal mol^{-1}).[39] While calculated and experimental measures of the coverage dependance of hydrogen adsorption are possible for well-defined surfaces such as Pt(111), similar reports for ill-defined, catalytic surfaces – especially those of binary materials – generally do not exist.[36,40,41] These limitations have limited the number of experimental studies which have probed the effect of coverage on the *kinetics* of hydrogen transfer from (nano)materials.[37,42]

This work probes the connections between hydrogen coverage, hydrogen adsorption free energy, and the rate of hydrogen transfer from colloidal nanoceria (CeO_2). We take advantage of our previous measurements of CeO–H bond dissociation free energies (BDFEs) for oleate-capped cerium oxide nanoparticle colloids (OLE-Ce) in tetrahydrofuran (THF) solutions.[43] This study analyzed equilibria between OLE-Ce and organic molecules that involved the exchange of H-atoms between the two; Addition of each H to OLE-Ce formed one surface O–H group with reduction of one Ce^{4+} to Ce^{3+}. The CeO–H BDFEs were shown to vary substantially with the average redox state (%Ce^{3+}) of OLE-Ce – which is equivalent to the surface coverage of H. The

wide range of BDFEs, over 13 kcal mol^{-1}, had not previously been shown for cerium oxide, although we expect that the general phenomenon is common to many binary materials. [43,44]

These results provide a unique opportunity to measure how the hydrogen adsorption free energy (and average redox state) of a metal oxide, in this case cerium oxide, controls the rate of net hydrogen atom (e^-/H^+), or equivalently proton-coupled electron transfer (PCET), from its surface. To simplify the system as much as possible, the studies reported below probe the net transfer of a single hydrogen atom from OLE-Ce to stable 2,2-diphenyl-1-picrylhydrazyl radicals (DPPH) (Scheme 4.1).

Scheme 4.1. Net Hydrogen Atom Transfer from OLE-Ce to Substituted Picrylhydrazyls

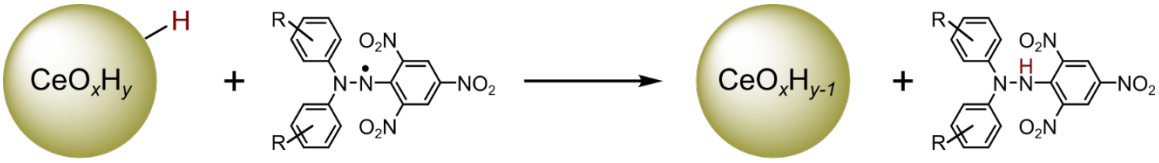

R = H, *tert*-octyl [$CMe_2(CH_2)_4Me$]

The data presented below demonstrate that the logarithm of the rate constant for net hydrogen atom transfer from nanoceria to DPPH varies linearly with the CeO–H BDFE, or hydrogen adsorption free energy, but only weakly. The slope of this relationship is only 0.2, over a 10 kcal mol^{-1} range of driving forces. The interpretation of this apparent Brønsted α and the possibility of more complex mechanistic pathways are discussed. This finding is potentially important for understanding why cerium oxide is so effective as a catalyst support.[41,45] More broadly, the study is one of the first to experimentally measure a coverage-dependent BEP relationship of hydrogen adsorption to a (nano)material, and has implications for the use of this relation in catalytic models.

4.2 Experimental

Oleate-capped cerium oxide nanoparticles (OLE-Ce) were prepared following a previously reported procedure.[43] Briefly, nanoparticles were precipitated through base hydrolysis of a cerium oleate complex formed from ceric ammonium nitrate and sodium oleate. After multiple washing and drying steps, nanoparticles were stored in an N_2-filled glovebox as a colloid in tetrahydrofuran (THF) at −30 °C.

Reaction kinetics were followed by monitoring the decay of an organic oxidant (usually DPPH) by UV-visible (UV-vis) absorption spectroscopy. Kinetics were always performed with a significant excess of hydrogen equivalents (on OLE-Ce) as compared to organic oxidant. Reactions were initiated by adding OLE-Ce to THF solution of the organic oxidant in an N_2-filled glovebox. Full experimental details are provided in Appendix D.

4.3 Results

4.3.1 Kinetics of nanoceria oxidation.

This study utilizes oleate-capped cerium oxide nanoparticles (OLE-Ce) reduced to varying extents to determine how the hydrogen adsorption free energy of OLE-Ce affects the rate of hydrogen atom transfer to a well-defined organic oxidant, Scheme 4.1. Studies were performed in tetrahydrofuran (THF) with two batches of OLE-Ce, one where the nanoparticles had an average diameter of 1.8 ± 0.2 nm (**Ce-1**) by transmission electron microscopy and another larger batch of nanoparticles (**Ce-L**, *d* = 4.0 ± 0.4). Further details on the characterization of these nanoceria colloids are provided in our previous work.[43] OLE-Ce colloids were first reduced by adding varying amounts of 1,8-dichloro-9,10-dihydroxyanthracene (H_2DCAQ, $BDFE_{avg}$ = 55.4 kcal mol^{-1} in THF), a strong PCET reductant.[43,46] The partially reduced OLE-Ce were then reacted with a small amount of DPPH, and the decay of the purple DPPH over seconds to minutes was evident to the eye as the reactions changed to orange.

The rates of DPPH decay in the presence of reduced stock solutions of either **Ce-1** or **Ce-L** were monitored by UV-Vis at the DPPH absorbance maximum, 519 nm (Figure D1). At this wavelength, and under the conditions used in this study, the primary contribution to the absorbance spectrum is DPPH before the reaction, and DPPH-H after completion (Figure 4.1A). Formation of the $1e^-/1H^+$ reduced product—1,1-diphenyl-2-picrylhydrazine (DPPH-H)—in these reactions was confirmed previously by ^{1}H NMR.[43] Dependences on the concentration of Ce atoms and DPPH were determined by the method of initial rates in order to ensure that the average redox state of OLE-Ce (%Ce^{3+})—and therefore the CeO–H bond strength and surface H coverage—changed very little over the course of the reaction. Minimal changes in %Ce^{3+} over the course of the reaction were also enforced by adding a significant excess of hydrogen equivalents (H's bound to OLE-Ce) as compared to DPPH. With this experimental design, the measured kinetics can be connected to a well-defined reaction driving force.

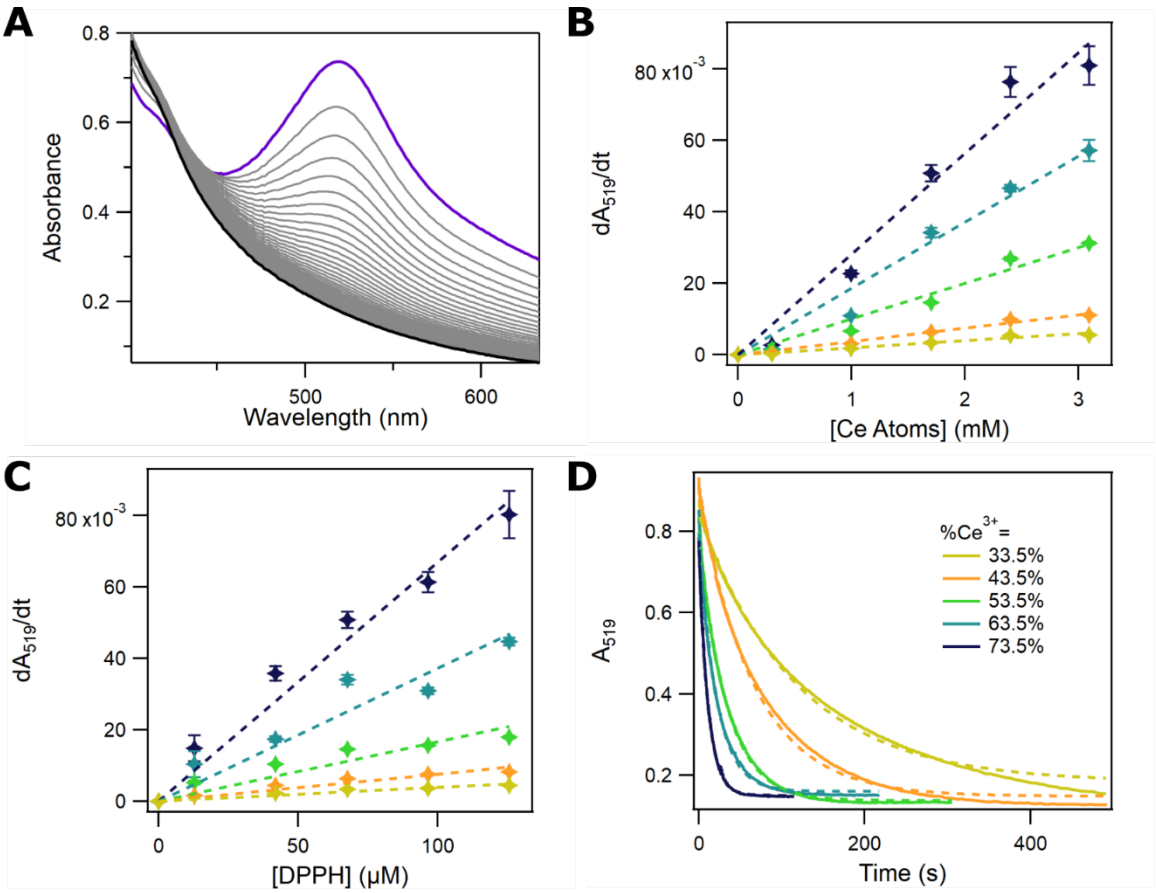

Figure 4.1. (A) Full spectrum kinetics collected by stopped-flow UV-vis measurements. Mixing was initiated between a solution containing 8.8 mM reduced Ce atoms so that the concentration of added hydrogen atoms is 2 mM, and a 134 μM solution of DPPH. The initial spectrum is denoted in purple, while the final is in black. The reaction took ~30 seconds to complete. (B) Initial rates kinetic dependence of DPPH decay on the concentration of Ce atoms at five different $\%Ce^{3+}$ levels in **Ce-1** nanoparticles (legend in part D). [DPPH] = 68 μM for all samples. (C) Initial rates kinetic dependence of DPPH decay on [DPPH] at varying $\%Ce^{3+}$ for **Ce-1**. [Ce atoms] = 1.7 mM for all samples. For (B) and (C) dashed lines are linear fits with the y-intercept set as zero. (D) Full single wavelength kinetic traces of DPPH decay at varying $\%Ce^{3+}$ for **Ce-1** where [Ce atoms] = 3.1 mM and [DPPH] = 68 μM for all samples. Dashed lines are single exponential fits.

Initial rates data were analyzed by linearizing the reaction over the segment from 5-15% of total reaction progress. Analysis of the 0-10% section gave similar results, but with larger error bars for several concentrations (Figure D3). The greatest change in $\%Ce^{3+}$ for **Ce-1** in a run analyzed by the method of initial rates was 2.3%, which would correspond to an error in the reaction free energy of 0.4 kcal mol^{-1} for **Ce-1** (see below). Dependences on the concentrations of Ce atoms and DPPH are both

first order across a range of %Ce^{3+} values for **Ce-1** (Figure 4.1B and C) and **Ce-L** (Figure D4), which leads to a simple bimolecular rate law (eq 4.2). As a result, the rate constant (k) for the reaction can be determined by taking the slopes of either the DPPH dependence or the Ce atom dependence. Samples with the highest ratio of reduced Ce atom (or hydrogen atom) equivalents to DPPH were also fit to exponentials as an alternative method for determining k (Figure 4.1D). The change in **Ce-1** %Ce^{3+} is 2.2% for the reaction to go to completion in these samples. For the kinetic studies of **Ce-1** colloids, these three ways of determining rate constants agree well, with a standard deviation of roughly ±25%.

$$\text{rate} = k[\text{DPPH}][\text{Ce atoms}] \qquad (4.2)$$

4.3.2 Kinetic-thermodynamic correlations.

The driving force ($\Delta G°$) for these reactions is the difference between the BDFE of the OLE-Ce colloid ($BDFE_{Ce}$) and that of DPPH-H. In order to determine $BDFE_{Ce}$ the relevant regions of previously reported relationships between %Ce^{3+} and BDFE for **Ce-1** and **Ce-L** were fit using linear regressions. These lines of best fit show R^2 values close to 1 and provide a simple method for determining the $BDFE_{Ce}$ for any level of OLE-Ce reduction (Figure D5). Subtraction of the BDFE of DPPH-H (73.5 kcal mol^{-1} in THF)[46] from the relevant $BDFE_{Ce}$ gives $\Delta G°$ for the reaction. In a typical example, a **Ce-1** sample with 54% Ce^{3+} was determined to have $BDFE_{Ce}$ = 60.7 kcal mol^{-1} so the $\Delta G°$ for the reaction was –12.8 kcal mol^{-1}. Overall, the experiments reported here covered a range of driving forces from 6.8 to 16.6 kcal mol^{-1}. The $\Delta G°$ values were converted to $\ln(K_{eq})$ values.

The rate constants were then correlated with the equilibrium constants. Plotting $\ln(k)$ versus $\ln(K_{eq})$, both experimentally determined, shows linear correlation for reactions between DPPH and both **Ce-1** and **Ce-L** (Figure 4.2A). This is what is predicted by the BEP principle (eq 4.4.1b above), as $\ln(K_{eq})$ and $\ln(k)$ are proportional to $\Delta G°$ and $\Delta G^{‡}$, respectively. The uncertainties in Figure 4.2 represent one standard deviation between the values of k determined from the three experimental approaches

above, the exponential fit, the DPPH dependence, and the Ce atom dependence. Uncertainties in K_{eq} are related to the 0.4 kcal mol^{-1} (0.7 natural log units) error in the reaction free energy described above, which is less than the width data points plotted.

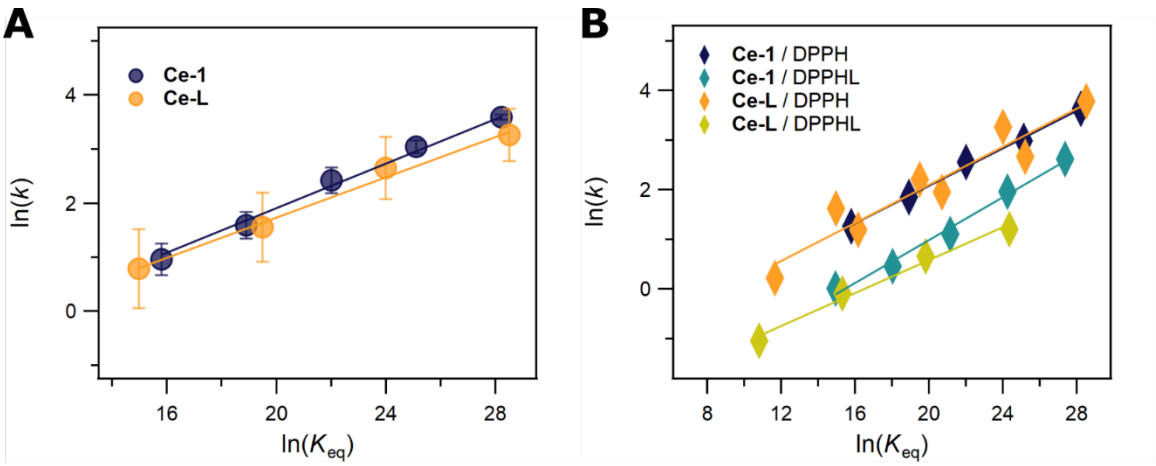

Figure 4.2. Dependence of reaction rate (ln(k)) on driving force ln(K_{eq}), for reactions of **Ce-1** and **Ce-L** nanoparticles with (**A**) DPPH, where values of k are the averages of values derived from the DPPH and Ce atom initial rates dependences using eq 4.2, as well as time constants from single exponential fits of full trace kinetics. Error bars denote the standard deviation from these three methods of measuring k. (**B**) Relationships are also shown for reactions with DPPH and DPPHL, where values of k are derived from exponential fits of data collected where [DPPH] = 68 μM, [DPPHL] = 79 μM, [Ce atoms] = 3.1 mM for **Ce-1**, and [Ce atoms] = 8.5 mM for **Ce-L**. Uncertainties are smaller than the diamond-shaped data points. For both figures, values of ln(K_{eq}) are determined by calculating ΔG_{rxn} = BDFE$_{Ce}$ – BDFE$_{DPPH(L)-H}$. In (**A**), the slope of the **Ce-1** linear fit is 0.21 ± 0.02 and that for **Ce-L** is 0.19 ± 0.06, while slopes of fits in (**B**) are given in Table 4.1.

Similar studies were also performed with 2,2-di(4-*tert*-octylphenyl)-1-picrylhydrazyl (DPPHL [L for large]). Using a recently published open-circuit potential method,[46] the BDFE of 1,1-di(4-*tert*-octylphenyl)-2-picrylhydrazine (DPPHL-H) was determined to be 73.0 kcal mol^{-1} in THF; or 0.5 ± 0.2 kcal mol^{-1} less oxidizing than DPPH (Figure D6). Kinetic studies of the reaction between reduced OLE-Ce and DPPHL were followed at absorbance maximum of the radical, 541 nm (Figure D1). As with DPPH, first order dependences on the concentrations of Ce atoms and DPPHL were observed (Figure D7). Therefore, the same bimolecular rate law applies and comparable k's could be obtained. The results of the DPPHL reactions form BEP relationships very similar to those for DPPH, just shifted down and to the left. They

are shifted left, to lower driving forces, because the DPPHL–H bond is 0.5 kcal mol^{-1} weaker than the DPPH–H bond.

Plots of BEP relationships for all four combinations of **Ce-1** or **Ce-L** with DPPH or DPPHL, ln(k) vs. ln(K_{eq}), are in Figure 4.2B and the data are in Table 4.1. These four Brønsted α values are essentially the same within the uncertainties, all 0.20 ± 0.03. This is in contrast to traditional Brønsted α values for single-step reactions that are not too exergonic or endergonic, which are typically close to ½. Since these reactions are only modestly exergonic, ΔG° between –6.8 and –16.6 kcal mol^{-1}, the α = 0.2 means that the rate constants of these reactions are only modestly sensitive to the overall reaction driving force.

The data shown in Figure 4.2B and slopes, or α's, given in Table 4.1 are from exponential fits. These fits, as shown in Figure 4.1C, are not perfect even with large excesses of Ce atoms. In order to confirm the validity of the exponential fit analysis we stretched the time axis to overlay exponential decays for **Ce-1** and **Ce-L** at differing values of $\%Ce^{3+}$ (Figure D8). This treatment gives a close overlay of all plots. Furthermore, the "stretch-factors" used to generate the overlaid plots should be a direct measure of the relative rates. Plotting the logarithm of the "stretch-factor" versus the logarithm of the K_{eq} gives a line with a slope of 0.20 ± 0.01, as expected. These analyses confirm that any deviations from the exponential fits do not lead to systematic errors in the reported rate constants which would significantly affect the slopes of the reported BEP relationships.

Table 4.1. BEP Relationships Slopes [a]

Reactants	Slope	Range of $\Delta G°$	Range of $\Delta G^{‡}$
Ce-1 / DPPH	0.19	7.2	1.4
Ce-1 / DPPHL	0.22	7.2	1.5
Ce-L / DPPH	0.19	9.8	2.1
Ce-L / DPPHL	0.17	7.9	1.3

[a] All slopes, or Brønsted alphas (α), are taken from plotting ln(k) vs ln(K_{eq}) where values of k are determined from exponential fits. The uncertainty for all values of α is ± 0.02. Values of $\Delta G°$ and $\Delta G^{‡}$ are in kcal mol^{-1}.

4.3.3 Additional mechanistic experiments.

The small dependence of rate constants on driving force raised questions about what other factors might influence the rates of net H-atom transfer. We therefore tested the effects of various additives on the kinetics. Addition of >3 mM of oleic acid or triphenyl phosphine oxide, or 150 μM of DPPH-H was shown to *decrease* the reaction rate by a factor of 2 or more (Figure D9). In contrast, the addition of >25 mM of MeOH or of H_2O was shown to *increase* the reaction rate by a factor of 2 or more (Figure D9C). Furthermore, cerium oleate ($Ce(OLE)_3$), a known species in OLE-Ce stock solutions,[43] had no effect on the rate (Figure D9C). The effect of the concentration of free oleate anions on the kinetics could not be tested due to incompatibilities with DPPH, DPPH-H, and DPPHL-H. Another compound that could potentially be important to the kinetics is 1,8-dichloroanthraquinone (DCAQ). This is because the OLE-Ce colloids are reduced to varying extents using H_2DCAQ, and therefore the final stocks contain varying amounts of the oxidized product, DCAQ. Addition of large excesses of DCAQ to nanoparticle stocks at a range of %Ce^{3+} values had no effect on reaction kinetics (Figure D10). Finally, we probed the effect of ionic strength on the kinetics by adding varying amounts of sodium tetrakis[3,5-bis(trifluoromethyl)phenyl]borate ($NaBAr^F$). Concentrations between 0 and 5.3 mM had no discernible effect on the reaction rate (Figure D11).

As the reaction involves the transfer of a proton, experiments were also undertaken to measure the H/D kinetic isotope effect (KIE). Our previous study concluded that the majority of redox active sites are surface CeO–H groups.[43] To form CeO-D groups, surface hydroxyl groups were exchanged with either dried perdeutero methanol (MeOH-d_4) or deuterium oxide (D_2O). Methanol and MeOH-d_4 were dried over 3Å sieves and distilled before use. Exchanges were performed through simple addition to the reduced OLE-Ce stock solution and by sequentially removing solvent *in vacuo* and adding deuterated solvent. All of the kinetic measurements, using both DPPHL and DPPH, gave KIEs of 1 within the uncertainties (1.01 ± 0.04 with DPPHL, 1.03 for DPPH).

The possibility that H-atoms are transferring between the ceria nanoparticles was also examined. This would lead to redox equilibration between the nanoparticles and could contribute kinetic complexity to the reactions under some conditions. This effect was, however, minimized by performing the reactions with excess CeO–H groups which ensured a small change in $\%Ce^{3+}$ (surface H coverage) over the course of the reaction. As described above, these reaction conditions were chosen to ensure a well-defined reaction driving force.

To test for the presence of H-exchange, three reactions were monitored in parallel with the same amount hydrogen atom equivalents loaded on different nanoceria, but otherwise identical conditions. Sample 1 contained one equivalent of highly reduced **Ce-1**; sample 2 contained one equivalent of the same highly reduced **Ce-1** plus one equivalent of as-prepared **Ce-1**, where the **Ce-1** mixture had had been left to equilibrate overnight; and sample 3 had contents identical to sample 2 except that the highly reduced and as-prepared **Ce-1** were kept separate until reaction initiation (Figure D12A). If there were no exchange of H between **Ce-1** nanoparticles, all three reactions would have proceeded similarly to consume the highly reduced **Ce-1**, and only later would oxidation of the as-prepared **Ce-1** occur. In the limit of very

fast redox exchange, sample 1 with only highly reduced **Ce-1** would react faster than the other two, which would both have had moderately reduced **Ce-1**.

The kinetic traces for samples 1 and 3 are very similar at short times, indicating that the 1 equivalent of highly reduced **Ce-1** in sample 3 had not rapidly equilibrated with the more oxidized nanoparticles. However, sample 2 reacted more slowly at short times, showing that redox equilibration did occur between the two types of **Ce-1** overnight. After 5-6 minutes, the traces of samples 2 and 3 become more similar, indicating that the redox exchange is occurring on this timescale (Figure D12B). These studies of hydrogen self-exchange provide one explanation for the long timescales required to reach equilibrium with cerium oxide nanoparticles in our previous work,[43] as well as a possible cause of the non-exponential shape of most kinetic traces for the reaction between OLE-Ce and the picrylhydrazyl oxidants.

4.4 Discussion

The reaction between DPPH (or DPPHL) and reduced OLE-Ce colloids involves the net transfer of one hydrogen atom. In Table 4.1 we demonstrate that the overall driving force for this reaction has only a small effect on the reaction rate across all conditions, as indicated by the slope of the lines which is 0.19 ± 0.02. This range falls within the more conservative uncertainty of ±0.06 for **Ce-L**/DPPH in Figure 4.2, suggesting that the slope is not significantly affected by either hydrazyl substitution or nanoparticle size. Furthermore, comparable lines for **Ce-1** and **Ce-L** effectively overlay in Figure 4.2. This is somewhat surprising, given the simplicity of the rate law presented in eq 4.2. While it is true that the expected rate law should be first order in [Ce atoms], not all cerium atoms are reactive. In our previous report, we demonstrated that the active sites are surface CeO–H groups.[43] Here we use previously determined ratios of surface to total cerium atoms (R_{surf}) to estimate [Ce_{active}] as

R_{surf}[Ce atoms]. Making this change in the rate law yields a corrected rate constant, $k_{corr} = k/R_{surf}$ (eq 4.3).

$$\text{rate} = k_{corr}[\text{DPPH}][\text{Ce}_{active}] \quad (4.3)$$

Importantly, application of this correction *does not change the slope* of any of the BEP relationships, but instead simply shifts the data vertically on the plot by $-\ln(R_{surf})$. Since R_{surf} for **Ce-1** is 0.85 and that for **Ce-L** is 0.39, the data for each are translated by 0.16 and 0.94, respectively.[43] Interestingly, this correction causes the relationships shown for **Ce-1** and **Ce-L** in Figure 4.2A to separate slightly, so that the kinetics of **Ce-L** reactivity are a little faster than those of **Ce-1** at the same driving force (Figure 4.3A). This difference is consistent with our previous observation that the hydrogen isotherms for **Ce-1** and **Ce-L** do not overlay even with this correction.[43] Despite this small difference, the closeness of the lines in Figure 4.3 indicates that the α = 0.2 is a characteristic of the reaction between OLE-Ce and DPPH(L), independent of the size or nanoparticle batch.

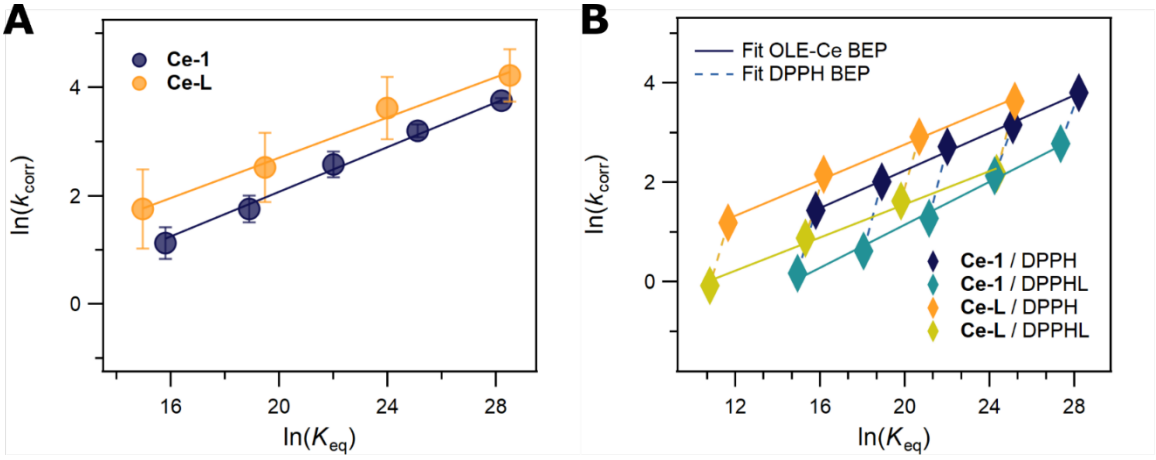

Figure 4.3. Dependence of the surface site adjusted reaction rate constants ($\ln(k_{corr})$) on reaction driving force $\ln(K_{eq})$. Values of k_{corr} are the same averages and standard deviations shown in (A) Figure 4.2A and (B) Figure 4.2B minus $\ln(R_{surf})$ Values of $\ln(K_{eq})$ are determined by calculating ΔG_{rxn} = $BDFE_{Ce}$ – $BDFE_{DPPH\text{-}H}$. In (A) the slope of the **Ce-1** linear fit is 0.21 ± 0.02 and that for **Ce-L** is 0.19 ± 0.06, while slopes of fits in (B) are given in Table 4.1. Some data points in Figure 4.2B for **Ce-L**/DPPH are removed for simplicity, as they were collected with **Ce-L** stocks at different levels of reduction than those used to create the **Ce-L**/DPPHL dataset.

The Ce_{active} correction does not, however, remove the gap between the DPPH and DPPHL relations (Figure 4.3B). In fact, the two-point lines between DPPH and DPPHL data points collected through reactions with the same OLE-Ce stocks represent another BEP relationship tuned by the driving force for the addition of $H^{\bullet}$ to the picrylhydrazyl with its own slope, α_{DPPH}. The fact that these lines do not overlay indicates that the slope of this BEP relationship is very different from the relationship derived from changing the $\%Ce^{3+}$ / surface H coverage of OLE-Ce. All nine of these two-point lines have quite similar slopes, with averages of α_{DPPH} = 1.4 ± 0.2 for **Ce-1** and 1.5 ± 0.3 for **Ce-L** when considering the uncertainty in ΔBDFE between DPPH and DPPHL. The lowest value for the slope of any single two-point line was 1.2 ± 0.4.

It is important to note that throughout this report it has been assumed that the RDS of the reaction involves a concerted $1e^{-}/1H^{+}$ transfer. For this relationship between driving force and rate constant to be a traditional BEP relationship, the driving force should describe the free energy of the rate-determining step. As described above, BEP relationships relate the thermodynamic and kinetic barriers for a *single* mechanistic step. In this case the mechanism could be one step if it is hydrogen atom transfer (HAT, or concerted proton-electron transfer (CPET)), as has been discussed for other metal oxide nanoparticle systems.[47-49] If the mechanism is HAT/CPET, the slopes of the lines in Figure 4.2 can properly be described as Brønsted alpha's (α) relating the rate constants with the CeO–H BDFEs.

Our data do not, however, completely rule out mechanisms other than HAT/CPET. The overall reaction could instead involve a stepwise process, such as electron transfer (ET) followed by proton transfer (PT), inner-sphere ET to involve binding of the DPPH to a surface cerium ion followed by PT and DPPH-H dissociation, the involvement of ligands, or other paths. Addition of excess oleic acid, triphenyl phosphine oxide, and DPPH-H all inhibit the reaction to a moderate extent (Figure D9B). This could suggest that dissociation of oleic acid or DPPH-H is involved in the

reaction rate, or perhaps more likely that added ligands make the nanoparticle surface more sterically congested, blocking reactive sites. This is a common observation for reactions of capped, colloidal nanoparticles.[50-53] On the other hand, the inhibition by oleic acid argues against the acid acting as some sort of proton donor in the reaction. The inhibition by DPPH-H may play a role in the non-exponential character of the kinetic traces. Oleate is also unlikely to be involved in the mechanism, as the addition of even small amounts results in rapid side reactions with DPPH, DPPH-H, and DPPHL-H. The product of this incompatibility absorbs in the region of the UV-vis spectra where the reaction is monitored, so it would be noticeable if oleate were formed.

To explore the possibility of rate-determining initial outer-sphere ET, we attempted to measure the 1e^- reduction potentials of OLE-Ce, DPPH, and DPPHL. Efforts with OLE-Ce suspensions were unsuccessful, as no faradaic features were observed by cyclic voltammetry (CV). CV experiments with both DPPH and DPPHL showed four reversible faradaic features for each substrate in THF with 0.1 M [Bu_4N][PF_6] (Figure D2). Based on prior studies in other organic solvents,[54,55] chemically reversible couples with $E_{1/2}$ = -0.329 (DPPH) and -0.261 (DPPHL) V vs ferrocene are assigned as the reductions of the radicals to their hydrazyl anions. The difference in half-wave potentials between DPPH and DPPHL ($\Delta E_{1/2}$) of 68 mV, or 1.6 kcal mol^{-1}, is ca. three times the difference in PCET driving force. This is consistent with the typical observation for PCET reagents that changes in $E_{1/2}$ are larger than those in BDFEs.[56] A mechanism of rate-limiting ET would be consistent with the H/D kinetic isotope effect of 1, measured under multiple conditions. It would also change the BEP analysis for DPPH vs DPPHL, as use of $\Delta E_{1/2}$ instead of ΔBDFE would reduce α_{DPPH} by a factor of three and bring it close to the expected value of 0.5. However, kinetic runs in the presence of 0, 2.7, and 5.3 mM $NaBAr^F$ (Figure D11) did not show any effect of solution ionic strength. Previous studies, also indicated similar timescales for reactions performed in THF and toluene, despite a factor of 3 difference in dielectric

constants between the two solvents.[43,57] These results suggest that there is little charge character in the transition state, arguing against ET.

Overall, it is challenging to achieve mechanistic clarity for reactions of these nanoparticles at the level obtainable with molecular reagents. While the ceria colloids used are as similar as we could make them—the same batch of material, just reduced by different amounts—our previous study did note reversible changes to the ligand shell and other features of the OLE-Ce with increasing surface coverages of hydrogen atoms.[43] These properties could be relevant to the mechanism of net hydrogen transfer to DPPH. Additionally, rate-limiting initial ET followed by proton transfer to make the reduced hydrazines is a possibility, though the available evidence suggests that charge species are not involved. Therefore, we favor the hydrogen atom transfer (HAT) mechanism, perhaps with a significant portion of the barrier being substrate penetration into the ligand shell. This would explain the relatively small changes in rate constants with changes in BDFE. Perhaps the larger DPPHL has more difficulty penetrating the ligand shell because of the *tert*-octyl groups, accounting for its slower reactions. This hypothesis also offers a possible explanation for the striking difference in the Brønsted α values for changes in surface BDFE (~0.2) and changes in hydrogen abstractor (~1.4). Differences in α when different aspects are changed within a series of reactions have also been recently reported for organic and inorganic HAT and multiple-site CPET reactions.[58-61]

Comparative experiments of how the reaction driving force of a single metal oxide material alters the kinetics of its reactivity at the solid/solution interface have not, to the best of our knowledge, previously been reported. However, computational approaches have been employed to estimate this effect on single crystal metal and metal heteroatom surfaces for both oxygen and hydrogen transfer.[17,62,63] These studies show that BEP relationships exist across a wide range of materials and reaction types, but also that their magnitude can change significantly within this parameter space. In

this context, the results of this work serve as important experimental verification and data which can serve as benchmarks for future theory studies. These results also have implications for "volcano plot" or similar analyses of reaction kinetics at surfaces. As described, above these analyses assume coverage effects do not need to be strongly considered either because they are small in magnitude or similar across all materials. However, the relationship between surface CeO–H coverage and reaction rate described here, demonstrates that surface H coverage can significantly affect the reaction kinetics. Therefore, we expect that these results will have implications for more broadly employed analyses of multi-electron/multi-proton reaction kinetics.

This report's finding that CeO–H BDFE only weakly affects the rate of net hydrogen transfer from cerium oxide nanoparticles ($\alpha \approx 0.2$) may provide insight into the application of the material catalyst support. In this capacity, nanoceria acts as either a thermodynamic source or sink of redox equivalents for many different processes.[41,45,64,65] Our previous study posited that the wide range of CeO–H BDFEs may enable the material to facilitate a wide range of reactions.[43] The shallow BEP relationship found here, takes that hypothesis one step further by demonstrating that over the wide range of CeO–H BDFEs, rates of net hydrogen transfer change by a relatively small amount. This is an advantageous property for a non-innocent support which must function well across a variety of reaction conditions and driving forces.[41,45] As a result, we once again posit that these thermodynamic and kinetic properties help to provide a fundamental basis for why cerium oxide is such an exceptional catalyst support.

4.5 References

1. Seh, Z. W.; Kibsgaard, J.; Dickens, C. F.; Chorkendorff, I.; Norskov, J. K.; Jaramillo, T. F., Combining theory and experiment in electrocatalysis: Insights into materials design. *Science* **2017,** *355* (6321).
2. Nørskov, J. K.; Bligaard, T.; Logadottir, A.; Kitchin, J. R.; Chen, J. G.; Pandelov, S.; Stimming, U., Trends in the Exchange Current for Hydrogen Evolution. *J. Electrochem. Soc.* **2005,** *152* (3).
3. Schmickler, W.; Trasatti, S., Comment on "Trends in the Exchange Current for Hydrogen Evolution" [J. Electrochem. Soc., 152, J23 (2005)]. *J. Electrochem. Soc.* **2006,** *153* (12).
4. Quaino, P.; Juarez, F.; Santos, E.; Schmickler, W., Volcano plots in hydrogen electrocatalysis - uses and abuses. *Beilstein. J. Nanotechnol.* **2014,** *5*, 846-54.
5. Bligaard, T.; Nørskov, J. K.; Dahl, S.; Matthiesen, J.; Christensen, C. H.; Sehested, J., The Brønsted–Evans–Polanyi relation and the volcano curve in heterogeneous catalysis. *J. Catal.* **2004,** *224* (1), 206-217.
6. Koper, M. T. M., Thermodynamic Theory of Multi-Electron Transfer Reactions: Implications for Electrocatalysis. *J. Electroanal. Chem.* **2011,** *660* (2), 254-260.
7. Cheng, J.; Hu, P.; Ellis, P.; French, S.; Kelly, G.; Lok, C. M., Brønsted−Evans−Polanyi Relation of Multistep Reactions and Volcano Curve in Heterogeneous Catalysis. *The Journal of Physical Chemistry C* **2008,** *112* (5), 1308-1311.
8. Exner, K. S.; Over, H., Kinetics of Electrocatalytic Reactions from First-Principles: A Critical Comparison with the Ab Initio Thermodynamics Approach. *Acc. Chem. Res.* **2017,** *50* (5), 1240-1247.
9. Lindgren, P.; Kastlunger, G.; Peterson, A. A., A Challenge to the $G \sim 0$ Interpretation of Hydrogen Evolution. *ACS Catal.* **2020,** *10* (1), 121-128.
10. Whittaker, T.; Kumar, K. B. S.; Peterson, C.; Pollock, M. N.; Grabow, L. C.; Chandler, B. D., H_2 Oxidation over Supported Au Nanoparticle Catalysts: Evidence for Heterolytic H_2 Activation at the Metal–Support Interface. *J. Am. Chem. Soc.* **2018,** *140* (48), 16469-16487.
11. Pérez-Ramírez, J.; López, N., Strategies to break linear scaling relationships. *Nat. Catal.* **2019,** *2* (11), 971-976.
12. Darby, M. T.; Stamatakis, M.; Michaelides, A.; Sykes, E. C. H., Lonely Atoms with Special Gifts: Breaking Linear Scaling Relationships in Heterogeneous Catalysis with Single-Atom Alloys. *The Journal of Physical Chemistry Letters* **2018,** *9* (18), 5636-5646.
13. Barteau, M. A., Linear free energy relationships for C_1-oxygenate decomposition on transition metal surfaces. *Catal. Lett.* **1991,** *8* (2), 175-183.
14. Akhade, S. A.; Nidzyn, R. M.; Rostamikia, G.; Janik, M. J., Using Brønsted-Evans-Polanyi relations to predict electrode potential-dependent activation energies. *Catal. Today* **2018,** *312*, 82-91.
15. van Santen, R. A.; Neurock, M.; Shetty, S. G., Reactivity Theory of Transition-Metal Surfaces: A Brønsted−Evans−Polanyi Linear Activation Energy−Free-Energy Analysis. *Chem. Rev.* **2010,** *110* (4), 2005-2048.
16. Panov, G. I.; Parfenov, M. V.; Parmon, V. N., The Brønsted−Evans−Polanyi Correlations in Oxidation Catalysis. *Catalysis Reviews* **2015,** *57* (4), 436-477.
17. Viñes, F.; Vojvodic, A.; Abild-Pedersen, F.; Illas, F., Brønsted–Evans–Polanyi Relationship for Transition Metal Carbide and Transition Metal Oxide Surfaces. *The Journal of Physical Chemistry C* **2013,** *117* (8), 4168-4171.
18. Jencks, W. P., A primer for the Bema Hapothle. An empirical approach to the characterization of changing transition-state structures. *Chem. Rev.* **1985,** *85* (6), 511-527.
19. Kresge, A. J., The Brønsted relation – recent developments. *Chem. Soc. Rev.* **1973,** *2* (4), 475-503.
20. Kresge, A. J., Deviant Broensted relations. *J. Am. Chem. Soc.* **1970,** *92* (10), 3210-3211.
21. Pross, A., *Theoretical and Physical Principles of Organic Reactivity*. Wiley: 1995.
22. Lowry, T. H.; Richardson, K. S., *Mechanism and Theory in Organic Chemistry*. 3rd ed.; Pearson: 1987.
23. Evans, M. G.; Polanyi, M., Inertia and driving force of chemical reactions. *Trans. Faraday Soc.* **1938,** *34* (0), 11-24.

24. Brönsted, J. N.; Pedersen, K., Die katalytische Zersetzung des Nitramids und ihre physikalisch-chemische Bedeutung. *Z. Phys. Chem.* **1924,** *108U* (1), 185-235.
25. Baran, J. D.; Grönbeck, H.; Hellman, A., Analysis of Porphyrines as Catalysts for Electrochemical Reduction of O_2 and Oxidation of H_2O. *J. Am. Chem. Soc.* **2014,** *136* (4), 1320-1326.
26. Wang, S.; Temel, B.; Shen, J.; Jones, G.; Grabow, L. C.; Studt, F.; Bligaard, T.; Abild-Pedersen, F.; Christensen, C. H.; Nørskov, J. K., Universal Brønsted-Evans-Polanyi Relations for C–C, C–O, C–N, N–O, N–N, and O–O Dissociation Reactions. *Catal. Lett.* **2011,** *141* (3), 370-373.
27. Wang, Y.; Montoya, J. H.; Tsai, C.; Ahlquist, M. S. G.; Nørskov, J. K.; Studt, F., Scaling Relationships for Binding Energies of Transition Metal Complexes. *Catal. Lett.* **2016,** *146* (2), 304-308.
28. Campbell, C. T., The Degree of Rate Control: A Powerful Tool for Catalysis Research. *ACS Catal.* **2017,** *7* (4), 2770-2779.
29. Campbell, C. T., Future Directions and Industrial Perspectives Micro- and macro-kinetics: Their relationship in heterogeneous catalysis. *Top. Catal.* **1994,** *1* (3), 353-366.
30. Cortright, R. D.; Dumesic, J. A., Kinetics of heterogeneous catalytic reactions: Analysis of reaction schemes. In *Advances in Catalysis*, Academic Press: 2001; Vol. 46, pp 161-264.
31. Motagamwala, A. H.; Dumesic, J. A., Microkinetic Modeling: A Tool for Rational Catalyst Design. *Chem. Rev.* **2021,** *121* (2), 1049-1076.
32. Stoltze, P., Microkinetic simulation of catalytic reactions. *Prog. Surf. Sci.* **2000,** *65* (3), 65-150.
33. Parsons, R., The rate of electrolytic hydrogen evolution and the heat of adsorption of hydrogen. *Trans. Faraday Soc.* **1958,** *54* (0), 1053-1063.
34. Thomas, J. G. N., Kinetics of electrolytic hydrogen evolution and the adsorption of hydrogen by metals. *Trans. Faraday Soc.* **1961,** *57* (0), 1603-1611.
35. Conway, B. E.; Gileadi, E., Kinetic Theory of Pseudo-Capacitance and Electrode Reactions at Appreciable Surface Coverage. *Trans. Faraday Soc.* **1962,** *58* (0), 2493-2509.
36. Campbell, C. T.; Sellers, J. R. V., Enthalpies and Entropies of Adsorption on Well-Defined Oxide Surfaces: Experimental Measurements. *Chem. Rev.* **2013,** *113* (6), 4106-4135.
37. Strmcnik, D.; Tripkovic, D.; van der Vliet, D.; Stamenkovic, V.; Marković, N. M., Adsorption of hydrogen on Pt(111) and Pt(100) surfaces and its role in the HOR. *Electrochem. Commun.* **2008,** *10* (10), 1602-1605.
38. Skúlason, E.; Tripkovic, V.; Björketun, M. E.; Gudmundsdóttir, S.; Karlberg, G.; Rossmeisl, J.; Bligaard, T.; Jónsson, H.; Nørskov, J. K., Modeling the Electrochemical Hydrogen Oxidation and Evolution Reactions on the Basis of Density Functional Theory Calculations. *The Journal of Physical Chemistry C* **2010,** *114* (42), 18182-18197.
39. Bard, A. J.; Faulkner, L. R., *Electrochemical Methods: Fundamentals and Applications*. John Wiley & Sons: NY, 2nd edition, 2001, p 591 for the CV of an ideal Nernstian reaction following a Langmuir isotherm.
40. Kibsgaard, J.; Tsai, C.; Chan, K.; Benck, J. D.; Nørskov, J. K.; Abild-Pedersen, F.; Jaramillo, T. F., Designing an improved transition metal phosphide catalyst for hydrogen evolution using experimental and theoretical trends. *Energy Environ. Sci.* **2015,** *8* (10), 3022-3029.
41. Ganduglia-Pirovano, M. V., The non-innocent role of cerium oxide in heterogeneous catalysis: A theoretical perspective. *Catal. Today* **2015,** *253*, 20-32.
42. Kunimatsu, K.; Senzaki, T.; Samjeské, G.; Tsushima, M.; Osawa, M., Hydrogen adsorption and hydrogen evolution reaction on a polycrystalline Pt electrode studied by surface-enhanced infrared absorption spectroscopy. *Electrochim. Acta* **2007,** *52* (18), 5715-5724.
43. Agarwal, R. G.; Kim, H.-J.; Mayer, J. M., Nanoparticle O–H Bond Dissociation Free Energies from Equilibrium Measurements of Cerium Oxide Colloids. *J. Am. Chem. Soc.* **2021,** *143* (7), 2896-2907.
44. Delley, M. F.; Wu, Z.; Mundy, M. E.; Ung, D.; Cossairt, B. M.; Wang, H.; Mayer, J. M., Hydrogen on Cobalt Phosphide. *J. Am. Chem. Soc.* **2019,** *141* (38), 15390-15402.
45. Sayle, T. X. T.; Caddeo, F.; Zhang, X.; Sakthivel, T.; Das, S.; Seal, S.; Ptasinska, S.; Sayle, D. C., Structure–Activity Map of Ceria Nanoparticles, Nanocubes, and Mesoporous Architectures. *Chem. Mater.* **2016,** *28* (20), 7287-7295.

46. Wise, C. F.; Agarwal, R. G.; Mayer, J. M., Determining Proton-Coupled Standard Potentials and X–H Bond Dissociation Free Energies in Nonaqueous Solvents Using Open-Circuit Potential Measurements. *J. Am. Chem. Soc.* **2020,** *142* (24), 10681-10691.
47. Schrauben Joel, N.; Hayoun, R.; Valdez Carolyn, N.; Braten, M.; Fridley, L.; Mayer James, M., Titanium and Zinc Oxide Nanoparticles Are Proton-Coupled Electron Transfer Agents. *Science* **2012,** *336* (6086), 1298-1301.
48. Braten, M. N.; Gamelin, D. R.; Mayer, J. M., Reaction Dynamics of Proton-Coupled Electron Transfer from Reduced ZnO Nanocrystals. *ACS Nano* **2015,** *9* (10), 10258-10267.
49. Volpato, G. A.; Bonetto, A.; Marcomini, A.; Mialane, P.; Bonchio, M.; Natali, M.; Sartorel, A., Proton coupled electron transfer from Co_3O_4 nanoparticles to photogenerated $Ru(bpy)_3^{3+}$: base catalysis and buffer effect. *Sustainable Energy & Fuels* **2018,** *2* (9), 1951-1956.
50. Ung, D.; Cossairt, B. M., Effect of Surface Ligands on CoP for the Hydrogen Evolution Reaction. *ACS Applied Energy Materials* **2019,** *2* (3), 1642-1645.
51. Kuhn, J. N.; Tsung, C.-K.; Huang, W.; Somorjai, G. A., Effect of organic capping layers over monodisperse platinum nanoparticles upon activity for ethylene hydrogenation and carbon monoxide oxidation. *J. Catal.* **2009,** *265* (2), 209-215.
52. Li, D.; Wang, C.; Tripkovic, D.; Sun, S.; Markovic, N. M.; Stamenkovic, V. R., Surfactant Removal for Colloidal Nanoparticles from Solution Synthesis: The Effect on Catalytic Performance. *ACS Catal.* **2012,** *2* (7), 1358-1362.
53. De Roo, J.; Van Driessche, I.; Martins, J. C.; Hens, Z., Colloidal metal oxide nanocrystal catalysis by sustained chemically driven ligand displacement. *Nature Materials* **2016,** *15* (5), 517-521.
54. Solon, E.; Bard, A. J., The Electrochemistry of Diphenylpicrylhydrazyl. *J. Am. Chem. Soc.* **1964,** *86* (10), 1926-1928.
55. Solon, E.; Bard, A. J., Coulometric Study of the Reaction of Diphenylpicrylhydrazyl and Bromide Ion[1]. *The Journal of Physical Chemistry* **1964,** *68* (5), 1144-1147.
56. Agarwal, R. G.; Coste, S. C.; Groff, B. D.; Heuer, A. M.; Noh, H.; Parada, G. A.; Wise, C. F.; Nichols, E. M.; Warren, J. J.; Mayer, J. M., Free Energies of Proton-Coupled Electron Transfer Reagents and Their Applications. *Chem. Rev., accepted* **2021**.
57. Lide, D. R., *CRC Handbook of Chemistry and Physics*. 90 ed.; CRC Press: Boca Raton, FL, 2009.
58. Bim, D.; Maldonado-Dominguez, M.; Rulisek, L.; Srnec, M., Beyond the Classical Thermodynamic Contributions to Hydrogen Atom Abstraction Reactivity. *Proc. Natl. Acad. Sci. U. S. A.* **2018,** *115* (44), E10287-E10294.
59. Darcy, J. W.; Kolmar, S. S.; Mayer, J. M., Transition State Asymmetry in C-H Bond Cleavage by Proton-Coupled Electron Transfer. *J. Am. Chem. Soc.* **2019,** *141* (27), 10777-10787.
60. Salamone, M.; Galeotti, M.; Romero-Montalvo, E.; van Santen, J. A.; Groff, B. D.; Mayer, J. M.; DiLabio, G. A.; Bietti, M., Bimodal Evans–Polanyi Relationships in Hydrogen Atom Transfer from C(sp3)–H Bonds to the Cumyloxyl Radical. A Combined Time-Resolved Kinetic and Computational Study. *J. Am. Chem. Soc.* **2021,** *143* (30), 11759-11776.
61. Barman, S. K.; Yang, M.-Y.; Parsell, T. H.; Green, M. T.; Borovik, A. S., Semiempirical method for examining asynchronicity in metal–oxido-mediated C–H bond activation. *Proceedings of the National Academy of Sciences* **2021,** *118* (36), e2108648118.
62. German, E. D.; Abir, H.; Sheintuch, M., A Tunnel Model for Activated Hydrogen Dissociation on Metal Surfaces. *The Journal of Physical Chemistry C* **2013,** *117* (15), 7475-7486.
63. Chun, H.-J.; Zeng, Z.; Greeley, J., Direct Demonstration of Unified Brønsted−Evans−Polanyi Relationships for Proton-Coupled Electron Transfer Reactions on Transition Metal Surfaces. *J. Electrochem. Soc.* **2020,** *167* (16), 166516.
64. Vilé, G.; Bridier, B.; Wichert, J.; Pérez-Ramírez, J., Ceria in Hydrogenation Catalysis: High Selectivity in the Conversion of Alkynes to Olefins. *Angew. Chem. Int. Ed.* **2012,** *51* (34), 8620-8623.
65. Luo, M.; Wang, Z.; Li, Y. C.; Li, J.; Li, F.; Lum, Y.; Nam, D.-H.; Chen, B.; Wicks, J.; Xu, A.; Zhuang, T.; Leow, W. R.; Wang, X.; Dinh, C.-T.; Wang, Y.; Wang, Y.; Sinton, D.; Sargent, E. H., Hydroxide promotes carbon dioxide electroreduction to ethanol on copper via tuning of adsorbed hydrogen. *Nature Communications* **2019,** *10* (1), 5814.

Chapter 5

Kinetic Solvent Isotope Effects in Heterogeneous Electrocatalysis

This project was part of a collaboration with the laboratory of Professor Hector Abrũna. The cumulative work is being compiled in multiple manuscripts in preparation. Dr. Yao Yang collected cyclic voltammograms of single crystal platinum electrodes, Xinyao Lu prepared the single crystal surfaces, and RGA developed the purification method for deuterium oxide, in addition to designing and executing experiments which probe the hydrogen evolution reaction at polycrystalline gold electrodes. We gratefully acknowledge Professor Marc Koper who provided the initial intellectual spark and initial support for this project while RGA was visiting his laboratory, as well as Hannah Nedzbala for helpful discussions.

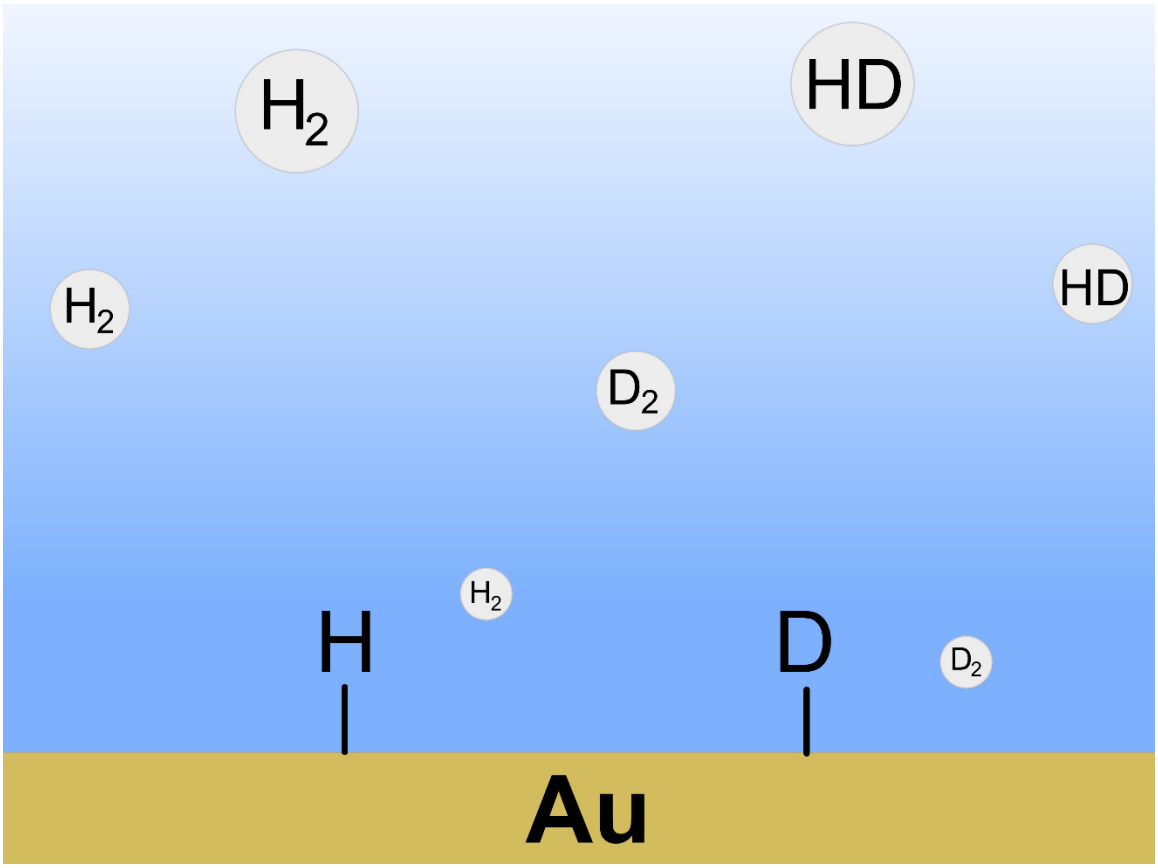

5.1 Introduction

Mechanistic knowledge about multi-electron, multi-proton processes important to energy systems is essential to the advance of both fundamental scientific inquiry and modern technology. Some of the best studied model systems involve electrocatalytic adsorption or desorption of hydrogen at well-defined platinum and gold surfaces.[1-9] Despite great progress, even in these systems there is still much to learn about the microscopic steps these catalysts go through during reaction turnover.[7,10]

One tool of broad utility in the study of mechanism in many systems is the kinetic isotope effect (KIE).[11-15] In the context of heterogeneous electrocatalysis, the most common experiment involves substituting protons in the electrolyte with deuterons by isotopically labeling the solvent.[16-21] This exchange of water for deuterium oxide (D_2O) tests the kinetic solvent isotope effect (KSIE). Although this technique has been employed in electrocatalytic systems, its application remains relatively sparse due to the challenge of preparing suitably purified deuterated electrolytes.[22-24] This is because many electrocatalytic surfaces are sensitive to trace organic and inorganic impurities which can absorb and block active sites, or can chemisorb and change the surfaces properties.[22,24] This issue has largely been solved for protic electrolytes, as the proliferation of laboratory scale ultrapure, or Type 1, water systems has made H_2O purification accessible.[25] While use of an ultrapure water system has been applied to the purification of D_2O,[24] this methodology remains cost-prohibitive for most laboratories and has not been broadly applied. Furthermore, the toughest tests of ultrapure D_2O have not been performed, including proof that the resulting electrolytes have sufficient chemical purity to be suitable even for hyper-sensitive single crystal surfaces. The effect of the purification procedure on the isotopic purity of the D_2O must also be considered. Below both are discussed although "purity" always refers to chemical purity unless otherwise stated.

In this chapter, we demonstrate a new methodology for the preparation of batch scale deuterium oxide suitable for voltametric investigations of platinum single crystal surfaces in both acidic and alkaline electrolytes. The need for deuterated electrolytes with this level of chemical purity is demonstrated through catalytic studies on stepped platinum single crystal surfaces. Voltammograms of both stepped and unstepped platinum surfaces are collected, and provide novel insights into the equilibrium solvent isotope effects for hydrogen and hydroxide adsorption to these surfaces.

Deuterium oxide electrolytes are then applied in the study of product solvent isotope effects for the hydrogen evolution reaction at polycrystalline gold electrodes. Product detection is accomplished using a home-built differential electrochemical mass spectrometer (DEMS) instrument to give time-resolved mass spectrometric cyclic voltammograms (MSCVs) for the production of H_2, HD, and D_2 gaseous products. These studies reveal a significant product solvent isotope effect in acidic electrolytes that cannot be explained by previous voltametric investigations of the KSIE for HER on gold surfaces. As a result, these studies provide novel insights into the kinetically invisible step(s) of hydrogen evolution on gold surfaces.

5.2 Purification of Deuterium Oxide for Heterogeneous Electrocatalysis

Water used to create electrolytes suitable for voltametric studies of heterogeneous electrocatalysis is typically Type 1, or ultrapure, water. The official standard designates that the water must have a resistivity of >18 MΩ•cm and <50 ppb total organic carbon (TOC).[25] However, many laboratories, including ours, employ Milli-Q water systems which further decrease the TOC to <5 ppb.[26] Preparing D_2O which approaches this standard of ionic and organic purity is therefore a daunting task.

A Milli-Q system utilizes ion-exchange resin and activated carbon columns to treat incoming water before irradiating the output with UV light and running the product through a 0.22 μm filter to remove bacteria.[26] This preparation of deuterium

oxide takes inspiration from this methodology, as well as the literature for producing conductivity-grade water.[27] In this method, water is distilled once before adding sodium hydroxide and potassium permanganate and distilling again. The logic behind this procedure is to remove ions via distillation and to oxidize trace organics to non-volatile species so that they too can be removed via distillation.

The above methods provide several avenues which have been proven successful in purifying water, however, in order to troubleshoot a methodology an appropriate test is required. One test would be to perform a voltametric experiment on a highly sensitive electrode surface. For our test we chose to use Pt(111), as the voltammogram of this flat and symmetric surface in ultrapure non-coordinating perchloric acid electrolytes shows distinctive surface adsorption features and is sensitive to trace impurities.[4,28] Adsorbed impurities can slow the hydrogen and hydroxide adsorption features in the voltammogram, thereby reducing the reversibility of the processes and changing the symmetry of the corresponding faradaic waves. They may also block sites entirely, thereby reducing the current density of faradaic features. Finally, the impurity adsorption event itself can show up as an unexpected faradaic feature or change the expected current density of double layer capacitance for the flat (111) surface. Cycling of a potential range also enables analysis of whether or not impurities grow in and on what timescale. This test, therefore, offers far more information than a standard measure of conductivity or total organic carbon, but in a less quantitative manner.

Troubleshooting with the Pt(111) test, more details below, lead to the development of an accessible procedure which can reproducibly be used to prepare D_2O suitable for voltammetry of Pt(111) and other single crystal facets of platinum. In the procedure, D_2O from Sigma-Aldrich (99.9 atom % D) is first passed through a home-built glass ion-exchange resin column. The glass column contains a low TOC mixed cation and anion exchange resin (UCW3700, Polysciences Inc.), which

exchanges ions for H^+ or OH^-. To improve product isotopic purity, 200 g of D_2O were run through the column before use and the column was kept sealed when not in use. After filtering the D_2O through the ion exchange resin column, 0.35 wt% KOH (Sigma, semiconductor grade) and 0.05 wt% $KMnO_4$ (Sigma, ACS reagent, ≥99.0%, low in mercury) were added. The resulting mixture was distilled using a short-path distillation head with 14/20 joints. Distillations were carried out using 2 x 100 g bottles of D_2O starting material with a 300 mL round bottom distillation flask and a 250 mL receiving flask under an N_2 flow to prevent CO_2 contamination. The yield for this procedure was ~180 g of purified D_2O. The remaining 20 mL was lost due to N_2 flow or left in the distillation flask to prevent $KMnO_4$ from coming over in the setup. In our experience, the flask is too hot and may bump $KMnO_4$ residue across the distillation head when the $KMnO_4$ residue in the round bottom flask turns from deep purple to turquoise. If this color change is seen, the heat must be lowered or the distillation should be stopped in order to prevent contamination of the product by $KMnO_4$. Final products were stored in flame-sealed 50 mL glass ampoules.

This procedure is successful when several experimental precautions are taken. In order to avoid contamination or sticking between ground glass joints, all joints which might reasonably come into contact with D_2O were sealed with PTFE sleeves. All glassware used (and the PTFE sleeves) was cleaned following a previously reported method.[6] Briefly, glassware was soaked overnight in a solution containing 1 g/L $KMnO_4$ and 0.5 M H_2SO_4, before decanting and dissolving remaining MnO_2 in dilute piranha etch solution. Dilute piranha etch solutions were prepared by adding H_2SO_4 (Sigma, 95.0 – 98.0 %, ACS reagent) and H_2O_2 (Fisher, 30 wt%, Certified ACS) slowly to water, as opposed to diluting the concentrated mixture which can present a significant safety hazard. Glassware was then boiled three times in ultrapure water from a Synergy®-R Millipore system and flame-dried before use. In this chapter, unless otherwise stated, all H_2O used was ultrapure and all glassware and fluoropolymer plastics used were

cleaned in the manner described above. The drying step of the cleaning procedure was only applied to glassware which might come in contact with deuterated electrolytes. The isotopic purity of the D_2O product was measured to be 95 atom % D by a method described below.

The single crystal platinum electrodes used for this study were prepared following the method of Clavilier.[4,5] Cyclic voltammograms of the Pt(111) facet in 0.1 M $HClO_4$ were collected using a coiled platinum wire counter electrode and a Ag/AgCl reference in 1M KCl (Figure 5.1A). For both proteo and deutero electrolytes, 70 wt% perchloric acid in H_2O (Supelco, 70%-72%, Emsure®) was used (*safety note: 70 wt% $HClO_4$ should be used in a well-ventilated area and should not be heated to avoid the release of toxic and potentially shock sensitive compounds).* This was to ensure equivalent levels of ionic and organic impurities. While the choice of a protic acid does introduce a greater concentration of isotopic impurities to the deuterated electrolyte, the amount is negligible given that the D_2O used is 95 atom % D and the HClO4 is diluted ca. 500 times. Reference scales were adjusted to the reversible hydrogen electrode (RHE) after the experiment. Note that RHE is nearly equivalent to the reversible deuterium electrode (RDeE) in acidic electrolytes.[29,30]

Interestingly, CVs of Pt(111) in $HClO_4$ and $DClO_4$ nearly overlay between 0 – 0.5 V vs RHE. Current passed in this region of the CV results from the adsorption of underpotential deposited hydrogen (H_{upd}) to the surface and from double layer capacitance.[4,28] The near perfect overlay observed here suggests that there is almost no equilibrium solvent isotope effect (ESIE) for hydrogen vs deuterium adsorption to Pt(111). The absence of more faradaic features in the $DClO_4$ CV indicated that there were no significant impurities in the prepared electrolyte. To further test the purity of the electrolyte, CVs were collected in 0.1 M NaOH (Figure 5.1B). Both proteo and deutero electrolytes were prepared from sodium hydroxide monohydrate (Supelco, 99.99%, Suprapur®). In this case, the asymmetric features at 0.2-0.3 V vs RHE

indicate the presence of small impurities in both electrolytes. However, the general overlay in the H_{upd} region suggests that there is still no ESIE, even though the proton donor has changed from H_3O^+ to H_2O. For both perchloric acid and sodium hydroxide electrolytes the region from 0.5 – 0.9 V vs RHE/RDeE does not overlay quite as well. This region is known to correspond with hydroxide adsorption to Pt(111),[4,31] and the shift indicates that there is a shift in the adsorption free energy of this process of 20 mV in 0.1 M $HClO_4$ and 40 mV in 0.1 M NaOH. While these shifts have been seen in previous attempts to characterize the surface of Pt(111) in deuterated electrolytes, previous data was collected in the presence of impurities which further convoluted the CV.[31] The critical importance of using chemically pure deuterated electrolytes is discussed in greater detail below.

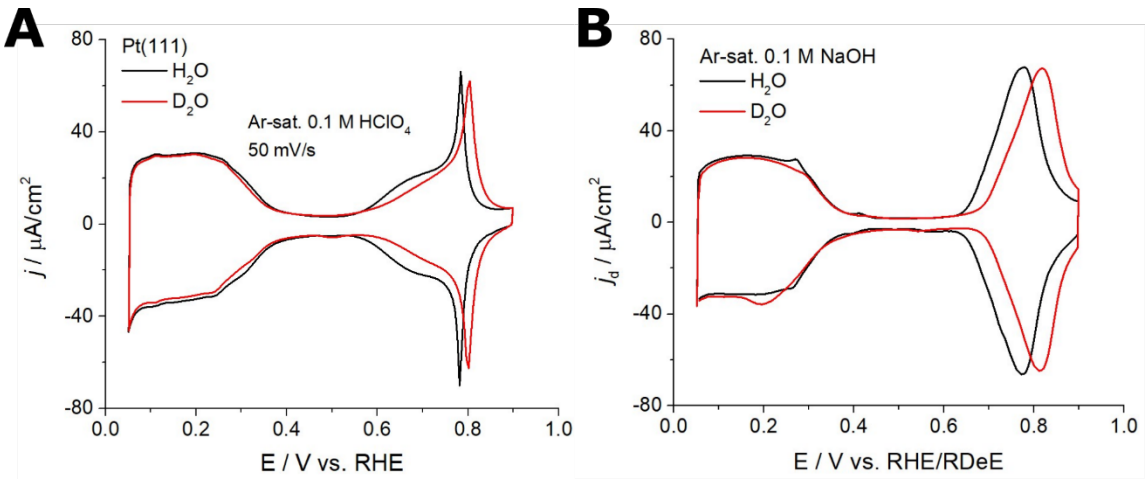

Figure 5.1. Cyclic voltammograms of a flame-annealed Pt(111) single-crystal electrode collected at 50 mV/s with a coiled Pt wire counter electrode and a Ag/AgCl reference electrode (1 M KCl). CVs were collected in either (**A**) 0.1 M $HClO_4$ and 0.1 M $DClO_4$ or (**B**) 0.1 M NaOH and 0.1 M NaOD.

To further demonstrate the robustness of the D_2O purification procedure, CV studies in 0.1 M $HClO_4$ were expanded to other single crystal facets of Pt including stepped surfaces. Stepped edges have undercoordinated Pt atoms, and are therefore more sensitive to the presence of electrolyte impurities.[4] As a result, they provide an even more rigorous test of D_2O purity. These platinum facets are denoted based on

the size of their terrace and the type of step on the surface, i.e. *n*(111)x(110) is an *n*-atom wide (111) terrace and a 1-atom high (110) step. CVs of nearly all tested surfaces show perfect overlays in the H_{upd} region and an anodic shift for hydroxide adsorption in D_2O, suggesting that these features are quite general (Figure 5.2). The one example which seems to show a small ESIE for H_{upd} adsorption is Pt[3(111)x(100)].

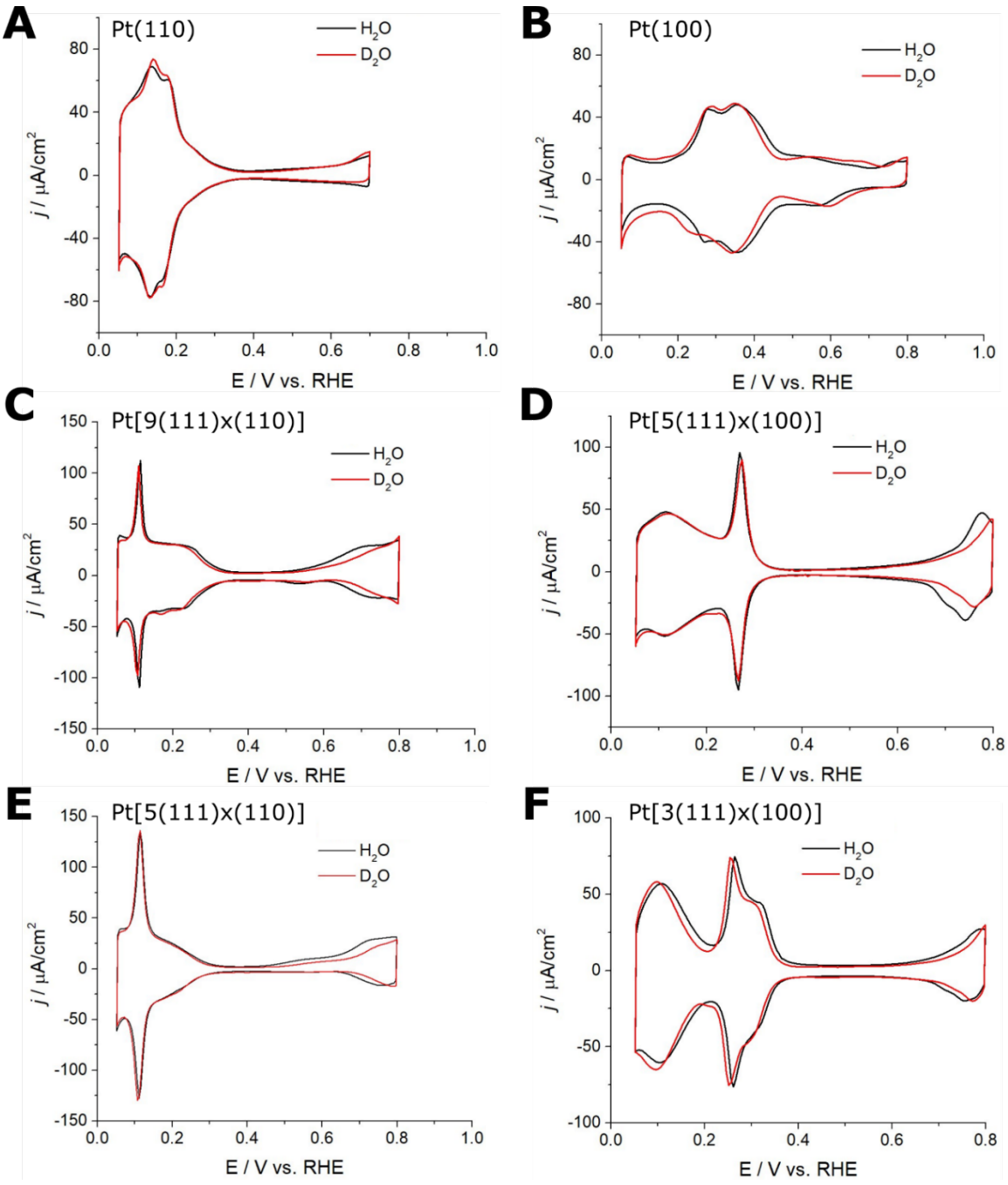

Figure 5.2. Cyclic voltammograms of flame-annealed Pt single-crystal electrodes collected at 50 mV/s with a coiled Pt wire counter electrode and a Ag/AgCl reference electrode (1 M KCl). Panels (**A**), (**C**), and (**E**) are for facets containing (110) steps, while panels (**B**), (**D**), and (**F**) are for facets containing (100) steps.

The presence of electrolyte impurities can have a significant effect on reaction kinetics. This has previously been shown in oxygen reduction reaction (ORR) at polycrystalline platinum electrodes, where measurements in as received D_2O and

ultrapure D_2O showed different KSIEs under alkaline conditions, but not under acidic ones.[24] We further emphasize this point by showing that, even under acidic conditions, Pt(110) electrodes can have significantly different ORR KSIEs due to impurities. Figure 5.3 shows three Pt(110) CVs collected in purified 0.1 M $DClO_4$ from different electrolytes that had been handled differently. Samples D_2O-2 and D_2O-3 were prepared from D_2O taken straight from an unopened ampoule of purified D_2O, while D_2O-1 was taken from an ampoule which had been left open for ~1 hour. This small deviation in procedure resulted in a drastically different CV. Furthermore, this change in CV had a significant effect on the kinetics of Pt(110) ORR reactivity as D_2O-1 gave a KSIE of 6, while D_2O-2 and D_2O-3 gave KSIEs of 1 and 0.5, respectively. This enormous effect demonstrates the extreme sensitivity of these surfaces, and the critical importance of using ultrapure electrolytes.

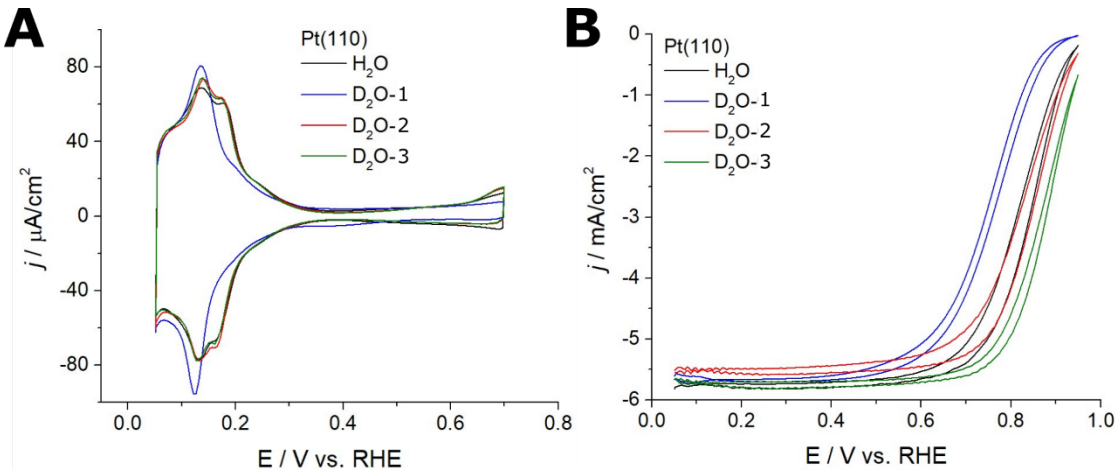

Figure 5.3. (**A**) Cyclic voltammograms of a Pt(110) single crystal electrode collected on different days in electrolytes prepared with ultrapure H_2O and purified D_2O. (**B**) Rotating disk voltammetry of the same electrodes collected at 1600 rpm in the presence of 1 atm O_2.

5.3 Product Solvent Isotope Effects for the Hydrogen Evolution Reaction at Polycrystalline Gold Electrodes

The hydrogen evolution reaction (HER) is one of the most fundamental reactions in electrochemistry, while also being one of the most important to society and as we move towards a green energy and chemical economy.[10,32,33] As a result, an understanding of every step of this reaction is of great interest. In the simplest case, the mechanism for HER follows two of the Volmer, Heyrovsky, and Tafel steps to form H_2 gas (eqs 5.1–5.3). In this model, the first step is always the Volmer reaction where H^+ in solution and an e^- from the circuit combine at the electrode surface to form a surface adsorbed hydrogen atom (H^*).

$$H^+ + e^- \rightarrow H^* \qquad \text{Volmer} \qquad (5.1)$$

$$H^+ + H^* \rightarrow H_2 \qquad \text{Heyrovsky} \qquad (5.2)$$

$$H^* + H^* \rightarrow H_2 \qquad \text{Tafel} \qquad (5.3)$$

Despite this relatively simple mechanistic model, the mechanism of HER on most surfaces remains a matter of debate.[7,17,18,30,34-40] Broadly, it can be stated that more mechanistic tools will be needed to further decipher this important puzzle. In this section, we study *product* solvent isotope effects (PSIEs) for HER in acidic electrolytes at a polycrystalline gold (pc-Au) electrode. We chose this system because voltametric data in chemically ultrapure deuterated electrolytes is already available to describe the KSIE for the reaction from CV.[24] Measurement of the PSIE should provide the overall reaction isotope effect including the ESIEs and KSIEs for all steps.

Measurement of a PSIE requires *operando* measurements of H_2, HD, and D_2 gases. This is achieved using a home-built differential electrochemical mass spectrometer (DEMS) setup, which resembles several others.[41-43] Briefly, the MS has two compartments separated by a 7 mm constriction (Figure 5.4). The first compartment contains a Pfeiffer HiQuad® QMA 430 quadrupole mass spectrometer

(QMS), while the second is where the sample stream enters from the DEMS cell, described below. Both compartments are pumped by Pfeiffer HiPace® 80 turbo pumps. In this setup, the QMS chamber operates at 1 x 10^{-5} mBar.

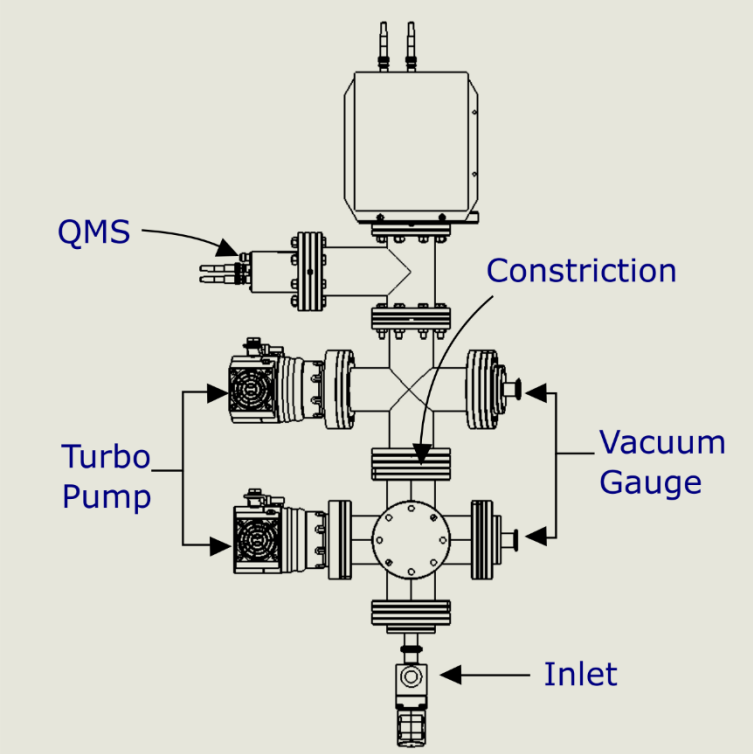

Figure 5.4. Technical drawing of the main QMS chamber and associated pumps. Differential pumping is achieved across the constriction.

The QMS setup is attached to a custom dual thin layer flow cell where voltammetry is performed. This setup mimics those previously published with minor changes to the cell design (Figure 5.5).[41,42] In this configuration, solution first flows to a compartment housing the electrode surface, which is sealed by 3 x 0.002" thick PTFE gaskets (McMaster-Carr, 8569K) that are $^1/_2$" wide and have $^1/_4$" holes. At the surface, a potential is applied and products are formed. The electrolyte then flows to another compartment housing a Gore-Tex pervaporation membrane with a mean thickness of 75 μm, a mean pore size of 0.02 μm, and a porosity of 50%. This membrane segregates gaseous products from electrolyte, and is sealed to the cell with a 0.002" thick PTFE gasket with the same characteristics as those used for the electrode

compartment. Finally, the electrolyte flows through an outlet, at a rate determined by a KD Scientific Legato® 110 syringe pump. To prevent competing ORR, the chambers are also purged with argon gas.

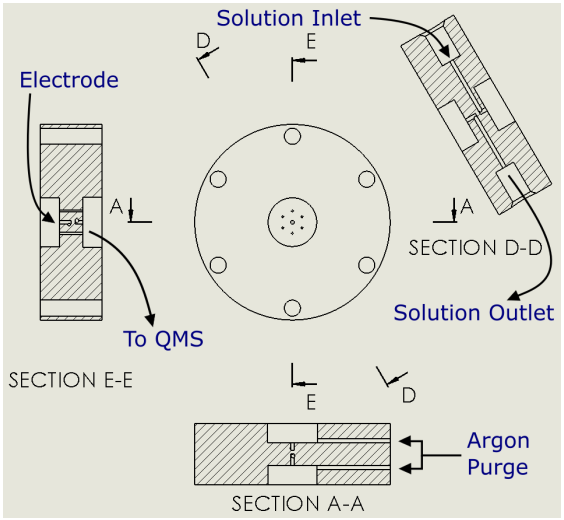

Figure 5.5. Top down view of DEMS cell along with slices along labeled axes. Cell is made of polychlorotrifluoroethylene (PCTFE).

The polycrystalline gold (pc-Au) electrode (d = 7.5 mm) used in these studies was purchased from Surface Preparation Laboratory and consists of 99.999% Au. To ensure a consistent surface for experiments, the electrode was polished and flame-annealed per a previously reported procedure.[6] The resulting surface was then characterized by CV in a standard 3-electrode setup, before being transferred to the DEMS cell shown in Figure 5.5. In both the cell and the 3-electrode setup, 70 wt% $HClO_4$ (Sigma, 99.999% trace metals basis) was diluted to 0.1 M and used as electrolyte. In the cell, two platinum wire counter electrodes are connected by a resistor (in this work, 3.3 MΩ) to compensate for the high resistance of the millimeter wide fluid channels. The reference electrode was a single junction Pine Ag/AgCl (sat'd KCl) connected via a Luggin capillary.

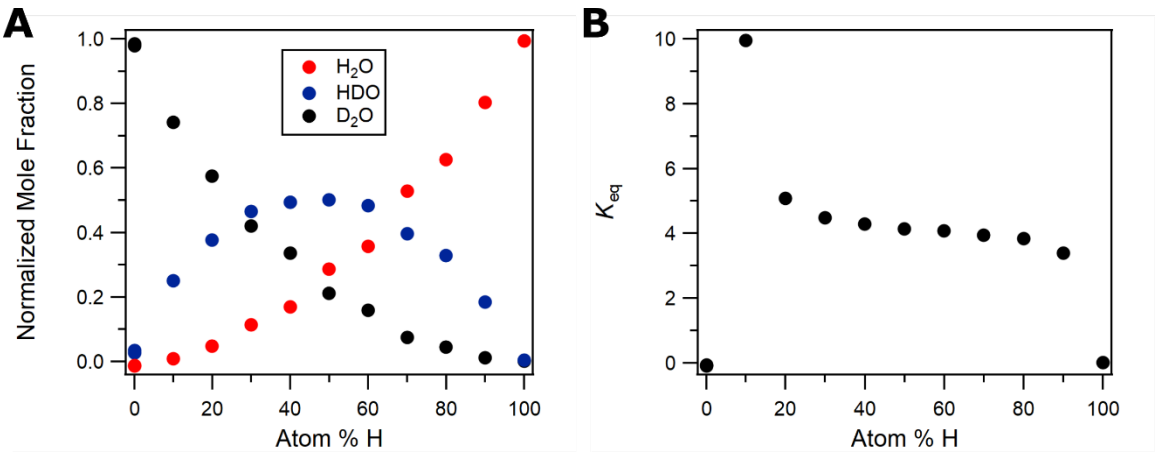

Figure 5.6. Premixed solutions of D_2O and H_2O were flowed through the DEMS cell described above. (**A**) Measured values for m/z = 18, 19, and 20 were corrected to give the fractions of H_2O, HDO, and D_2O in solution. (**B**) These values were used to determine the K_{eq} for HDO disproportionation to H_2O and D_2O.

For these studies, the isotopic composition of the electrolyte was systematically varied to range from nearly all H^+ to nearly all D^+ in solution. Direct quantification of the atom % H in solution was achieved during studies by measuring m/z values 18, 19, and 20. These correspond to the ionized products of D_2O, HDO, and H_2O. However, simply taking the ratios of these ion currents is not enough as the OD fragment from both HDO and D_2O will alter the measured value at m/z = 18. The fragmentation of these molecules for a QMS with a cathode voltage of −70 V (same as these studies) has previously been reported.[44] Here we apply these reported ratios to calibrate the QMS and measure the atom % H of electrolytes. To calibrate this method for the setup used in these studies, the baseline for m/z = 18 needed to be determined, as there is an unknown amount of adventitious H_2O in the chamber at the operating pressure. For the calibration, known mixtures of H_2O and D_2O were prepared and the known isotopic purity of the as received D_2O (99.9% from certificate of analysis) was used to determine the baseline ion current of m/z = 18. Baseline ion currents for m/z = 19 and 20 were low enough to not be significant in the calculation. Compilation of these data gives a symmetric Job plot demonstrating how the solution fraction of H_2O, HDO, and D_2O change as a function of atom % H (Figure 5.6A). The symmetry of this plot

demonstrates the robustness of this method. As a caveat, measurement of the K_{eq} for HDO disproportionation to form H_2O and D_2O was close to the expected value of 3.85 (eq 5.4),[44] but deviated severely at either high or low atom % H (Figure 5.6B). Under these conditions, there will be error in deriving values of atom % H from this method.

$$H_2O + D_2O \rightarrow 2HDO \qquad K_{eq} = \frac{[HDO]^2}{[H_2O][D_2O]} \tag{5.4}$$

In the DEMS studies described below, the effect of electrolyte isotopic composition on the ratio of H_2, HD, and D_2 products is examined. These data have not previously been collected from nearly 100 atom % H to nearly 100 atom % D for gold, or any other material to the best of our knowledge. As a result, we sought to first measure a full set of data using as received D_2O.

Cyclic voltammetry studies involved multiple cycles of scanning to cathodic potentials, while flowing electrolyte at ≥ 0.6 mL/min. All CVs were collected with an Ivium Compactstat.h10030 potentiostat to apply an analog ramp of the applied potential. The flow rate and potential scan range were optimized to avoid bubble formation, as $H_{2(g)}$ is sparingly soluble in water and bubbles lead to a loss of electrical contact in the thin fluidic channels of the DEMS cell.[45] During the scan, measurements of m/z = 2, 3, and 4 were made to follow production of the expected H_2, HD, and D_2 products. After collection of concurrent MS and CV data, the electrolyte composition was changed and the process repeated.

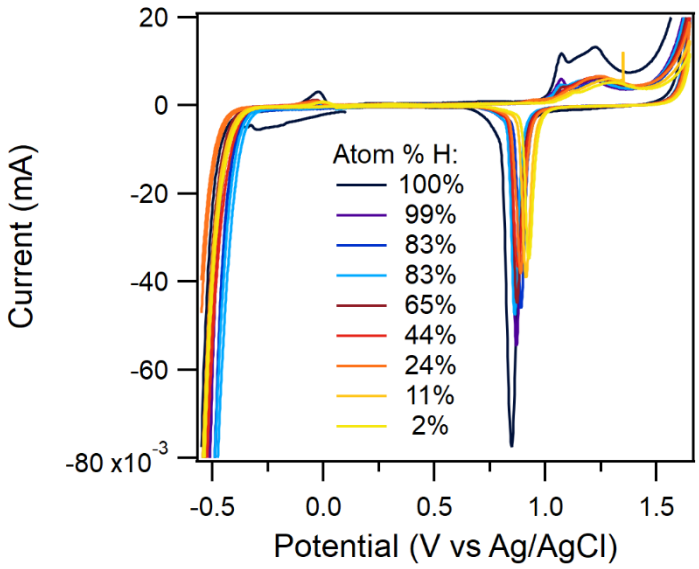

Figure 5.7. Single cycle CVs for each solution condition collected at 50 mV/s with data collected every 5 mV. Scans cover HER onset, surface hydroxide formation and desorption, and the onset of the oxygen evolution reaction.

The resulting CVs are shown as a function of solution isotopic composition (Figure 5.7). Several trends are apparent, including an anodic shift of hydroxide adsorption features positive of 0.75 V vs Ag/AgCl and cathodic shifts in the onset of HER with decreasing atom % H. Importantly, these trends are not perfectly quantitative given the poorly defined *iR* drop in the DEMS cell makes accurate referencing of potentials challenging. Nevertheless, they mirror the results of the more quantitative single-crystal platinum studies above which demonstrated a similar shift in hydroxide adsorption free energy (Section 5.2).

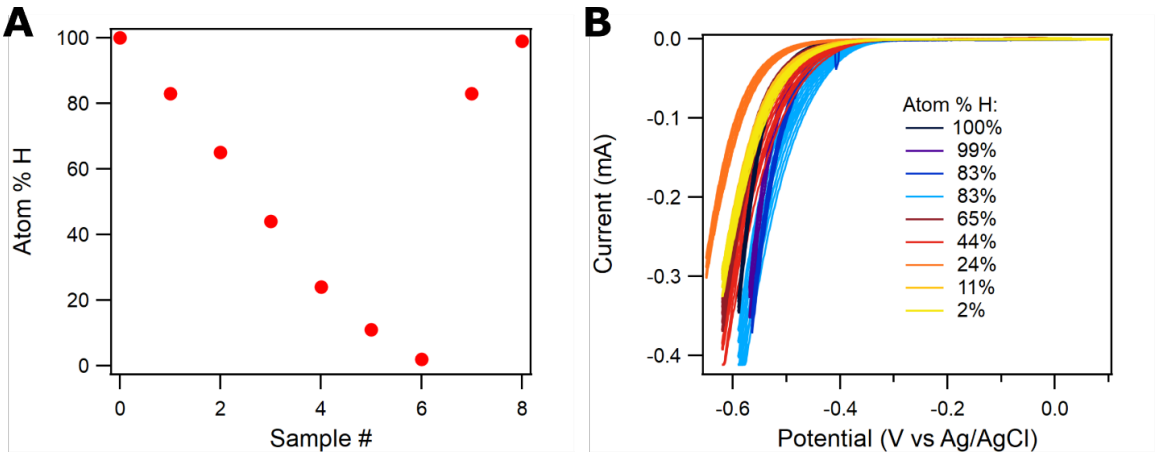

Figure 5.8. (**A**) Order of changes to electrolyte isotopic composition. (**B**) Cyclic voltammograms of HER onset collected for each solution condition at 20 mV/s with data collected every 1 mV.

Quantification of the HER region involved both QMS and CV data. Data were collected by starting in isotopically pure H_2O electrolyte and then slowly changing the isotopic composition to be nearly 100 atom % D, before returning to nearly 100 atom % H (Figure 5.8). This experimental design was pursued to reduce effects from the trace electrolyte of the previous run, and to ensure that changes to the current response are not simply due to drift over time. Cycling in the same potential range often showed small changes to both the ion current and current versus bias responses, with a general trend towards less current passed in successive scans. As a result, the CVs for each electrolyte show some spread, as shown in the overlaid traces in the same color in Figure 5.8B. The origin of this effect is unclear, although it may be due to slow equilibration of the *iR* drop in the cell upon altering electrolyte isotopic composition. Despite uncertainty in the potential for HER onset, a kinetic solvent isotope effect is clearly visible in the CVs as the slope of the current-voltage response tends to be greater for electrolytes with higher atom % H.

The corresponding QMS data qualitatively demonstrate a significant product solvent isotope effect (Figure 5.9). Plots show the ion current responses for m/z = 2, 3, and 4 as a function of time. Each CV cycle generates an MS response indicated by the characteristic rise and fall of the data. Raw data is baseline corrected using a linear

fit to subtract drift in the ion current baseline. Additionally, the true MS response lags slightly behind the CV current response, but the time axes in Figure 5.9 are adjusted so that they match. This adjustment relies on the assumption that the peak ion current is directly related to the peak current passed at the gold electrode; a warranted assumption given that a faradaic efficiency of 100% can be assumed for HER in this electrolyte.

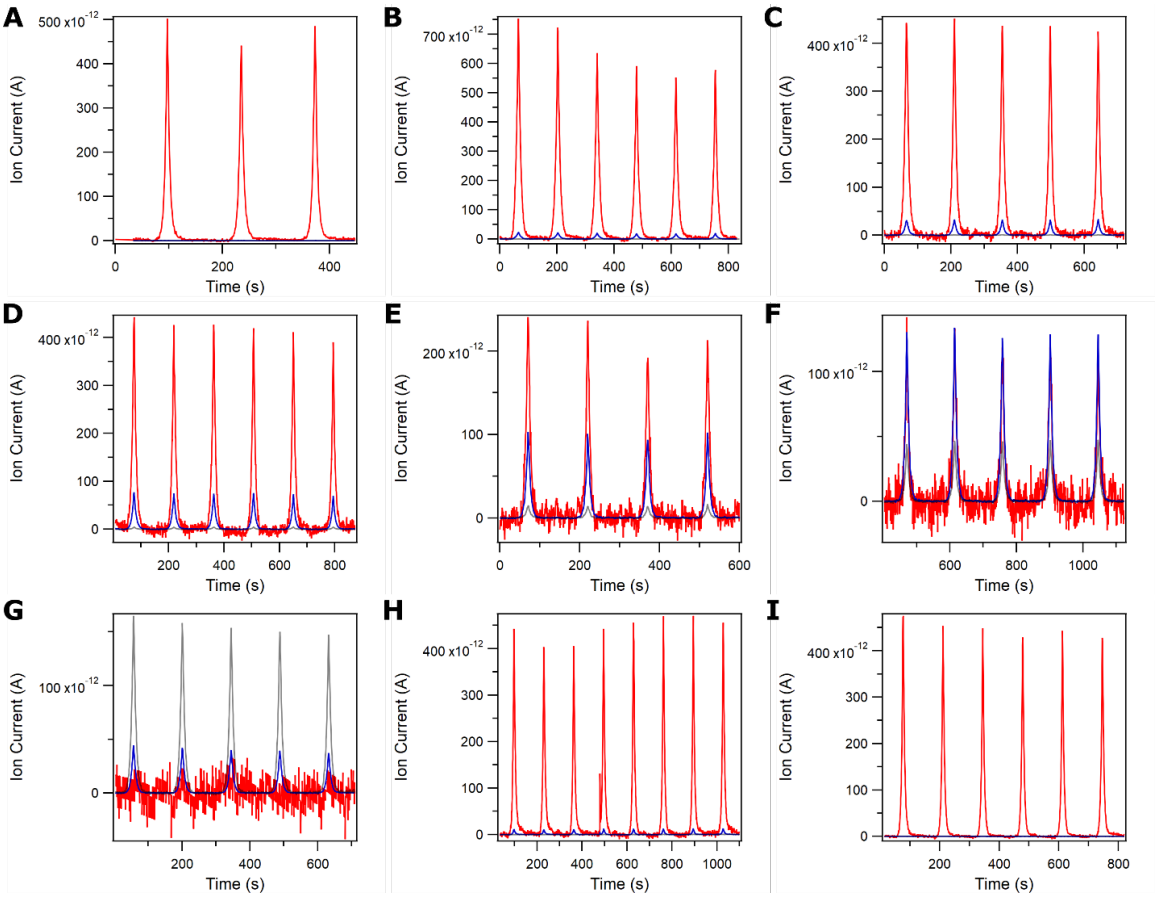

Figure 5.9. Baseline corrected ion current responses of CVs shown in Figure 5.8B for m/z = 2 (red), m/z = 3 (blue), and m/z = 4 (gray). Order of panels follows order of measurement shown in Figure 5.8A, where the atom % H is (**A**) 100%, (**B**) 83%, (**C**) 65%, (**D**) 44%, (**E**) 24%, (**F**) 11%, (**G**) 2%, (**H**) 83%, (**I**) 99%.

The QMS data must be calibrated for differences in the ionization and transfer efficiencies of H_2, HD, and D_2 before quantitatively comparing it to that from voltammetry. This was accomplished by injecting known volumes of H_2 (Airgas, 99.999%), HD (Cambridge Isotope, Lot #: M-1854-2), and D_2 (Cambridge Isotope,

D_2, 99.6%+HD,0.4%) into the QMS setup. Injections were done immediately after the DEMS voltammetry described above, while the cell remained attached. Linear correlations between peak area and moles of gas added were then used to calibrate the ionization efficiency of each product. Full calibration of the DEMS cell requires several other pieces of information.[42] Faradaic efficiency (FE) for product formation must be known, and the HER offers a simple case for this as FE = 100%. Secondly, the relative transfer efficiency of each product through the cell must be known. This is to make sure that H_2 is not more efficiently transferred from the electrode to, and through, the pervaporation membrane than HD or D_2. Here, we assume that the transfer efficiencies of all three gases are constant, although control experiments are in progress. With these assumptions the ionization efficiency of H_2 vs HD vs D_2 was found to be 2.8:1.2:1.0 in this experiment (Figure 5.10). We note that these relative ratios are fairly constant across different days, pervaporation membrane samples, and settings, with the exception of changing the QMS dwell time differently for different m/z values. These data allow for ion current data for H_2, HD, and D_2 to be calibrated.

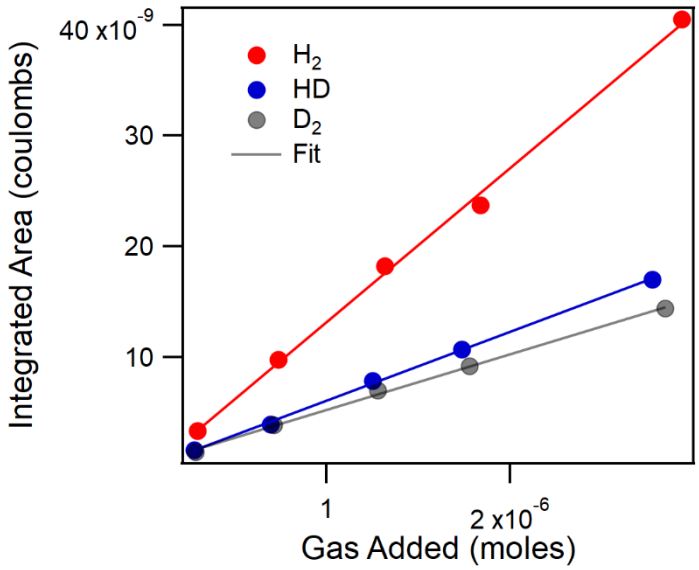

Figure 5.10. A known mixture of H_2, HD, and D_2 (close to 1:1:1) was injected at varying volumes. The slopes of each linear fit give the relative ionization efficiencies of each product.

The combination of cyclic voltammetry and *operando* QMS data gives mass spectrometric cyclic voltammograms (MSCVs) for each solution condition. In MSCVs the calibrated ion current for H_2, HD, and D_2 is plotted as a function of applied potential (Figure 5.11). These plots clearly demonstrate a significant product solvent isotope effect, as even at 11 atom % H equal amounts of H_2 and D_2 are formed.

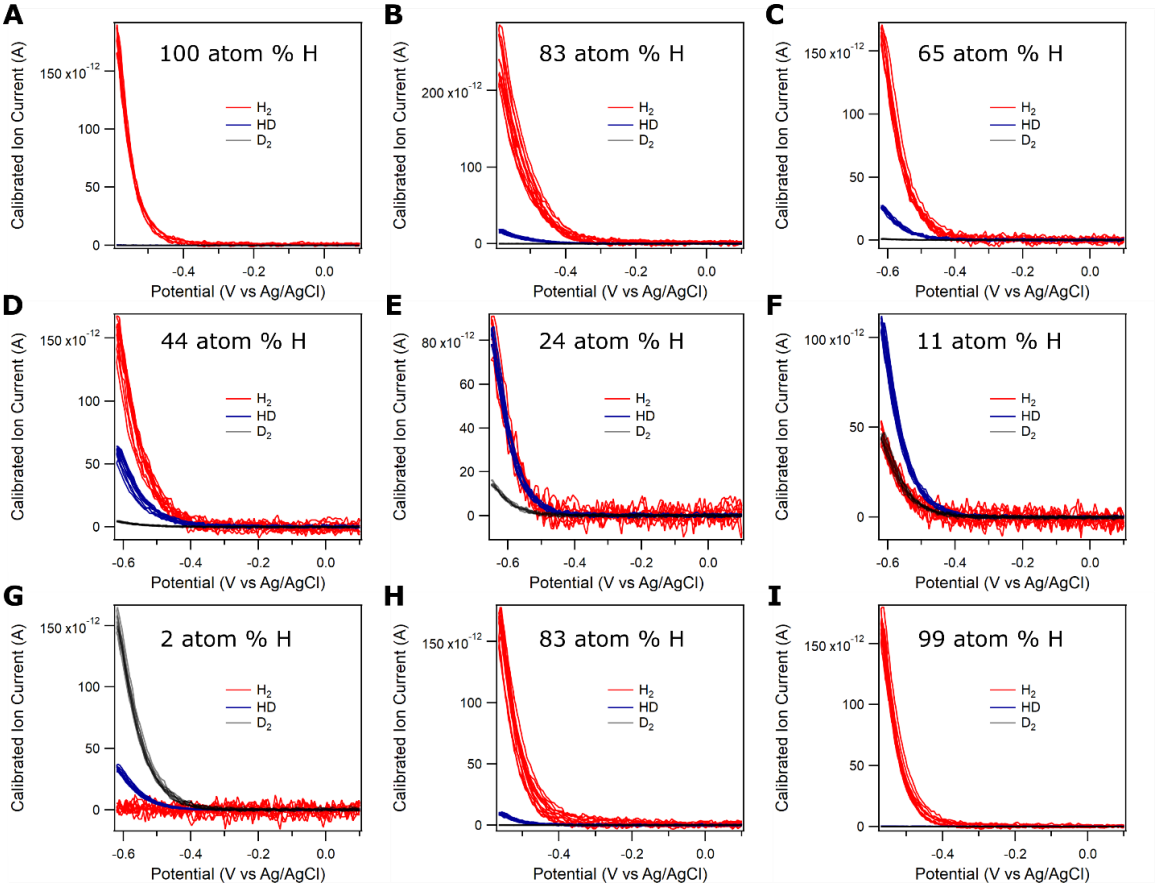

Figure 5.11. Baseline corrected and calibrated ion current responses plotted versus applied potential of CVs shown in Figure 5.8B for H_2 (red), HD (blue), and D_2 (gray). Order of panels follows order of measurement shown in Figure 5.8A.

The sum of the calibrated ion currents should reproduce the current-voltage response of the CVs. A comparison of the two demonstrates that both the shape of the waves and their onsets mimic those of the original voltammograms (Figure 5.12A). However, multiplying total calibrated ion current to overlay with the current from CV reveals that there are some small differences between the methods (Figure 5.12B). Broadly, this suggests that calibration of the DEMS cell is imperfect in these studies.

Error in the calibration may come from our assumption that the transfer efficiencies for H_2, HD, and D_2 are equal. The possible repercussions of error in the calibration are discussed further below.

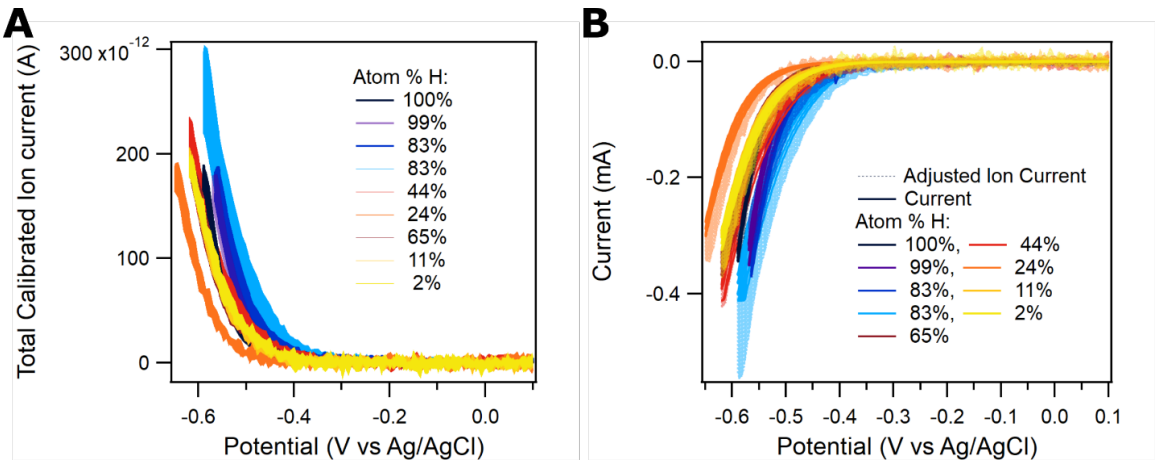

Figure 5.12. (**A**) Sum of the calibrated ion currents for H_2, HD, and D_2 plotted for each solution condition. (**B**) Ion currents multiplied by -1.8×10^9 to normalize to current observed by CV for the 100 atom % H solution condition, and overlayed with current vs potential responses of the CVs shown in Figure 5.8B.

The ratio of products formed is observed to be effectively constant with applied potential. In Figure 5.13, data is shown for 44 atom % H, and similar results were achieved for all solution conditions. This potential-independent product ratio for HER at gold electrodes was previously observed by Kretschmer and Heitbaum.[46] The *operando* data collected here offers better time resolution, but the significant noise in the baseline ion current for H_2 precludes analysis of how this ratio changes at the onset of catalysis. Therefore, we cannot rule out a potential dependence at very low overpotentials. The general lack of potential dependence on the isotopic composition of the products has implications for the mechanism of HER.

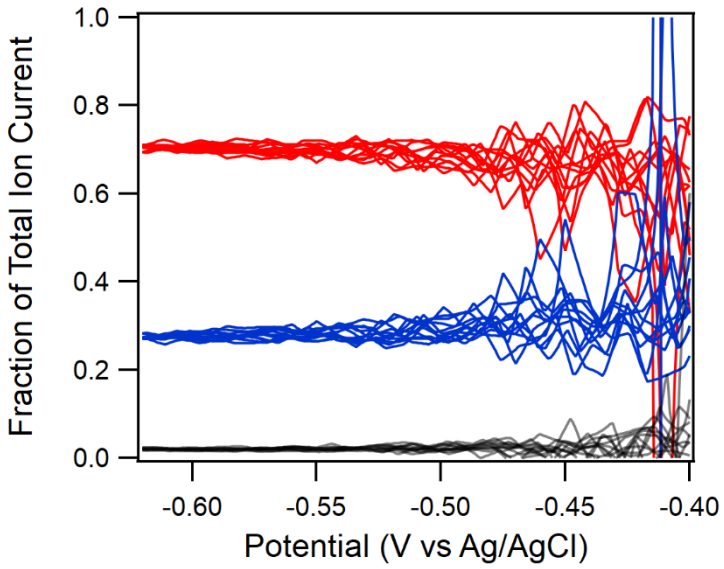

Figure 5.13. Product fraction of H_2 (red), HD (blue), and D_2 (black) as a function of applied potential for the 44 atom % H solution condition.

Due to the potential independence of these data, analysis of how the product fractions change as a function of atom % H can be done at any potential. To better capture the trends, we average the fractions of total ion current collected from the most cathodic potential to 50 mV positive of that value. These values can then be compared across the range of atom % H. The resulting plot demonstrates that the fraction of D_2 remains low until rapidly increasing around 24 atom % H (Figure 5.14A). Meanwhile, the HD fraction rises slowly to a peak of ~0.5 at 11 atom % H before falling back down. If the rates of H_2, D_2, and HD production were equal, the maximum fraction of HD should have occurred at 50 atom % H. Therefore, the observed deviation reveals a significant isotope effect on the distribution of evolved products. The steady patterns in the changes of H_2, HD, and D_2 product fractions with electrolyte isotopic composition also rule out significant effects from changes in the proton donor identity from H_3O^+ to DH_2O^+ to HD_2O^+ to D_3O^+ which have previously been discussed.[17]

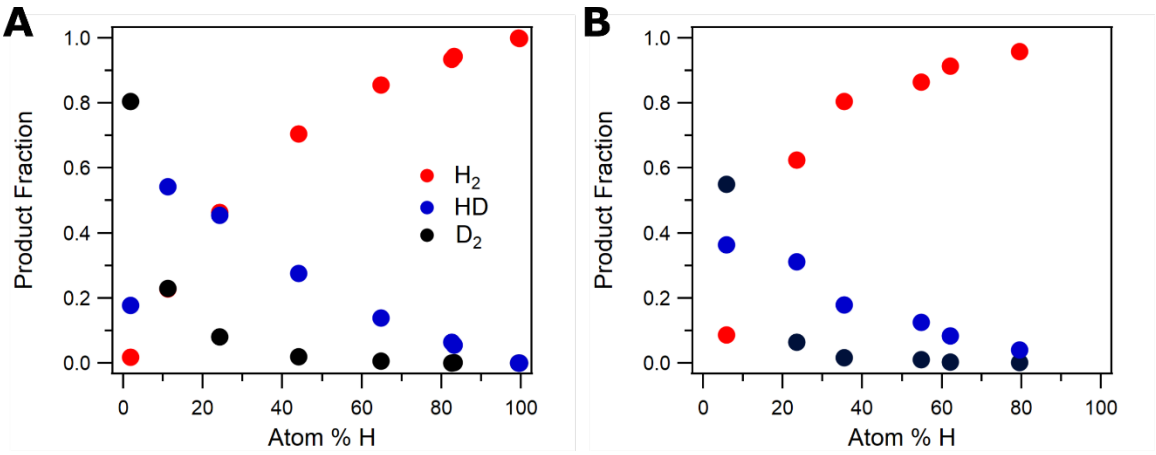

Figure 5.14. Product fraction as a function of atom % H for electrolytes containing (**A**) as received D_2O, and those containing (**B**) purified D_2O.

To corroborate the data collected in as received D_2O, above, experiments were repeated with D_2O purified per the procedure specified above (Section 5.2). These DEMS studies are direct competition experiments, so any impurities in the electrolyte should affect the rates of both H_2 and D_2 evolution. As a result, experiments should be less sensitive to trace impurities than similar KSIE studies where data collected in two separate electrolytes are compared. Nevertheless, the possibility of an unequal impurity effect remains. The treated D_2O is free from significant ionic and organic impurities, but loses isotopic purity during the purification process. As a result, data at very high atom % D cannot be obtained in these experiments. Broadly, voltametric and mass spectrometric data collected in as-received and purified D_2O are very similar in their trends and magnitudes. However, comparison of the relationships between atom % H and product fraction for both as received and purified D_2O electrolytes reveals that more H_2 and less HD is evolved in the purified D_2O (Figure 5.14). This observation suggests that purification of D_2O increases the fraction of H containing products.

5.4 Modelling the Product Solvent Isotope Effects for HER at Polycrystalline Gold Electrodes

The trends in the H_2, HD, and D_2 fractions are quite distinctive, leading to the question of whether or not they can be fit by a mechanistic model. As discussed above, the minimal model of HER consists of the Volmer reaction (eq 1) followed by either a Tafel (eq 5.2) or Heyrovsky (eq 5.3) step to evolve products. The potentials probed are well negative of the reversible hydrogen potential (RHE), and therefore we can assume that evolution of hydrogen by either a Tafel or Heyrovsky step is irreversible. For the Volmer step, it is assumed that the coverages of H^* (θ_H) and D^* (θ_D) reach steady state. This state is defined by a quasi-equilibrium constant *K*, which describes the competition between the electrosorption of H^+ in solution to form H^* and the analogous process to form D^* from D^+ (eq 5.5).

$$H^+ + D^* \rightarrow H^* + D^+ \qquad K = \frac{\theta_H[D^+]}{[H^+]\theta_D} \tag{5.5}$$

Since the concentrations of H^+ and D^+ are known, the concentrations of H^* and D^* can be used to predict reaction rates at constant bias by assuming a value for *K*. Of course, the amount of current passed and product evolved is potential dependent. In the case where the product determining step is a Tafel step, the rate laws for each product would be described by eqs 5.6-5.8.

$$I_{H_2} = -k_{H_2}\theta_H\theta_H \tag{5.6}$$

$$I_{HD} = -k_{HD}\theta_H\theta_D \tag{5.7}$$

$$I_{D_2} = -k_{D_2}\theta_D\theta_D \tag{5.8}$$

In the case where there is a Heyrovsky step, they would be described by eqs 5.9-5.11.

$$I_{H_2} = -k_{H_2}\theta_H[H^+] \quad (5.9)$$

$$I_{HD} = -(k_{HD}\theta_H[D^+] + k_{DH}[H^+]\theta_D) \quad (5.10)$$

$$I_{D_2} = -k_{D_2}\theta_D[D^+] \quad (5.11)$$

In principle, these equations enable calculation of the rate constants for H_2, HD, and D_2 formation in either a Tafel or Heyrovsky step. For example, k_{H2} can be determined by plotting I_{H2} vs either $\theta_H{}^2$ or $\theta_H[H^+]$ at constant overpotential. Unfortunately, the data collected cannot easily be compared at constant overpotential because of anomalous shifts in the HER onset potential, which likely result from changes in the *iR* drop across different electrolyte compositions (Figure 5.8B). This issue can be circumvented because the *ratio* of products evolved is constant over the full range of overpotentials sampled (Figure 5.13). As a result, an equation which describes the ratio of ion currents will be potential independent. Depending on if the product determining step is Tafel or Heyrovsky the corresponding equation for the ratio of H_2 to D_2 products is given by either eq 5.12 or 13. Applying the steady state for hydrogen adsorption described by eq 5.5, eqs 5.12 and 5.13 relate the concentrations of H^+ and D^+ in solution with the H_2 to D_2 product ratio. In both of eqs 5.12 and 5.13, the ratio of I_{H2} and I_{D2} is predicted to have a parabolic relationship with the ratio of proton and deuteron concentrations in solution.

$$\frac{I_{H_2}}{I_{D_2}} = \frac{k_{H_2}}{k_{D_2}} \times \frac{\theta_H{}^2}{\theta_D{}^2} = K^2 \frac{k_{H_2}}{k_{D_2}} \times \frac{[H^+]^2}{[D^+]^2} \quad \text{Tafel} \quad (5.12)$$

$$\frac{I_{H_2}}{I_{D_2}} = \frac{k_{H_2}}{k_{D_2}} \times \frac{\theta_H[H^+]}{\theta_D[D^+]} = K \frac{k_{H_2}}{k_{D_2}} \times \frac{[H^+]^2}{[D^+]^2} \quad \text{Heyrovsky} \quad (5.13)$$

Fitting either eq 5.12 or 5.13 as a parabola gives a fit parameter equal to the product of all equilibrium and kinetic solvent isotope effects in the reaction mechanism. We refer to this composite isotope effect as the H_2 to D_2 product solvent isotope effect, or PSIE. Application of this analysis to data collected in purified and as received D_2O

electrolytes gives good fits (Figure 5.15A), where the fit parameter, or PSIE, is 50 ± 3 for as received D_2O and 73 ± 2 for purified D_2O electrolytes. Data collected in nearly 100 atom % H electrolytes was excluded from the fits since error in the quantification of atom % H greatly skews the measured ratio of protons to deuterons.

$$\frac{I_{H_2}}{I_{HD}} = \frac{k_{H_2}}{k_{HD}} \times \frac{{\theta_H}^2}{\theta_H \theta_D} = K^2 \frac{k_{H_2}}{k_{HD}} \times \frac{[H^+]}{[D^+]} \qquad \text{Tafel} \qquad (5.14)$$

$$\frac{I_{H_2}}{I_{HD}} = \frac{k_{H_2} \theta_H [H^+]}{(k_{HD} \theta_H [D^+] + k_{DH} \theta_D [H^+])} = \frac{k_{H_2}}{k_{HD} + k_{DH} K} \times \frac{[H^+]}{[D^+]} \qquad \text{Heyrovsky} \qquad (5.15)$$

A similar analysis can be applied to the product solvent isotope effect on the ratio of H_2 and HD ion currents ($PSIE_{HD}$) using eqs 5.14 and 5.15. Unlike eqs 5.12 and 5.13, here the ion current ratio is related linearly to the ratio of proton and deuteron concentrations in solution. Fits of these data are shown in Figure 5.15B, where the slope, or PSIE is 3.3 ± 0.1 for as received D_2O and 6.0 ± 0.2 for purified D_2O electrolytes. The significant differences in PSIE and $PSIE_{HD}$ values for as received and purified D_2O electrolytes further emphasizes the importance of using ultrapure electrolytes for isotope effect studies (Table 5.1).

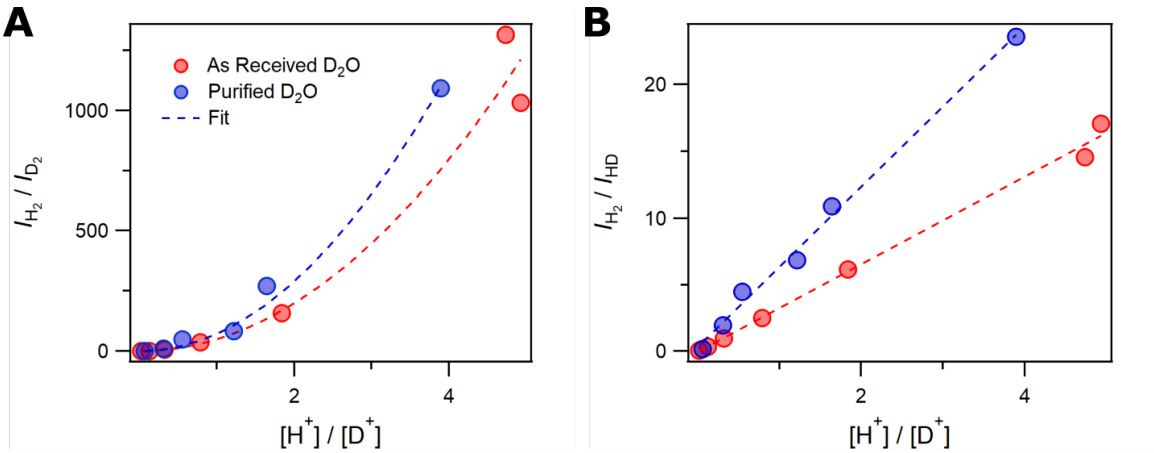

Figure 5.15. (**A**) Plot of either eq 5.12 or 5.13 with the corresponding parabolic fits. (**B**) Plot of either eq 5.14 or 5.15 with the corresponding linear fits.

The H_2 to D_2 PSIE is significantly larger than previous measurements of the KSIE for HER at pc-Au electrodes by cyclic voltammetry. These studies found the KSIE to be between 3-5 under acidic conditions.[18,47,48] This KSIE is associated with the rate-

limiting step and any ESIEs for prior steps. The identity of the rate-limiting step (RLS) for HER at pc-Au has been the subject of some debate.[37,47,49] The *potential* determining step for HER on pc-Au is clearly the Volmer reaction as multiple studies have calculated hydrogen adsorption to the surface to be well cathodic of RHE.[50,51] The potential and rate determining steps are often, but not always, the same.[52]

Under the assumption of a minimal model for HER (eqs 5.1–5.3) the KSIE measured by CV should only differ from the PSIE if the Volmer step is the RLS. This is because if either the Tafel or Heyrovsky steps are the RLS, the measured isotope effect would include the KSIE for the product evolution step multiplied by the ESIE for the previous Volmer step. In eqs 5.12 and 5.13 the steady state *K* term is the KSIE for the Volmer step. Therefore, if eq 5.12 is operative the KSIE for the Tafel step would be calculated to as the PSIE (~73) divided by the square of the quasi *K* or KSIE (between 3-5), or ≥3. If eq 5.13 is operative the KSIE for the Heyrovsky step would be calculated to as the PSIE divided by the quasi *K*, or ≥15. It is important to emphasize that these predicted KSIEs are only valid if a minimal model for HER can be assumed. Any mechanism involving more than two steps, as has been discussed by at least one previous work,[37] would lead to a different interpretation. Furthermore, comparison of these PSIEs to previous works is slightly complicated by possible differences in the transfer efficiencies of H_2, HD, and D_2 which were not calibrated for in this study.

Table 5.1. Compilation of Product Solvent Isotope Effects

Electrolyte	PSIE	$PSIE_{HD}$	*S*
As-Prepared D_2O	50 ± 3	3.3 ± 0.1	6.9 ± 0.5
Purified D_2O	73 ± 2	6.0 ± 0.2	9.0 ± 1.7

The PSIE data rest on the calibration of the H_2, HD, and D_2 mass spectral responses. To test this concern, the measured PSIE can be compared with available

data on the product solvent isotope effect for HER on pc-Au surfaces. Although this topic has not received much attention in the past few decades, significant effort was put towards the measurement of such product solvent isotope effects more than 50 years ago.[17,53-56] These were denoted as 'separation factors' (*S*) and were defined as the ratio of hydrogen to deuterium in the gaseous products versus the ratio of protons to deuterons in solution (eq 5.16).

$$S = \frac{2I_{H_2} + I_{HD}}{2I_{D_2} + I_{HD}} \times \frac{[D^+]}{[H^+]} \tag{5.16}$$

While most studies of separation factors did not include direct quantification of products, Heitbaum and co-workers explored this effect with electrochemical mass spectrometry on a sputtered gold electrode in a pioneering work.[46] In contrast to the studies reported here, these data do not have the time-resolution on the CV timescale and so experiments were done with chronoamperometry and less well-defined mass transport conditions. Additionally, electrolytes used were not ultrapure. Nevertheless, this study provides a useful comparison, as the authors report a separation factor of 5.2 ± 0.4.[46] Converting the data shown above into separation factors (Figure 5.16), it is found that S = 6.9 ± 0.5 for as received D_2O and S = 9.0 ± 1.7 for purified D_2O (Table 5.1). These values are both higher than that reported by Heitbaum suggesting either that the as-received D_2O used in their study was of a lower chemical purity, or that issues with the calibration in these studies have inflated the values measured above. Considering that the separation factor trends roughly with the square root of the PSIE, we estimate that even if $S \approx 5$ the PSIE would be significantly larger than previously reported values of the KSIE for HER at pc-Au electrodes (3-5). Therefore, we conclude that a significant KSIE exists for the kinetically invisible second step of HER at pc-Au electrodes within a minimal kinetic model. Further work is necessary to determine the nature of this kinetic step.

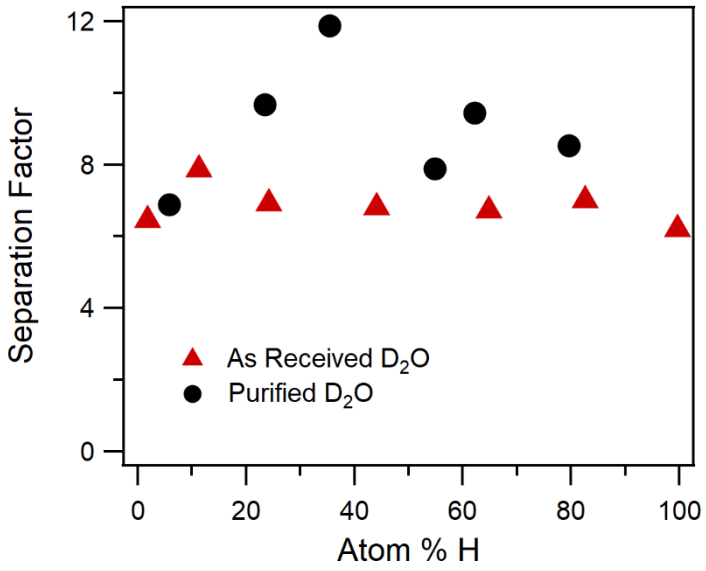

Figure 5.16. Separation factors for studies using as received D_2O to prepare electrolytes and purified D_2O to prepare electrolytes.

5.5 Conclusions

The hydrogen evolution reaction remains a fertile area of study, and it is of increasing importance as society moves towards a less carbon-intensive energy system. In this chapter, we explore several fundamental aspects of this process through isotope effect studies. Central to novelty of this work is a new method for preparing D_2O suitable for electrochemistry of highly sensitive single crystal electrodes. The development of this process enabled new insights into the hydrogen and hydroxide adsorption processes on platinum single crystals. Interestingly, no ESIE is observed for underpotential deposition of hydrogen while that of hydroxide shows a significant isotope effect. This result is true across a range of platinum single crystal surfaces which include (111) terraces, (110) steps, and (100) steps.

The product solvent isotope effect of HER at a pc-Au electrode in 0.1 M $HClO_4$ was then explored to investigate mechanistic steps which might otherwise be kinetically invisible. Quantification of products used a homemade DEMS, which provided *operando* detection of H_2, HD, and D_2 products formed during CV studies. Voltammetry was performed across a range of electrolyte isotopic compositions. The

resulting dataset was then utilized to quantify the product solvent isotope effect for HER on pc-Au with as received and purified D_2O electrolytes. The measured PSIEs were found to be significantly larger than previous measurements of the KSIE, suggesting large isotope effects in steps other than the rate-limiting one. Further experimental and computational studies will work to elucidate the origin of this effect.

5.6 References

1. Frumkin, A. N.; Bagotskii, V. S.; Iofa, Z.; Kobanov, B. *Kinetics of Electrode Processes*; Moscow, USSR, 1967; pp 194-306.
2. Conway, B. E.; Tilak, B. V., Interfacial processes involving electrocatalytic evolution and oxidation of H_{het}, and the role of chemisorbed H. *Electrochim. Acta* **2002,** *47* (22), 3571-3594.
3. Marković, N. M.; Ross, P. N., Surface science studies of model fuel cell electrocatalysts. *Surf. Sci. Rep.* **2002,** *45* (4), 117-229.
4. Climent, V.; Feliu, J. M., Thirty years of platinum single crystal electrochemistry. *J. Solid State Electrochem.* **2011,** *15* (7), 1297.
5. Clavilier, J.; Faure, R.; Guinet, G.; Durand, R., Preparation of monocrystalline Pt microelectrodes and electrochemical study of the plane surfaces cut in the direction of the {111} and {110} planes. *J. Electroanal. Chem. Interfacial Electrochem.* **1980,** *107* (1), 205-209.
6. Monteiro, M. C. O.; Koper, M. T. M., Alumina contamination through polishing and its effect on hydrogen evolution on gold electrodes. *Electrochim. Acta* **2019,** *325*, 134915.
7. Ledezma-Yanez, I.; Wallace, W. D. Z.; Sebastián-Pascual, P.; Climent, V.; Feliu, J. M.; Koper, M. T. M., Interfacial water reorganization as a pH-dependent descriptor of the hydrogen evolution rate on platinum electrodes. *Nat. Energy* **2017,** *2* (4), 17031.
8. McCrum, I. T.; Koper, M. T. M., The Role of Adsorbed Hydroxide in Hydrogen Evolution Reaction Kinetics on Modified Platinum. *Nat. Energy* **2020,** *5* (11), 891-899.
9. Mariano, R. G.; Kang, M.; Wahab, O. J.; McPherson, I. J.; Rabinowitz, J. A.; Unwin, P. R.; Kanan, M. W., Microstructural origin of locally enhanced CO2 electroreduction activity on gold. *Nature Materials* **2021,** *20* (7), 1000-1006.
10. Zeradjanin, A. R.; Grote, J.-P.; Polymeros, G.; Mayrhofer, K. J. J., A Critical Review on Hydrogen Evolution Electrocatalysis: Re-exploring the Volcano-relationship. *Electroanalysis* **2016,** *28* (10), 2256-2269.
11. Klein, F. S., Isotope Effects in Chemical Kinetics. *Annu. Rev. Phys. Chem.* **1975,** *26* (1), 191-210.
12. Thornton, E. R., Physical Organic Chemistry. *Annu. Rev. Phys. Chem.* **1966,** *17* (1), 349-372.
13. Costentin, C., Electrochemical Approach to the Mechanistic Study of Proton-Coupled Electron Transfer. *Chem. Rev.* **2008,** *108* (7), 2145-2179.
14. Costentin, C.; Robert, M.; Savéant, J.-M., Update 1 of: Electrochemical Approach to the Mechanistic Study of Proton-Coupled Electron Transfer. *Chem. Rev.* **2010,** *110* (12), PR1-PR40.
15. Dempsey, J. L.; Winkler, J. R.; Gray, H. B., Proton-Coupled Electron Flow in Protein Redox Machines. *Chem. Rev.* **2010,** *110* (12), 7024-7039.
16. Horiuti, J.; Okamoto, G., The Mechanism of the Hydrogen Electrode Process. I. The Catalytic Mechanism. *Bull. Chem. Soc. Jpn.* **1938,** *13* (1), 216-227.
17. Conway, B. E.; Steacie, E. W. R., The electrolytic hydrogen–deuterium separation factor and reaction mechanism. *Proceedings of the Royal Society of London. Series A. Mathematical and Physical Sciences* **1958,** *247* (1250), 400-419.
18. Conway, B. E.; Steacie, E. W. R., Kinetics of electrolytic hydrogen and deuterium evolution. *Proceedings of the Royal Society of London. Series A. Mathematical and Physical Sciences* **1960,** *256* (1284), 128-144.
19. Xu, J.; Huang, W.; McCreery, R. L., Isotope and surface preparation effects on alkaline dioxygen reduction at carbon electrodes. *J. Electroanal. Chem.* **1996,** *410* (2), 235-242.
20. Tse, E. C. M.; Hoang, T. T. H.; Varnell, J. A.; Gewirth, A. A., Observation of an Inverse Kinetic Isotope Effect in Oxygen Evolution Electrochemistry. *ACS Catal.* **2016,** *6* (9), 5706-5714.
21. Sakaushi, K.; Kumeda, T.; Hammes-Schiffer, S.; Melander, M. M.; Sugino, O., Advances and challenges for experiment and theory for multi-electron multi-proton transfer at electrified solid–liquid interfaces. *PCCP* **2020,** *22* (35), 19401-19442.
22. Conway, B. E.; Angerstein-Kozlowska, H.; Sharp, W. B. A.; Criddle, E. E., Ultrapurification of water for electrochemical and surface chemical work by catalytic pyrodistillation. *Anal. Chem.* **1973,** *45* (8), 1331-1336.
23. Hetland, E., Electrolytic Conductivity of NaOH in H_2O and of NaOD in D_2O at 25°. A Vacuum Distilling Apparatus for Deuterium Oxide. *J. Am. Chem. Soc.* **1946,** *68* (12), 2532-2535.

24. Sakaushi, K., Observation of kinetic isotope effect in electrocatalysis with fully deuterated ultrapure electrolytes. *J. Electroanal. Chem.* **2019,** *849*, 113372.
25. ASTM D1193-99e1 *Standard Specification for Reagent Water*; ASTM International: West Conshohocken, PA, 1999.
26. PB1032ENUS Ver. 2.0. KGaA, M., Ed. Darmstadt, Germany, 2020.
27. Amarego, W. L. F.; Perrin, D. D., Purification of Inorganic and Metal-Organic Chemicals. In *Purification of Laboratory Chemicals*, 4th ed.; 1996.
28. Ojha, K.; Arulmozhi, N.; Aranzales, D.; Koper, M. T. M., Double Layer at the Pt(111)–Aqueous Electrolyte Interface: Potential of Zero Charge and Anomalous Gouy–Chapman Screening. *Angew. Chem. Int. Ed.* **2020,** *59* (2), 711-715.
29. Gold, V.; Lowe, B. M., Behaviour of hydrogen electrode in H_2O + D-$_2$O mixtures. *Trans. Faraday Soc.* **1969,** *65* (0), 3037-3041.
30. Lam, Y.-C.; Soudackov, A. V.; Hammes-Schiffer, S., Kinetics of Proton Discharge on Metal Electrodes: Effects of Vibrational Nonadiabaticity and Solvent Dynamics. *The Journal of Physical Chemistry Letters* **2019,** *10* (18), 5312-5317.
31. Rebollar, L.; Intikhab, S.; Snyder, J. D.; Tang, M. H., Kinetic Isotope Effects Quantify pH-Sensitive Water Dynamics at the Pt Electrode Interface. *The Journal of Physical Chemistry Letters* **2020,** *11* (6), 2308-2313.
32. Bockris, J. O. M., A Hydrogen Economy. *Science* **1972,** *176* (4041), 1323-1323.
33. Dubouis, N.; Grimaud, A., The hydrogen evolution reaction: from material to interfacial descriptors. *Chem. Sci.* **2019,** *10* (40), 9165-9181.
34. Conway, B. E.; Tessier, D. F.; Wilkinson, D. P., Kinetic behaviour of electrochemical proton discharge in relation to the proton source and its environment. *J. Electroanal. Chem. Interfacial Electrochem.* **1986,** *204* (1), 111-130.
35. Pentland, N.; Bockris, J. O. M.; Sheldon, E., Hydrogen Evolution Reaction on Copper, Gold, Molybdenum, Palladium, Rhodium, and Iron. *J. Electrochem. Soc.* **1957,** *104* (3), 182.
36. Durst, J.; Simon, C.; Hasché, F.; Gasteiger, H. A., Hydrogen Oxidation and Evolution Reaction Kinetics on Carbon Supported Pt, Ir, Rh, and Pd Electrocatalysts in Acidic Media. *J. Electrochem. Soc.* **2014,** *162* (1), F190-F203.
37. Kahyarian, A.; Brown, B.; Nesic, S., Mechanism of the Hydrogen Evolution Reaction in Mildly Acidic Environments on Gold. *J. Electrochem. Soc.* **2017,** *164* (6), H365-H374.
38. Haghighat, S.; Dawlaty, J. M., pH Dependence of the Electron-Transfer Coefficient: Comparing a Model to Experiment for Hydrogen Evolution Reaction. *The Journal of Physical Chemistry C* **2016,** *120* (50), 28489-28496.
39. Jackson, M. N.; Jung, O.; Lamotte, H. C.; Surendranath, Y., Donor-Dependent Promotion of Interfacial Proton-Coupled Electron Transfer in Aqueous Electrocatalysis. *ACS Catal.* **2019,** *9* (4), 3737-3743.
40. Lam, Y.-C.; Soudackov, A. V.; Hammes-Schiffer, S., Theory of Electrochemical Proton-Coupled Electron Transfer in Diabatic Vibronic Representation: Application to Proton Discharge on Metal Electrodes in Alkaline Solution. *The Journal of Physical Chemistry C* **2020,** *124* (50), 27309-27322.
41. Baltruschat, H., Differential electrochemical mass spectrometry. *J. Am. Soc. Mass. Spectrom.* **2004,** *15* (12), 1693-1706.
42. Bondue, C. J.; Koper, M. T. M., A DEMS approach for the direct detection of CO formed during electrochemical CO_2 reduction. *J. Electroanal. Chem.* **2020,** *875*, 113842.
43. Wang, H.; Alden, L.; DiSalvo, F. J.; Abruña, H. D., Electrocatalytic mechanism and kinetics of SOMs oxidation on ordered PtPb and PtBi intermetallic compounds: DEMS and FTIRS study. *PCCP* **2008,** *10* (25), 3739-3751.
44. Meija, J.; Mester, Z.; D'Ulivo, A., Mass Spectrometric Separation and Quantitation of Overlapping Isotopologues. H_2O/HOD/D_2O and H_2Se/HDSe/D_2Se Mixtures. *J. Am. Soc. Mass. Spectrom.* **2006,** *17* (7), 1028-1036.
45. Kaye, G. W. C.; Laby, T. H., *Tables of Physical and Chemical Constants*. 15th ed.; Longman: NY, 1986.
46. Kretschmer, J.; Heitbaum, J., An e.m.s. study of the cathodic H/D separation factor at gold electrodes in sulfuric acid. *J. Electroanal. Chem. Interfacial Electrochem.* **1979,** *97* (2), 211-218.

47. Sakaushi, K., Quantum proton tunneling in multi-electron/-proton transfer electrode processes. *Faraday Discuss.* **2020,** *221* (0), 428-448.
48. Kopple, K.; Meyerstein, D.; Meisel, D., Mechanism of the catalytic hydrogen production by gold sols. Hydrogen/deuterium isotope effect studies. *The Journal of Physical Chemistry* **1980,** *84* (8), 870-875.
49. Kuhn, A. T.; Byrne, M., The hydrogen- and deuterium-evolution reactions on gold in acid solutions. *Electrochim. Acta* **1971,** *16* (3), 391-399.
50. Santos, E.; Quaino, P.; Schmickler, W., Theory of electrocatalysis: hydrogen evolution and more. *PCCP* **2012,** *14* (32), 11224-11233.
51. Lindgren, P.; Kastlunger, G.; Peterson, A. A., A Challenge to the $G \sim 0$ Interpretation of Hydrogen Evolution. *ACS Catal.* **2020,** *10* (1), 121-128.
52. Koper, M. T. M., Analysis of electrocatalytic reaction schemes: distinction between rate-determining and potential-determining steps. *J. Solid State Electrochem.* **2013,** *17* (2), 339-344.
53. Bockris, J. O. M.; Koch, D. F. A., COMPARATIVE RATES OF THE ELECTROLYTIC EVOLUTION OF HYDROGEN AND DEUTERIUM ON IRON, TUNGSTEN AND PLATINUM. *The Journal of Physical Chemistry* **1961,** *65* (11), 1941-1948.
54. Rowland, P. R., Electrolytic Separation Factor of Protium and Deuterium. *Nature* **1968,** *218* (5145), 945-946.
55. Lewis, G. P.; Ruetschi, P., THE DEPENDENCE OF THE ELECTROLYTIC HYDROGEN-DEUTERIUM SEPARATION FACTOR ON THE ELECTRODE POTENTIAL. *The Journal of Physical Chemistry* **1962,** *66* (8), 1487-1492.
56. Enyo, M., Change of mechanism of the hydrogen electrode reaction with overpotential—III. Potential dependence of the deuterium separation factor on Pt, Au and Ni cathodes. *Electrochim. Acta* **1976,** *21* (1), 15-20.

Appendix A Supplementary Information for Chapter 1

Adapted from the supporting information for Agarwal, R. G.; Coste, S. C.; Groff, B. D.; Heuer, A. M.; Noh, H. N.; Parada, G. P.; Wise, C. W.; Nichols, E. N.; Warren, J. J.; Mayer, J. M. "Free Energies of Proton-Coupled Electron Transfer and Their Applications." *Chem. Rev. Accepted*.

A.1 General Considerations

Reagents were purchased from Sigma-Aldrich or Alfa Aesar. TEMPO• and 4-oxo-TEMPO• were sublimated under vacuum prior to use. TEMPO-H was prepared as reported previously.[1] Hexanes (mixture of isomers, HPLC grade) were purchased from Sigma-Aldrich and dispensed from an Argon-atmosphere solvent system with alumina drying columns. All reactions were performed in a nitrogen-filled glovebox (working O_2 level < 5 ppm). UV–Vis spectra were collected on an Agilent Cary 60 UV–Vis or Agilent Cary 5000 UV–Vis–NIR spectrophotometer inside of a nitrogen-filled glovebox.

A.2 UV-Vis characterization of 4-oxo-TEMPO• and TEMPO•

A.2.1 UV–Vis spectra of pure reagents

Individual UV–Vis spectra were taken of 4-oxo-TEMPO• (oxo•, λ_{max}= 459 nm), TEMPO• (λ_{max}= 473 nm), and TEMPO-H in hexane. The spectra were normalized to a concentration of 40 mM and are shown overlaid in Figure A1. TEMPO-H displayed a negligible UV–Vis trace, confirming it was free from TEMPO• contamination.

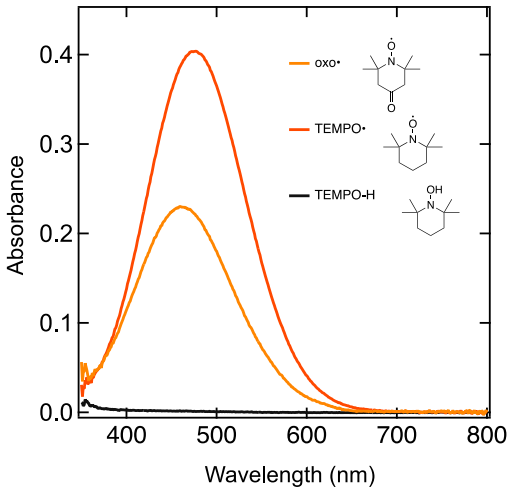

Figure A1. UV–Vis spectra of 40 mM oxo•, TEMPO•, and TEMPO-H in hexane.

A.2.2 Molar absorptivities (ε) of 4-oxo-TEMPO• and TEMPO•

Beer's law plots were constructed for oxo• (Figure A2a) and TEMPO• (Figure A2b) in hexane. The molar absorptivities were determined to be ε_{459nm} = 5.86 M^{-1} cm^{-1} and ε_{473nm} = 10.27 M^{-1} cm^{-1} for oxo• and TEMPO•, respectively. These values were in good agreement with the experimental values for $\varepsilon_{\lambda max}$ when ε was calculated at each wavelength (Figure A2c).

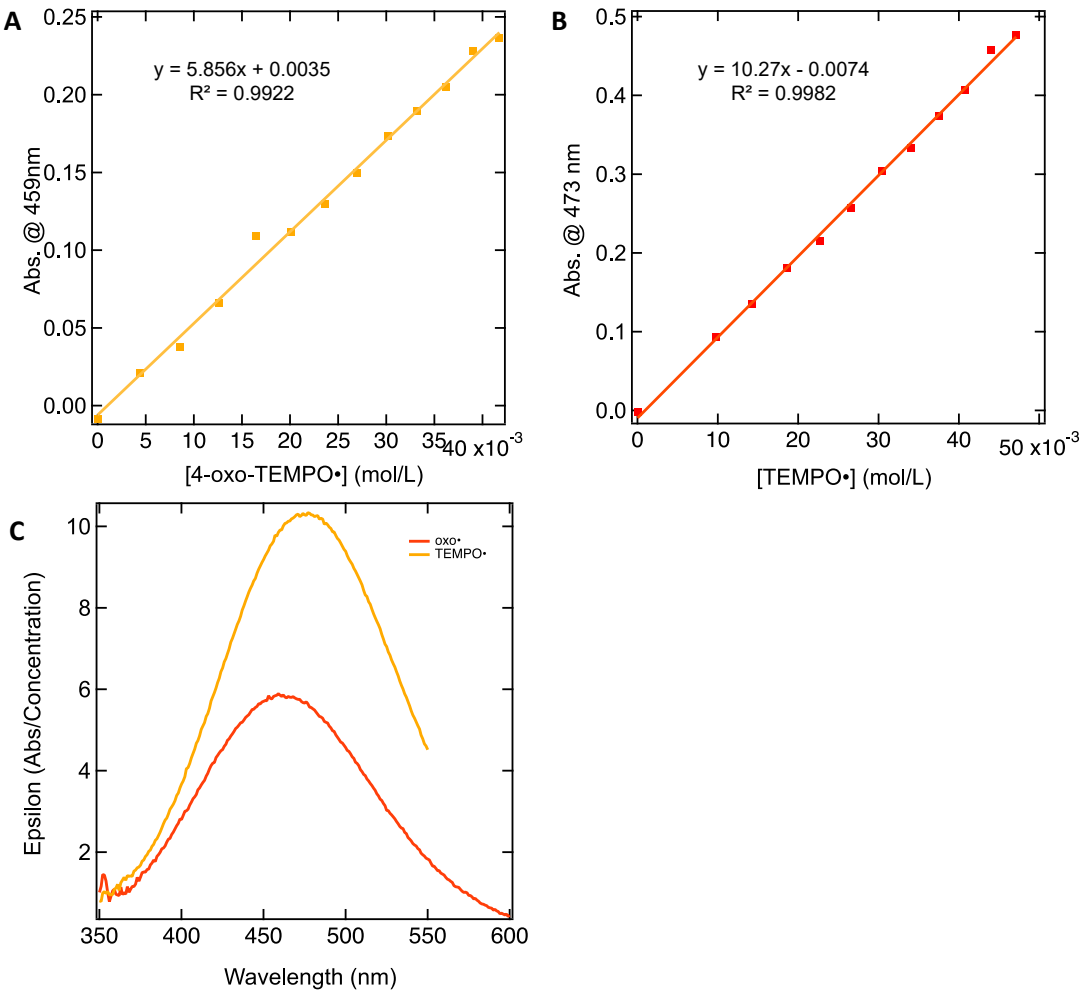

Figure A2. Concentration was plotted against absorbance at the λ_{max} for (**A**) oxo• and (**B**) TEMPO• in hexane. The slope of the resulting line is equal to $\varepsilon_{\lambda max}$ for each species. (**C**) The absorbance at each wavelength was divided by concentration of the sample to provide the epsilon at each wavelength.

A.3 UV–Vis Equilibration

Scheme A1. Reaction between TEMPO-H and oxo•. K_{eq} of this reaction is directly related to the relative bond strength of TEMPO-H and oxo-H.

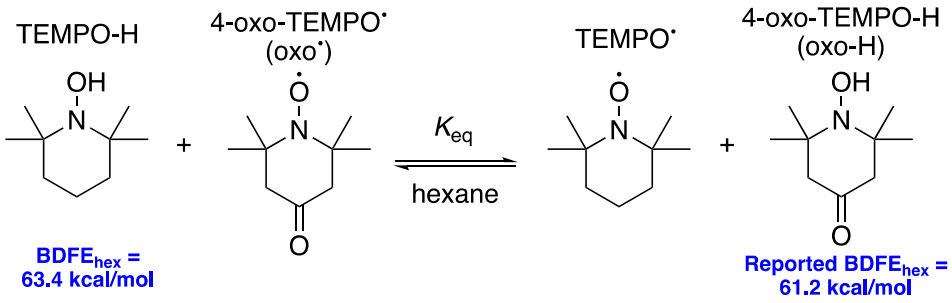

The pseudo-self exchange reaction between 4-oxo-TEMPO• (oxo•) and TEMPO-H (Scheme A1) was analyzed to determine the bond dissociation free energy (BDFE) of 4-oxo-TEMPO-H (oxo-H) in hexanes. The equilibrium constant for this reaction, K_{eq}, gives the free energy of the reaction, $\Delta G°$. This free energy relates the BDFEs of the H-atom donor, TEMPO-H, and the H-atom receptor, oxo• (eq A1). Utilizing the known TEMPO-H BDFE$_{hexane}$[2] = 63.4 kcal mol^{-1}, we were able to calculate the BDFE of oxo-H.

$$X–H + Y \rightarrow X + Y–H \qquad \Delta G° = BDFE(XH) – BDFE(YH) \qquad (A1)$$

A range of experimental initial concentrations were chosen for the equilibration reaction, ranging from 1:0.33 – 1:1.2 oxo•:TEMPO-H (Table A1). A 2mL solution of 30 mM oxo• in hexanes was prepared in a quartz cuvette equipped with a stir bar. TEMPO-H stock solution in hexane (0.1933 M) was titrated incrementally across the range of oxo•:TEMPO-H molar ratios. After each TEMPO-H addition, the reaction was equilibrated with stirring for 20 min until the UV–Vis trace was constant. Sequential addition of TEMPO-H stock solution and subsequent equilibration resulted in seven experimental equilibrations with UV–Vis spectra shown in Figure A3. Addition of TEMPO-H resulted in a slight red shift in λ_{max} and an increase in absorbance as more TEMPO• was formed at equilibrium.

Table A1. Experimental setup for seven equilibration reactions between oxo • and TEMPO-H.[a]

Sample	oxo• equiv.	TEMPOH equiv.	mmol oxo•	mmol TEMPOH	Total volume (mL)	$[oxo^{\bullet}]_i$ (mol/L)	$[TEMPOH]_i$ (mol/L)
A	1.0	0.33	0.060	0.020	2.103	0.0285	0.0095
B	1.0	0.50	0.060	0.030	2.289	0.0262	0.0131
C	1.0	0.63	0.060	0.038	2.328	0.0258	0.0161
D	1.0	0.71	0.060	0.043	2.356	0.0255	0.0182
E	1.0	0.83	0.060	0.050	2.393	0.0251	0.0209
F	1.0	1.0	0.060	0.060	2.444	0.0245	0.0245
G	1.0	1.2	0.060	0.072	2.506	0.0239	0.0287

[a] A solution of oxo• (0.817 mL, 0.0734 M) was reacted with increasing amounts of TEMPO-H stock solution and equilibrated for 20 min. $[oxo^{\bullet}]_i$ and $[TEMPO\text{-}H]_i$ are initial concentrations of these species in solution.

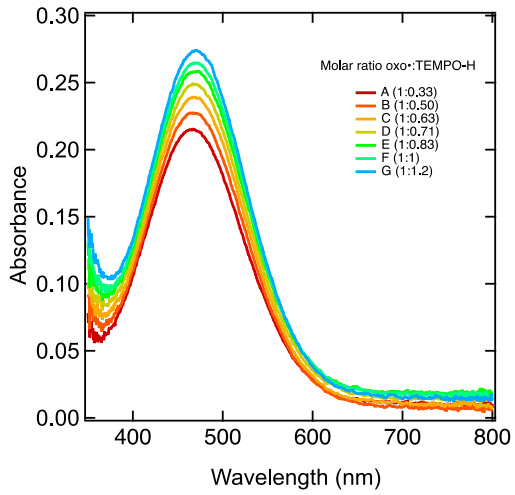

Figure A3. UV–Vis absorbances of oxo• + TEMPO-H reactions corrected against a hexane blank.

A4 Calculation of 4-oxo-TEMPO-H $BDFE_{hex}$

The concentrations of each species – oxo•, oxo-H, TEMPO•, and TEMPO-H – can be calculated at equilibrium using the total absorbance, the molar absorptivities of the two colored species (oxo• and TEMPO•), and the initial concentrations of oxo• and TEMPO-H. The total absorbance at each wavelength is the sum of the absorbance of each species (eq. A2). Mass balance dictates that the sum of the concentrations of related species (oxo• + oxo-H; TEMPO• + TEMPO-H) at equilibrium must be equal the

initial concentration of the related reactant species (eqs. A3 and A4). Additionally, the concentration of the products oxo-H and TEMPO• must be equivalent (eq. A5) in the absence of decomposition or side reactivity (of which none was observed by NMR or UV–Vis spectroscopies).

$$\mathrm{Abs}^{\lambda} = l(\varepsilon^{\lambda}_{\mathrm{TEMPO}\bullet}[\mathrm{TEMPO}^{\bullet}] + \varepsilon^{\lambda}_{\mathrm{oxo}\bullet}[\mathrm{oxo}\bullet]) \quad \text{(A2)}$$

$$[\mathrm{oxo}^{\bullet}]_{\mathrm{i}} = [\mathrm{oxo}^{\bullet}] + [\mathrm{oxo\text{-}H}] \quad \text{(A3)}$$

$$[\mathrm{TEMPO\text{-}H}]_{\mathrm{i}} = [\mathrm{TEMPO\text{-}H}] + [\mathrm{TEMPO}^{\bullet}] \quad \text{(A4)}$$

$$[\mathrm{oxo\text{-}H}] = [\mathrm{TEMPO}^{\bullet}] \quad \text{(A5)}$$

The system of equations above were solved for [oxo•] and [TEMPO•], resulting in equations A6 and A7.

$$[\mathrm{oxo}^{\bullet}] = \frac{(\mathrm{Abs}^{\lambda}/l) - \varepsilon^{\lambda}_{\mathrm{TEMPO}\bullet}[\mathrm{oxo}\bullet]_{\mathrm{i}})}{\varepsilon^{\lambda}_{\mathrm{oxo}\bullet} - \varepsilon^{\lambda}_{\mathrm{TEMPO}\bullet}} \quad \text{(A6)}$$

$$[\mathrm{TEMPO}^{\bullet}] = \frac{(\mathrm{Abs}^{\lambda}/l) - \varepsilon^{\lambda}_{\mathrm{oxo}\bullet}[\mathrm{oxo}^{\bullet}]}{\varepsilon^{\lambda}_{\mathrm{TEMPO}\bullet}} \quad \text{(A7)}$$

For each sample A-G, the concentrations of all species at equilibrium were calculated from the absorbance at each integer wavelength, $\varepsilon^{\lambda}_{\mathrm{TEMPO}\bullet}$ and $\varepsilon^{\lambda}_{\mathrm{oxo}\bullet}$. A range of 450-550 nm was chosen due to the relatively large difference in ε between the species within these values. Representative data from sample B is provided in Table A2. At each wavelength (and for each sample) K_{eq} was determined using the calculated concentrations of the species at equilibrium, yielding an average K_{eq} = 3.9 ± 2.0. This corresponds to $\Delta G°$= -0.8 ± 0.4. Utilizing the known BDFE_{hex} of TEMPO-H (63.4 kcal mol^{-1}), the BDFE_{hex} of oxo-H was calculated to be 64.2 ± 0.4 kcal mol^{-1} (eq A1).

Table A2. UV–Vis spectroscopy data and calculated concentrations of reaction species from wavelengths 550-450 nm.

Wavelength (nm)	$\varepsilon_{oxo\bullet}$	$\varepsilon_{TEMPO\bullet}$	Sample B, raw Abs data	Sample B, corrected Abs data
550	1.83	4.52	0.0765	0.0809
545	2.06	5.02	0.0858	0.0901
540	2.28	5.47	0.0945	0.0992
535	2.58	6.01	0.105	0.109
530	2.82	6.55	0.115	0.119
525	3.03	7.05	0.126	0.130
520	3.38	7.59	0.135	0.140
515	3.69	8.09	0.147	0.151
510	3.98	8.56	0.156	0.160
505	4.30	8.97	0.166	0.170
500	4.57	9.39	0.174	0.179
495	4.83	9.71	0.183	0.187
490	5.10	9.99	0.191	0.195
485	5.32	10.2	0.197	0.202
480	5.52	10.3	0.202	0.206
475	5.66	10.3	0.206	0.210
470	5.77	10.3	0.207	0.211
465	5.83	10.1	0.206	0.211
460	5.86	9.91	0.205	0.209
455	5.76	9.57	0.203	0.206
450	5.71	9.19	0.197	0.201

Sample B, calculated values				
[oxo•]	**[TEMPO•]**	**[oxo-H]**	**[TEMPO-H]**	K_{eq}
0.0167	0.0111	0.0111	0.00279	2.66
0.0168	0.0110	0.0110	0.00288	2.52
0.0167	0.0112	0.0112	0.00273	2.75
0.0170	0.0109	0.0109	0.00304	2.29
0.0169	0.0110	0.0110	0.00294	2.44
0.0164	0.0114	0.0114	0.00249	3.19
0.0170	0.0108	0.0108	0.00308	2.24
0.0168	0.0111	0.0111	0.00287	2.53
0.0170	0.0108	0.0108	0.00309	2.23

0.0171	0.0108	0.0108	0.00316	2.15
0.0170	0.0108	0.0108	0.00308	2.24
0.0171	0.0107	0.0107	0.00321	2.08
0.0170	0.0109	0.0109	0.00304	2.30
0.0169	0.0109	0.0109	0.00298	2.38
0.0168	0.0110	0.0110	0.00290	2.49
0.0165	0.0113	0.0113	0.00261	2.97
0.0167	0.0112	0.0112	0.00275	2.73
0.0166	0.0113	0.0113	0.00266	2.87
0.0164	0.0114	0.0114	0.00248	3.21
0.0159	0.0120	0.0120	0.00194	4.65
0.0157	0.0122	0.0122	0.00173	5.48

A5 References

1. Wu, A.; Masland, J.; Swartz, R. D.; Kaminsky, W.; Mayer, J. M., Synthesis and Characterization of Ruthenium Bis(β-diketonato) Pyridine-Imidazole Complexes for Hydrogen Atom Transfer. *Inorg. Chem.* **2007,** *46* (26), 11190-11201.
2. Malievskii, A. D.; Koroteev, S. V.; Shapiro, A. B., Kinetics and Thermodynamics of Hydrogen Atom Exchange Reactions in Sterically Hindered Hydroxylamine-Nitroxyl Radical Systems. *Kinet. Catal.* **2005,** *46* (6), 812-820.

Appendix B Supplementary Information for Chapter 2

Adapted from the supporting information for Wise, C. W.; Agarwal, R. G.; Mayer, J. M. "Determining Proton-Coupled Standard Potentials and X–H Bond Dissociation Free Energies in Nonaqueous Solvents using Open-Circuit Potential Measurements." *J. Am. Chem. Soc.* **2020**, *142*, 10681-10691.

B.1 General Considerations

B.1.1 Materials

Azobenzene (Sigma-Aldrich, 98%), phenazine (Sigma-Aldrich, 98%), 1,4-hydroquinone (Sigma-Aldrich, >99.5%), 2,6-di-*tert*-butyl-4-methoxyphenol (Sigma-Aldrich, 97%), 1,1-diphenyl-2-picrylhydrazine (TCI, > 98%), and 2,2-diphenyl-1-picrylhydrazyl (Sigma-Aldrich), 2,7-di-*tert*-butyl-1,4-naphthoquinone (Sigma-Aldrich), tetrabutylammonium hexafluorophosphate ($[Bu_4N][PF_6]$, Sigma-Aldrich, > 99%), tetrabutylammonium tetrafluoroborate ($[Bu_4N][BF_4]$, Acros, 98%), trifluoroacetic acid (Sigma-Aldrich, 99%), sodium trifluoroacetate (Sigma-Aldrich, 98%), tetrabutylammonium acetate (Sigma-Aldrich, 97%), tetrafluoroboric acid diethyl ether complex (Sigma-Aldrich, 50-55% w/w HBF_4), pyridine (Sigma-Aldrich, anhydrous, 99.8%), 2,6-lutidine (Sigma-Aldrich, 98%), triethylamine (Alfa Aesar, 99%), trifluoromethanesulfonic acid (Acros, 99%), were used as received. Acetonitrile (Burdick & Jackson, 99.9%) was sparged with argon and dispensed directly into a glove box. 2,4,6-tri-*tert*-butylphenol (2,4,6-$^tBu_3PhOH$, Sigma-Aldrich, 98%) and 1,8-dichloroanthraquinone (Sigma-Aldrich, 97%) were recrystallized from ethanol and a 1:1 mixture of chloroform and ethanol, respectively, prior to use. *N*,*N*'-dimethylformamide (DMF, Sigma-Aldrich, 99.8% anhydrous), diethyl ether (Sigma-Aldrich, 99.9%, inhibitor-free), and tetrahydrofuran (Sigma-Aldrich, >99.9%, inhibitor-free) were degassed with argon and dried using a Pure Process Technology solvent system and dispensed directly into a glove box. Both MeCN and THF measured less than 20 ppm H_2O by Karl-Fischer titration. Isopropanol (Fisher Chemical, 99.5%) was degassed with N_2 and dried over 3Å molecular sieves. 1,4-benzoquinone (Fluka,

99.5%), 2,6-dimethyl-1,4-benzoquinone (Sigma-Aldrich, 99%), 2,6-dimethoxy-1,4-benzoquinone (Alfa Aesar, 98%), 2,6-di-*tert*-butyl-1,4-benzoquinone (Sigma-Aldrich, 98%), 1,4-naphthoquinone (Sigma-Aldrich, 97%), and (2,2,6,6-tetramethylpiperidin-1-yl)oxyl (TEMPO$^{\bullet}$, Sigma-Aldrich, 98%) were sublimed before use.

1,2-diphenylhydrazine,[1] 5,10-dihydrophenazine,[2] 2,2,6,6-tetramethyl-1-hydroxypiperidine (TEMPOH),[3] 2,4,6-tri-*tert*-butylphenoxyl radical (2,4,6-^{t}Bu$_3$PhO$^{\bullet}$),[4] 4-methoxy-2,6-di-*tert*-butylphenoxyl radical (4-MeO-2,6-^{t}Bu$_2$PhO$^{\bullet}$),[5] iron(II) tris(2,2′-bi-imidazoline)diperchlorate ($Fe^{II}H_2bim$) and $[Fe^{III}(Hbim)(H_2bim)_2](ClO_4)_2$ (the oxidized and deprotonated form of $Fe^{II}H_2bim$),[6] tetrafluoroborate salts of pyridinium, lutidinium, and triethylammonium,[7] and [H$^+$-DMF]OTf [8] were prepared according to literature procedures.

Substituted hydroquinones (2,6-dimethyl-1,4-hydroquinone, 2,6-dimethoxy-1,4-hydroquinone, 2,6-di-*tert*-butyl-1,4-hydroquinone, 1,4-dihydroxynaphthalene, 2,7-di-*tert*-butyl-1,4-dihydroxynaphthalene, 1,8-dichloro-9,10-dihydroxyanthracene) were prepared by a modified literature procedure.[9] The corresponding quinone was dissolved in THF, and an aqueous solution of equal volume containing 10-fold excess sodium dithionite (with respect to quinone) was added. The resulting solution was stirred for 10-15 minutes, or until the yellow color had disappeared, indicating complete reduction of the quinone. The hydroquinone product was extracted with diethyl ether, dried with $MgSO_4$, and filtered. Solvent was removed in vacuo, leaving off-white solid products. The identity and purity of the hydroquinones was confirmed by ^{1}H NMR spectroscopy.

B.1.2 Instrumentation

Electrochemical measurements were performed with CH Instruments potentiostats (models 600D/650D) using a 3 mm glassy carbon working electrode, a platinum wire auxiliary electrode, and a Ag wire pseudo-reference electrode. To prepare the reference electrode, 0.1 M $[Bu_4N][PF_6]$ in MeCN or THF was added to a

jacketed compartment (separated from solution with a glass frit) and allowed to equilibrate for 24 hours prior to use. A silver wire roughened with 600 grit sand paper was then immersed in the jacketed compartment. Glassy carbon working electrodes were polished for 30-60 seconds using 0.05 μm alumina and then rinsed with DI water and dried before every measurement. For cyclic voltammetry measurements, the potential was compensated for the internal resistance of the cell, and ferrocene was added as an internal reference. Measurements of the hydrogen standard potential in THF were performed with a Pt wire working electrode that had been cleaned in aqua regia for 5-10 seconds, annealed in a hydrogen flame, and stored under a H_2 atmosphere prior to use.

CAUTION: Aqua regia, a roughly 1:3 mixture of concentrated nitric acid and hydrochloric acid, is highly corrosive and oxidizing. It should be handled with great care, in small quantities, using specialized acid and oxidant-gloves that extend well beyond the wrist. Readers should consult one of the many Standard Operating Procedures (SOPs) available for aqua regia on the web. Our SOP can be found at: *ehs.yale.edu › sites › default › files › files › aqua-regia-sop.*

All ^{1}H NMR spectra were collected on Agilent 400 MHz or 500 MHz spectrometers and referenced to proteo solvent impurities.[10]

B.2 Open Circuit Potential Measurements of PCET Substrates

The substrates examined and their abbreviations are shown in Figure B1. For each substrate, open-circuit potential measurements were collected at several ratios of the oxidized:reduced form ($X:XH_n$), typically ranging between 0.4:1 and 2.5:1. Figure B2-B23(A) are representative OCP vs time plots for each substrate at a 1:1 ratio of $X:XH_n$. Note that the y-axes of these plots span only ± 3 mV from the average potential. OCP values at the various substrate ratios were averaged over 5-10 minutes, referenced to a hydrogen scale, and plotted against $\log([XH_n]/[X])$ (Figure B2-B23

(B)). The error bars in these figures represent one standard deviation from the OCP vs time traces at each $X:XH_n$ ratio. See Section B.3 for a more detailed discussion of error analysis.

Per the Nernst equation, a linear relationship between OCP and $\log([XH_n]/[X])$ is expected, and the slope of the line should reflect the number of electrons transferred (n) during the redox process. For $n = 1$, the expected slope is 59.2 mV, and for $n = 2$, the expected slope is 29.6 mV. The y-intercept of the line is the standard potential vs H_2 for the PCET reduction of the substrate. As shown here, we recommend extracting standard potentials from the intercept of OCP vs $\log([XH_n]/[X])$ lines rather than from point measurements at a 1:1 $X:XH_n$ ratio.

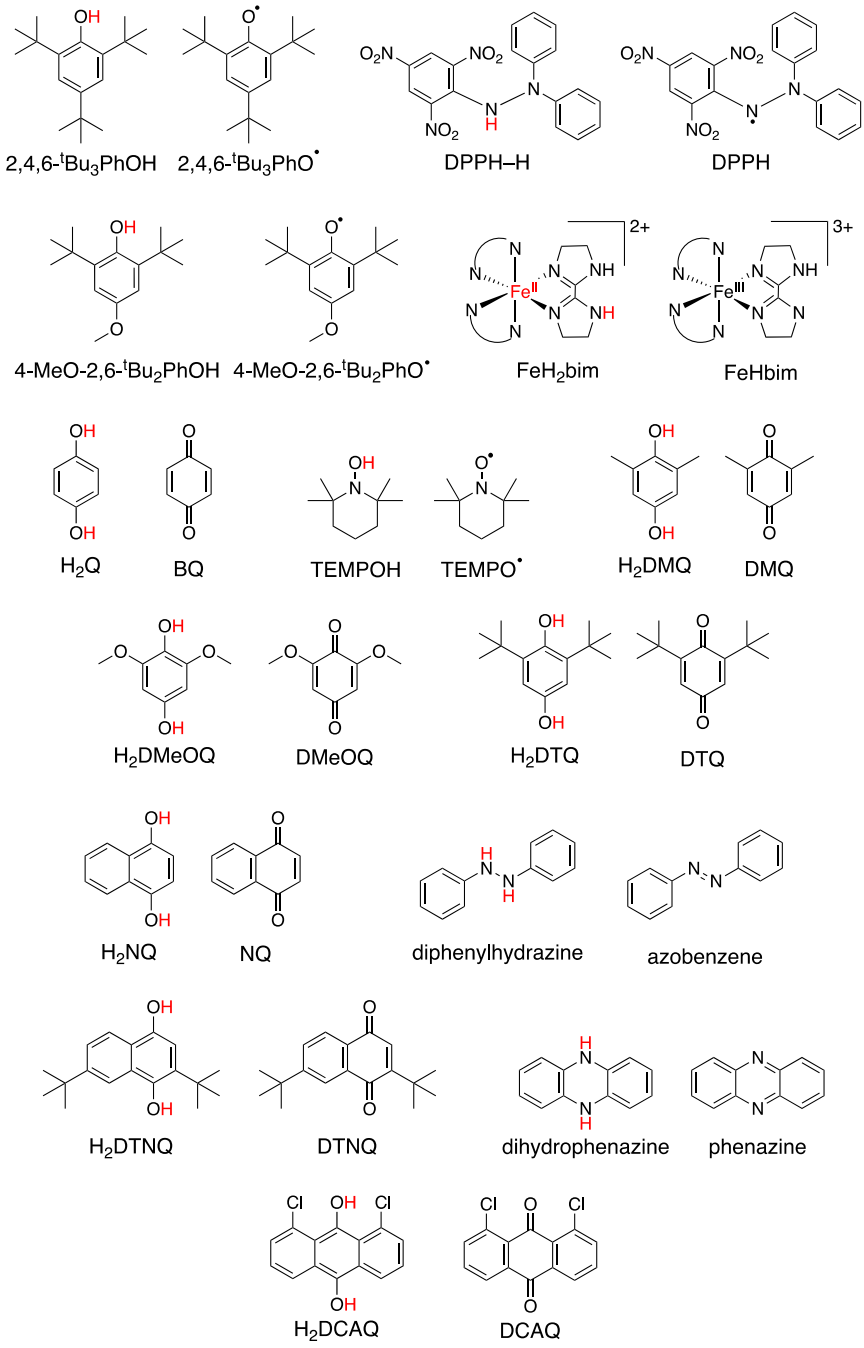

Figure B1. Structures of all substrates examined, with names or abbreviations listed below. Relevant H atom(s) shown in red.

B.2.1 OCP Data for PCET Reagents in MeCN

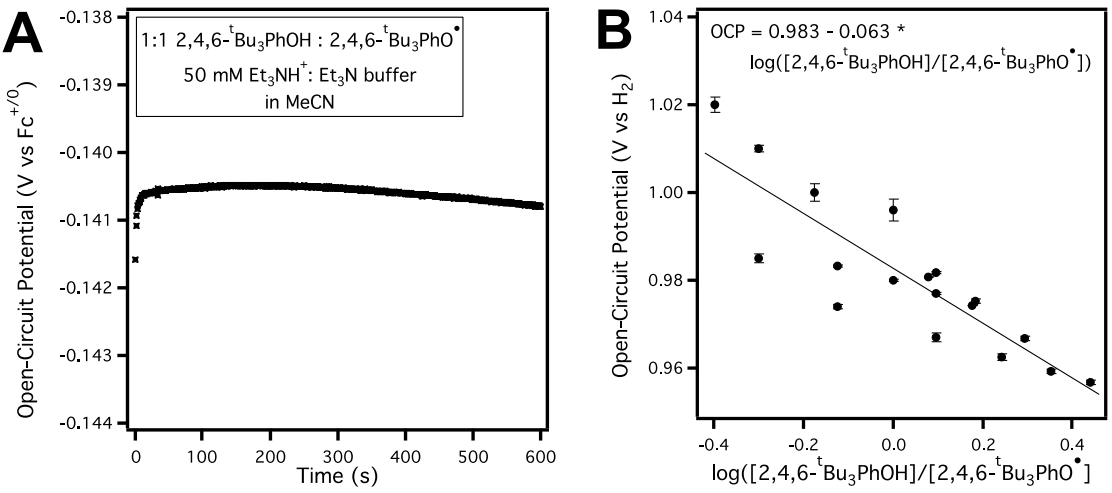

Figure B2. **(A)** Open-circuit potential measurements collected every second for 600 s of a solution containing 0.7 mM 2,4,6-^{t}Bu$_3$PhOH, 0.7 mM 2,4,6-^{t}Bu$_3$PhO$^\bullet$, and a 50 mM Et_3NH^+/Et_3N buffer with 0.1 M $[Bu_4N][PF_6]$ supporting electrolyte in MeCN. **(B)** Average OCP value at different ratios of 2,4,6-^{t}Bu$_3$PhO$^\bullet$: 2,4,6-^{t}Bu$_3$PhOH, plotted as the log ratio of the substrates. Data collected in either 50 mM Et_3NH^+/Et_3N or 50 mM $pyrH^+$/pyr buffer solutions. Error bars represent one standard deviation from OCP vs time traces.

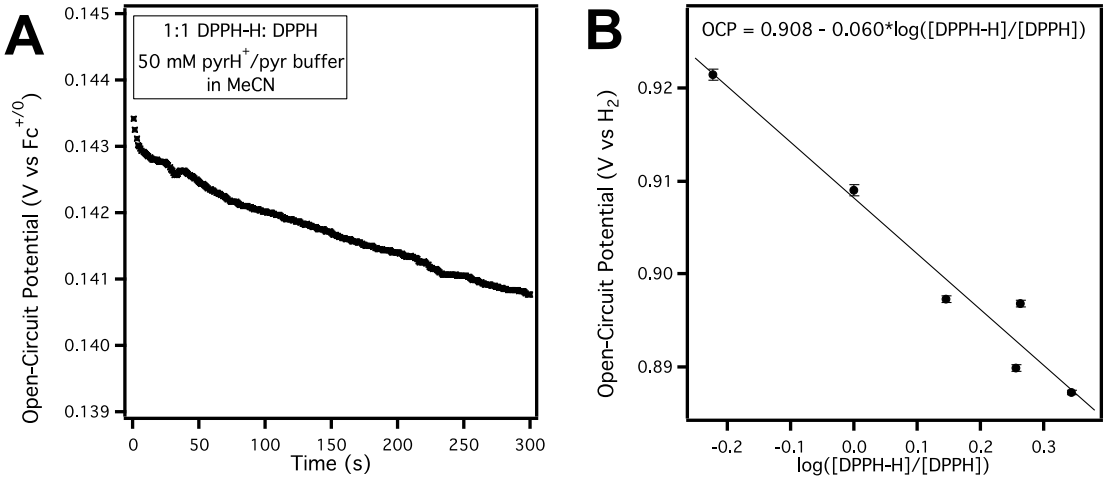

Figure B3. **(A)** Open-circuit potential measurements collected every second for 300 s of a solution containing 0.5 mM DPPH-H, 0.5 mM DPPH, and a 50 mM $pyrH^+$/pyr buffer with 0.1 M $[Bu_4N][PF_6]$ supporting electrolyte in MeCN. **(B)** Average OCP value at different ratios of DPPH:DPPH-H, plotted as the log ratio of the substrates. Error bars represent one standard deviation from OCP vs time traces.

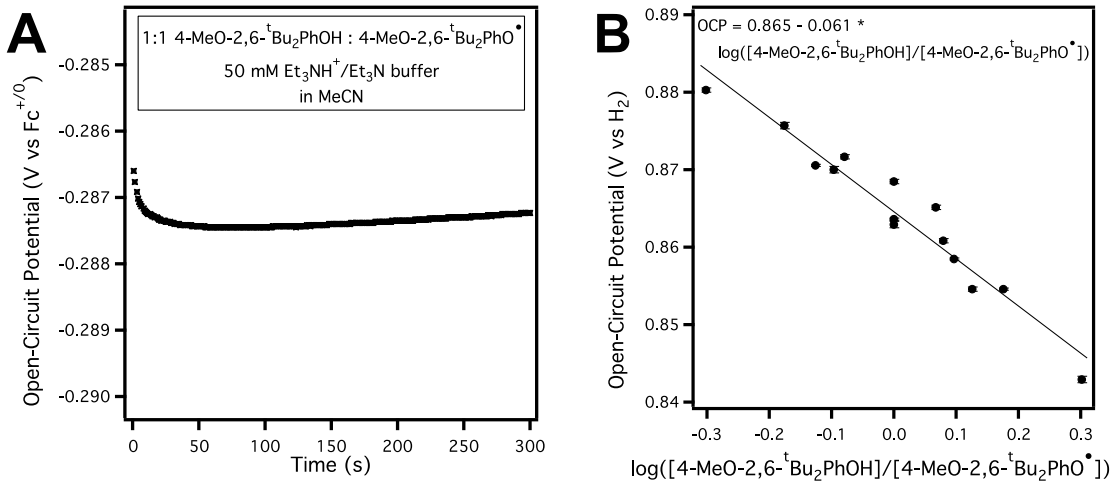

Figure B4. **(A)** Open-circuit potential measurements collected every second for 300 s of a solution containing 0.8 mM 4-MeO-2,6-^{t}Bu$_2$PhOH, 0.8 mM 4-MeO-2,6-^{t}Bu$_2$PhO$^{\bullet}$, and a 50 mM Et_3NH^+/Et_3N buffer with 0.1 M $[Bu_4N][PF_6]$ supporting electrolyte in MeCN. **(B)** Average OCP value at different ratios of 4-MeO-2,6-^{t}Bu$_2$PhO$^{\bullet}$: 4-MeO-2,6-^{t}Bu$_2$PhOH, plotted as the log ratio of the substrates. Error bars represent one standard deviation from OCP vs time traces.

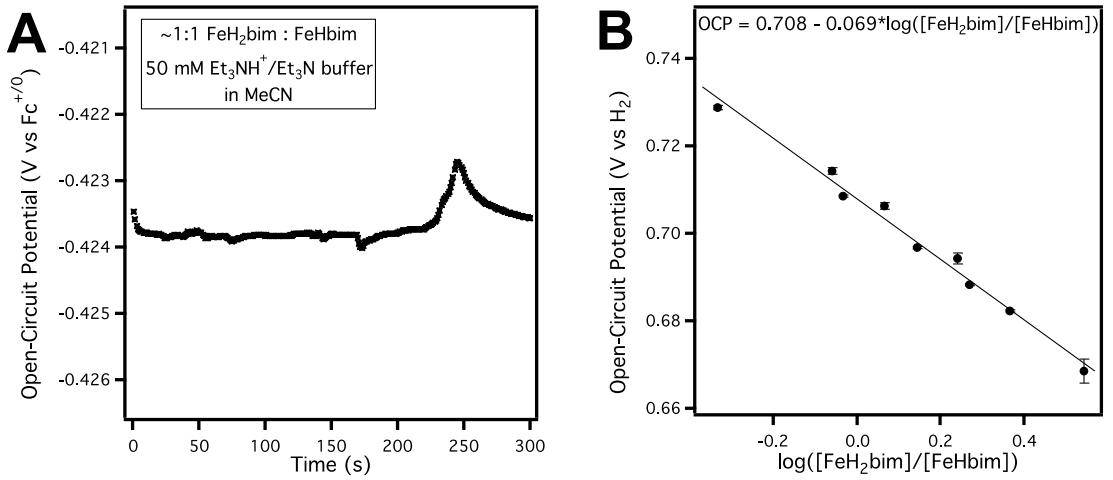

Figure B5. **(A)** Open-circuit potential measurements collected every second for 300 s of a solution containing 0.6 mM $Fe^{II}H_2bim$, 0.7 mM $Fe^{III}Hbim$, and a 50 mM Et_3NH^+/Et_3N buffer with 0.1 M $[Bu_4N][PF_6]$ supporting electrolyte in MeCN. **(B)** Average OCP value at different ratios of $Fe^{III}Hbim$:$Fe^{II}H_2bim$, plotted as the log ratio of the substrates. Error bars one represent standard deviation from OCP vs time traces.

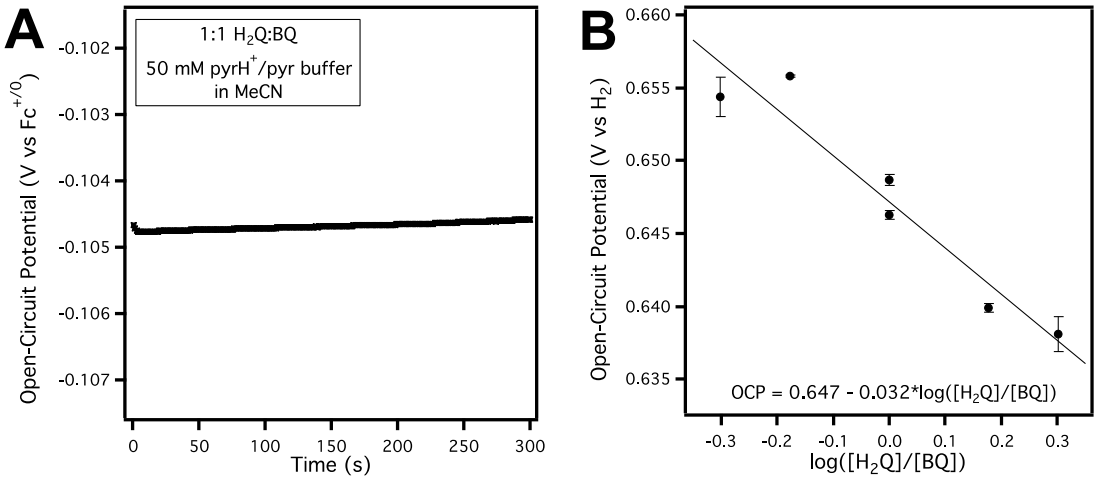

Figure B6. (A) Open-circuit potential measurements collected every second for 300 s of a solution containing 1.2 mM H_2Q, 1.2 mM BQ, and a 50 mM $pyrH^+$/pyr buffer with 0.1 M $[Bu_4N][PF_6]$ supporting electrolyte in MeCN. **(B)** Average OCP value at different ratios of BQ:H_2Q, plotted as the log ratio of the substrates. Error bars represent one standard deviation from OCP vs time traces.

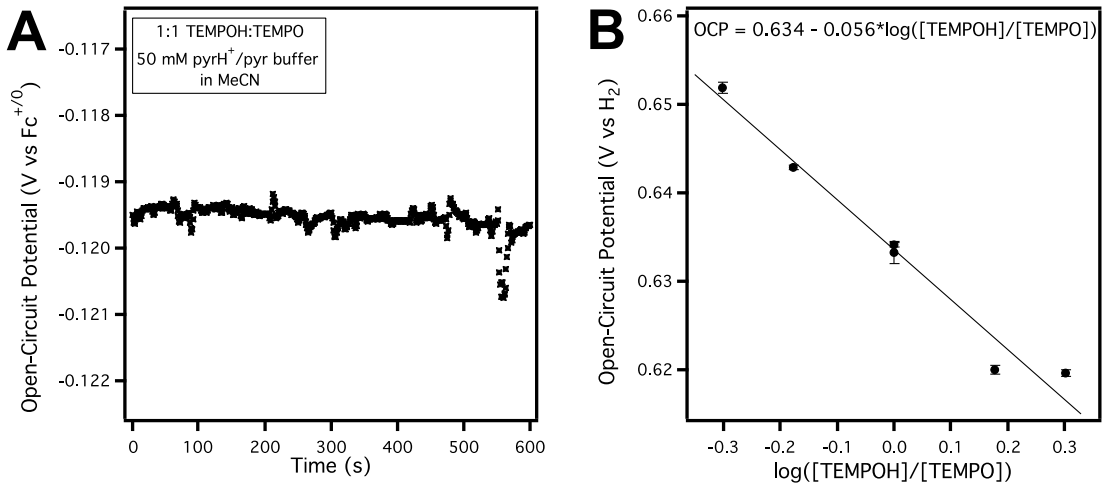

Figure B7. **(A)** Open-circuit potential measurements collected every second for 300 s of a solution containing 1.2 mM TEMPOH, 1.2 mM TEMPO, and a 50 mM $pyrH^+$/pyr buffer with 0.1 M $[Bu_4N][PF_6]$ supporting electrolyte in MeCN. **(B)** Average OCP value at different ratios of TEMPO:TEMPOH, plotted as the log ratio of the substrates. Error bars represent one standard deviation from OCP vs time traces.

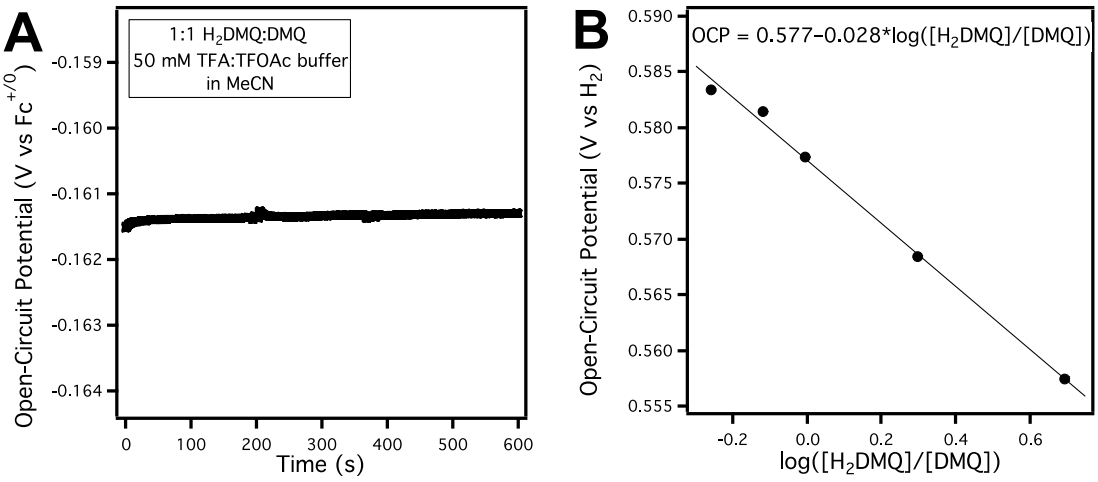

Figure B8. **(A)** Open-circuit potential measurements collected every second for 600 s of a solution containing 1.0 mM 2,6-dimethyl-1,4-hydroquinone (H_2DMQ), 1.0 mM 2,6-dimethyl-1,4-benzoquinone (DMQ), and a 50 mM trifluoroacetic acid/sodium trifluoroacetate (TFA/TFOAc) buffer with 0.1 M [Bu_4N][PF_6] supporting electrolyte in MeCN. **(B)** Average OCP value at different ratios of DMQ:H_2DMQ, plotted as the log ratio of the substrates. Error bars representing one standard deviation from the OCP vs time traces are smaller than the data points.

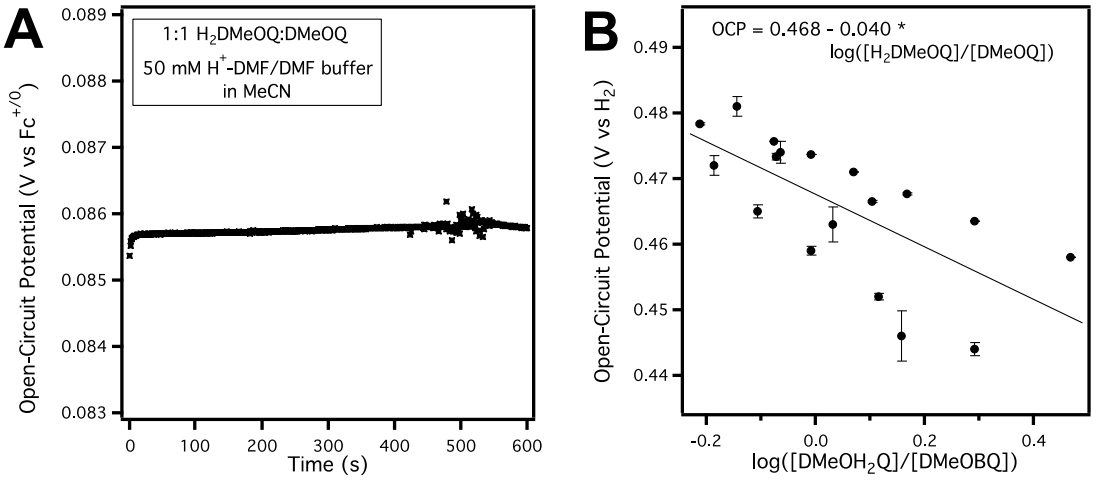

Figure B9. **(A)** Open-circuit potential measurements collected every second for 600 s of a solution containing 1.6 mM 2,6-dimethoxy-1,4-hydroquinone (H_2DMeOQ), 1.6 mM 2,6-dimethoxy-1,4-benzoquinone (DMeOQ), and a 50 mM H^+-DMF/DMF buffer with 0.1 M [Bu_4N][PF_6] supporting electrolyte in MeCN. **(B)** Average OCP value at different ratios of DMeOQ:H_2DMeOQ, plotted as the log ratio of the substrates. Data collected in either 50 mM H^+-DMF/DMF or 50 mM pyrH^+/pyr buffer solutions. Error bars represent one standard deviation from OCP vs time traces.

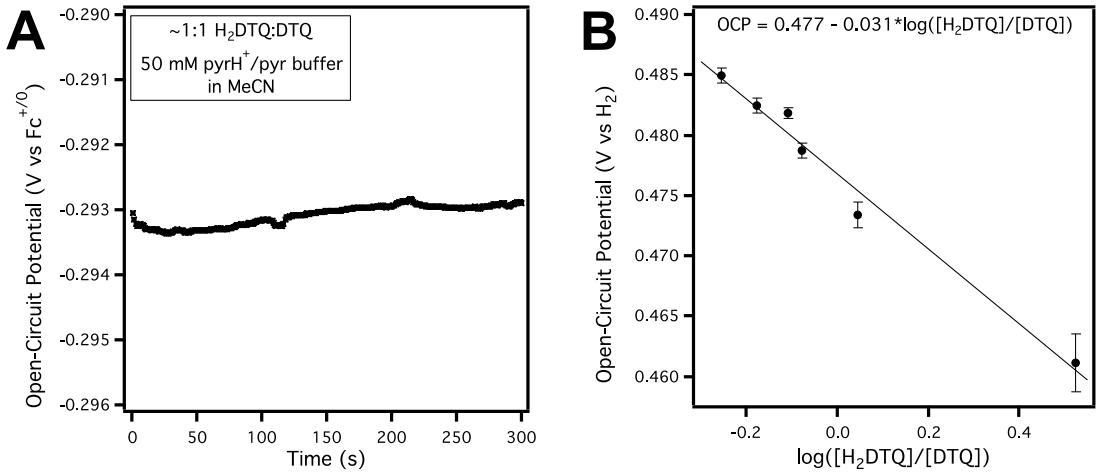

Figure B10. **(A)** Open-circuit potential measurements collected every second for 300 s of a solution containing 1.0 mM 2,6-di-*tert*-butyl-1,4-hydroquinone (H_2DTQ), 0.9 mM 2,6-di-*tert*-butyl-1,4-benzoquinone (DTQ), and a 50 mM pyrH^+/pyr buffer with 0.1 M [Bu_4N][PF_6] supporting electrolyte in MeCN. **(B)** Average OCP value at different ratios of DTQ:H_2DTQ, plotted as the log ratio of the substrates. Error bars represent one standard deviation from OCP vs time traces.

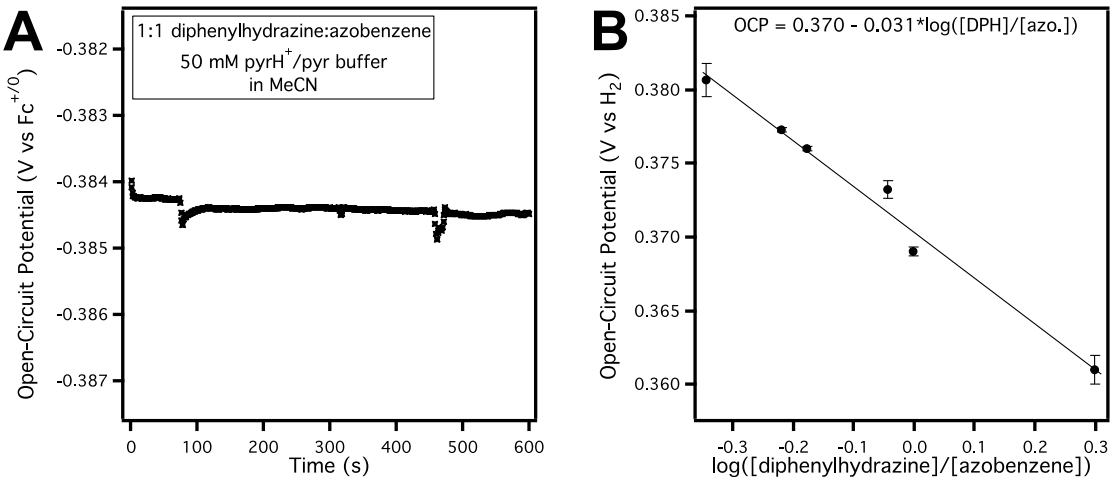

Figure B11. **(A)** Open-circuit potential measurements collected every second for 600 s of a solution containing 1.1 mM 1,2-diphenylhydrazine (DPH), 1.1 mM azobenzene, and a 50 mM pyrH^+/pyr buffer with 0.1 M [Bu_4N][PF_6] supporting electrolyte in MeCN. **(B)** Average OCP value at different ratios of azobenzene:DPH, plotted as the log ratio of the substrates. Error bars represent one standard deviation from OCP vs time traces.

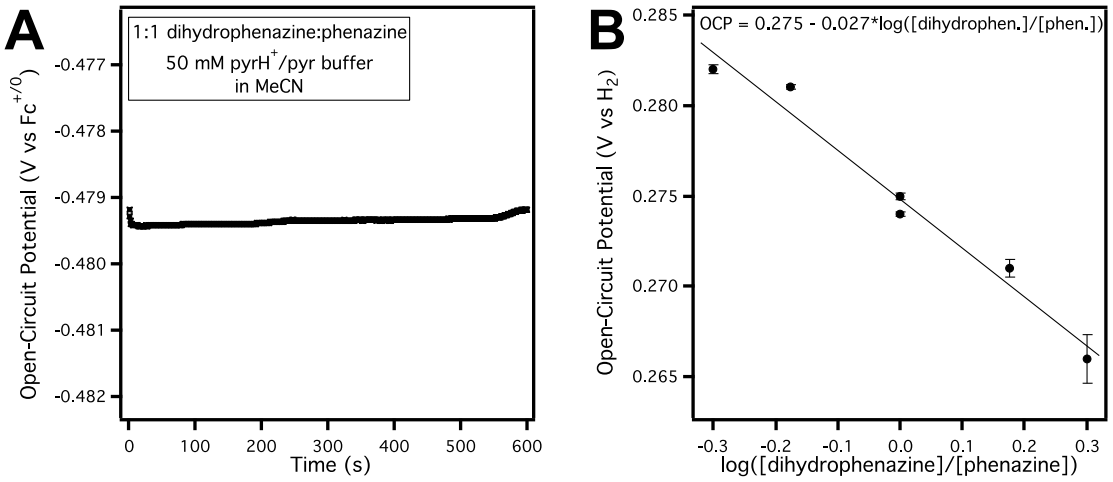

Figure B12. **(A)** Open-circuit potential measurements collected every second for 600 s of a solution containing 1.2 mM 5,10-dihydrophenazine, 1.2 mM phenazine, and a 50 mM $pyrH^+$/pyr buffer with 0.1 M $[Bu_4N][PF_6]$ supporting electrolyte in MeCN. **(B)** Average OCP value at different ratios of phenazine:dihydrophenazine, plotted as the log ratio of the substrates. Error bars represent one standard deviation from OCP vs time traces.

B.2.2 OCP Data for PCET Reagents in THF

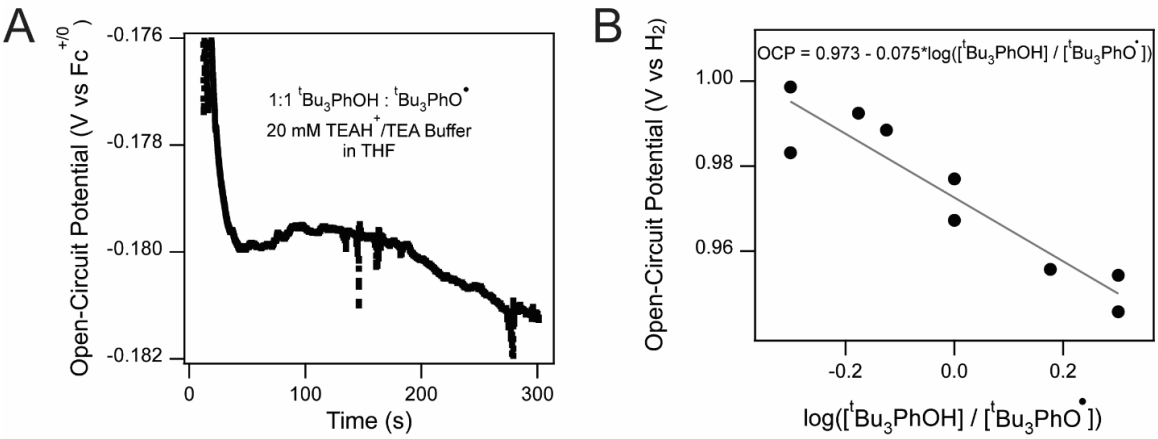

Figure B13. **(A)** Open-circuit potential measurements collected every 0.1 s of a solution containing 0.7 mM 2,4,6-^{t}Bu$_3$PhOH, 0.7 mM 2,4,6-^{t}Bu$_3$PhO$^\bullet$, and a 20 mM Et_3NH^+/Et_3N buffer with 0.1 M $[Bu_4N][PF_6]$ supporting electrolyte in THF. **(B)** Average OCP value at different ratios of 2,4,6-^{t}Bu$_3$PhO$^\bullet$: 2,4,6-^{t}Bu$_3$PhOH, plotted as the log ratio of the substrates. Data points are averages of the final 150 seconds of OCP vs time traces. Error bars (one standard deviation) are smaller than the data points.

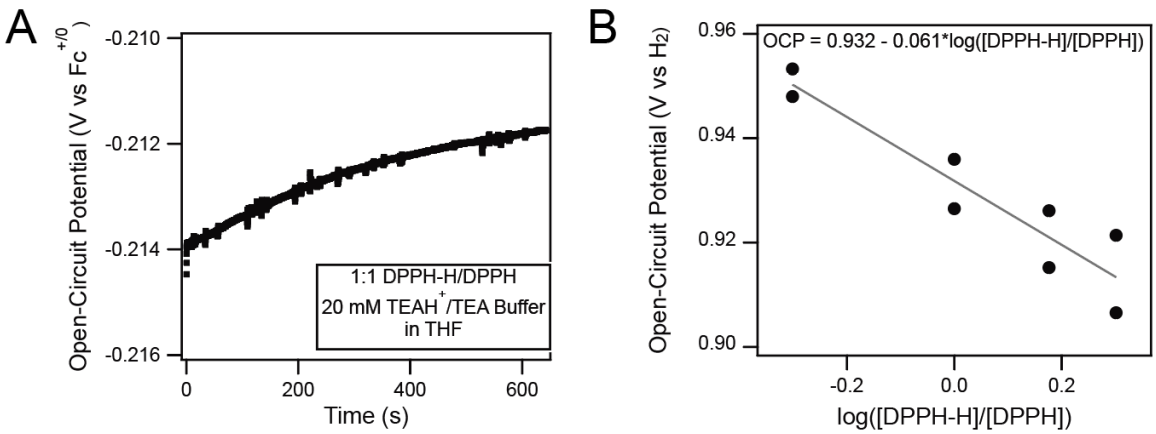

Figure B14. **(A)** Open-circuit potential measurements collected every 0.1 s of a solution containing 0.6 mM DPPH-H, 0.6 mM DPPH, and a 20 mM Et_3NH^+/Et_3N buffer with 0.1 M $[Bu_4N][PF_6]$ supporting electrolyte in THF. **(B)** Average OCP value at different ratios of DPPH:DPPH–H, plotted as the log ratio of the substrates. Data points are averages of the final 150 seconds of OCP vs time traces. Error bars (one standard deviation) are smaller than the data points.

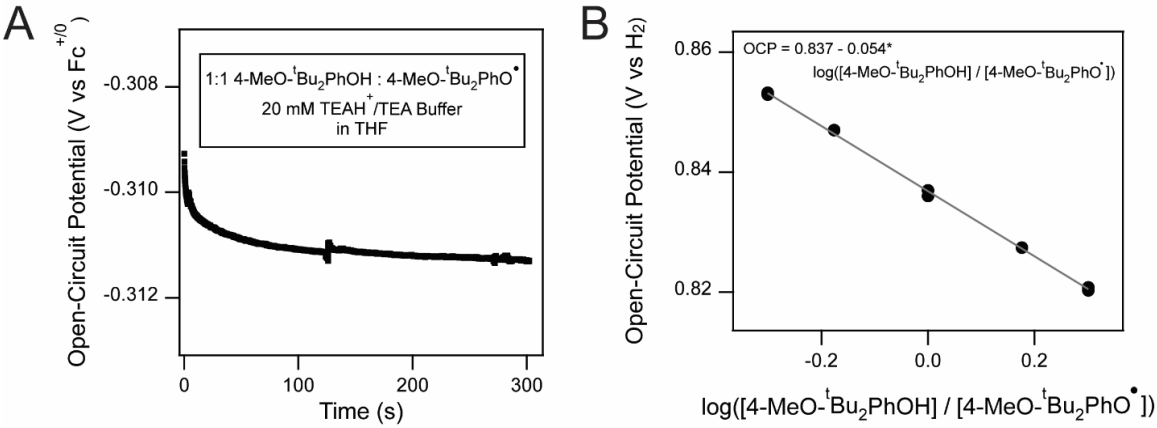

Figure B15. **(A)** Open-circuit potential measurements collected every 0.1 s of a solution containing 1.0 mM 4-MeO-2,6-^{t}Bu$_2$PhOH, 1.0 mM 4-MeO-2,6-^{t}Bu$_2$PhO$^\bullet$, and a 20 mM Et_3NH^+/Et_3N buffer with 0.1 M $[Bu_4N][PF_6]$ supporting electrolyte in THF. **(B)** Average OCP value at different ratios of 4-MeO-2,6-^{t}Bu$_2$PhO$^\bullet$: 4-MeO-2,6-^{t}Bu$_2$PhOH, plotted as the log ratio of the substrates. Data points are averages of the final 150 seconds of OCP vs time traces. Error bars (one standard deviation) are smaller than the data points.

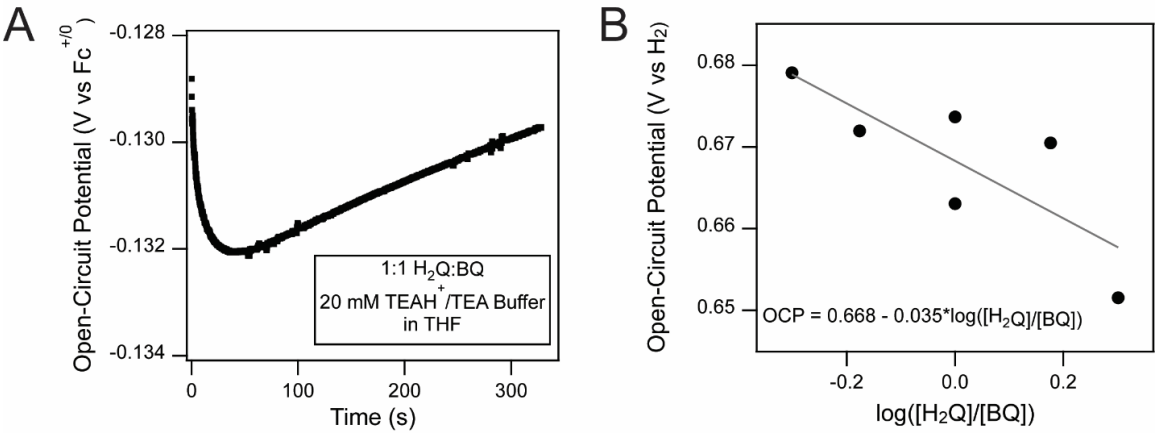

Figure B16. (A) Open-circuit potential measurements collected every 0.1 s of a solution containing 1.0 mM H_2Q, 1.0 mM BQ, and a 20 mM Et_3NH^+/Et_3N buffer with 0.1 M $[Bu_4N][PF_6]$ supporting electrolyte in THF. **(B)** OCP value at different ratios of BQ:H_2Q, plotted as the log ratio of the substrates. Data points are averages of the final 150 seconds of OCP vs time traces. Error bars (one standard deviation) are smaller than the data points.

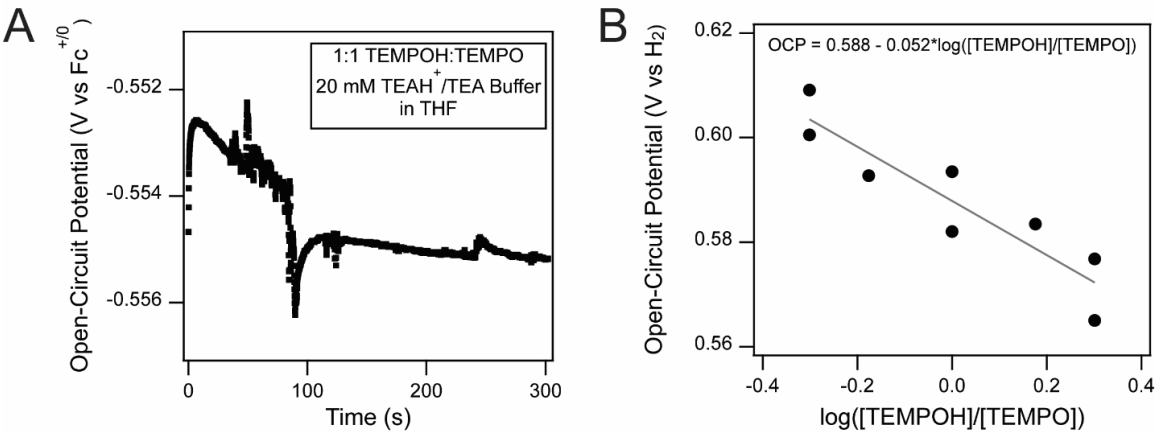

Figure B17. **(A)** Open-circuit potential measurements collected every 0.1 s of a solution containing 0.8 mM TEMPOH, 0.8 mM TEMPO, and a 20 mM Et_3NH^+/Et_3N buffer with 0.1 M $[Bu_4N][PF_6]$ supporting electrolyte in THF. **(B)** Average OCP value at different ratios of TEMPO:TEMPOH, plotted as the log ratio of the substrates. Data points are averages of the final 150 seconds of OCP vs time traces. Error bars (one standard deviation) are smaller than the data points.

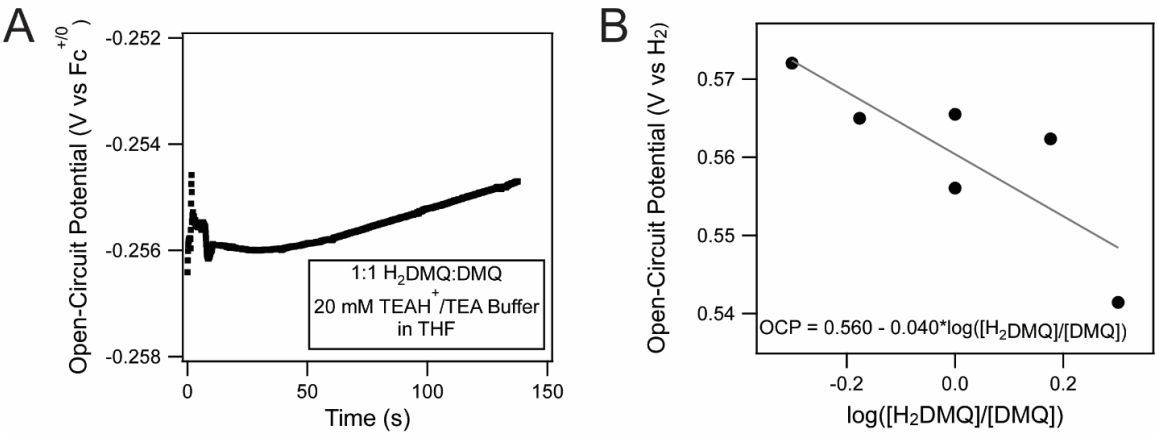

Figure B18. **(A)** Open-circuit potential measurements collected every 0.1 s of a solution containing 1.0 mM H_2DMQ, 1.0 mM DMQ, and a 20 mM Et_3NH^+/Et_3N buffer with 0.1 M $[Bu_4N][PF_6]$ supporting electrolyte in THF. **(B)** Average OCP value at different ratios of DMQ:H_2DMQ, plotted as the log ratio of the substrates. Data points are averages of the final 150 seconds of OCP vs time traces. Error bars (one standard deviation) are smaller than the data points.

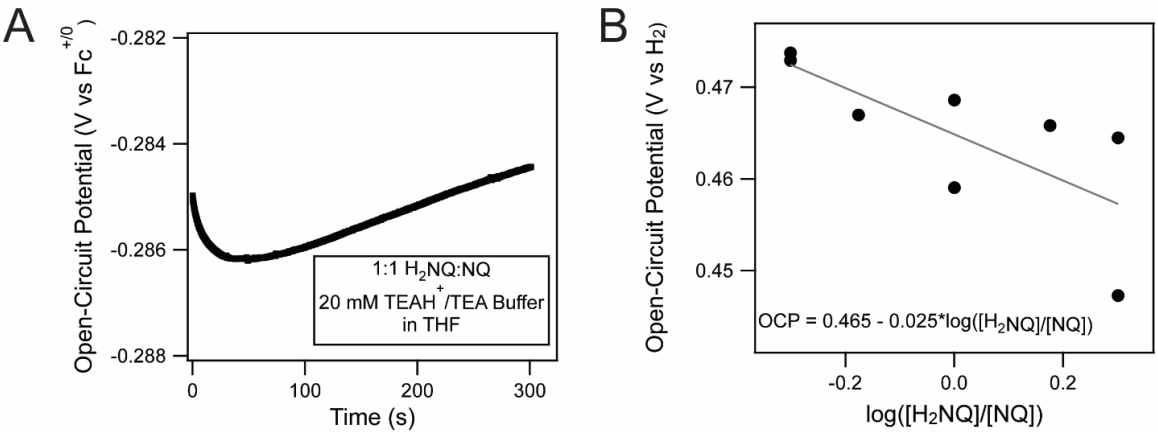

Figure B19. **(A)** Open-circuit potential measurements collected every 0.1 s of a solution containing 0.5 mM H_2NQ, 0.5 mM NQ, and a 20 mM Et_3NH^+/Et_3N buffer with 0.1 M $[Bu_4N][PF_6]$ supporting electrolyte in THF. **(B)** Average OCP value at different ratios of NQ:H_2NQ, plotted as the log ratio of the substrates. Data points are averages of the final 150 seconds of OCP vs time traces. Error bars (one standard deviation) are smaller than the data points.

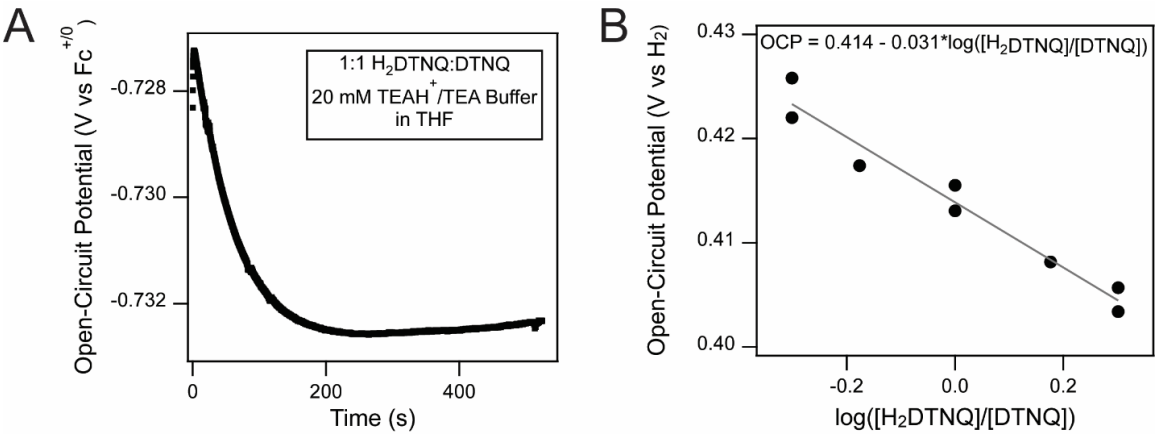

Figure B20. **(A)** Open-circuit potential measurements collected every 0.1 s of a solution containing 1.0 mM H_2DTNQ, 1.0 mM DTNQ, and a 20 mM Et_3NH^+/Et_3N buffer with 0.1 M $[Bu_4N][PF_6]$ supporting electrolyte in THF. **(B)** Average OCP value at different ratios of DTNQ:H_2DTNQ, plotted as the log ratio of the substrates. Data points are averages of the final 150 seconds of OCP vs time traces. Error bars (one standard deviation) are smaller than the data points.

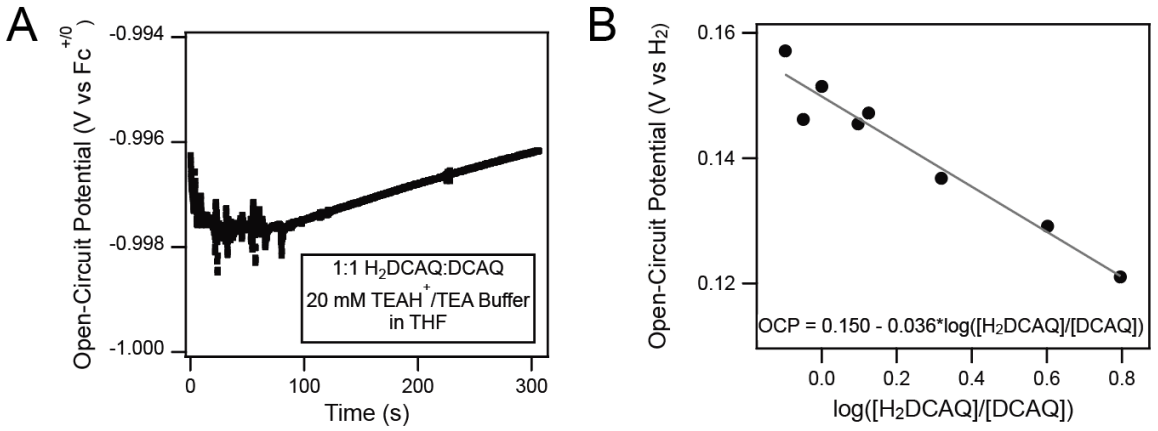

Figure B21. **(A)** Open-circuit potential measurements collected every 0.1 s of a solution containing 0.7 mM H_2DCAQ, 0.7 mM DCAQ, and a 20 mM Et_3NH^+/Et_3N buffer with 0.1 M $[Bu_4N][PF_6]$ supporting electrolyte in THF. **(B)** Average OCP value at different ratios of DCAQ:H_2DCAQ, plotted as the log ratio of the substrates. Data points are averages of the final 150 seconds of OCP vs time traces. Error bars (one standard deviation) are smaller than the data points.

B.2.3 OCP Data for DMQ/H_2DMQ in DMF

The OCP method was further validated by measuring the DMQ/H_2DMQ potential in *N,N*-dimethylformamide (DMF) using the same experimental set-up and procedure described in the main text for MeCN and THF. Prior to sample preparation, the DMF solvent was sparged with N_2 for 25 minutes to remove dimethylamine impurities.

Measurements of the OCP over time showed rapid changes in potential for the first ~30 s but then remained stable over minutes (Figure B22A). The OCP was measured at DMQ:H_2DMQ ratios between 0.7:1 and 1.7:1, and the resulting plot of OCP versus log([H_2DMQ]/[DMQ]) showed the expected Nernstian dependence (Figure B). The formal potential, $E^{\circ\prime}_{OCP}$(DMQ/H_2DMQ), in a pyrH^+/pyr buffer was determined to be –0.279(1) V vs $Fc^{+/0}$. This value corresponds to a standard potential, E°(DMQ/H_2DMQ), of 0.578(2) V vs H_2, following Scheme 2.1 of the main text and using pK_a(pyrH^+) = 3.3 in DMF[11] and E°(H^+/H_2) = –0.662 V vs $Fc^{+/0}$ in DMF.[12] The corresponding BDFE was calculated via Scheme 2.3 of the main text as 65.6(2) kcal mol^{-1}, which is within 1 kcal mol^{-1} of the values obtained in MeCN and THF.

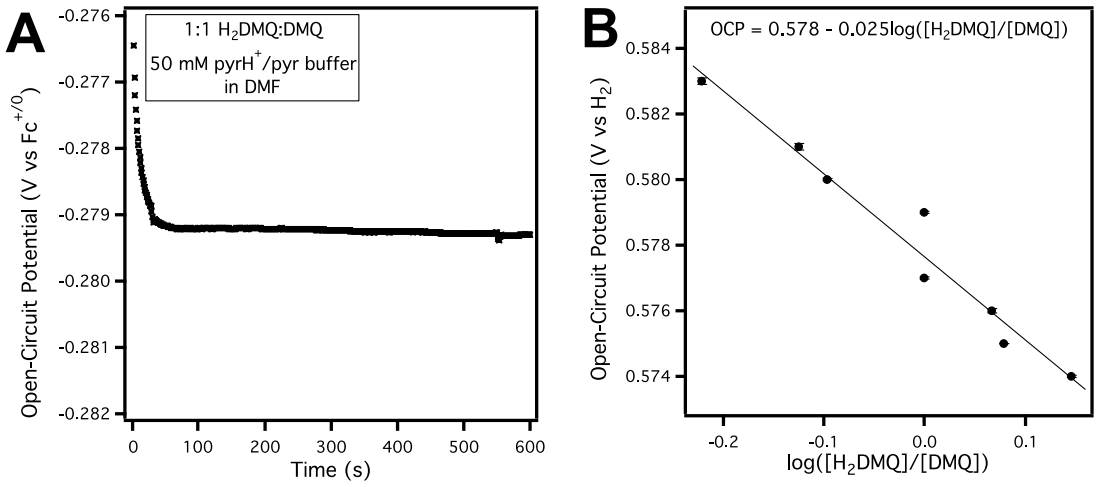

Figure B22. **(A)** Open-circuit potential measurements collected every second for 600 s of a solution containing 1.4 mM 2,6-dimethyl-1,4-hydroquinone (H_2DMQ), 1.4 mM 2,6-dimethyl-1,4-benzoquinone (DMQ), and a 50 mM pyrH^+/pyr buffer with 0.1 M [Bu_4N][PF_6] supporting electrolyte in DMF. **(B)** Average OCP value at different ratios of DMQ:H_2DMQ, plotted as the log ratio of the substrates. Error bars represent one standard deviation from OCP vs time traces.

B.2.4 OCP Data for DMQ/H_2DMQ in IPA

To demonstrate the generality of the OCP method to nonaqueous, protic solvents, the DMQ/H_2DMQ potential was measured in isopropanol (IPA) containing 50 mM of a 1:1 acetic acid: tetrabutylammonium acetate buffer (AcOH:AcO^-) and 0.1 M [Bu_4N][BF_4] electrolyte. Measurements of the OCP over time showed rapid changes in

potential for the first 30 s but then remained stable within about 1 mV over 5 minutes. The OCP was measured at DMQ:H_2DMQ ratios between 0.5:1 and 1.5:1, and the resulting plot of OCP versus log([H_2DMQ]/[DMQ]) showed the expected Nernstian dependence. Under these conditions, $E^{\circ\prime}_{OCP}$(DMQ/H_2DMQ) = –0.597(5) V vs $Fc^{+\backslash 0}$. Combining $E^{\circ\prime}_{OCP}$(DMQ/H_2DMQ) with E(H^+/H_2) for AcOH:AcO^- in IPA (see Section 4.2 below) per Scheme 2.3 of the main text yields E°(DMQ/H_2DMQ) = 0.566(5) V vs H_2.

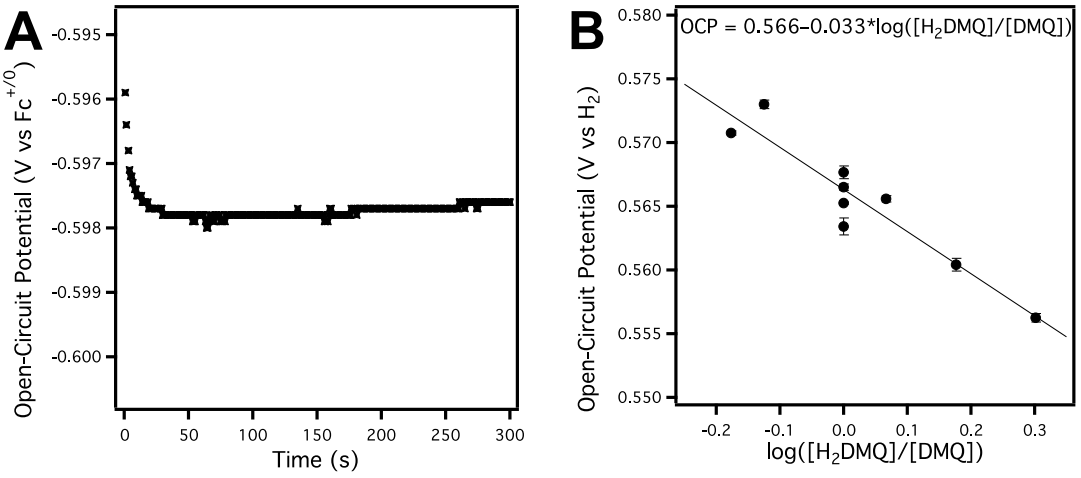

Figure B23. (A) Open-circuit potential measurements collected every second for 300 s of a solution containing 1.2 mM 2,6-dimethyl-1,4-hydroquinone (H_2DMQ), 1.2 mM 2,6-dimethyl-1,4-benzoquinone (DMQ), and a 50 mM AcOH/AcO^- buffer with 0.1 M [NBu_4][BF_4] supporting electrolyte in IPA. **(B)** Average OCP value at different ratios of DMQ:H_2DMQ, plotted as the log ratio of the substrates. Error bars represent one standard deviation from OCP vs time traces.

B.2.5 Analysis of OCP Data for 2,4,6-^{t}Bu$_3$PhOH in MeCN

At the suggestion of a reviewer, we provide here a more detailed analysis of data from of the worst-behaved substrates, 2,4,6-^{t}Bu$_3$PhOH in MeCN (see Figure B2). For this substrate, the measured potential at a given substrate ratio showed day-to-day variations of up to ~20 mV (~0.5 kcal mol^{-1}), which we attribute to small weighing errors, slow equilibration times, and long timescale drift in the reference electrode potential. Despite the apparent scatter, both the slope and y-intercept obtained from a linear fit of all data points have a standard deviation of less than 10 mV (Figure B24).

Independent trials showed a higher degree of linearity, as depicted in Figure B24A, which replots Figure B2B but distinguishes the data by trial and buffer condition. The scatter observed in Trial #3 (gray data points in Figure B24A) arises from varying the substrate ratio in both directions, which was done to offset error due to reference electrode drift. Figure B24B shows only the data from this trial and indicates whether the points were collected after addition of 2,4,6-^{t}Bu$_3$PhOH or 2,4,6-^{t}Bu$_3$PhO$^{\bullet}$. The individual data sets for moving in each direction are highly linear ($R^2 > 0.99$).

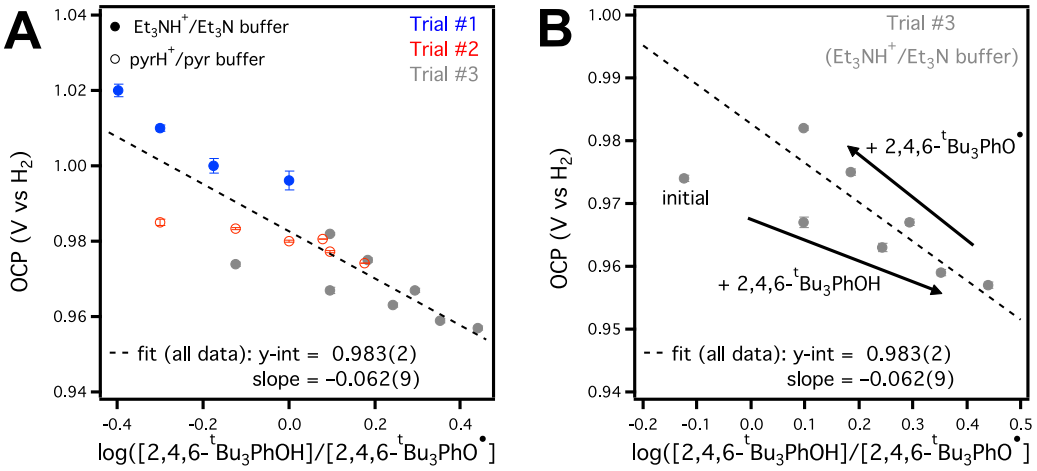

Figure B24. (**A**) Data from Figure B2 replotted to distinguish between different experimental trials (blue, red, and gray points) and buffer conditions (filled circles = Et_3NH^+/Et_3N, open circles = $pyrH^+/pyr$). Dashed line is linear fit of all data, and the slope and intercept are reported with a one standard deviation error. Error bars on individual data points represent one standard deviation from OCP vs time traces. (**B**) Trial #3 data (gray points in part **A**) plotted to show order of data collection. The substrate ratio was first varied by adding 2,4,6-^{t}Bu$_3$PhOH and then by adding 2,4,6-^{t}Bu$_3$PhO$^{\bullet}$ in order to offset experimental error caused by slow drift in the reference electrode potential over the course of the measurement.

B.3 Error Analysis

B.3.1 Inherent Uncertainty in Values Derived from OCP Measurements

OCP measurements and the subsequent conversions to standard potentials and BDFEs have several inherent sources of uncertainty. These uncertainties are discussed below and separated by the different measurements or reference states.

B.3.1.1 OCP vs time traces

The measured OCP for a given $X:XH_n$ ratio typically drifted slightly over time. The absolute magnitude of the drift varied with solvent, substrate, and $X:XH_n$ ratio but was usually less than ~1.5 mV/5 min. Substrates measured in THF tended to show larger drift than those measured in MeCN, as evident in Figure B2-B21(A). Regardless of solvent, the drift was higher at $X:XH_n$ ratios far from 1:1, and we therefore typically operated at $X:XH_n$ ratios between 0.4:1 and 2.5:1. To account for uncertainty in the actual equilibrium potential associated with this drift, we report errors of one standard deviation from the average measured OCP (see Figure B2-B23(B)).

B.3.1.2 Formal potential vs $Fc^{+/0}$ ($E^{o\prime}_{OCP}(X/XH_n)$)

The open-circuit potentials were measured against a Ag pseudoreference electrode and then converted to a Fc reference state, as is standard for nonaqueous potential measurements. This conversion introduced some uncertainty that, like the OCP drift, varied between solvents. In MeCN, $E_{1/2}(Fc^+/Fc)$ was generally reproducible to within ± 1 mV on a given day, as long as the CVs were properly compensated for the internal resistance of the solution. On the other hand, in THF, even with iR compensation, the peak-to-peak separation for the Fc couple could exceed 70 mV, which would correlate to about ± 7 mV uncertainty in $E_{1/2}(Fc^+/Fc)$.

To determine the reproducibility of the method, OCP measurements of the same substrate were collected on different days using different stock solutions of substrate. In each experiment, the OCP was measured at several $X:XH_n$ ratios, and formal potentials were obtained as described in Section 2.2.2 of the Results in the

main text. One standard deviation of these multiple measurements of $E^{\circ\prime}_{OCP}(X/XH_n)$ was propagated with the uncertainty in $E_{1/2}(Fc^{+/0})$ to determine the total uncertainties reported in Table 2.1 in the main text.

B.3.1.3 Standard potential vs $Fc^{+/0}$ ($E^{\circ}_{OCP}(X/XH_n)$)

If the same substrate was examined in multiple buffer conditions, the *standard* potential vs $Fc^{+/0}$ was needed to evaluate the reproducibility of the measured values. Values of $E^{\circ\prime}_{OCP}(X/XH_n)$ were converted to the corresponding $E^{\circ}_{OCP}(X/XH_n)$ by adding $0.0592(pK_a)$, and then the same error analysis as described above for formal potentials was applied.

B.3.1.4 Standard potential vs H_2 ($E^{\circ}(X/XH_n)$)

The sources of uncertainty in converting the reference state from Fc to hydrogen depend on whether Scheme 2.1 or Scheme 2.2 in the main text is used to perform the conversion. In this report, we use Scheme 2.1 to obtain $E^{\circ}(X/XH_n)$ for substrates in MeCN and Scheme 2.2 for substrates in THF.

Scheme 2.1 requires the pK_a of the buffer and the standard hydrogen potential ($E^{\circ}(H^+/H_2)$) in that solvent, both of which can have associated uncertainties. For example, the pK_a of pyridinium has been reported as 12.53 and 12.3 in acetonitrile (ref. [13] and [11], respectively), and the difference between these values would give a 14 mV uncertainty in potential. We chose the 12.53 value for all conversions herein since it appears to be more widely used in the literature, and we did not account for the possible 14 mV uncertainty in our error analysis. The $E^{\circ}(H^+/H_2)$ for acetonitrile is reported to ± 4 mV.[14] We propagated this uncertainty with the uncertainties in $E^{\circ\prime}_{OCP}(X/XH_n)$ (calculated as described above) to obtain the total uncertainties in $E^{\circ}(X/XH_n)$ that are reported in Table 2.2 of the main text.

Scheme 2.2 does not require pK_a values or standard hydrogen potentials, but the uncertainty in $E^{\circ\prime}(H^+/H_2)$ must be considered. For THF, we measured $E^{\circ\prime}(H^+/H_2)$ in 1:1 Et_3NH^+:Et_3N solutions of different buffer strength, as described in Section B4

below. One standard deviation from the average of the measured potentials gave a 7 mV uncertainty in $E°'(H^+/H_2)$. The total uncertainty in $E°(X/XH_n)$ in THF accounted for this uncertainty in $E°'(H^+/H_2)$ as well as the uncertainties in $E°'_{OCP}(X/XH_n)$ (calculated as described above).

B.3.1.5 BDFEs

The *relative* uncertainties in BDFE for the substrates examined in this report can be determined by simply converting the uncertainties in $E°(X/XH_n)$ from V to kcal mol^{-1}. For most substrates, these values are $\leq$ 0.3 kcal mol^{-1}. The *absolute* uncertainties in BDFE are larger and are dominated by uncertainties in the free energy to convert ½ H_2 (g) to $H^{\bullet}_{1M}$ ($\Delta G°(½H_2/H^{\bullet})$). A rigorous analysis in water that considered multiple methods for approximating the solubility of $H^{\bullet}$ estimated the uncertainty in $\Delta G°(½H_2/H^{\bullet})$ to be $\pm$ 0.03 V, or about 0.7 kcal mol^{-1}.[15] Assuming a similar uncertainty for our values in organic solvents, we conservatively report BDFEs to $\pm$ 1 kcal mol^{-1}.

B.3.2 Other Possible Sources of Error in OCP Measurements

Additional systematic errors could arise from side reactions of the substrate under the experimental conditions, several examples of which are discussed below. Careful consideration of the experimental conditions can minimize some of these errors.

The choice of buffer can in some cases affect the accuracy of the OCP measurement, for instance if the buffer (de)protonates one of the substrates or reacts with substrate to cause decomposition. One indication that such undesired side reactivity could be occurring is the measurement of significantly different standard potentials (V vs H_2) for the same substrate in multiple buffers. For example, we compared OCP measurements of $FeH_2bim/FeHbim$ collected in Et_3NH^+/Et_3N and $pyrH^+$/pyr buffer solutions. The $pK_a(Fe^{III}H_2bim)$ is 17.5 in acetonitrile,[16] so $Fe^{III}Hbim$ should exist as predominantly $Fe^{III}Hbim$ in Et_3NH^+/Et_3N (pK_a = 18.82, ref. [13]) and as predominantly $Fe^{III}H_2bim$ in $pyrH^+$/pyr (pK_a = 12.53, ref.[13]). Indeed, upon addition of

pyrH$^+$/pyr buffer to a solution of Fe^{III}Hbim solution, a color change from dark blue to bright red was observed, suggesting protonation. The measured standard potentials ($E°_{OCP,}$ V vs Fc$^{+/0}$) in the two buffer conditions differed by 140 mV. This potential difference would correspond to about 3 kcal mol^{-1} in BDFE, a much larger error than is typical for the OCP method.

Other side reactions of substrate, such as comproportionation and disproportionation, could also lead to systematic errors in the OCP measurements. For instance, the dependence of the measured OCP on log([XH$_n$]/[X]) did not trend as predicted by the Nernst equation for TEMPO/TEMPOH in strongly acidic conditions in acetonitrile. This observation can likely be attributed to the proton-induced disproportionation of TEMPO (eq B1), which has been documented.[17] The reaction in eq B1 forms a new electroactive species, TEMPO$^+$, which will contribute to the measured potential. Additionally, the concentrations of TEMPO and TEMPOH will not be those experimentally added to the solution, so the true X:XH$_n$ ratio is unknown. As a result, the OCP measurements are not reporting on the simple TEMPO/TEMPOH equilibrium under these conditions.

$$\text{TEMPO}^{\bullet} + \text{H}^+ \rightarrow \text{TEMPOH} + \text{TEMPO}^+ \qquad \text{(B1)}$$

B.4 Hydrogen Open-Circuit Potential Measurements

All hydrogen open-circuit potential measurements were done following a previously reported procedure.[14] Briefly, hydrogen was bubbled through THF or isopropanol (IPA) solutions containing the buffer of choice and 0.1 M electrolyte ([Bu$_4$N][PF$_6$] for THF, [Bu$_4$N][BF$_4$] for IPA). All measurements were performed in 1:1 acid:base buffers to mitigate issues with homoconjugation. The OCP was measured at a hydrogen flame-annealed Pt wire working electrode using a Pt auxiliary electrode, and Ag pseudoreference electrode. After the OCP measurement, ferrocene was added to the sample, and a CV was collected at a glassy carbon working electrode.

B.4.1 Measurements in THF

In THF, the buffer identity was restricted to Et_3NH^+/Et_3N or trifluoroacetic acid/sodium trifluoroacetate (TFA/TFOAc) due to solubility limitations. For Et_3NH^+/Et_3N, data was collected at buffer concentrations of 10 and 30 mM, giving $E^{\circ\prime}(H^+/H_2$, vs $Fc^{+/0}) = -1.148(7)$ (Figure B25A). For TFA/TFOAc data was collected at buffer concentrations of 10, 20, and 60 mM, giving $E^{\circ\prime}(H^+/H_2$, vs $Fc^{+/0}) = -0.94(3)$ (Figure B25B). We note that the difference in $E^{\circ\prime}(H^+/H_2)$ between the two buffers provides an estimate of the difference in pK_a between Et_3NH^+ and TFA in THF (ΔpK_a = 3.6 ± 0.6). This calculation does not rigorously account for known ion pairing effects in THF.

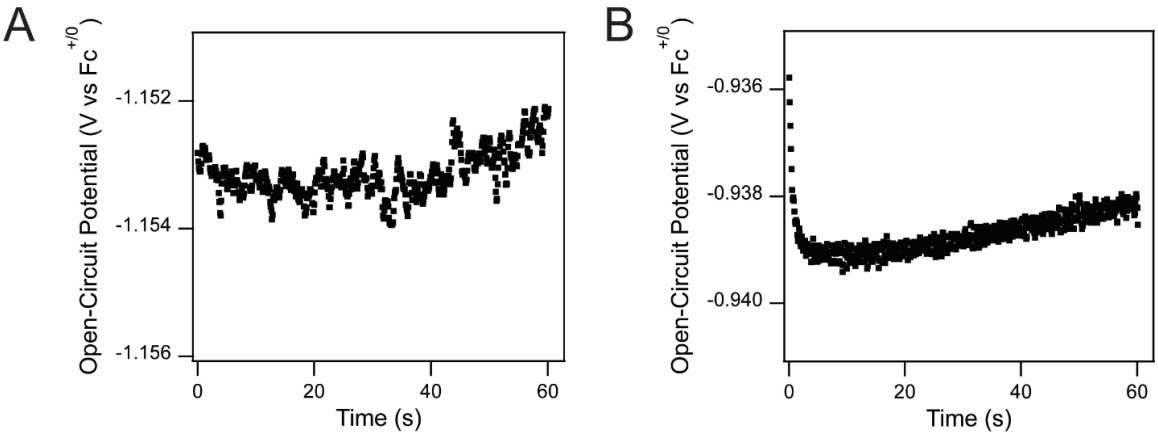

Figure B25. (A) OCP vs. time trace for 30 mM Et_3NH^+/Et_3N buffer. **(B)** OCP vs. time trace for 20 mM TFA/TFOAc buffer. Both measurements performed in THF containing 0.1 M $[Bu_4N][PF_6]$ electrolyte.

B.4.2 Measurements in IPA

In isopropanol, measurements were performed in acetic acid/tetrabutylammonium acetate ($AcOH/AcO^-$) buffer solutions. Ten buffer concentrations were tested between 1 and 100 mM, and the OCP was collected every 0.1 s for 1–2 minutes at each concentration. A representative OCP vs time trace is shown in Figure B26A. The OCP drifted significantly over time (> 15 mV/min) at the lowest buffer strength of 1 mM, so this data point was removed from analysis. Averaging the measured OCP values from the other nine solution conditions (Figure B26B) gave $E^{\circ\prime}(H^+/H_2)$ = –1.163(2) V vs $Fc^{+/0}$, which corresponds to $E^{\circ}(H^+/H_2)$ = –0.494 V vs $Fc^{+/0}$ using the reported pK_a(AcOH) in IPA of 11.3.[18]

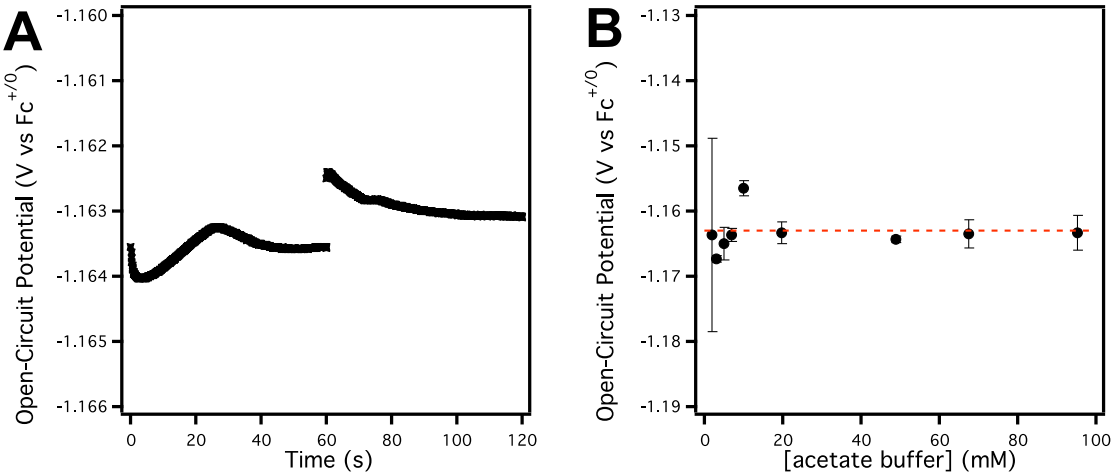

Figure B26. A) OCP vs time for a solution of 20 mM $AcOH/AcO^-$ buffer in IPA with 1 atm H_2 and 0.1 M $[Bu_4N][BF_4]$ electrolyte. **(B)** Average OCP sat different $AcOH/AcO^-$ buffer strengths. Error bars represent one standard deviation in measured value over 1–2 minutes. Red dashed line is average OCP over all concentrations.

B.5 Solvation Free Energy of H_2

The free energy to convert ½H_2 (g) to H• in the solvent of interest is required to convert from a standard potential to a bond dissociation free energy. This free energy term can be broken into two components, the dissociation of ½H_2 to H• in the gas phase and the transfer of H• from the gas (at 1 atm) to solution phase (at 1 M) (eq 2.10-2.11 in the main text, reproduced as B2 and B3 below).

$$\tfrac{1}{2}\mathrm{H_2(g)} \rightleftharpoons \mathrm{H^{\bullet}(g)} \qquad \text{(B2)}$$

$$\mathrm{H^{\bullet}(g)} \rightleftharpoons \mathrm{H^{\bullet}(solv)} \qquad \text{(B3)}$$

The free energy change for eq B2 was calculated from gas phase thermochemistry data[19] and is 48.6 kcal mol^{-1} at 298 K. The entropy and enthalpy of formation values used for this calculation are shown in Table B1.

Table B1. Gas Phase Enthalpies of Formation and Entropies for H• and H_2[a]

Thermochemical Quantity	H• (g)	½H_2 (g)
ΔH_f° (kcal mol^{-1})	52.1	0
S° (cal mol^{-1} K^{-1})	27.4	½(31.2)

[a] From reference [19].

The enthalpies and entropies for the solvation of H• (g) are typically approximated as the same as for H_2,[20] which have been reported in a variety of organic solvents using a standard state of unit mole fraction (χ = 1) (equation B4).[21] Deriving a BDFE requires this free energy term to use a standard state of 1 M for solvated H•. Thus, the literature thermochemical values must be converted between standard states following equation B5.

$$\mathrm{H^{\bullet}(g)} \rightleftharpoons \mathrm{H^{\bullet}(solv, \chi = 1)} \qquad \Delta G_{\mathrm{solv.}} = \Delta H_{\mathrm{solv.}} - \mathrm{T}\Delta S_{\mathrm{solv.}} \qquad \text{(B4)}$$

$$\mathrm{H^{\bullet}(solv, \chi = 1)} \rightleftharpoons \mathrm{H^{\bullet}(solv, 1\ M)} \qquad \Delta G_{\mathrm{conv.}} = \Delta H_{\mathrm{conv.}} - \mathrm{T}\Delta S_{\mathrm{conv.}} \qquad \text{(B5)}$$

There is no enthalpy change in converting between these standard states ($\Delta H_{conv} = 0$), but the entropy term must account for the difference in concentration of H• between $\chi = 1$ and 1 M. This can be calculated per equations B6-B8 using the definition of chemical potential.

$$-T\Delta S_{conv.} = \mu^{\circ}_{1\,M} - \mu^{\circ}_{\chi=1} \quad \text{(B6)}$$

$$-T\Delta S_{conv.} = \mu^{\circ}_{1\,M} - (\mu^{\circ}_{1\,M} + RT ln([H_{\chi=1}])) \quad \text{(B7)}$$

$$-T\Delta S_{conv.} = -RT ln([H_{\chi=1}]) \quad \text{(B8)}$$

Equation B7 requires knowing the concentration of H• at $\chi = 1$ ($[H]_{\chi = 1}$), which can be derived using reported values of χ_H at 1 atm.[21] The mole fraction χ_H equals the moles of H• (n_H) divided by the total moles in solution (equation B9).

$$\chi_{H,1\,atm} = \frac{n_H}{n_H + n_{liquid}} \quad \text{(B9)}$$

Solving for n_H and dividing by the volume of solution (V_{liquid}) yields the concentration of H• at 1 atm ($[H]_{1\,atm}$) (equation B10).

$$[H]_{1\,atm} = \frac{\chi_{H,1\,atm}(n_{liquid})}{(1-\chi_{H,1\,atm})V_{liquid}} \quad \text{(B10)}$$

The definition of $\frac{V_{liquid}}{n_{liquid}}$ is the molar volume (V_m) of the solution. Thus,

$$[H]_{1\,atm} = \frac{\chi_{H,1\,atm}}{(1-\chi_{H,1\,atm})V_m} \quad \text{(B11)}$$

Via the proportionality shown in equation B12, $[H]_{\chi=1}$ can then be calculated.

$$\frac{[H]_{1\,atm}}{[H]_{\chi=1}} = \frac{\chi_{H,1\,atm}}{1} \quad \text{(B12)}$$

Combining equations B11 and B12 yields

$$[H]_{\chi=1} = \frac{1}{V_m(1-\chi_{H,1\,atm})} \quad \text{(B13)}$$

Values of $[H]_{\chi=1}$ obtained from eq B13 can then be used in eq B8 to calculate $-T\Delta S_{conv}$. Finally, the solvation free energy for H• (g) to H• (1 M) (eq B3) can be determined via equations B14-B15.

$$\Delta G_{\text{total}} = (\Delta H_{\text{solv.}} - T\Delta S_{\text{solv.}}) + (\Delta H_{\text{conv.}} - T\Delta S_{\text{conv.}}) \quad \text{(B14)}$$

$$\Delta G_{\text{total}} = (\Delta H_{\text{solv.}} - T\Delta S_{\text{solv.}}) - RT ln([H^{\bullet}_{\chi=1}]) \quad \text{(B15)}$$

The results of these calculations for a number of solvents are given in Table B2.

Table B2. Thermochemical Values for H• Solvation and ΔG°(½ H_2 (g)/H•$_{1\ M}$)[a]

Solvent	$\Delta G_{solv.}$[b]	$-T\Delta S_{conv.}$[c]	$\Delta G°$(½ H_2 (g)/H•$_{1\ M}$)[d]
Acetonitrile	5.12	–1.75	52.0
N,N-dimethylformamide	5.23	–1.51	52.3
1,4-dioxane	5.10	–1.46	52.2
Acetone	4.83	–1.54	51.9
Tetrahydrofuran	4.87	–1.49	52.0
Toluene	4.78	–1.33	52.0
n-hexane	4.30	–1.20	51.7

[a] calculated using data from references [19] and [21], values in kcal mol^{-1} at 298 K; [b] ΔG_{solv} corresponding to eq B4; [c] $-T\Delta S_{conv}$ calculated per eq B8; [d] $\Delta G°$ corresponding to eq B2–B3 (eq 10–11 in main text). Uncertainty on these values estimated at ± 1 kcal mol^{-1}, largely from the assumption that the solvation of H• approximately equals that of H_2. See Section B.3.1.5 above and reference [15] for details.

We also note that the free energy for the solvation of H• and ΔG°(½ H_2 (g)/H•$_{1\ M}$) have been estimated in H_2O, which allows the standard potentials and BDFEs of select substrates to be compared across MeCN, THF, and H_2O (Table B3).

Table B3. Solvent dependence of standard potentials and BDFEs for PCET substrates and comparison with computed values.

Substrate	Solvent	$E°$ (V vs H_2)[a]	BDFE (kcal mol^{-1})[b]
1,4-hydroquinone	MeCN	0.664(4)	67.3
	THF	0.66(1)	67.4
	H_2O (expt.)	0.643	68.1
	H_2O (DFT)	0.690	69.2
2,6-dimethyl-1,4-hydroquinone	MeCN	0.550(7)	64.6
	THF	0.56(1)	64.9
	DMF	0.578(2)	65.6
	IPA	0.566(5)	nd[c]
	H_2O (expt.)	0.5475	65.9
	H_2O (DFT)	0.553	66.1
2,6-dimethoxy-1,4-hydroquinone	MeCN	0.469(7)	62.8
	H_2O (expt.)	0.473	64.2
	H_2O (DFT)	0.493	64.7
1,4-dihydroxynaphthalene	THF	0.46(1)	62.7
	H_2O (expt.)	0.377	62.0
	H_2O (DFT)	0.409	62.7
1,8-dichloro-9,10-dihydroxyanthracene	THF	0.150(8)	55.4
	H_2O (expt.)	0.115	56.0
	H_2O (DFT)	0.276	59.7

[a] Values for $E°$(V vs. H_2) in MeCN and THF are taken from Table 2.2 of the main text; values for DMF and IPA are from Sections B.2.3 and B.2.4 above; experimental and computed values in water are from ref. [22]. [b] BDFEs in MeCN and THF from Table 2.2 of the main text. Aqueous BDFEs calculated as $BDFE(X–H) = 23.06E°(X/XH_n) + \Delta G°(½H_2(g)/H^{\bullet}_{1M})$, using $\Delta G°(½H_2(g)/H^{\bullet}_{1\ M}) = 53.3$ kcal mol^{-1} for H_2O from ref. [15]. Absolute uncertainties in all BDFE values are ~ 1 kcal mol^{-1} and are dominated by the uncertainty in estimating the solvation of $H^{\bullet}$, as described in ref [15] and Section B.3 above. [c] not determined.

B.6 Calculating C_G Terms

C_G terms can be calculated per Scheme B1 using the standard hydrogen potential and free energy to convert ½H_2 (g) to 1M $H^{\bullet}$ in the solvent of interest. The resulting C_G values are with reference to $Fc^{+/0}$, the IUPAC standard for nonaqueous solvents.

Scheme B1. Thermochemical Cycle for Calculating C_G Term

$$H^+ + e^- \xrightleftharpoons{\Delta G^\circ = -FE^\circ(H^+/H_2)} (^1/_2)H_2\,(g) \qquad \text{(S16)}$$

$$(^1/_2)H_2\,(g) \xrightleftharpoons{\Delta G^\circ(^1/_2H_2\,(g)\,/H^\bullet{}_{1\,M})} H^\bullet\,(solv,\,1\,M) \qquad \text{(S17)}$$

$$H^+ + e^- \xrightleftharpoons{\Delta G^\circ(H^+/H^\bullet) \equiv C_G} H^\bullet\,(solv,\,1M) \qquad \text{(S18)}$$

Here we report corrected C_G values for acetonitrile and *N,N*-dimethylformamide to fix a sign error in our previous derivation of free energies corresponding to eq B17.[3] The corrected derivation is shown in Section B.5 above. Using $E^\circ(H^+/H_2)$ = –0.028 V vs $Fc^{+/0}$ (ref. [14]) and $\Delta G^\circ(½\ H_2\,(g)/H^\bullet{}_{1\,M})$ = 52.0 kcal mol^{-1} (Table B2) gives C_G(MeCN) = 52.6 kcal mol^{-1}. Similarly, for DMF, combining the reported $E^\circ(H^+/H_2)$ = –0.662 V vs $Fc^{+/0}$ (ref. [12]) and $\Delta G^\circ(½\ H_2\,(g)/H^\bullet{}_{1\,M})$ = 52.3 kcal mol^{-1} (Table B2) yields C_G(DMF) = 67.6 kcal mol^{-1}.

B.7 Comparing Open-Circuit Potential and Cyclic Voltammetry Measurements

In many cases, cyclic voltammograms (CVs) of PCET substrates in organic solvents show significant electrochemical irreversibility despite being chemically reversible. An example is depicted below in Figure B27A. CVs collected of DMQ and DTQ in a $pyrH^+$/pyr buffer in MeCN had peak-to-peak separations exceeding 500 mV, indicating electrochemical irreversibility of the $2e^-/2H^+$ process. The chemical reversibility of DMQ is evident from the equal amount of charge passed in the cathodic and anodic peaks. Given the nearly 1 V peak separation in the CV of DTQ, its apparent quasi-reversibility can likely be attributed to diffusion of H_2DTQ away from the electrode prior to being oxidized on the anodic sweep. The midpoint potentials of these CVs indicated that DMQ is more reducing than DTQ by about 20 mV. In contrast, OCP measurements collected in the same buffer condition showed the *opposite* ordering,

with DTQ being more reducing than DMQ by nearly 100 mV (Figure B27B). The expected Nernstian dependences of the OCP on the log ratio of hydroquinone to quinone were observed for both substrates.

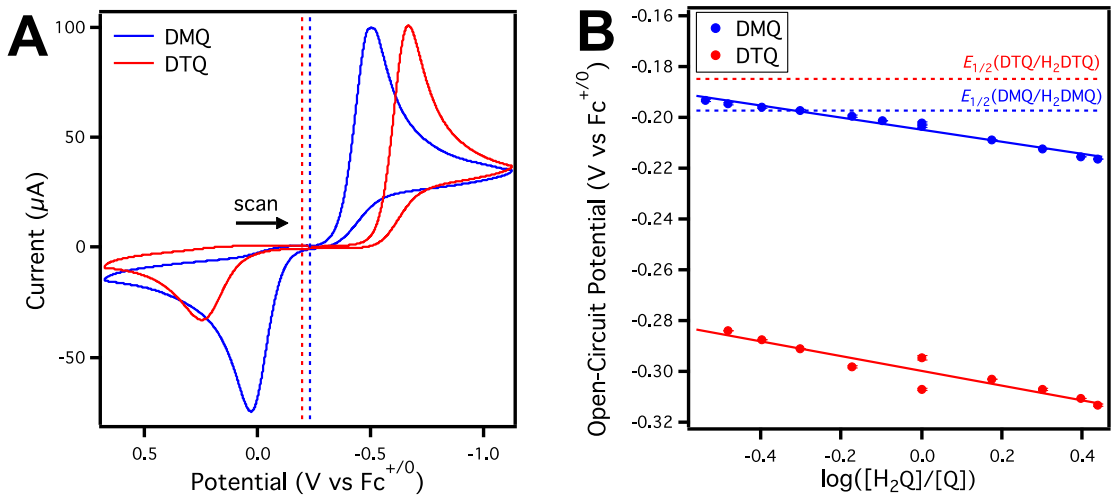

Figure B27. **(A)** CVs of 2 mM DMQ (blue) and 2 mM DTQ (red) in MeCN containing 50 mM pyrH$^+$/pyr buffer and 0.1 M [Bu$_4$N][PF$_6$] supporting electrolyte. Measurements collected at a 100 mV/s scan rate using a glassy carbon working electrode, Pt auxiliary electrode, and Ag pseudoreference electrode. Dashed lines are the midpoint potentials, suggesting that DMQ is more reducing than DTQ. **(B)** Open-circuit potentials measured at different ratios of DMQ:H$_2$DMQ (blue points) and DTQ:H$_2$DTQ (red points) in MeCN containing 50 mM pyrH$^+$/pyr buffer and 0.1 M [Bu$_4$N][PF$_6$] supporting electrolyte. Potentials plotted as a function of the log ratio of reduced to oxidized substrate. Measurements suggest that DTQ is more reducing than DMQ. Midpoint potentials from **A** shown as horizontal dashed lines for reference.

To probe whether the OCP or CV result was more accurate, the equilibration of H$_2$DTQ and DMQ was directly monitored by ^{1}H NMR spectroscopy. Qualitatively, the sample showed conversion to predominantly DTQ and H$_2$DMQ over time (Figure B28), consistent with the OCP result. Quantitative analysis was more challenging, as an expected potential difference of 100 mV corresponds to more than 3 orders of magnitude in K_{eq} for a redox process involving the transfer of 2e^-. The K_{eq} for eq B19 was determined from integrating the aromatic proton peaks of each quinone/hydroquinone species in the ^{1}H NMR spectrum collected after 54 hours of equilibration. The measured K_{eq} of 0.021 corresponds to ~50 mV in potential, with DTQ being more reducing. The ordering of potentials of the two quinones was

consistent with the OCP data, though the potential difference was smaller than what was observed by OCP measurements. There is likely significant uncertainty associated with the ^{1}H NMR equilibrium experiment, since the measured K_{eq} is so far from 1 and quinone decomposition can occur on such long timescales. Overall, this result suggests that the OCP method is more appropriate than CV for electrochemically measuring nonaqueous PCET potentials.

$$K_{eq} = \frac{[H_2DTQ][DMQ]}{[DTQ][H_2DMQ]} \quad \text{(B19)}$$

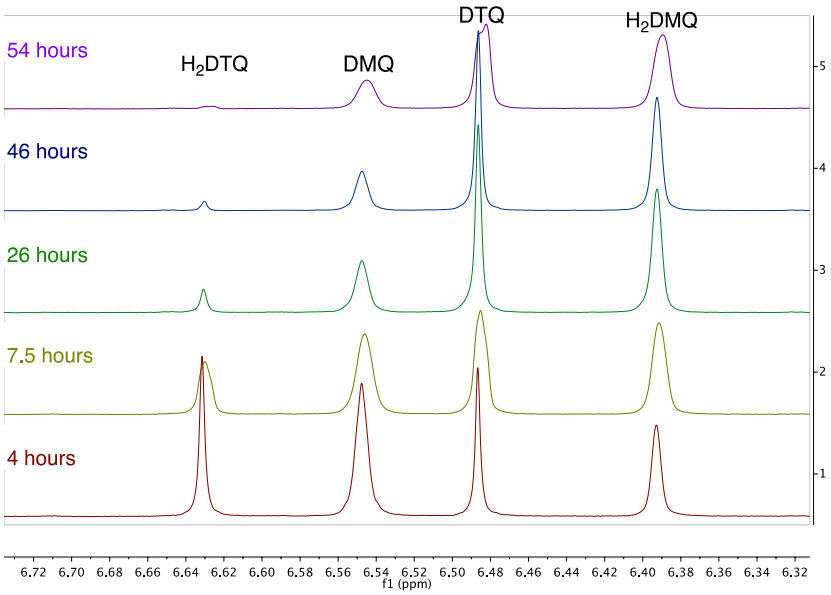

Figure B28. Aromatic region of ^{1}H NMR spectra of an equimolar mixture of H_2DTQ and DMQ in CD_3CN, showing conversion to predominantly DTQ and H_2DMQ over time.

To further investigate the accuracy of OCP and CV measurements for determining PCET potentials in organic solvents, we performed both techniques on the same buffered solution of DMQ/H_2DMQ at different working electrodes (Figure B29, Table B4). At gold, boron-doped diamond, and glassy carbon working electrodes, the OCP measurement plateaued around the same potential, –0.218 ± 0.003 V vs $Fc^{+/0}$. However, the variability in midpoint potential measured by CV was much larger, –0.19 ± 0.02 V vs $Fc^{+/0}$. This result suggests that the longer timescale OCP measurements

are more robust to reactions that are complicated by slow electrochemical kinetics, such as the PCET processes described here.

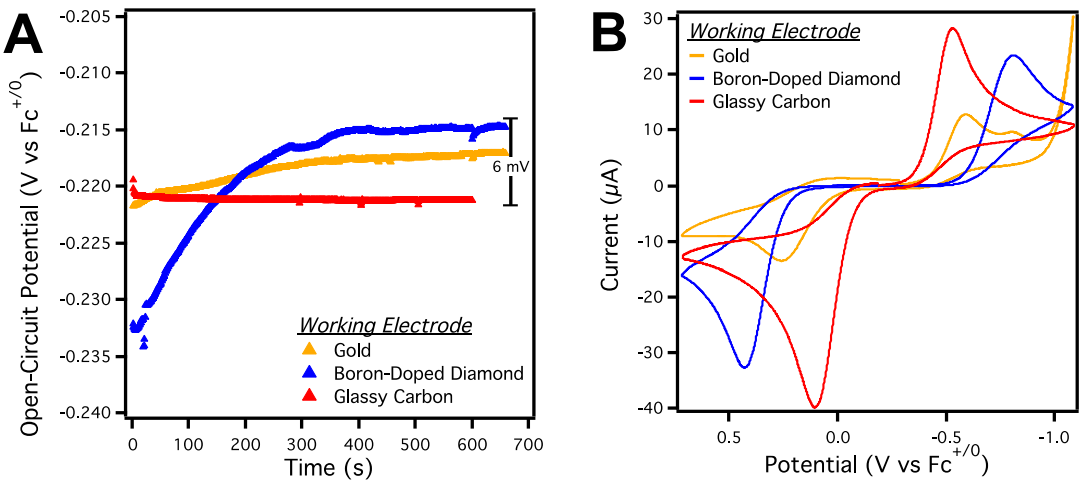

Figure B29. **(A)** Open-circuit potential measurements of a solution containing 0.6 mM H_2DMQ, 0.6 mM DMQ, and a 50 mM pyrH^+/pyr buffer with 0.1 M [Bu_4N][PF_6] supporting electrolyte collected at gold (gold), boron-doped diamond (blue), and glassy carbon (red) working electrodes in MeCN. For all measurements, data were collected every second for 600 s, and a Pt auxiliary electrode and Ag pseudoreference electrode were used. **(B)** Cyclic voltammograms of the same solution as in **A** at gold (gold), boron-doped diamond (blue), and glassy carbon (red) working electrodes. All collected at 100 mV/s scan rate.

Table B4. Comparison of Open-Circuit Potential and Midpoint Potential Measurements of the Same Solution at Different Working Electrodes

Working Electrode	OCP (V vs $Fc^{+/0}$)	$E_{1/2}$ (V vs $Fc^{+/0}$)
Gold	−0.217	−0.168
Boron-Doped Diamond	−0.215	−0.192
Glassy Carbon	−0.221	−0.215

In summary, these experiments indicate that the midpoint potential measured by CV often does not provide accurate thermodynamic information about PCET substrates in nonaqueous conditions, and we therefore highly recommend the OCP method instead.

B.8 References

1. Mann, F. G.; Saunders, B. C., Practical Organic Chemistry 4th ed.; Longman, Inc. : New York, 1960; pp 215-216.
2. Lee, J.; Shizu, K.; Tanaka, H.; Nakanotani, H.; Yasuda, T.; Kaji, H.; Adachi, C., Controlled emission colors and singlet–triplet energy gaps of dihydrophenazine-based thermally activated delayed fluorescence emitters. *J. Mater. Chem. C* **2015,** *3* (10), 2175-2181.
3. Mader, E. A.; Davidson, E. R.; Mayer, J. M., Large Ground-State Entropy Changes for Hydrogen Atom Transfer Reactions of Iron Complexes. *J. Am. Chem. Soc.* **2007,** *129* (16), 5153-5166.
4. Manner, V. W.; Markle, T. F.; Freudenthal, J. H.; Roth, J. P.; Mayer, J. M., The first crystal structure of a monomeric phenoxyl radical: 2,4,6-tri-tert-butylphenoxyl radical. *Chem. Commun.* **2008,** (2), 256-258.
5. Wittman, J. M.; Hayoun, R.; Kaminsky, W.; Coggins, M. K.; Mayer, J. M., A C–C Bonded Phenoxyl Radical Dimer with a Zero Bond Dissociation Free Energy. *J. Am. Chem. Soc.* **2013,** *135* (35), 12956-12959.
6. Burnett, M. G.; McKee, V.; Nelson, S. M., 5T2⇌1A1 and 6A1⇌2T2 spin transitions in iron(II) and iron(III) complexes of 2,2′-bi-2-imidazoline and related ligands. *J. Chem. Soc., Dalton Trans.* **1981,** (7), 1492-1497.
7. McCarthy, B. D.; Dempsey, J. L., Decoding Proton-Coupled Electron Transfer with Potential–pKa Diagrams. *Inorg. Chem.* **2017,** *56* (3), 1225-1231.
8. Favier, I.; Duñach, E., New protic salts of aprotic polar solvents. *Tetrahedron Lett.* **2004,** *45* (17), 3393-3395.
9. De Vries, J. G.; Kellogg, R. M., Reduction of aldehydes and ketones by sodium dithionite. *The Journal of Organic Chemistry* **1980,** *45* (21), 4126-4129.
10. Fulmer, G. R.; Miller, A. J. M.; Sherden, N. H.; Gottlieb, H. E.; Nudelman, A.; Stoltz, B. M.; Bercaw, J. E.; Goldberg, K. I., NMR Chemical Shifts of Trace Impurities: Common Laboratory Solvents, Organics, and Gases in Deuterated Solvents Relevant to the Organometallic Chemist. *Organometallics* **2010,** *29* (9), 2176-2179.
11. Izutsu, K., *Electrochemistry in Nonaqueous Solutions*. Wiley-VCH: Weinheim, 2002.
12. Pegis, M. L.; Roberts, J. A. S.; Wasylenko, D. J.; Mader, E. A.; Appel, A. M.; Mayer, J. M., Standard Reduction Potentials for Oxygen and Carbon Dioxide Couples in Acetonitrile and N,N-Dimethylformamide. *Inorg. Chem.* **2015,** *54* (24), 11883-11888.
13. Kaljurand, I.; Kütt, A.; Sooväli, L.; Rodima, T.; Mäemets, V.; Leito, I.; Koppel, I. A., Extension of the Self-Consistent Spectrophotometric Basicity Scale in Acetonitrile to a Full Span of 28 pKa Units: Unification of Different Basicity Scales. *The Journal of Organic Chemistry* **2005,** *70* (3), 1019-1028.
14. Roberts, J. A. S.; Bullock, R. M., Direct Determination of Equilibrium Potentials for Hydrogen Oxidation/Production by Open Circuit Potential Measurements in Acetonitrile. *Inorg. Chem.* **2013,** *52* (7), 3823-3835.
15. Armstrong, D. A.; Huie, R. E.; Koppenol, W. H.; Lymar, S. V.; Merényi, G.; Neta, P.; Ruscic, B.; Stanbury, D. M.; Steenken, S.; Wardman, P., Standard electrode potentials involving radicals in aqueous solution: inorganic radicals (IUPAC Technical Report). *Pure Appl. Chem.* **2015,** *87* (11-12), 1139-1150.
16. Warren, J. J.; Tronic, T. A.; Mayer, J. M., Thermochemistry of Proton-Coupled Electron Transfer Reagents and Its Implications. *Chem. Rev.* **2010,** *110*, 6961-7001.
17. Gerken, J. B.; Stahl, S. S., High-Potential Electrocatalytic O_2 Reduction with Nitroxyl/NO_x Mediators: Implications for Fuel Cells and Aerobic Oxidation Catalysis. *ACS Cent. Sci.* **2015,** *1* (5), 234-243.
18. Chantooni, M. K.; Kolthoff, I. M., Resolution of acid strength in tert-butyl alcohol and isopropyl alcohol of substituted benzoic acids, phenols, and aliphatic carboxylic acids. *Anal. Chem.* **1979,** *51* (1), 133-140.
19. Linstrom, P. J.; Mallard, W. G., NIST Chemistry WebBook, NIST Standard Reference Database Number 69. National Institute of Standards and Technology Gaithersburg, MD 20899.

20. Roduner, E.; Bartels, D. M., Solvent and isotope effects on addition of atomic hydrogen to benzene in aqueous solution. *Berichte der Bunsengesellschaft für physikalische Chemie* **1992,** *96* (8), 1037-1042.
21. Brunner, E., Solubility of hydrogen in 10 organic solvents at 298.15, 323.15, and 373.15 K. *J. Chem. Eng. Data* **1985,** *30* (3), 269-273.
22. Huynh, M. T.; Anson, C. W.; Cavell, A. C.; Stahl, S. S.; Hammes-Schiffer, S., Quinone $1e^-$ and $2e^-/2H^+$ Reduction Potentials: Identification and Analysis of Deviations from Systematic Scaling Relationships. *J. Am. Chem. Soc.* **2016,** *138* (49), 15903-15910.

Appendix C Supplementary Information for Chapter 3

Adapted from the supporting information for Agarwal, R. G.; Kim, H. J.; Mayer, J. M. "Nanoparticle O–H Bond Dissociation Free Energies from Equilibrium Measurements of Cerium Oxide Colloids." *J. Am. Chem. Soc.* **2021**, *143*, 2896-2907.

C.1 General Considerations

C.1.1 Materials

All chemicals were purchased commercially (vendor given as mentioned) and used without further purification, unless otherwise specified. 1,3,5-trimethoxybenzene (TMB) was purchased from Sigma-Aldrich. See Section C.5 for details on the purification of quinones and synthesis of hydroquinones used in this study. All deuterated solvents were purchased from Cambridge Isotope Laboratories, degassed, and dried over sieves for >2 days before use. All proteo solvents used were treated using a Pure Process Technology solvent purification system which degassed solvent with Argon and dried it over activated alumina, unless otherwise specified. Tetrahydrofuran (THF) was always inhibitor-free (Fisher, HPLC grade). All water was dispensed from a Synergy®-R Millipore system as ultra-pure water (18.2 MΩ·cm) unless otherwise specified.

C.1.2 Instruments

Powder X-ray diffraction (p-XRD) patterns were obtained on Rigaku MiniFlex600 Powder X-Ray Diffractometer with sealed Cu X-ray source (λ = 1.5418 Å). ^{1}H NMR spectra for reactions were always collected on an Agilent DD2 500 MHz spectrometer, while those for characterization were also carried out on an Agilent DD2 400 MHz spectrometer and an Agilent DD2 600 MHz spectrometer. Data were processed using MestReNova© software. Chemical shifts were reported relative to TMS by referencing the residual proteo solvent in THF-d_8 solutions or a 1,3,5-trimethoxybenzene internal standard for THF/THF-d_8 mixtures. Dynamic Light Scattering (DLS) data was collected on a NanoBrook Omni, Brookhaven Instruments using a 640 nm laser. Transmission

Electron Microscopy (TEM) images were obtained on FEI Tecnai Osiris 200kV transmission electron microscope operating at 200kV. TEM samples were prepared on the bench by dropping 10 μL of a [Ce atoms] = 1 mM solution in cyclohexane (Sigma-Aldrich, Spectroscopy grade, used from bottle) on a lacey carbon 400 mesh Cu grid (Ted Pella, Inc.) and allowing the grid to air-dry. The size and the distribution of NCs were obtained by counting nanoparticles with ImageJ software. Inductively-coupled plasma mass spectroscopy (ICP-MS) was carried out using a Perkin Elmer ICP-MS Elan DRC-e instrument with Fluka TraceCERT® High Purity brand Ce standard (1000 ± 2 mg/L in 2% HCl). UV-Vis data were collected using an Agilent Cary 60 UV-Vis spectrophotometer.

C.1.3 Nanoparticle Preparation

Oleate-capped ceria NCs (OLE-Ce) were synthesized through modification of a published procedure.[1] Sodium oleate ($C_{17}H_{33}COONa$, STREM, 99%, 2.12 g, 7.0 mmol) was dissolved in 15 mL of warmed ultra-pure water (18.2 MΩ·cm). The resulting solution was then allowed to cool to room temperature before dropwise addition to a stirring solution of 1.92 g (3.5 mmol) ceric ammonium nitrate ($(NH_4)_2Ce(NO_3)_6$, Sigma-Aldrich, 99.9%) in 15 mL ultra-pure water to give a fine white precipitate. Subsequently, 4.5 mL of aqueous ammonia solution (28 wt. % (≥99.99% trace metals basis), Sigma-Aldrich) was added dropwise under vigorous stirring to the reaction mixture over the course of ~1 minute. After ~10 minutes a homogeneous light tan colloid formed. The mixture was stirred for an additional 45 minutes. Products were collected by centrifugation (6500 rpm for 15 min.), followed by decantation, two washes with ultra-pure water to remove excess starting materials, and two washes with ethanol to remove excess oleic acid. After the last centrifugation and decantation, the remaining tan solids were consolidated into two glass test tubes and dried at 90 ºC for 24 h in an oven under air. The resulting black glassy solid was brought into an

N_2 glovebox, and dissolved in tetrahydrofuran, although a small amount of precipitate remained. These precipitates were removed by filtration. The resulting clear brown solution was stored under N_2 in the freezer at –30 ºC (Figure C1).

Two batches of oleate-capped cerium oxide nanoparticles (**Ce-1** and **Ce-2**) were prepared using the procedure above. A third batch (**Ce-L**) was synthesized following the same procedure except that the tan colloid formed after addition of $NH_{3\,(aq)}$ solution was heated to 150 °C for 21 hours in a Parr bomb reactor while stirring.[1] The subsequent washing procedure was modified so that the solids were washed three times with ultra-pure water.

Figure C1. Picture of **Ce-1** colloid in THF.

C.1.4 ^{1}H NMR Spectroscopy Time Course Experimental Details

Quantitative ^{1}H NMR measurements were performed in mixtures of THF-d_8 and proteo-THF with the aid of solvent suppression (PreSat pulse sequence) using 1,3,5-trimethoxybenzene (TMB) as an internal standard. Samples were measured in the presence of proteo-THF in order to avoid the extra manipulation involved in creating a stock of the nanoceria colloid in THF-d_8. No significant differences were observed between measurements run in mixtures as opposed to only THF-d_8. NMR Experiments used 16 scans and a relaxation delay of 40 seconds (5 times the highest T_1 for an integrated peak) to ensure proper quantitation. For stoichiometric and equilibration

reactions with oleate-capped cerium oxide nanoparticles, the concentration of Ce atoms was generally 9 mM and 8 mM TMB was present. In equilibration reactions, an excess of the organic PCET reagent was always added (~10 mM of hydrogen atom equivalents).

All samples were prepared in NMR tubes equipped with J. Young valves using standard glovebox procedures in an air-free N_2 environment at room temperature. For time courses, samples were stored in the glovebox and covered with aluminum foil between measurements. These steps were necessary to prevent O_2 leakage through the J. Young seal and the light induced reaction of THF and quinones over the long timescales of experiments.[2] Spectra were referenced to the aromatic peak of TMB, whose chemical shift (6.043 ppm) was identified from experiments in THF-d_8. MestReNova® was used to phase, baseline correct, and integrate spectra. Reactions were nearly complete in two days, but demonstrated multi-exponential kinetics. As a result, they were followed for over 1-2 weeks to ensure thermal equilibrium had been reached. Reactions were considered complete when the quantity of product had plateaued by ^{1}H NMR. Values of organic product produced were determined by averaging all time points in the plateau region.

C.2 Characterization of OLE-Ce

C.2.1 Sizing by p-XRD, TEM, and DLS

Sizing of OLE-Ce colloids was evaluated by up to three methods. TEM (Figure C2) gave the size of the inorganic core of the nanoparticle and standard deviation over a relatively small sample size (>200 nanoparticles), p-XRD (Figure C3) gave the size of crystalline domains for the bulk sample via the Scherrer equation, and DLS (Figure C4) probed the solution dispersity and hydrodynamic radius of OLE-Ce. The values determined from these three methods were self-consistent for **Ce-2**. The size determined from p-XRD is the smallest at 1.4 ± 0.3 nm while the values from TEM is

slightly larger at 1.9 ± 0.3 nm consistent with an amorphous surface and crystalline core as TEM measures the size of the entire inorganic core, while p-XRD only measures the size of the crystalline domains. Additionally, sizing by DLS gives a significantly larger value of 4.7 ± 1.0 nm because it should measure the size of the entire nanoparticle including ligands and associated solvent. Given that an unkinked structure of oleate is ~2.1 nm this data is consistent with a non-aggregated solution nanoparticle structure.

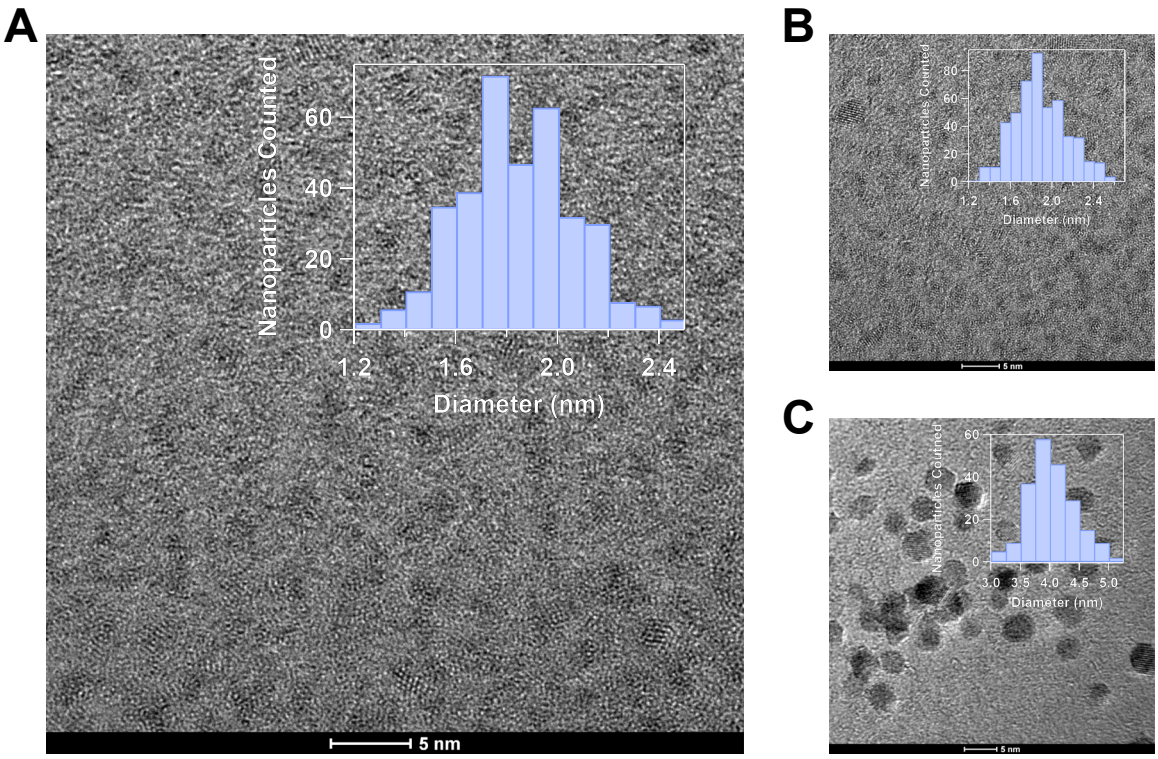

Figure C2. TEM images with size histograms of (A) **Ce-1** with an avg. diameter of 1.8 ± 0.2 nm, (B) **Ce-2** with an avg. diameter of 1.9 ± 0.3 nm, and (C) **Ce-L** with an avg. diameter of 4.0 ± 0.4 nm.

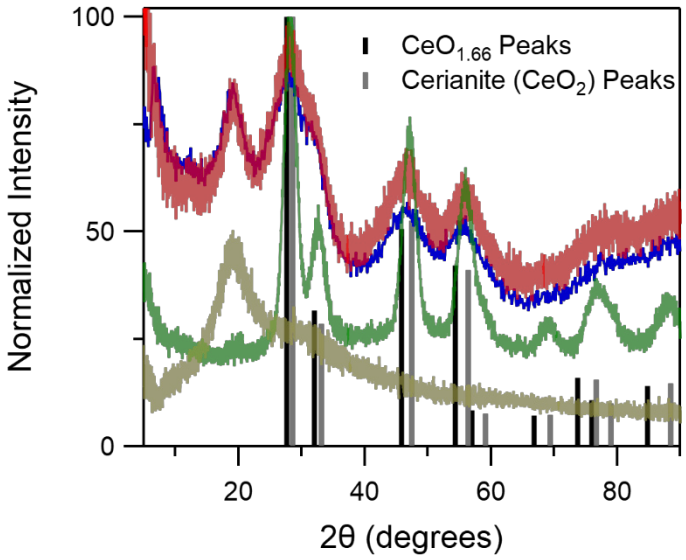

Figure C3. Powder XRD data of **Ce-1** (blue), **Ce-2** (red), **Ce-L** (green), and oleic acid (gold). Peak positions are best fit by cerianite (CeO_2, COD ID: 9009008) and $CeO_{1.66}$ (COD ID: 1521459). Samples were prepared on glass slides on the benchtop by concentrating OLE-Ce stock solutions with a hot plate. Estimated sizes are 1.3 ± 0.3 nm, 1.4 ± 0.3 nm, and 3.2 ± 0.5 nm for **Ce-1**, **Ce-2**, and **Ce-L**, respectively. Peak fits and size estimations were performed using Rigaku PDXL software.

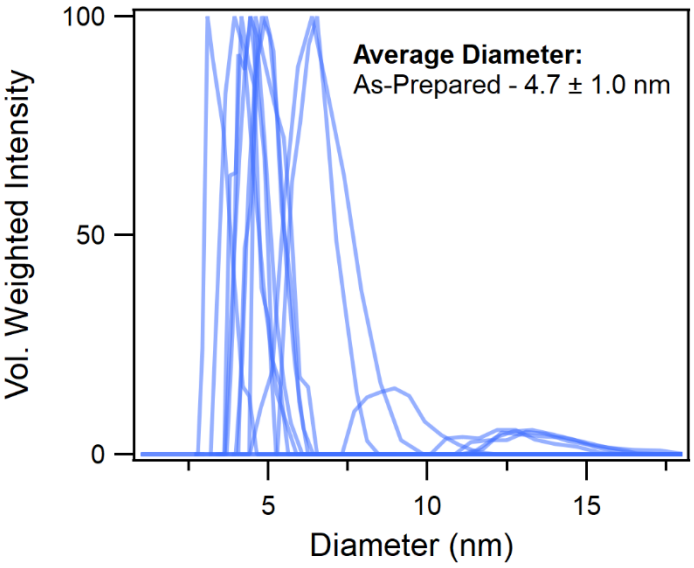

Figure C4. DLS data of **Ce-2** One data set consists of ten runs and all are shown above. The average diameter was calculated to be 4.7 ± 1.0 nm by averaging the diameter for the peak of Volume (Vol.) Weighted Intensity in each run. Calculation of the Vol. Weighted Intensity was achieved with Brookhaven Particle Solutions software. Samples were measured under air in glass cuvettes.

C.2.2 Nanoparticle Statistics

Calculation of cerium atoms per nanoparticle:

The lattice parameter (a) for fluorite unit cell of cerium oxide is 0.5411 nm. We note that previous investigations have shown that the lattice parameter of cerium oxide nanoparticles is size dependent, but that this correction is smaller than the errors associated with this analysis.[3]

The volume of a nanoparticle (V_{NP}) is $4/3\pi r^3$ calculated assuming a sphere of radius r, and the volume of the unit cell (V_{uc}) is a^3 for a fluorite structure. Therefore, since there are 4 Cerium atoms per unit cell, the number of cerium atoms per nanoparticle (N_{NP}) is calculated as follows:

$$N_{NP} = 4*(V_{NP} / V_{uc}) \quad \text{(C1)}$$

The number of surface cerium atoms per nanoparticle was estimated using two methods:

Method 1:

The surface is estimated as a symmetric truncated octahedron with 6 square (100) and 8 hexagonal (111) facets, as has been previously observed for uncapped ceria nanoparticles (3-10 nm) in this size regime.[4] Under these assumptions the nanoparticle surface is 77.6% (111) and 22.4% (100) by area. Based upon the fluorite structure of the cerium oxide unit cell there are 1.875 cerium atoms per unit cell area of (111) facet and 0.875 cerium atoms per unit cell area of (100) facet. Furthermore, since cerium oxide adopts a fluorite structure the areas (A) of the (111) and (100) facets is as follows:

$$A_{(111)} = \sqrt{3}/2*a^2 \quad \text{(C2)}$$

$$A_{(100)} = a^2 \quad \text{(C3)}$$

The number of surface cerium atoms per nanoparticle (N_{surf}) is shown in eq C4 where the total surface area is estimated as that of a sphere ($4\pi r^2$).

$$N_{surf} = 1.875\frac{0.776(4\pi r^2)}{A_{(111)}} + 0.875\frac{0.224(4\pi r^2)}{A_{(100)}} \quad \text{(C4)}$$

Method 2:

The number of surface cerium atoms was also estimated by assuming the thickness of the surface layer is the length of a typical Ce-O bond which is estimated as 0.2094 nm.[5] The volume of the surface (V_s) was then calculated for two Ce-O bond lengths to consider both surface and near surface sites:

$$V_s = 4/3\pi(r^2 - (r - (2 \times 0.2094))^2) \quad \text{(C5)}$$

From here N_{surf} is easily calculated via a method analogous to equation C2:

$$N_{NP} = 4*(V_s / V_{uc}) \quad \text{(C6)}$$

Table C1. Nanoparticle statistics for various sizes of cerium oxide nanoparticles

		Method 1 [b]		Method 2 [c]	
Diameter (nm)	N_{NP} [a]	N_{surf}	N_{surf} / N_{NP}	N_{surf}	N_{surf} / N_{NP}
1.6	54	52	0.95	48	0.89
1.7	65	58	0.90	56	0.87
1.8	77	65	0.85	65	0.85
1.9	91	73	0.80	75	0.83
2.0	106	81	0.76	85	0.80
2.1	122	89	0.73	96	0.78
2.2	141	97	0.69	107	0.76
3.6	617	261	0.42	338	0.55
4.0	846	322	0.38	428	0.51
4.4	1126	390	0.35	528	0.47

[a] The total number of cerium atoms is estimated by approximating the nanoparticle as a sphere. [b] The number of surface sites is estimated by approximating the surface as a symmetric truncated octahedron with (111) and (100) facets exposed. [c] The number of surface sites is estimated by approximating the surface as a spherical shell with a thickness of two Ce-O bond lengths.

Applying the values above to OLE-Ce colloids is complicated by the distribution of nanoparticle sizes considered observed by TEM (see Figure C2). However, even after considering this range and two different methods for calculating the number of surface sites the percentage of surface cerium atoms changes significantly from **Ce-1** and **Ce-2** (69-95%) to the larger **Ce-L** (35-55%).

C.2.3 ICP-MS Determinations of the Concentration of Cerium Atoms in OLE-Ce Colloids

The concentration of cerium atoms in OLE-Ce stock solutions was determined by taking an aliquot (<0.1 mL) of the THF stock solution and calcining the residual organic matter. The resulting yellow solid was digested in a 1 mL mixture of 1:1 concentrated H_2SO_4 and 50 wt. % $H_2O_{2\,(aq)}$. *We caution the reader that this mixture is hazardous so it should always be freshly prepared and quickly disposed, the volume*

should be kept to a minimum, and all manipulations should be done in a fumehood. Four samples were prepared via serial dilutions of the digested nanoparticles and the Fluka Ce standard. ICP-MS analysis of the samples by the method of standard additions gave the cerium concentration of the initial OLE-Ce stock solution. All concentration measurements shown in Table C2 were done starting from the calcination.

Table C2. Compilation of ICP-MS analyses for different batches of nanoceria colloids including repeats.

Sample [a]	Concentration of Ce Atoms (mM)	R^2 [b]
Ce-1	130.1	0.999
Ce-1	131.1	0.999
Ce-2	80.4	0.999
Ce-2	85.3	0.999
Ce-L	146.6	0.999

[a] For each entry sample preparation began by calcining an aliquot of the referenced stock solution. [b] Propagation of error associated with fit gives a standard deviation less than 0.1 mM. As a result, final values and errors were determined by averaging data from multiple runs when possible.

C.2.4 ^{1}H NMR Determination of the Concentration of Oleate/Oleic Acid Capping Ligands

The concentration of oleate/oleic acid capping ligands was measured for the **Ce-1** colloid by adding 5 uL 37 wt% $HCl_{(aq)}$ to an NMR sample containing [Ce atoms] = 9.1 mM and [TMB] = 4.7 mM in THF/THF-d_8. After this procedure all bound ligands are protonated and can be observed as free oleic acid in the ^{1}H NMR spectrum. The total amount of oleate/oleic acid in the as-prepared **Ce-1** colloid was then quantified vs the TMB standard as 139 mM. This corresponds to roughly a 1:1 ratio between oleate/oleic acid and cerium atoms.

C.3 X-ray Absorption Spectroscopy Experimental Details

XAS measurements were performed at the Advanced Photon Source on the bending-magnet beamline 9-BM-B with electron energy of 7 GeV and average current of 100 mA. The radiation was monochromatized by a Si (111) double-crystal monochromator. Fluorescence data were collected at the Ce L_{III}-edge (5723 eV) using a Vortex-ME™ multi-element Silicon drift detector, manufactured by SII NanoTechnology USA, Inc. Energies were calibrated to a Cr (5989.02 eV) foil reference. Samples were prepared in Charles Supper Company 1.0 mm OD quartz capillaries (wall thickness of 0.01 mm) that are 80 mm in length. Addition of liquid samples to these capillaries was accomplished in an N_2 glovebox atmosphere before sealing with Apiezon M-grease. Samples were then removed from the glovebox and sealed with hot wax. This procedure proved robust for preventing degradation of even the most air-sensitive samples. Iron bis(trimethylsilyl)amide (a pyrophoric liquid) was stable over the course of weeks in these capillaries. Sealed capillaries were shipped to APS and loaded onto a metal support with double sided tape (Figure C5). An X-Y positional fluorescence scan was then used to locate each sample prior to data collection.

Spectra were normalized using standard procedures in Athena.[6] Edge positions were determined by locating the maximum of the first peak in the first-derivative spectrum. The ratio of cerium oxidation states was determined using Athena by fitting the XANES region (-6 to +22 eV) with an arctan edge step and five unit normalized Gaussian functions, and using equation C6. Peak widths were held constant throughout the fitting procedure, while peak positions were allowed to float within a reasonable range as described in Table C3.[7-9]

$$\%Ce^{3+} = \frac{C}{A_1+A_2+B+C} \times 100\% \qquad \text{(C6)}$$

Table C3. Ce L_{III}-edge XANES assignments and information about peaks fits.

Peak	Assignment	Transition [a]	Center (eV)	Function	Step	Width (eV)
A_1	Ce^{4+}	$2p_{3/2}4f^0 \rightarrow 2\underline{p}_{3/2}4f^05d^*$	5741.5	Gaussian	--	2.0
A_2	Ce^{4+}	$2p_{3/2}4f^0 \rightarrow 2\underline{p}_{3/2}4f^05d^*$	5737.7	Gaussian	--	2.4
B	Ce^{4+}	$2p_{3/2}4f^1\underline{L} \rightarrow 2\underline{p}_{3/2}4f^15d^*\underline{L}$	5730.9	Gaussian	--	2.6
C	Ce^{3+}	$2p_{3/2}4f^0 \rightarrow 2\underline{p}_{3/2}4f^15d^*$	5726.3	Gaussian	--	2.2
D	--	$2p_{3/2}4f^0 \rightarrow 2\underline{p}_{3/2}4f^*$	5720.4	Gaussian	--	2.0
--	--	--	5725.0	ArcTan	1.0	0.94

[a] These transition assignments are based on previous work.[7-9] An underlined state indicates a hole, whereas an asterisk indicates an excited electron.

Figure C5. Set-up for XANES measurements of air-free solutions in quartz capillaries.

C.4 Reversibility of OLE-Ce Redox Reactions

C.4.1 Limits of OLE-Ce Redox

Addition of excess H_2DCAQ results in new peaks in the ^{1}H NMR below 0 ppm (Figure C6) and a loss of mass balance with respect to the total amount of H_2DCAQ and DCAQ in solution from >90% to <80%. As a result, the maximum extent of OLE-Ce reduction was defined by the maximum %Ce^{3+} achieved via the oxidation of H_2DCAQ before new peaks below 0 ppm appeared in the ^{1}H NMR spectrum. These

peaks likely correspond to a solution-phase oleate-bound cerium species based on the identification of similar peaks below zero for cerium(III) oleate (Figure C6).

The lowest $\%Ce^{3+}$ characterized by both ^1H NMR and XANES for OLE-Ce colloids was achieved using excess DPPH as an oxidant and following production of DPPH-H which plateaus after several days. Both the minimum and maximum $\%Ce^{3+}$ states were characterized by XANES and ^1H NMR (Table C4).

Additionally, OLE-Ce treated initially with excess *meta*-chloroperoxybenzoic acid (*m*CPBA) was observed to react subsequently with DPPH-H. Characterization of the reaction between OLE-Ce and *m*CPBA was challenging as addition of excess *m*CPBA to a solution of OLE-Ce causes displacement of oleate ligands such that significantly more free oleic acid is observed by ^1H NMR. We hypothesize that the excess *m*CPBA is binding to the nanoparticle surface as even upon addition of significant excesses of *m*CPBA only the product *meta*-chlorobenzoic acid is observed by ^1H NMR. Additionally, *m*CPBA decomposes in THF solutions by an unknown process which is accelerated in the presence of OLE-Ce. As a result, the extent of OLE-Ce oxidation by *m*CPBA was characterized by following the decrease in DPPH-H ^1H NMR signal over time, which reaches a plateau. Loss of DPPH-H integration occurred concurrently with a change in solution color from orange (DPPH-H) to purple (DPPH). It is notable that *m*CPBA does not oxidize DPPH-H in the absence of OLE-Ce. These data indicate that an equilibrium state is reached between OLE-Ce and the DPPH/DPPH-H $1e^-/1H^+$ redox couple.

Table C4. Limits of OLE-Ce Redox by ^{1}H NMR

Reactant [a]	Anchor [b]	$\Delta\%Ce^{3+}$	$\%Ce^{3+}$ by XANES
H_2DCAQ [c]	as-prepared **Ce-1**	50 – 54%	--
DPPH	as-prepared **Ce-1**	-6%	23
*m*CPBA/DPPH-H	**Ce-1**/*m*CPBA	1%	21
H_2DCAQ	**--**	--	76
H_2DCAQ [d]	**--**	--	72
DPPH [d]	**Ce-2**	-10.7%	16
H_2DCAQ [e]	**--**	--	30
DPPH [e]	**Ce-L**	-2.4%	11

[a] In all cases reagents were added in excess unless otherwise specified. If two reagents are listed, they were added one after another so that the first reaction had reached completion before the second reagent was added. [b] This refers to the state from which $\Delta\%Ce^{3+}$ was calculated in ^{1}H NMR experiments. [c] Addition was stoichiometric such that **Ce-1** was reduced to the maximum extent before new peaks appeared below 0 ppm in the ^{1}H NMR spectrum (see Figure C6). [d] Reacted with as-prepared **Ce-2**. [e] Reacted with as-prepared **Ce-L**.

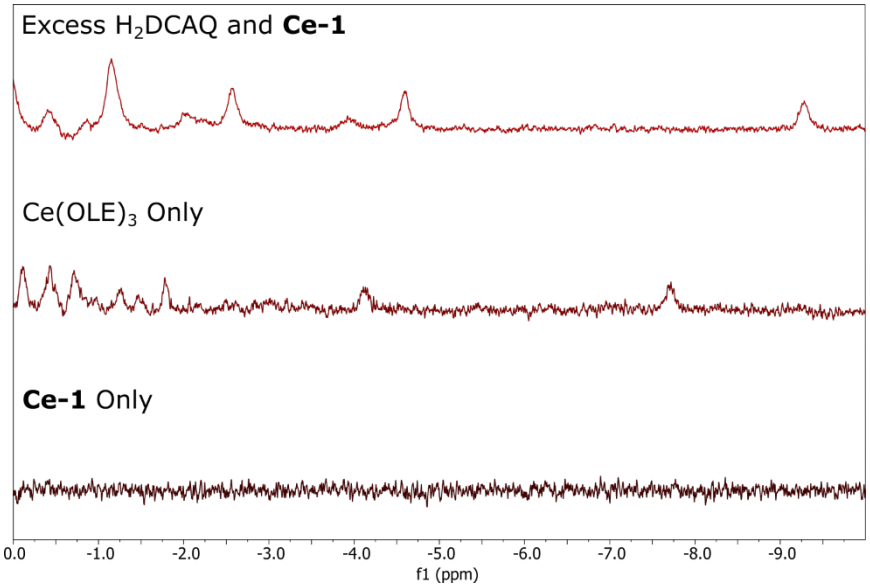

Figure C6. ^{1}H NMR samples of **Ce**-**1** (bottom), $Ce(OLE)_3$ (middle), and **Ce**-**1** with excess H_2DCAQ (top) in d_8-THF. **Ce**-**1**/H_2DCAQ sample contained 8 mM Ce atoms and 5 mM H_2DCAQ before reaction and was measured one day after H_2DCAQ addition.

C.4.2 Linear Correlations between Molar Absorptivity and %Ce^{3+} for OLE-Ce Colloids

Previous work by our group established that linear correlations are observed between the molar optical density of nanoceria colloids at 340 nm (Molar OD_{340}) and their %Ce^{3+} determined by XANES.[10] Here we build upon these studies by demonstrating linear correlations between Molar OD_{340} and %Ce^{3+} determined by ^{1}H NMR for both **Ce-1** and **Ce-L** (Figure C7).

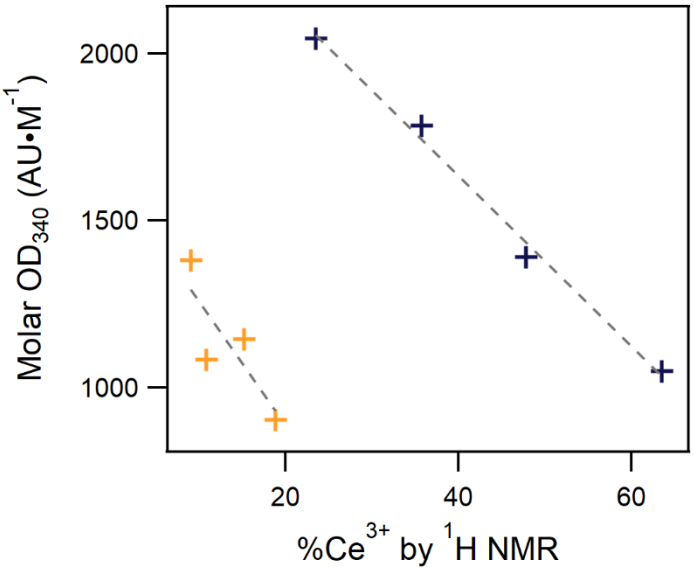

Figure C7. The %Ce^{3+} of **Ce-1** (blue) and **Ce-L** (orange) were varied using H_2DCAQ. Molar OD_{340} values were determined by subtracting contributions of leftover DCAQ (quantity determined by ^{1}H NMR) from the overall UV-Vis spectrum.

C.4.3 Redox Effects on OLE-Ce Size and Capping Ligands

The effect of %Ce^{3+} changes on OLE-Ce size were evaluated by DLS. Samples of **Ce-2** were measured before and after photolysis and showed no measurable change in size distribution (Figure C8). See our previous work with OLE-Ce colloids for further information on photolysis procedures and evidence by TEM that redox state changes do not affect size.[10]

Additionally, the effect of %Ce^{3+} on the oleate/oleic acid capping ligands was examined by following changes to their alkenyl C-H protons by ^{1}H NMR (Figure C9A). Results demonstrate that while changes to the peak do occur, they are reversible

(Figure C9B). The origin of the loss oleate/oleic acid mass balance at high $\%Ce^{3+}$ is unknown, but may be related to the increase in paramagnetic Ce^{3+} sites. In order to better explore this phenomenon spectra of **Ce-1** were collected at -50 °C, where the contributions to the alkenyl C-H peak deconvolute, while varying the $\%Ce^{3+}$ in both directions (Figure C10A). In these experiments only contributions from free oleic acid are visible at low $\%Ce^{3+}$, but at high $\%Ce^{3+}$ two new peaks steadily grow in while the quantity of oleic acid decreases (Figure C10B). While it is unclear what causes the growth of these new contributions to the spectrum, these changes are reversible upon oxidation of **Ce-1**.

Finally, the effect of redox changes on water ligands, and vice versa, was studied by ^1H NMR. A linear correlation between $\%Ce^{3+}$ and $[H_2O]$ is observed (Figure C11). However, addition of 3Å sieves to remove H_2O had no effect on the reversibility of redox reactions at **Ce-1** (Figure C12). In summary, while there are clearly changes to the ligand sphere of OLE-Ce with changes in $\%Ce^{3+}$ the studies we have performed indicate that these changes are largely reversible and have little effect on redox reactivity of OLE-Ce (see also Table C7).

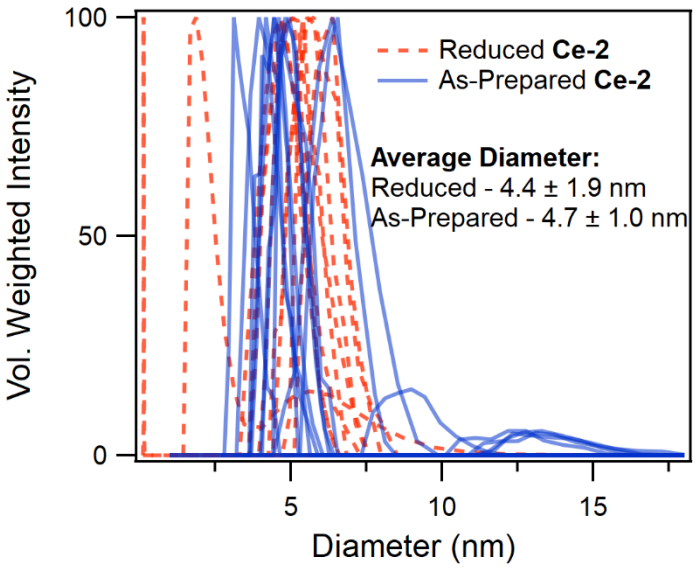

Figure C8. Sizing data of as-prepared (blue solid) and photochemically reduced (red dashed) **Ce-2** by DLS. Each data set consists of 10 run (shown as separate peaks) that are plotted in terms of the diameter for the peak of Volume (Vol.) Weighted Intensity in each run. Calculation of the Vol. Weighted Intensity was achieved with Brookhaven Particle Solutions software. Samples were measured under air in glass cuvettes.

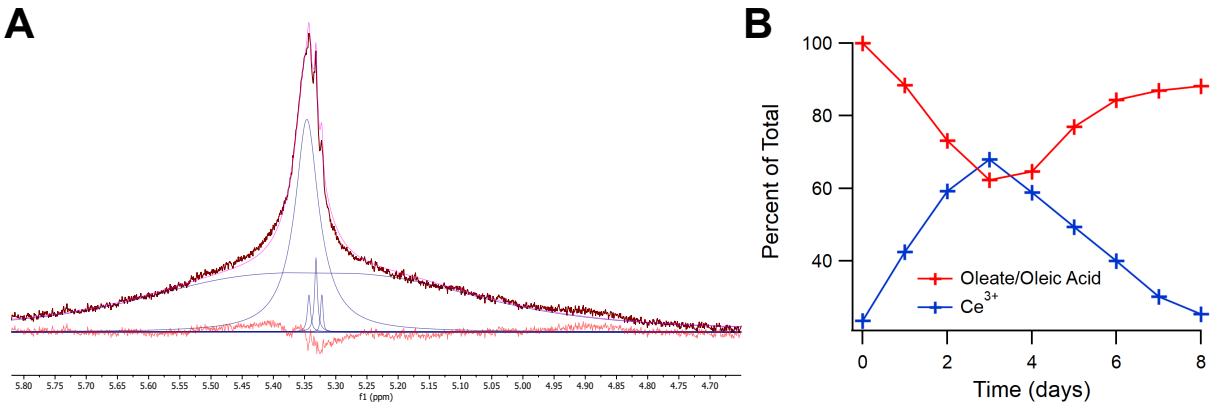

Figure C9. The sample solution contains as-prepared **Ce-1** to which aliquots of H_2DCAQ and DPPH stock solutions are added, respectively, to either increase or decrease %Ce^{3+}. (A) ^{1}H NMR spectrum (dark red) of the alkenyl proton region of bound/free oleate/oleic acid fit to five voigt lineshapes (blue). The overall fit (pink) and residual (red) are also included. The two voigt lineshapes of significant integration are assigned to bound oleate/oleic acid, whereas the remaining three smaller lineshapes are assigned to free oleic acid based on spectra of just the free acid. Fits were done in MestReNova®. (B) Trend between %Ce^{3+} and changes in mass balance of alkenyl proton peaks assigned to bound oleate/oleic acid, as determined vs. an internal 1,3,5-trimethoxybenzene standard.

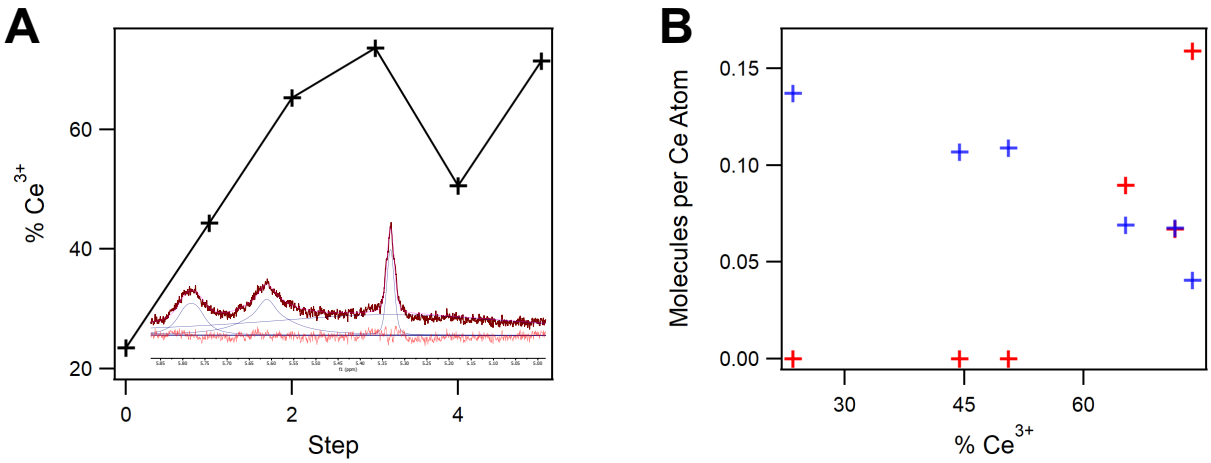

Figure C10. The sample solution contains as-prepared **Ce-1** to which aliquots of H_2DCAQ and DPPH stock solutions are added, respectively, to either increase or decrease %Ce^{3+}. All spectra were taken at -50 °C. In (A) the main plot describes how the %Ce^{3+} of **Ce-1** was varied during this experiment. Each step refers to the addition of an aliquot of either H_2DCAQ or DPPH stock solutions in order to either increase or decrease %Ce^{3+} in time. Additionally, the inset shows a representative ^{1}H NMR spectrum (dark red) of the alkenyl proton region of bound/free oleate/oleic acid for reduced **Ce-1** fit to four voigt lineshapes (blue) where the first two peaks are unknown species (UL), which appear in roughly a 1:1 ratio, and the sharper feature to the right is assigned as free oleic acid (OA) based on spectra of just the pure acid. Fits were done in MestReNova®. (B) Plot of the amounts of UL (red) and OA (blue) per cerium atom, as determined vs. an internal 1,3,5-trimethoxybenzene standard, as a function of %Ce^{3+}.

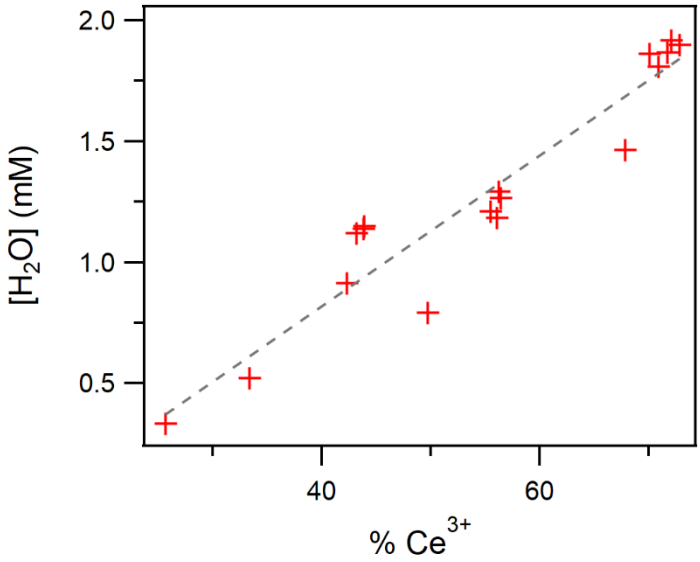

Figure C11. Data points are measured from ^{1}H NMR spectra of reactions between either H_2BQ, H_2DMQ, H_2NQ, or H_2DTNQ (5 mM) and **Ce-1** ([Ce atoms] = 9 mM) in d_8-THF. The gray trace is a linear fit for reference. Changing the plot to units of [H_2O] vs. [Ce^{3+}] gives a plot of slope 0.35.

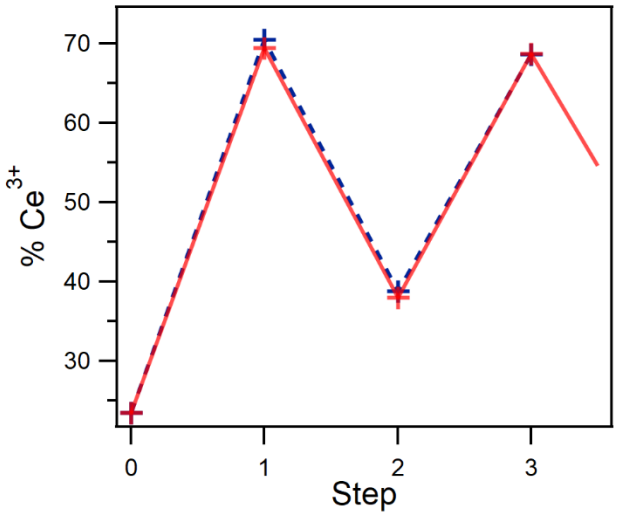

Figure C12. Redox cycling of **Ce-1** using H_2DCAQ as the reductant and DPPH as the oxidant. NMR samples were prepared using stock solutions of H_2DCAQ and DPPH in THF-d_8. Trace of $\%Ce^{3+}$ upon addition of set aliquots of H_2DCAQ followed by DPPH in the presence (blue, dashed) and absence (red, solid) of 3Å sieves.

C.5 Synthesis and Characterization of Organic PCET Reagents

All PCET reagents except 2,7-di-tert-butyl-1,4-napthoquinone (DTNQ, Sigma Aldrich), 2,2-diphenyl-1-picrylhydrazyl (DPPH, Sigma Aldrich), and 1,1-diphenyl-2-picrylhydrazine (DPPH-H, Sigma Aldrich) were purified before use. Quinones of a lower molecular weight (1,4-benzoquinone (BQ), 2,6-dimethyl-1,4-benzoquinone (DMQ), 1,4-naphthoquinone (NQ)) were purified by sublimation. Additionally, 1,8-dichloro-9,10-anthraquinone was purified by recrystallization in a 1:1 mixture of $CHCl_3$ and EtOH to give yellow needle-like crystals.

All hydroquinones except 1,4-hydroquinone were synthesized with few modifications from a reported literature procedure.[11-14] All manipulations were performed under a glovebox N_2 atmosphere in order to avoid oxidation of the hydroquinone product. Purified quinone (~0.3 mmol) dissolved in THF and excess sodium dithionite ($Na_2S_2O_4$, technical grade (ca. 85%), Fisher Scientific) (~3 mmol) dissolved in H_2O were added to a 20 mL glass vial. The two-phase mixture was stirred

vigorously for >15 minutes (color change noticeable within 1 minute). The mixture was then separated in a separatory funnel by adding 3 mL of Et_2O. The organic phase was then collected, and the aqueous phase was extracted with an additional 2 x 3 mL Et_2O. The collected organics were then dried over $MgSO_4$ and filtered. The leftover $MgSO_4$ was also washed with ~4 mL Et_2O to remove leftover hydroquinone. The compound was then isolated by removing volatile organics *in vacuo* and triturating with pentane. Most impurities in crude reaction mixtures could be removed with a pentane wash. Except for H_2DTNQ, all hydroquinones have been previously reported and the spectra reported here match previous reports.

1,4-benzoquinone (BQ)

^{1}H NMR (400 MHz, THF-d_8) δ 6.76 (s, 4H)

1,4-hydroquinone (H_2BQ)

^{1}H NMR (400 MHz, THF-d_8) δ 7.43 (s, 2H), 6.52 (s, 4H)

2,6-dimethyl-1,4-benzoquinone (DMQ)

^{1}H NMR (400 MHz, THF-d_8) δ 6.53 (s, 2H), 1.99 (s, 6H)

2,6-dimethyl-1,4-hydroquinone (H_2DMQ)

^{1}H NMR (400 MHz, THF-d_8) δ 7.23 (s, 1H), 6.43 (s, 1H), 6.29 (s, 2H), 2.10 (s, 6H)

1,4-naphthoquinone (NQ)

^{1}H NMR (400 MHz, THF-d_8) δ 8.03 (m, 2H), 7.78 (m, 2H), 6.98 (s, 2H)

1,4-dihydroxynapthalene (H_2NQ)

^{1}H NMR (400 MHz, THF-d_8) δ 8.10 (m,2H), 8.09 (s, 2H, -OH), 7.34 (m, 2H), 6.53 (s, 2H)

2,7-di-tert-butyl-1,4-naphthoquinone (DTNQ)

^{1}H NMR (400 MHz, THF-d_8) δ 8.12 (s, 1H), 7.92 (d, 1H), 7.81 (d, 1H), 6.79 (s, 1H), 1.39 (s, 9H), 1.37 (s, 9H)

2,7-di-tert-butyl-1,4-dihydroxynaphthalene (H_2DTNQ)

^{1}H NMR (600 MHz, THF-d_8) δ 8.04 (s, 1H), 8.01 (d, 1H), 7.98 (d, 1H), 7.43 (dd, 1H), 7.17 (s, 1H), 6.73 (s, 1H), 1.48 (s, 9H), 1.42 (s, 9H)

^{13}C NMR (150 MHz, THF-d_8) δ 148.12 (s, 1C), 147.63 (s, 1C), 143.79 (s, 1C), 133.04 (s, 1C), 128.79 (s, 1C), 123.37 (s, 1C), 123.08 (s, 1C), 123.06 (s, 1C), 116.91 (s, 1C), 107.49 (s, 1C), 35.87 (s, 1C), 35.64 (s, 1C), 31.93 (s, 9C), 30.77 (s, 9C)

1,8-dichloro-9,10-anthraquinone (DCAQ)

^{1}H NMR (400 MHz, THF-d_8) δ 8.18 (d, 2H), 7.85 (2H, d), 7.71 (t, 2H)

1,8-dichloro-9,10-dihydroxyanthracene (H_2DCAQ)

^{1}H NMR (400 MHz, THF-d_8) δ 8.59 (s, 1H), 8.52 (s, 1H), 8.30 (d, 2H), 7.46 (d, 2H), 7.28 (t, 2H)

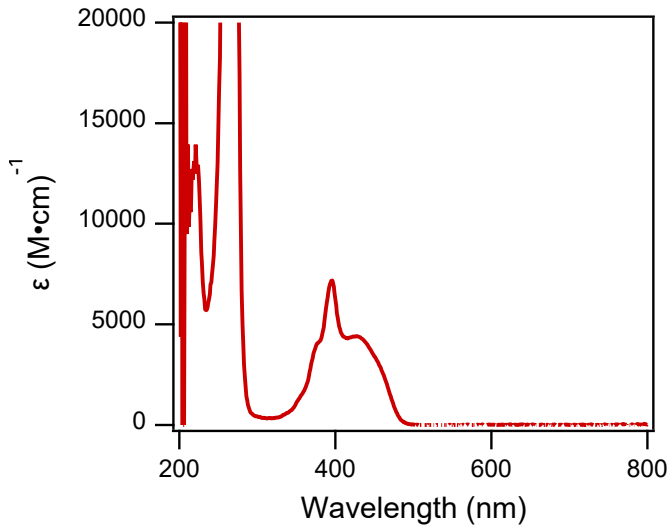

Figure C13. Normalized UV-Vis spectrum of H_2DCAQ in THF. Characteristic absorbance feature at ~400 nm matches previous reports.[14]

1,1-diphenyl-2-picrylhydrazine (DPPH-H)

^{1}H NMR (400 MHz, THF-d_8) δ 10.55 (s, 1H, -NH), 9.09 (s, 1H), 8.73 (s, 1H), 7.29 (t, 4H), 7.19 (d, 4H), 7.10 (t, 2H)

C.6 Establishing Equilibrium between OLE-Ce and PCET Reagents in THF

C.6.1 ^{1}H NMR spectra for Equilibrium of OLE-Ce and PCET Reductants

These spectra are typical of the plateau region for equilibration experiments for the respective PCET reagents. Spectra below detail before addition of **Ce-1** and at plateau region with **Ce-1** ^{1}H NMR spectra for each equilibration.

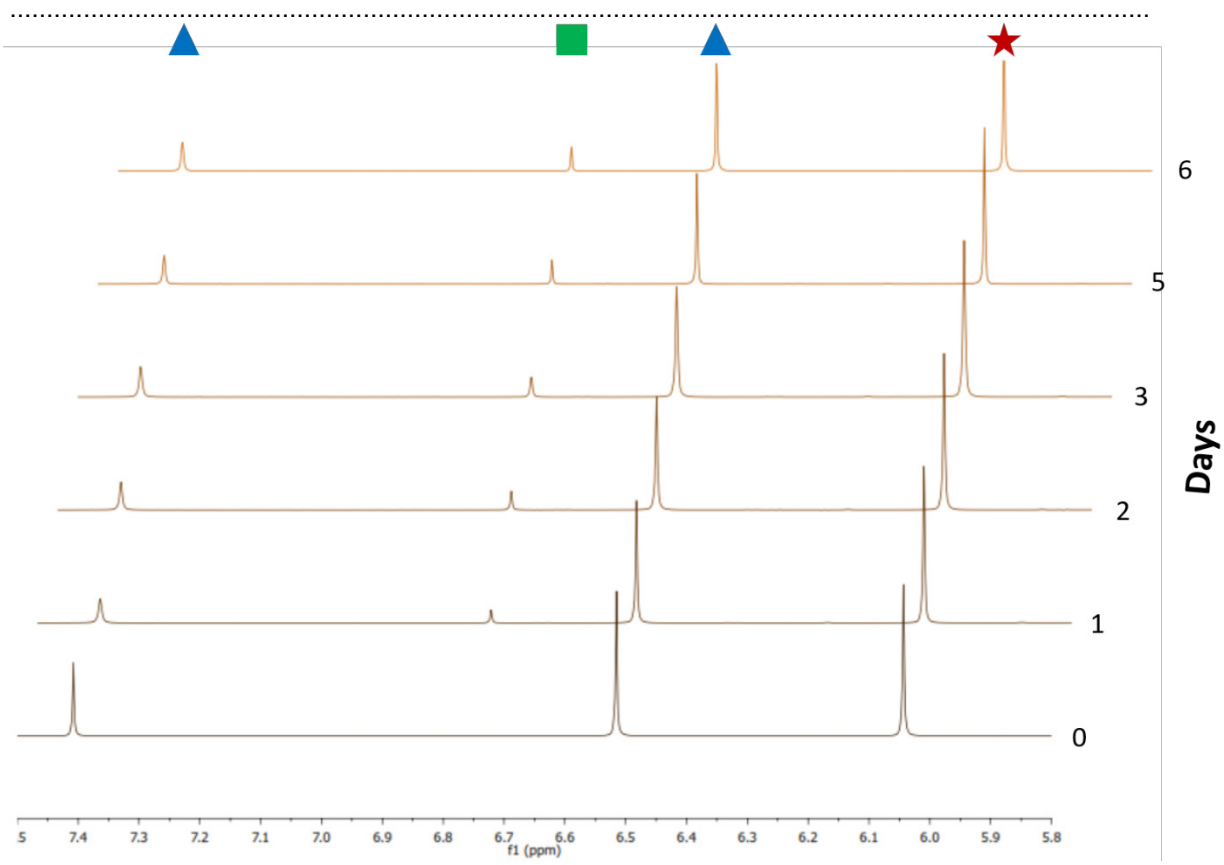

Figure C14. Time course of equilibration between **Ce-1** and H_2BQ. Initial concentrations of the reaction mixture were [Ce atoms] = 9.0 mM, [TMB] = 8.2 mM, and [H_2BQ] = 5.5 mM. The TMB peak (red star), hydroquinone peak (blue triangle), and quinone peak (green square) chosen for integration are denoted.

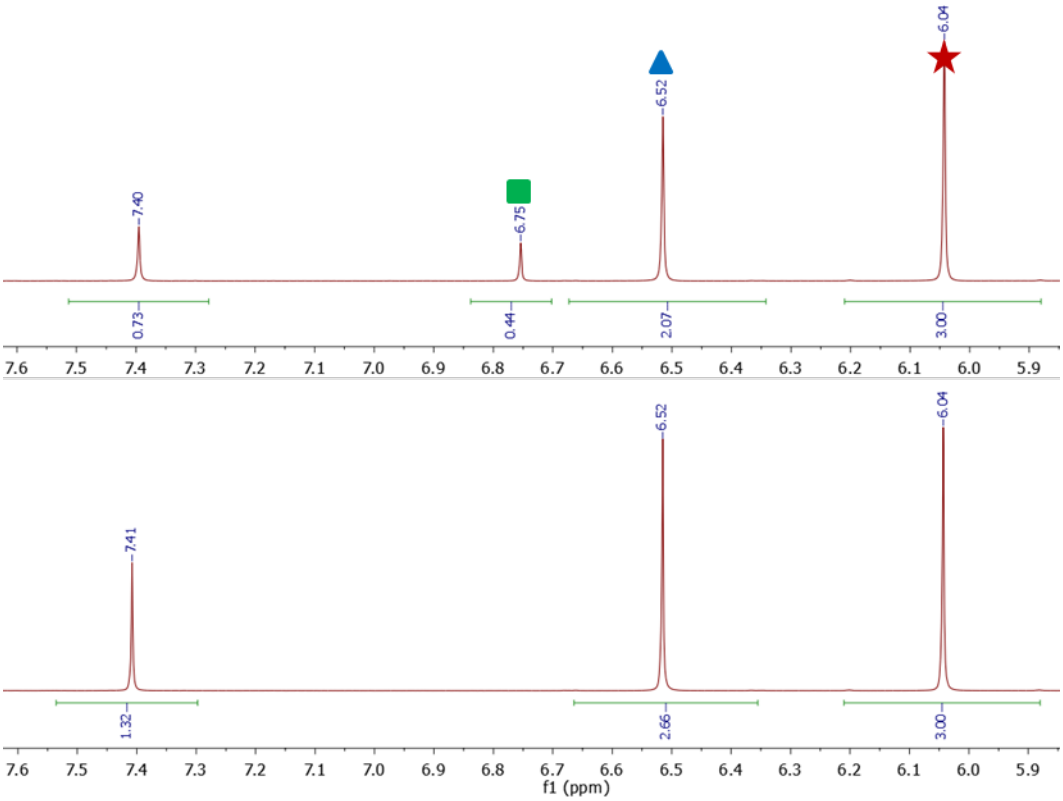

Figure C15. Initial (bottom) and final (top) ^{1}H NMR spectra of equilibration between **Ce-1** and H_2BQ. Initial concentrations in the reaction mixture were [Ce atoms] = 9.0 mM, [TMB] = 8.2 mM, and [H_2BQ] = 5.5 mM. The TMB peak (red star), hydroquinone peak (blue triangle), and quinone peak (green square) chosen for integration are denoted.

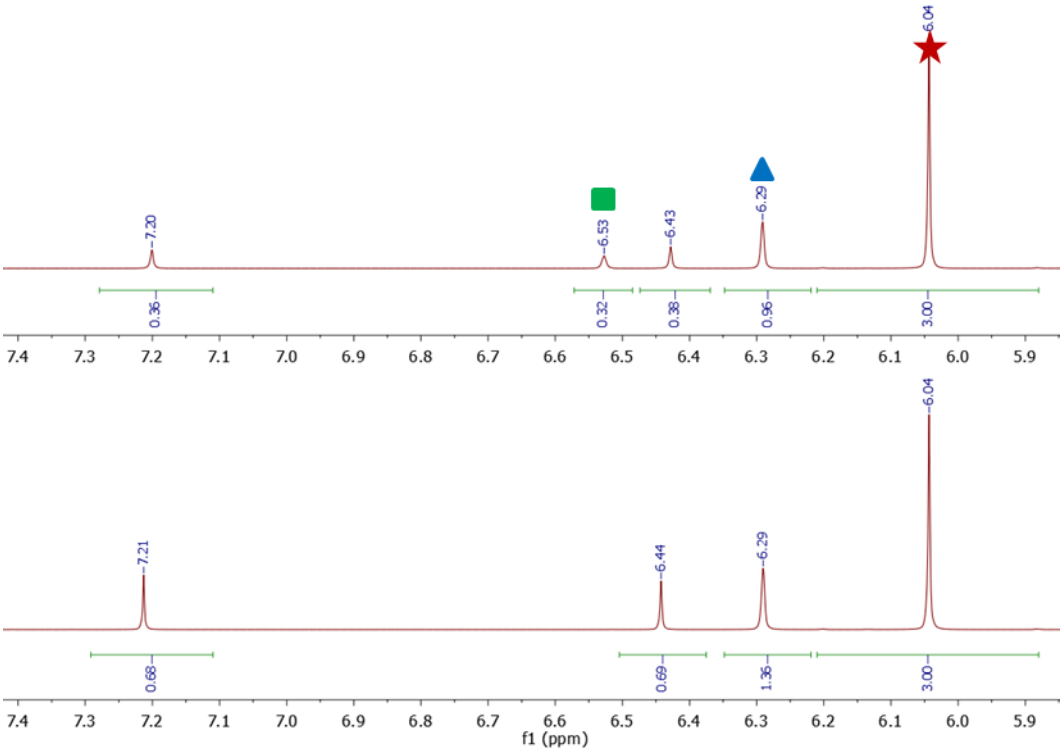

Figure C16. Initial (bottom) and final (top) ^{1}H NMR spectra of equilibration between **Ce-1** and H_2DMQ. Initial concentrations in the reaction mixture were [Ce atoms] = 9.0 mM, [TMB] = 8.2 mM, and [H_2DMQ] = 5.6 mM. The TMB peak (red star), hydroquinone peak (blue triangle), and quinone peak (green square) chosen for integration are denoted.

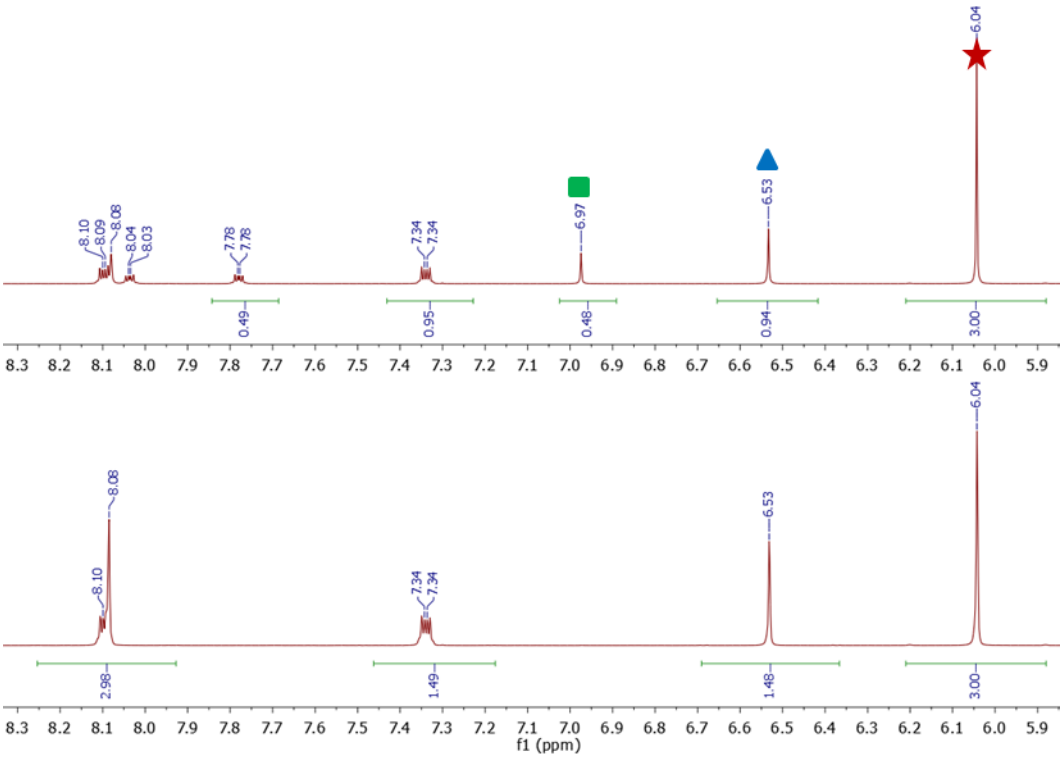

Figure C17. Initial (bottom) and final (top) ^{1}H NMR spectra of equilibration between **Ce-1** and H_2NQ. Initial concentrations in the reaction mixture were [Ce atoms] = 9.0 mM, [TMB] = 7.2 mM, and [H_2NQ] = 5.3 mM. The TMB peak (red star), hydroquinone peak (blue triangle), and quinone peak (green square) chosen for integration are denoted.

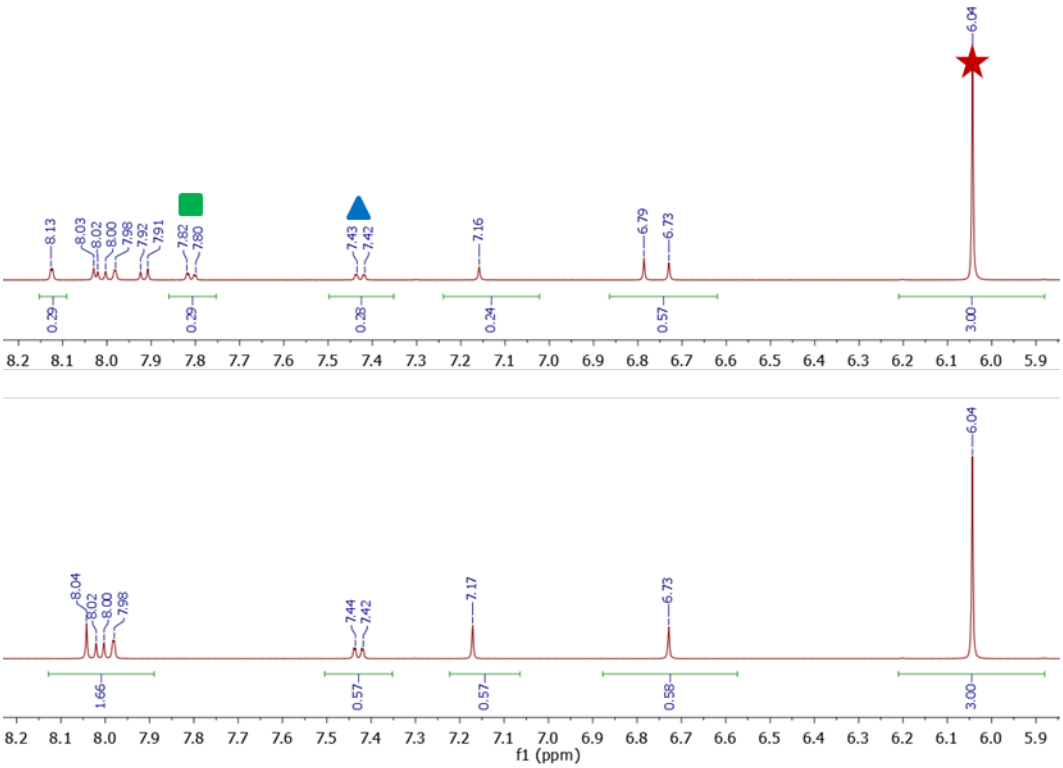

Figure C18. Initial (bottom) and final (top) ^{1}H NMR spectra of equilibration between **Ce-1** and H_2DTNQ. Initial concentrations in the reaction mixture were [Ce atoms] = 9.0 mM, [TMB] = 7.6 mM, and [H_2DTNQ] = 4.4 mM. The TMB peak (red star), hydroquinone peak (blue triangle), and quinone peak (green square) chosen for integration are denoted.

C.6.2 ^{1}H NMR spectra for Equilibrium of OLE-Ce and PCET Oxidants

These spectra are typical of the plateau region for equilibration experiments. For the respective quinones, spectra below detail the ^{1}H NMR spectra of OLE-Ce reduced by a stoichiometric amount of H_2DCAQ before the addition of quinone and at plateau region with OLE-Ce after addition.

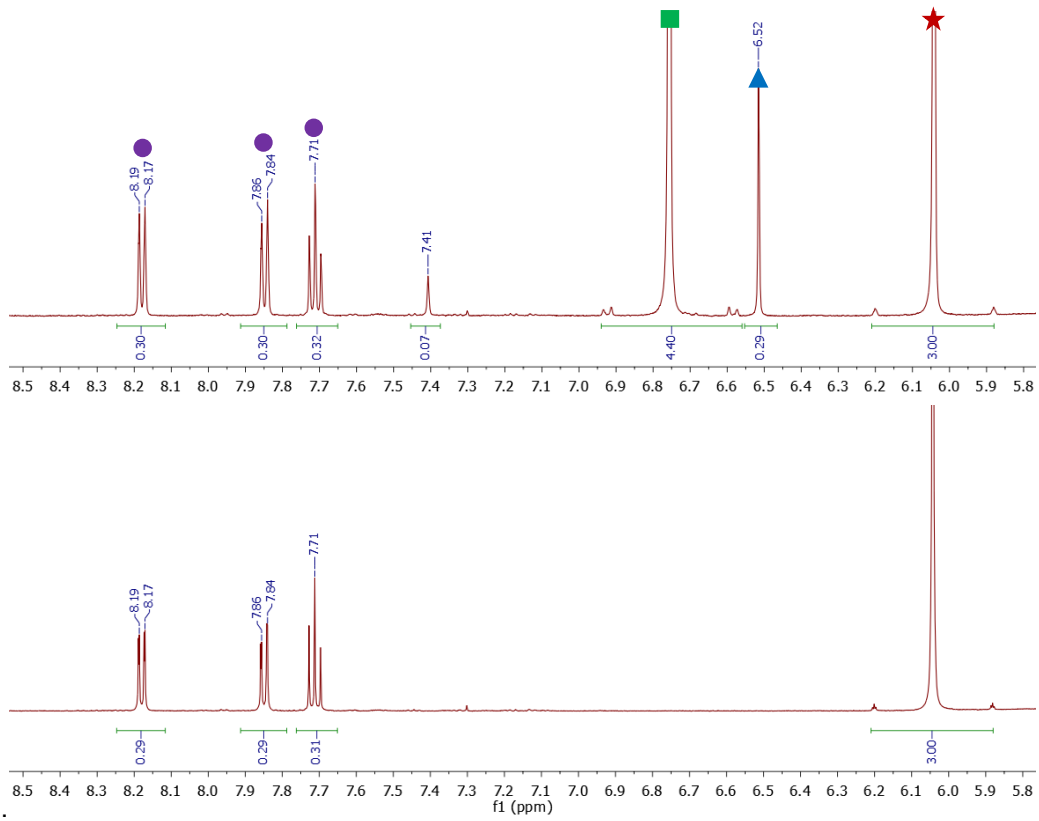

Figure C19. Initial (top) and final (bottom) ^{1}H NMR spectra of equilibration between reduced **Ce-1** and BQ. Initial concentrations in the reaction mixture after reduction of **Ce-1** with H_2DCAQ were [Ce atoms] = 9.1 mM, [TMB] = 7.9 mM, [DCAQ] = 1.1 mM, and [BQ] = 9.3 mM. The TMB peak (red star), hydroquinone peak (blue triangle), quinone peak (green square), and DCAQ peaks (purple circle) chosen for integration are denoted.

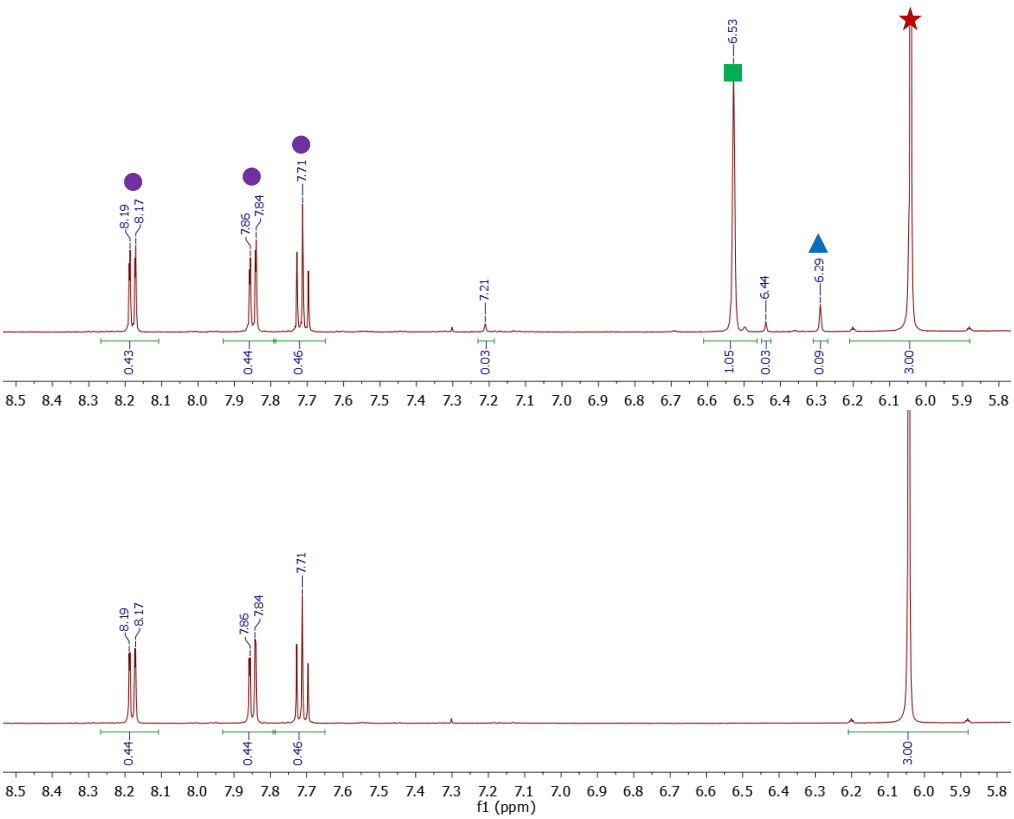

Figure C20. Initial (top) and final (bottom) ^{1}H NMR spectra of equilibration between reduced **Ce-1** and DMQ. Initial concentrations in the reaction mixture after reduction of **Ce-1** with H_2DCAQ were [Ce atoms] = 9.1 mM, [TMB] = 7.4 mM, [DCAQ] = 1.7 mM, and [DMQ] = 4.3 mM. The TMB peak (red star), hydroquinone peak (blue triangle), quinone peak (green square), and DCAQ peaks (purple circle) chosen for integration are denoted.

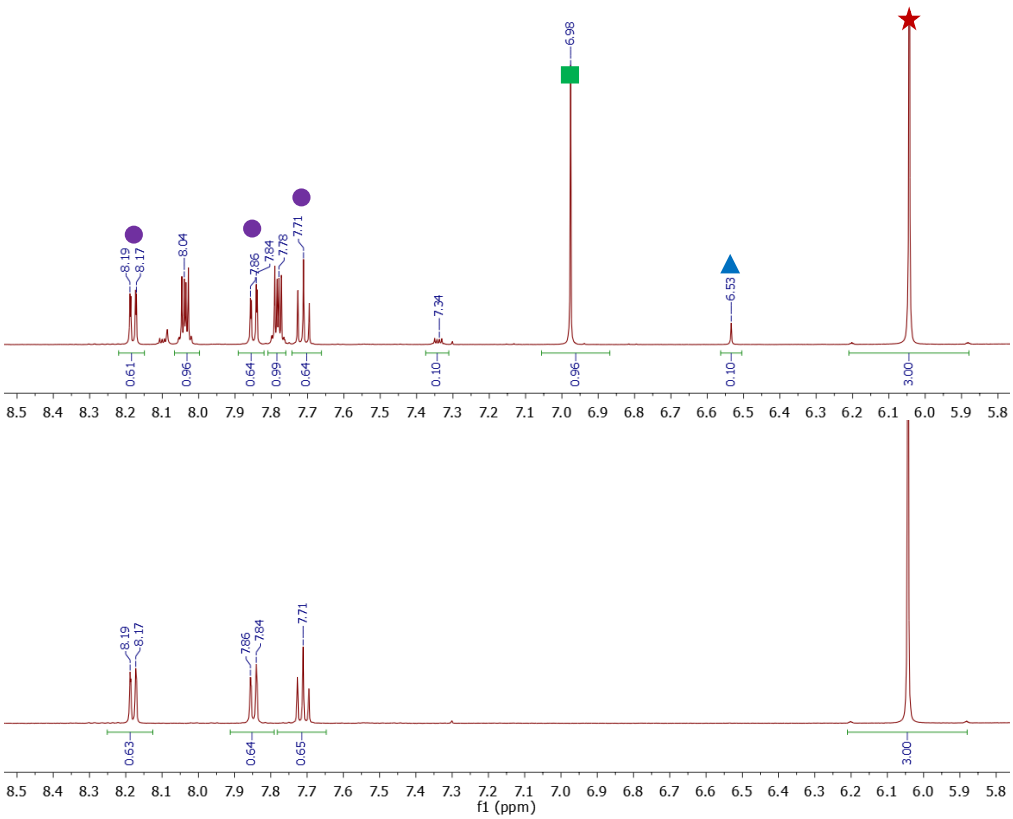

Figure C21. Initial (top) and final (bottom) ^{1}H NMR spectra of equilibration between reduced **Ce-1** and NQ. Initial concentrations in the reaction mixture after reduction of **Ce-1** with H_2DCAQ were [Ce atoms] = 9.1 mM, [TMB] = 7.0 mM, [DCAQ] = 2.1 mM, and [NQ] = 7.5 mM. The TMB peak (red star), hydroquinone peak (blue triangle), quinone peak (green square), and DCAQ peaks (purple circle) chosen for integration are denoted.

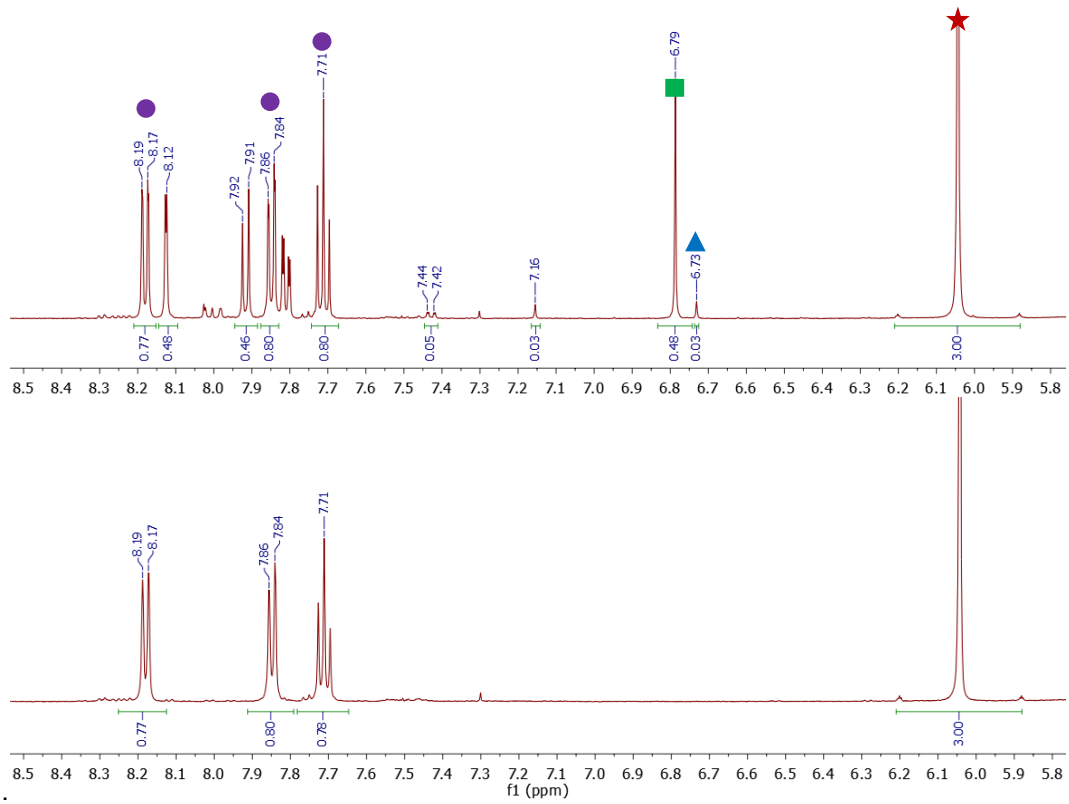

Figure C22. Initial (top) and final (bottom) ^{1}H NMR spectra of equilibration between reduced **Ce-1** and DTNQ. Initial concentrations in the reaction mixture after reduction of **Ce-1** with H_2DCAQ were [Ce atoms] = 9.1 mM, [TMB] = 6.5 mM, [DCAQ] = 2.4 mM, and [DTNQ] = 3.7 mM. The TMB peak (red star), hydroquinone peak (blue triangle), quinone peak (green square), and DCAQ peaks (purple circle) chosen for integration are denoted.

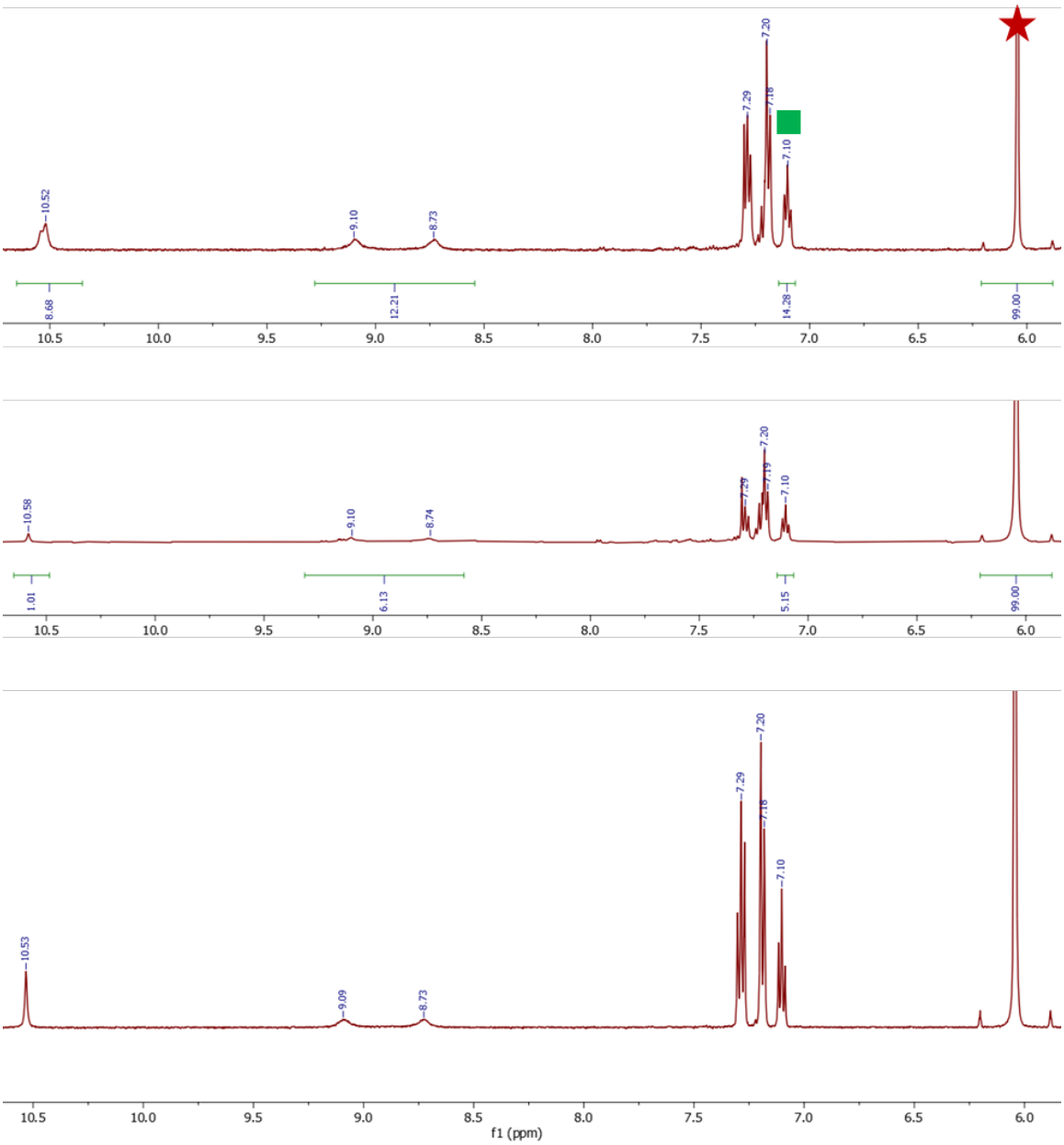

Figure C23. ^{1}H NMR spectra of DPPH-H (bottom), DPPH before addition of **Ce-1** (middle), and after addition (top). Initial concentrations in the reaction mixture after addition of **Ce-1** were [Ce atoms] = 11.5 mM, [TMB] = 4.6 mM, [DPPH-H] = 0.4 mM, and [DPPH] = 4.1 mM. The TMB peak (red star) and DPPH-H peak chosen for integration are denoted. The initial [DPPH] was estimated based on the known weight of solid added and the assumption that all mass was from either DPPH or DPPH-H impurities.

C.6.3 Compiled ^{1}H NMR and XAS Data for Equilibrations

Time courses of ^{1}H NMR data are compiled along with the associated fluctuations in organic reagent and product mass balance for reactions between OLE-Ce colloids and both quinones and hydroquinones (Figure C24). Compilations of XANES spectra of equilibrated OLE-Ce samples are also included (Figure C25). Finally, the values from all OLE-Ce equilibrations are compiled for both ^{1}H NMR (Table C5) and XANES studies (Table C6).

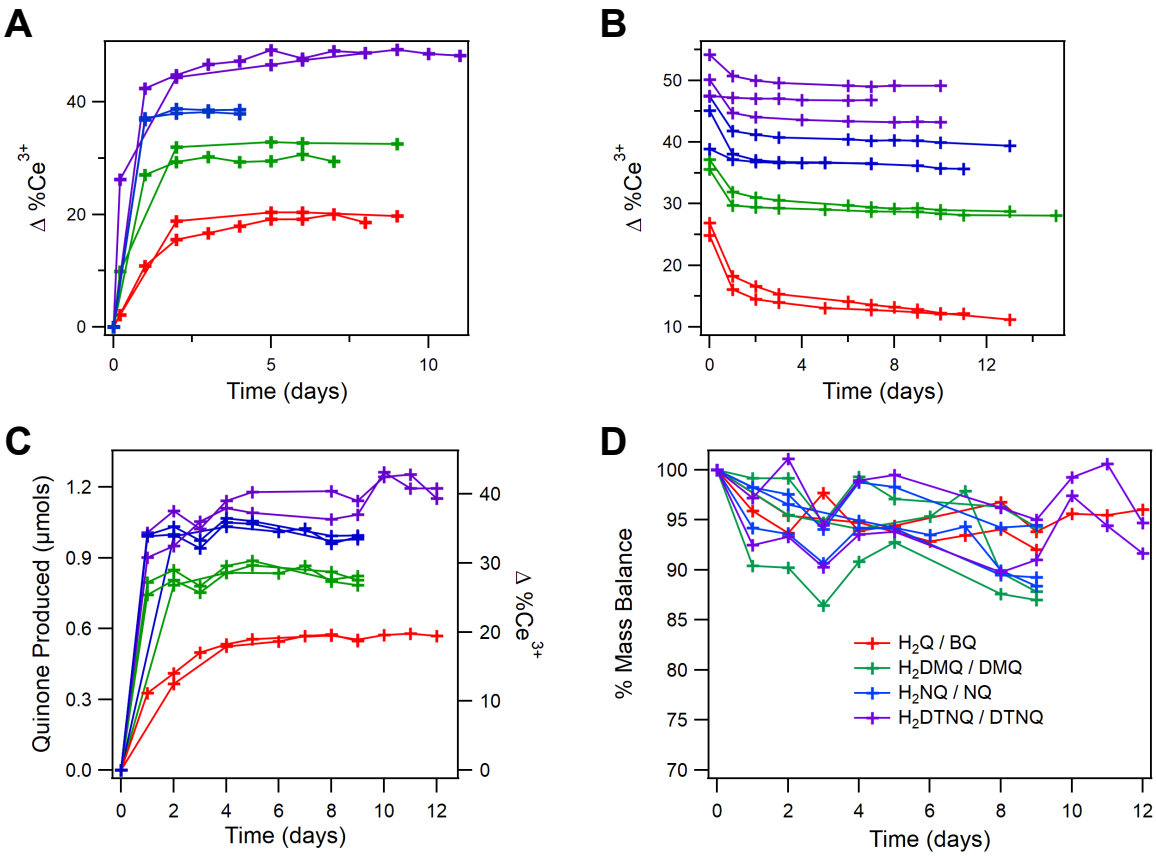

Figure C24. Time courses between OLE-Ce colloids and H_2BQ/BQ (red), H_2DMQ/DMQ (green), H_2NQ/NQ (blue), and H_2DTNQ/DTNQ (purple) by ^{1}H NMR. Data plotted for (A) hydroquinone oxidation by **Ce-1** and (B) quinone reduction by **Ce-1**. Additionally, time courses for (C) hydroquinone oxidation by **Ce-2** and the associated (D) mass balance of hydroquinone and quinone for each run as a function of time. Values determined by ^{1}H NMR vs. a 1,3,5-trimethoxybenzene internal standard.

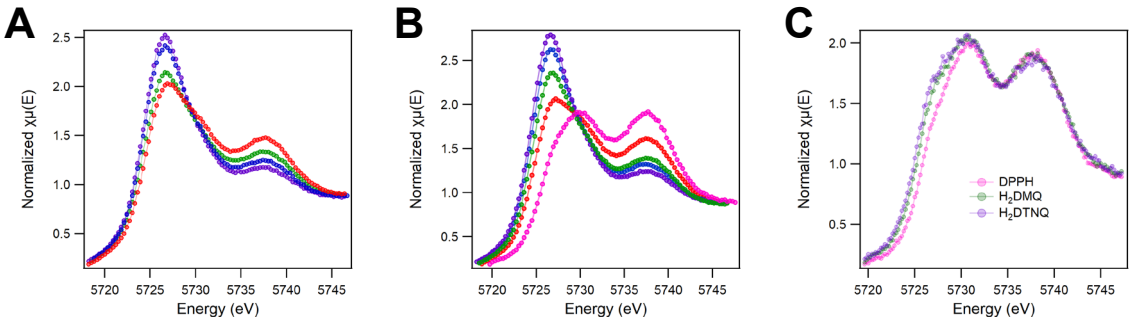

Figure C25. XANES spectra at the Ce L_{III}-edge of DPPH/DPPH-H (pink), H_2BQ/BQ (red), H_2DMQ/DMQ (green), H_2NQ/NQ (blue), and H_2DTNQ/DTNQ (purple) equilibrated with either (A) **Ce-1**, (B) **Ce-2**, or (C) **Ce-L**.

Table C5. ^{1}H NMR Data for Equilibrated OLE-Ce Samples. [a]

Reagent	XH_n	X	$\Delta\%Ce^{3+}$	$BDFE_{Ce}$	$E°$(V vs H_2)
DTNQ [b]	0.15	2.01	49.1	62.3	0.45
H_2DTNQ [c]	2.70	1.42	48.7	61.3	0.40
H_2DTNQ [c]	1.40	1.42	48.7	61.5	0.41
DTNQ [b]	0.02	0.87	46.8	62.6	0.46
DTNQ [b]	0.20	2.16	43.3	62.2	0.44
NQ [b]	0.22	2.17	40.1	63.4	0.49
H_2NQ [c]	2.20	1.11	38.7	62.5	0.46
H_2NQ [c]	0.96	1.13	38.0	62.7	0.46
NQ [b]	0.07	1.64	36.6	63.6	0.50
NQ [b]	0.26	4.57	36.2	63.6	0.50
H_2DMQ [c]	3.04	0.96	32.7	64.6	0.55
H_2DMQ [c]	2.58	0.87	29.7	64.6	0.55
DMQ [b]	0.24	2.10	29.1	65.5	0.59
DMQ [b]	0.22	2.53	28.2	65.6	0.59
H_2BQ [c]	3.28	0.59	20.1	66.9	0.65
H_2BQ [c]	2.77	0.56	19.2	66.9	0.65
BQ [b]	0.42	3.64	12.6	68.0	0.69
BQ [b]	0.36	5.62	12.5	68.2	0.70
DPPH [c]	0.67	2.37	−5.5	74.2	0.96
DPPH [c]	0.60	2.19	−6.0	74.3	0.97
H_2DTNQ [d]	1.73	1.19	40.8	61.4	0.41
H_2DTNQ [d]	1.66	1.14	39.4	61.4	0.41
H_2NQ [d]	1.75	1.02	35.0	62.5	0.46
H_2NQ [d]	1.69	1.00	34.5	62.5	0.46
H_2NQ [d]	1.74	1.00	34.3	62.5	0.46
H_2DMQ [d]	2.18	0.83	28.6	64.6	0.55
H_2DMQ [d]	2.17	0.82	28.1	64.6	0.55
H_2DMQ [d]	2.17	0.81	27.8	64.6	0.55
H_2BQ [d]	2.30	0.56	19.4	67.0	0.65
H_2BQ [d]	2.32	0.56	19.3	67.0	0.65
DPPH [d]	0.63	0.12	−9.8	72.5	0.89
DPPH [d]	0.53	0.29	−10.7	73.1	0.92
H_2DTNQ [e]	2.93	0.24	9.8	60.7	0.38
H_2NQ [e]	3.04	0.22	9.3	61.9	0.43
H_2DTNQ [e]	2.93	0.24	9.2	60.8	0.38
DTNQ [f]	0.31	1.11	8.6	61.9	0.43
H_2NQ [e]	3.06	0.20	7.7	61.9	0.43
H_2DMQ [e]	3.39	0.15	6.8	64.0	0.52
H_2DMQ [e]	3.40	0.14	5.8	64.0	0.52
H_2BQ [e]	2.95	0.07	3.8	66.3	0.62
H_2BQ [e]	2.94	0.07	3.3	66.3	0.62
DPPH [e]	0.43	0.38	−2.4	73.4	0.93

[a] Units are kcal mol^{-1} for $BDFE_{Ce}$, V vs. $E°(H^+/H_2)$ for $E°$(V vs H_2), and μmols for the other columns. [b] Reacted with **Ce-1** that was first reduced with H_2DCAQ. [c] Reacted with **Ce-1**. [d] Reacted with **Ce-2**. [e] Reacted with **Ce-L** with equilibrium plateau at ≥24 days. [f] Reacted with **Ce-L** that was first reduced with H_2DCAQ.

Table C6. XANES Data for OLE-Ce Samples. [a]

Sample	%Ce^{3+}	Sample	%Ce^{3+}
Ce-1	29.5	**Ce-1** – DPPH-H [c]	21.0
Ce-2	30.9	**Ce-1** – *m*CPBA	24.7
Ce-L	20.5	**Ce-2** – H_2DTNQ	65.4
Ce-1 – H_2DCAQ	75.9	**Ce-2** – H_2NQ	59.2
Ce-1 – H_2DTNQ	65.9	**Ce-2** – DTNQ [b]	53.9
Ce-1 – H_2NQ	62.3	**Ce-2** – H_2DMQ	52.6
Ce-1 – DTNQ [b]	58.0	**Ce-2** – BQ [b]	42.4
Ce-1 – H_2DMQ	56.2	**Ce-2** – H_2BQ	38.7
Ce-1 – NQ [b]	52.6	**Ce-2** – DPPH	15.9
Ce-1 – H_2DMQ	53.4	**Ce-L** – H_2DCAQ	30.4
Ce-1 – DMQ [b]	52.4	**Ce-L** – H_2DTNQ	19.5
Ce-1 – H_2BQ	43.6	**Ce-L** – H_2DMQ	16.6
Ce-1 – BQ [b]	37.3	**Ce-L** – DPPH	10.8
Ce-1 – DPPH	22.7	**Ce-L** – *m*CPBA	12.1

[a] All reagents were added in excess of Ce atoms [b] OLE-Ce was first reduced with H_2DCAQ before addition of organic reagent. [c] **Ce-1** was first oxidized with *m*CPBA before addition of DPPH-H.

C.7 BDFE Analyses

The effect of correcting the equilibrium state data for the law of mass action is presented in Figure C26. Additionally, full fit parameters and lines of best fit to the Frumkin isotherm described in the main text (eq 3.8) are presented in Figure C27. Finally, a comparison between μ_O from high-temperature studies of oxygen atom transfer by bulk ceria are compared to the $BDFE_{Ce}$ values for **Ce-1** collected in this study (Figure C28).

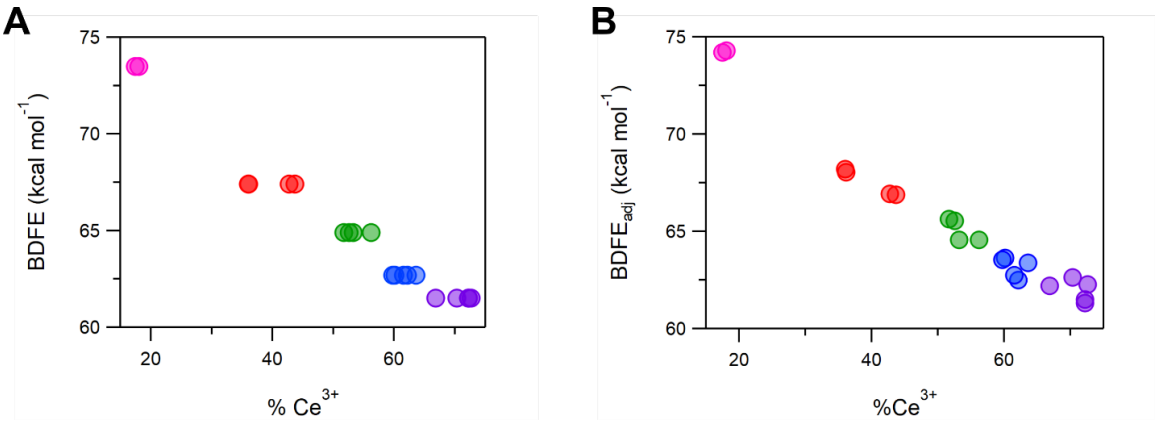

Figure C26. The %Ce^{3+} at equilibrium for reactions between **Ce-1** and DPPH-H/DPPH (pink), H_2BQ/BQ (red), H_2DMQ/DMQ (green), H_2NQ/NQ (blue), and H_2DTNQ/DTNQ (purple) is plotted against (A) the avg. O–H BDFE of the hydroquinone, and (B) the adjusted avg. O–H BDFE of the hydroquinone as determined by the Nernst equation taking into consideration the concentration of quinone and hydroquinone in solution once equilibrium was reached (eq 3.2 in main text).

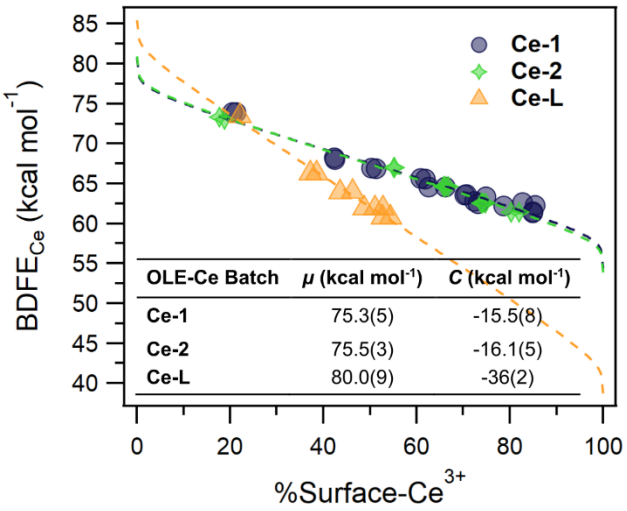

OLE-Ce Batch	μ (kcal mol^{-1})	C (kcal mol^{-1})
Ce-1	75.3(5)	-15.5(8)
Ce-2	75.5(3)	-16.1(5)
Ce-L	80.0(9)	-36(2)

Figure C27. Plot of $BDFE_{Ce}$ vs. %Surface-Ce^{3+} with Frumkin isotherms fits and in-set table including fit parameters from eq 3.8.

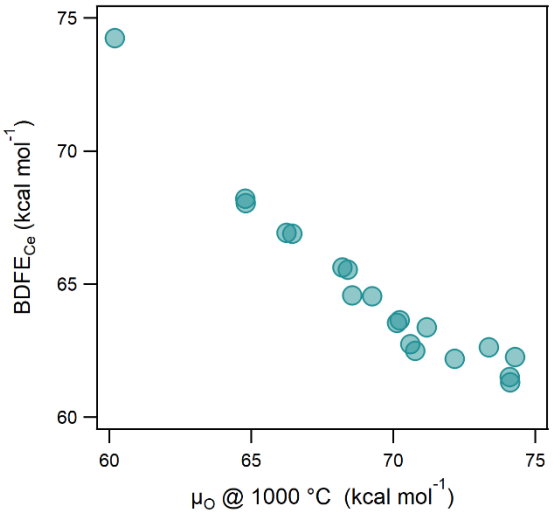

Figure C28. The quantitative relationship between the chemical potential of oxygen (μ_O) and hydrogen (μ_H) in ceria is estimated. $BDFE_{Ce}$ values for **Ce-1** from Table 3.1 quantify μ_H and are compared with values of μ_O at 1,000 °C derived from a relationship between the equilibrium partial pressure of oxygen (P_{O2}) and oxygen vacancy concentration of bulk ceria.[15] Per Bevan et al., μ_O can be estimated as $^1/_2RT\ln(P_{O2})$.[16] All chemical potentials are collected at the same ratio of reduced active sites. The number of active sites is estimated as 70% of all cerium atoms for bulk ceria[15] and all surface cerium atoms for **Ce-1**. The slope of the relationship is -0.86(5), but is highly dependent on the temperature at which μ_O is calculated, where higher temperatures increase the range of μ_O.

C.8 Equilibrations under other conditions

The effect of solvent on the equilibration of OLE-Ce with various quinones was tested by repeating equilibrations in C_6D_6 (ε = 2.3) and Toluene-d_8 (ε = 2.4), and repeating an equilibration in THF/THF-d_8 (ε = 7.6) in the presence of 100 mM $TBAPF_6$ (Table C7)**.**[17]

The effect of additives of the equilibration of **Ce-1** with H_2DMQ was also tested. Tetrabutylammonium oleate (TBA^+OLE^-) and cerium(III) oleate ($Ce(OLE)_3$) were synthesized by mixing sodium oleate with either tetrabutylammonium chloride or cerium(III) chloride in aqueous solution and then washing and isolating the insoluble product. The additions of $Ce(OLE)_3$ and H_2O are shown in Table C7. Additionally, time courses for the **Ce-1**/H_2DMQ equilibrium reaction in the presence of no additives, oleic acid, and $Ce(OLE)_3$ are shown in Figure C29.

Table C7. %Ce^{3+} of OLE-Ce at Equilibrium under Non-Standard Solution Conditions

Sample	%Ce^{3+} by ^1H NMR	%Ce^{3+} by XANES	%Ce^{3+} for Standard Solvent Condition [a]
H_2BQ/**Ce-2** + 100 mM $TBAPF_6$ [b]	45	--	44
H_2DMQ/ **Ce-1** in C_6D_6 [c]	68	58	53
H_2DMQ/ **Ce-2** in Toluene-d_8 [d]	65	--	53
H_2BQ/**Ce-2** flame-sealed tube [e]	42	--	44
H_2DMQ/**Ce-1** with H_2O [f]	52	--	53
H_2DMQ/**Ce-1** with $Ce(OLE)_3$ [g]	52	--	53

[a] The standard solvent condition is a mixture of THF/THF-d_8 with no supporting electrolyte. [b] [Ce atoms] = 8.3 mM, [TMB] = 8.0 mM, and [H_2BQ] = 4.7 mM. [c] [Ce atoms] = 8.6 mM, [TMB] = 10.0 mM, and [H_2DMQ] = 5.0 mM. [d] [Ce atoms] = 8.3 mM, [TMB] = 9.0 mM, and [H_2DMQ] = 5.4 mM. [e] [Ce atoms] = 8.3 mM, [TMB] = 8.0 mM, and [H_2BQ] = 4.6 mM. [f] [Ce atoms] = 8.9 mM, [TMB] = 8.0 mM, [H_2DMQ] = 4.8 mM, and [H_2O] = 49.5 mM. [g] [Ce atoms] = 8.6 mM, [TMB] = 5.8 mM, [H_2DMQ] = 4.2 mM, and [$Ce(OLE)_3$] = 7.0 mM.

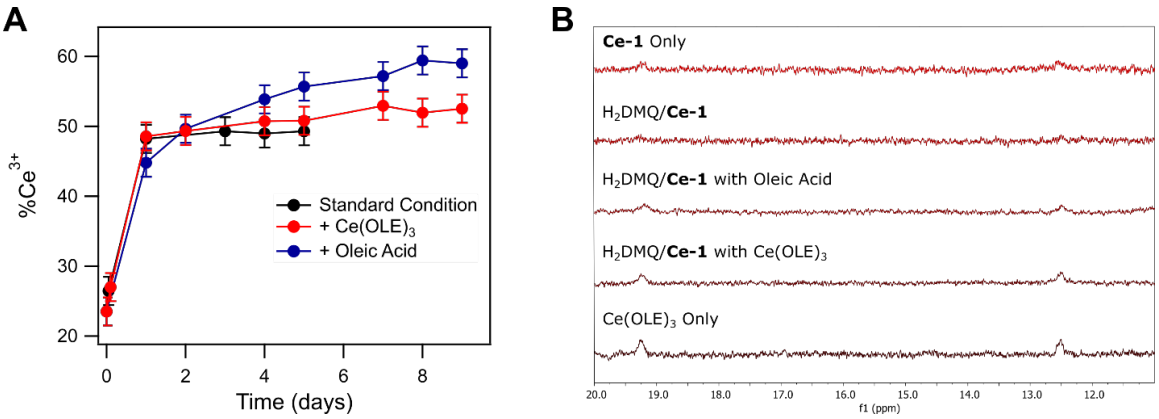

Figure C29. (A) Time courses for H_2DMQ/**Ce-1** equilibration with various additives. Standard condition contains [Ce atoms] = 9.1 mM, [TMB] = 6.2 mM, and [H_2DMQ] = 3.9 mM. Sample with added $Ce(OLE)_3$ contains [Ce atoms] = 8.6 mM, [TMB] = 5.8 mM, [H_2DMQ] = 4.2 mM, and [$Ce(OLE)_3$] = 7.0 mM. Sample with added oleic acid (OA) contains [Ce atoms] = 9.0 mM, [TMB] = 6.2 mM, [H_2DMQ] = 3.8 mM, and [OA] = 24.4 mM. Error bars are estimated at ≤ 2 %Ce^{3+}. (B) Selected sections of ^{1}H NMR spectra for same samples after reaction has been going for 5 days.

C.9 References

1. Taniguchi, T.; Watanabe, T.; Sakamoto, N.; Matsushita, N.; Yoshimura, M., Aqueous Route to Size-Controlled and Doped Organophilic Ceria Nanocrystals. *Crystal Growth & Design* **2008,** *8* (10), 3725-3730.
2. Bruce, J. M., Light-induced reactions of quinones. *Quarterly Reviews, Chemical Society* **1967,** *21* (3), 405.
3. Tsunekawa, S.; Ishikawa, K.; Li, Z. Q.; Kawazoe, Y.; Kasuya, A., Origin of Anomalous Lattice Expansion in Oxide Nanoparticles. *Phys. Rev. Lett.* **2000,** *85* (16), 3440-3443.
4. Wang, Z. L.; Feng, X., Polyhedral Shapes of CeO_2 Nanoparticles. *The Journal of Physical Chemistry B* **2003,** *107* (49), 13563-13566.
5. Roulhac, P. L.; Palenik, G. J., Bond Valence Sums in Coordination Chemistry. The Calculation of the Oxidation State of Cerium in Complexes Containing Cerium Bonded Only to Oxygen. *Inorg. Chem.* **2003,** *42* (1), 118-121.
6. Ravel, B.; Newville, M., ATHENA, ARTEMIS, HEPHAESTUS: data analysis for X-ray absorption spectroscopy using IFEFFIT. *Journal of Synchrotron Radiation* **2005,** *12* (4), 537-541.
7. Nachimuthu, P.; Shih, W.-C.; Liu, R.-S.; Jang, L.-Y.; Chen, J.-M., The Study of Nanocrystalline Cerium Oxide by X-Ray Absorption Spectroscopy. *J. Solid State Chem.* **2000,** *149* (2), 408-413.
8. Cafun, J.-D.; Kvashnina, K. O.; Casals, E.; Puntes, V. F.; Glatzel, P., Absence of Ce^{3+} Sites in Chemically Active Colloidal Ceria Nanoparticles. *ACS Nano* **2013,** *7* (12), 10726-10732.
9. Zhang, J.; Wu, Z.; Liu, T.; Hu, T.; Wu, Z.; Ju, X., XANES study on the valence transitions in cerium oxide nanoparticles. *Journal of Synchrotron Radiation* **2001,** *8* (2), 531-532.
10. Damatov, D.; Laga, S. M.; Mader, E. A.; Peng, J.; Agarwal, R. G.; Mayer, J. M., Redox Reactivity of Colloidal Nanoceria and Use of Optical Spectra as an In Situ Monitor of Ce Oxidation States. *Inorg. Chem.* **2018,** *57* (22), 14401-14408.
11. De Vries, J. G.; Kellogg, R. M., Reduction of aldehydes and ketones by sodium dithionite. *The Journal of Organic Chemistry* **1980,** *45* (21), 4126-4129.
12. Wise, C. F.; Agarwal, R. G.; Mayer, J. M., Determining Proton-Coupled Standard Potentials and X–H Bond Dissociation Free Energies in Nonaqueous Solvents Using Open-Circuit Potential Measurements. *J. Am. Chem. Soc.* **2020,** *142* (24), 10681-10691.
13. Carpino, L. A.; Triolo, S. A.; Berglund, R. A., Reductive lactonization of strategically methylated quinone propionic acid esters and amides. *The Journal of Organic Chemistry* **1989,** *54* (14), 3303-3310.
14. Nakayama, T.; Nakamura, N.; Miki, S.; Hamanoue, K., Formation of anthrahydroquinones ($XAQH_2$)via excited singlet charge-transfer complexes (or singlet ion pairs) of anthraquinones with 2,5-dimethylhexa-2,4-diene (DMHD), and photochemical reaction of $XAQH_2$ with DMHD. *J. Chem. Soc., Faraday Trans.* **1995,** *91* (4), 607.
15. Bulfin, B.; Lowe, A. J.; Keogh, K. A.; Murphy, B. E.; Lübben, O.; Krasnikov, S. A.; Shvets, I. V., Analytical Model of CeO2 Oxidation and Reduction. *The Journal of Physical Chemistry C* **2013,** *117* (46), 24129-24137.
16. Bevan, D. J. M.; Kordis, J., Mixed oxides of the type MO_2 (fluorite)—M_2O_3—I oxygen dissociation pressures and phase relationships in the system CeO_2□Ce_2O_3 at high temperatures. *J. Inorg. Nucl. Chem.* **1964,** *26* (9), 1509-1523.
17. Lide, D. R., *CRC Handbook of Chemistry and Physics*. 90 ed.; CRC Press: Boca Raton, FL, 2009.

Appendix D Supplementary Information for Chapter 4

Adapted from the supporting information for Agarwal, R. G.; Mayer, J. M. "CeO-H Bond Strength Modulated Brønsted-Evans Polanyi Relationships for Cerium Oxide Nanoparticle Colloids." *Manuscript in Preparation*.

D.1 General Considerations

D.1.1 Materials

2,2-diphenyl-1-picrylhydrazyl (DPPH, Sigma-Aldrich), 2,2-Di(4-*tert*-octylphenyl)-1-picrylhydrazyl, free radical (DPPHL, Sigma-Aldrich), 1,1,-diphenyl-2-picrylhydrazine (DPPH-H, Sigma-Aldrich, 97%), oleic acid (Sigma-Aldrich, technical grade), triphenylphosphine oxide (Sigma-Aldrich, 98%), and tetrabutylammonium hexafluorophosphate ($[Bu_4N][PF_6]$, Sigma-Aldrich, > 99%) were used as received. Methanol (MeOH, EMD Millipore, OmniSolv) and methanol-d_4 (CD_3OD, Cambridge Isotope Laboratories, 99.8% D) were dried over activated 4Å sieves and then distilled. 1,8-dichloroanthraquinone (DCAQ, Sigma-Aldrich, 97%) was recrystallized from a 1:1 mixture of CH_3Cl and ethanol. 1,8-dichloro-9,10-dihydroxyanthracene (H_2DCAQ) was synthesized from DCAQ as previously described.[1]

All solvents were treated using a Pure Process Technology solvent purification system which degassed solvent with Argon and dried it over activated alumina, unless otherwise specified. Tetrahydrofuran (THF) was always inhibitor-free (Fisher, HPLC grade). Water was dispensed from a Synergy®-R Millipore system (ultrapure, 18.2 MΩ•cm) unless otherwise specified.

D.1.2 Instrumentation

Samples were stored in a N_2-filled MBRAUN glovebox workstation. All UV-Vis spectra were collected on an Agilent Cary 60 UV-Vis spectrophotometer connected to the glovebox by fiber optic cabling. Stopped flow measurements made at room temperature were taken on an Olis RSM-1000 single mixing stopped flow instrument.

Cyclic voltammograms were collected using a CH Instruments model 600 D potentiostat using a three-electrode set-up in a N_2 glovebox.

D.1.3 Nanoparticle Preparation and Characterization

The preparation and characterization of these nanoparticle batches was described in a previous report.[1]

D.1.4 UV-Vis Data Workup Procedure

Single wavelength kinetic traces were collected which monitored the decay of the picrylhydrazyl oxidant. Analysis of the traces was carried out by extrapolating the expected initial absorbance of all species in the cuvette (reduced OLE-Ce and the picrylhydrazyl) at time zero, as well as the expected final absorbance at reaction completion. These values were determined by accounting for absorbance from DPPH-H formed and from the OLE-Ce stock. Since OLE-Ce stocks should not have been oxidized or changed greatly in any way, it was assumed that the initial and final absorptivity of the colloid were the same. The extrapolated initial and final absorbances were then used to define reaction progress, where at time zero there is 0% reaction progress and at reaction completion it is 100%. Initial rates were analyzed from 5-15% whereas exponential fits were done using 0-100%.

D.2 Characterization of DPPH and DPPHL

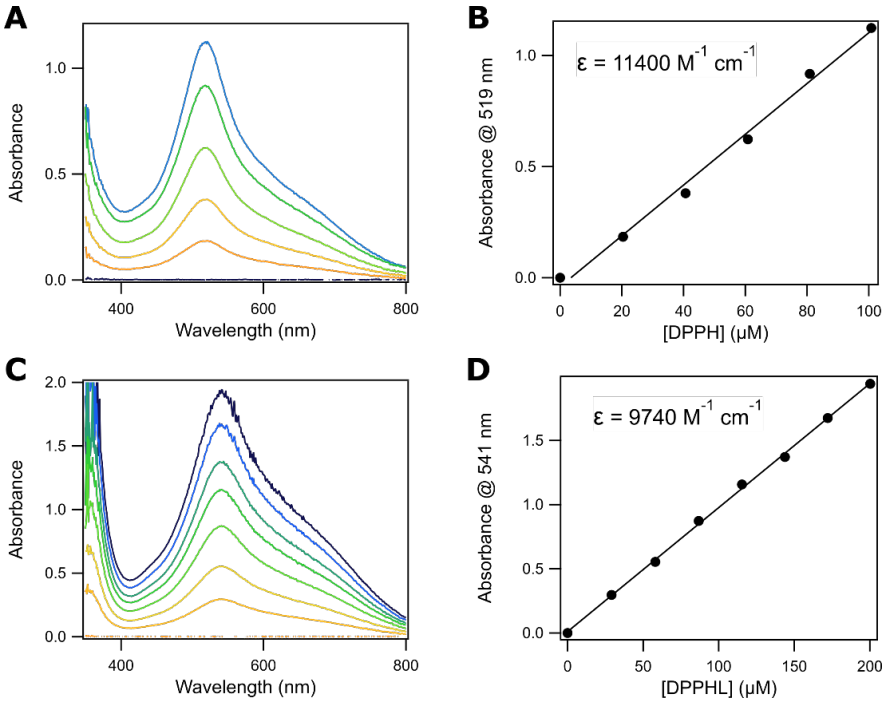

Figure D1. Panels (A) and (B) are for DPPH, while panels (C) and (D) are for DPPHL. Panels (A) and (C) show the full traces for DPPH and DPPHL, respectively, at varying concentrations. Panels (B) and (D) show absorbance at the λ_{max} which is 519 nm for DPPH and 541 nm for DPPHL. The textboxes denote the molar absorptivity (ε) at this wavelength.

A

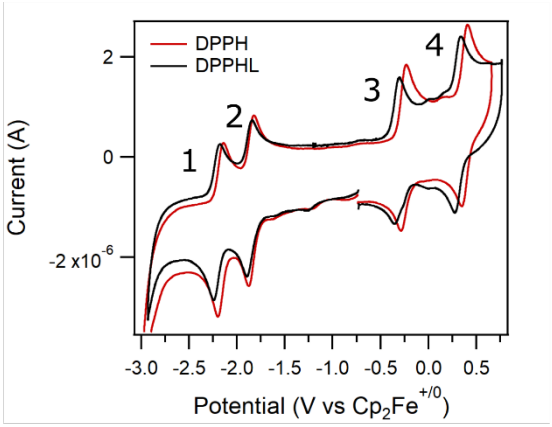

B

Wave	DPPH $E_{1/2}$	DPPHL $E_{1/2}$	$\Delta E_{1/2}$
1	-2.213	-2.171	0.042
2	-1.871	-1.852	0.019
3	-0.329	-0.261	0.068
4	0.305	0.379	0.075

Figure D2. (**A**) Cyclic voltammograms collected in THF containing 0.1 M $[Bu_4N][PF_6]$ under an inert N_2 atmosphere at 100 mV/s. The three-electrode setup included a glassy carbon working electrode, platinum counter electrode, and a Ag/Ag^+ jacketed pseudo-reference. After measurement, voltammograms were referenced to the potential of $Cp_2Fe^{+/0}$ measured in the same solution. (**B**) Table with $E_{1/2}$ data for each labeled faradaic feature. $\Delta E_{1/2} = E_{1/2}(\text{DPPHL}) - E_{1/2}(\text{DPPH})$.

D.3 Figures

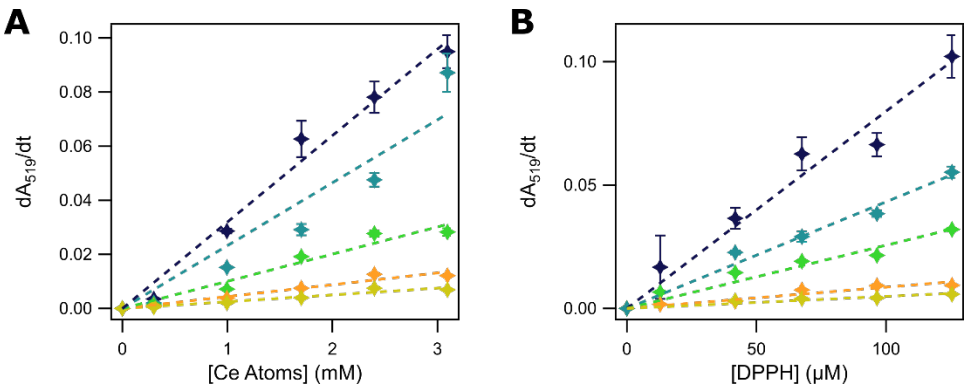

Figure D3. Initial rates kinetic dependences analyzed by linearizing the reaction over the segment from 0-10% of total reaction progress. (A) Dependence of DPPH decay on [Ce atoms] at varying $\%Ce^{3+}$ for **Ce-1**. [DPPH] = 68 μM for all samples. (B) Dependence of DPPH decay on [DPPH] at varying $\%Ce^{3+}$ for **Ce-1**. [Ce atoms] = 1.7 mM for all samples. For (A) and (B) dashed lines are linear fits with the y-intercept set as zero.

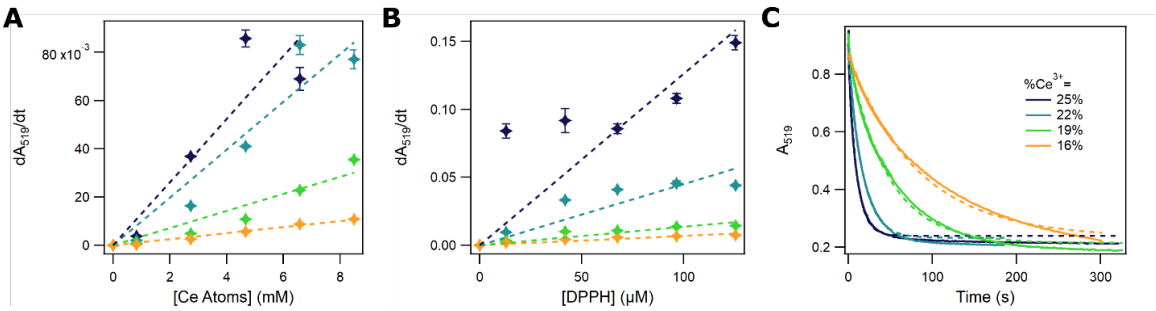

Figure D4. (A) Initial rates kinetic dependence of DPPH decay on [Ce atoms] at varying $\%Ce^{3+}$ for **Ce-L**. [DPPH] = 68 μM for all samples. (B) Initial rates kinetic dependence of DPPH decay on [DPPH] at varying $\%Ce^{3+}$ for **Ce-L**. [Ce atoms] = 4.7 mM for all samples. For (A) and (B) dashed lines are linear fits with the y-intercept set as zero. (C) Full single wavelength kinetic traces of DPPH decay at varying $\%Ce^{3+}$ for **Ce-L** where [Ce atoms] = 8.5 mM and [DPPH] = 68 μM for all samples. Dashed lines are single exponential fits.

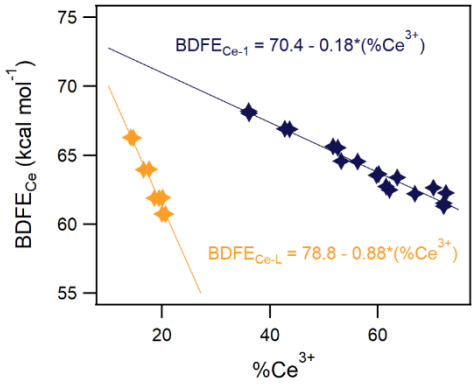

Figure D5. All data shown was collected in a previous report.[1] Here the data for **Ce-1** (blue) and **Ce-L** (orange) are limited to the relevant region of $\%Ce^{3+}$ for the reactivity studies in this work and lines are linear fits.

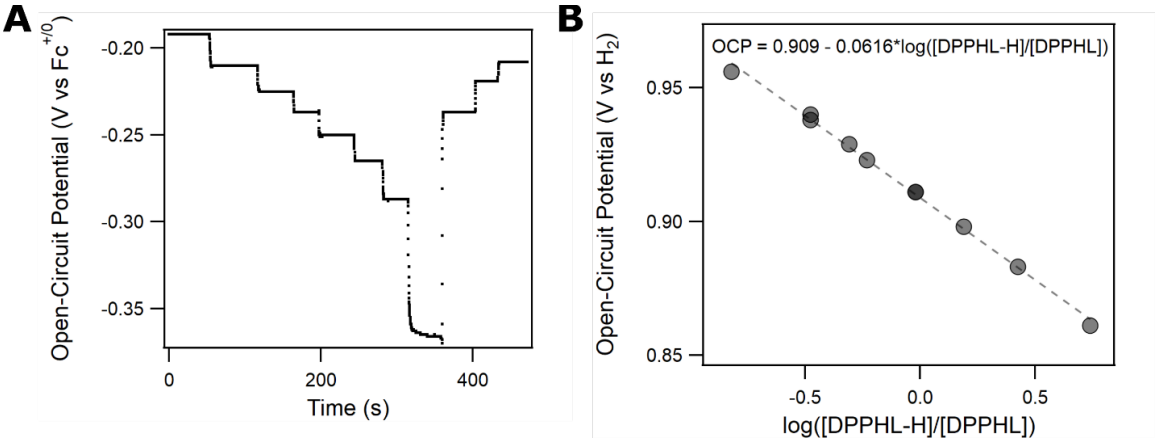

Figure D6. Open-circuit potential (OCP) measurements of the potential of the DPPHL/DPPHL-H 1e^-/1H^+ redox couple in THF. (A) Single OCP measurement of DPPHL titration with H_2DCAQ to stoichiometrically form DPPHL-H *in situ*. This titration systematically alters the [DPPHL-H]/[DPPHL] ratio. The ratio is also altered in opposite direction through the addition of DPPHL. (B) Plot of the OCP average for each plateau associated with a specific [DPPHL-H]/[DPPHL] ratio. Figure is plotted vs log([DPPHL-H]/[DPPHL]) since the Nernst equation predicts a 0.0592 V/decade dependence. The y-intercept of the linear fit (dashed line) is the potential of hydrogenation or *E*°(V vs H_2).

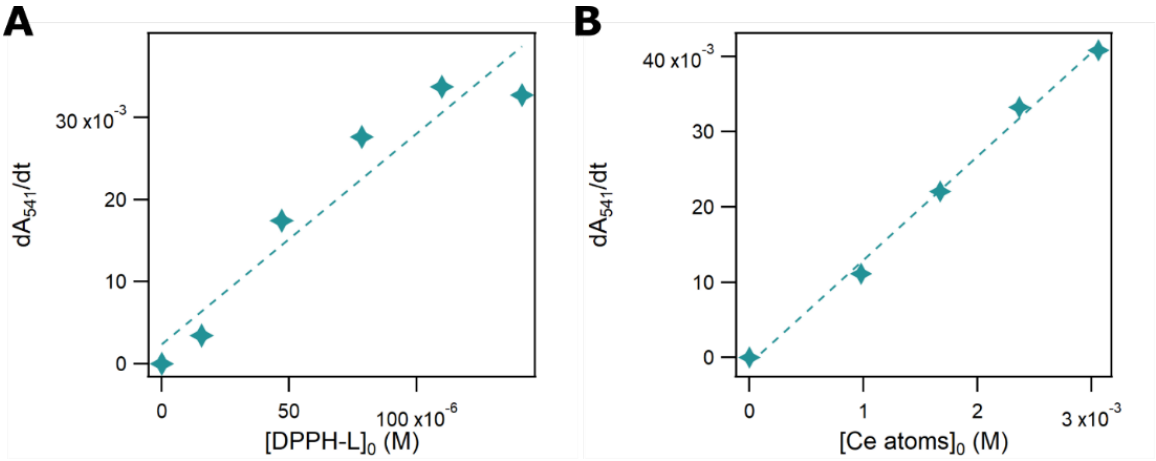

Figure D7. (A) Initial rates kinetic dependence of DPPHL decay on [Ce atoms] at %Ce^{3+} = 73.5% for **Ce-1**. [DPPHL] = 79 μM for all samples. (B) Initial rates kinetic dependence of DPPH decay on [DPPH] at %Ce^{3+} = 73.5% for **Ce-1**. [Ce atoms] = 1.7 mM for all samples. For (A) and (B) dashed lines are linear fits.

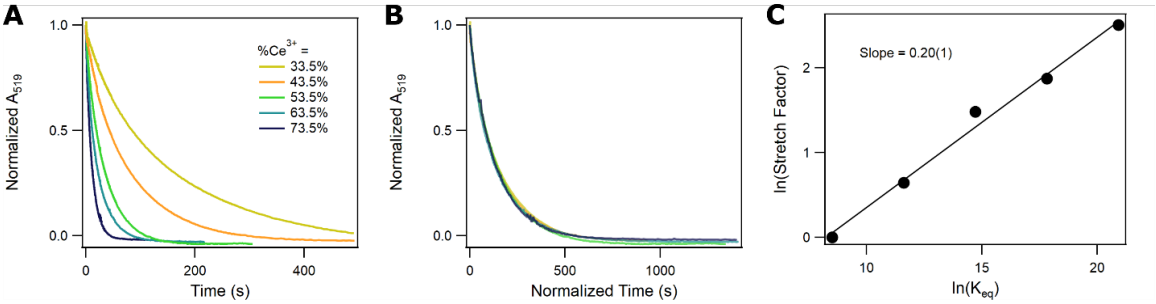

Figure D8. (A) Full normalized kinetic traces at 519 nm for reactions with initial concentrations of [DPPH] = 68 μM and [Ce atoms] = 3.1 mM. Different traces are for varying %Ce^{3+} of the **Ce-1** stock. (B) Traces are plotted versus "normalized time" meaning that every actual time value was multiplied by a constant, here denoted as the 'Stretch Factor' in order to get the traces to overlay. (C) Plot of ln(Stretch Factor) vs ln(K_{eq}).

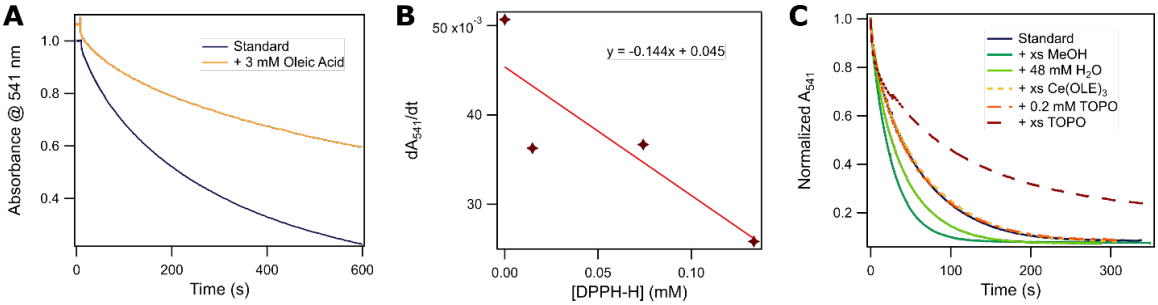

Figure D9. (A) Full kinetic traces for the decay of DPPHL in the presence and absence of 3 mM oleic acid. [Ce atoms] = 1.7 mM, [DPPHL] = 79 μM, and %Ce^{3+} of **Ce-1** stock is 53.5%. (B) Dependence of reaction rate for DPPH decay on [DPPH-H]. Reactions contain [Ce atoms] = 1.7 mM, [DPPH] = 68 μM, and %Ce^{3+} of **Ce-1** stock is 73.5%. (C) Full kinetic traces for the decay of DPPHL in the presence and absence of various additives. Only a single additive is present in each run, in addition to the contents of the "standard" sample which contained [Ce atoms] = 1.7 mM, [DPPHL] = 79 μM, and %Ce^{3+} of **Ce-1** stock is 73.5%.

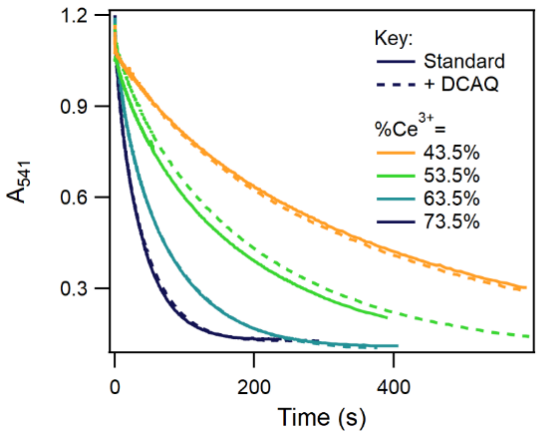

Figure D10. Initial concentrations for all samples were [Ce atoms] = 3.1 mM and [DPPHL] = 79 μM. Dashed traces of the same color as the solid trace are the same sample, but with 1,8-dichloroanthraquinone (DCAQ) added to the **Ce-1** stock such that [DCAQ] was raise by more than 5 mM. [DCAQ] in samples denoted by solid traces varied between 16 – 78 μM with more reduced stocks containing more DCAQ.

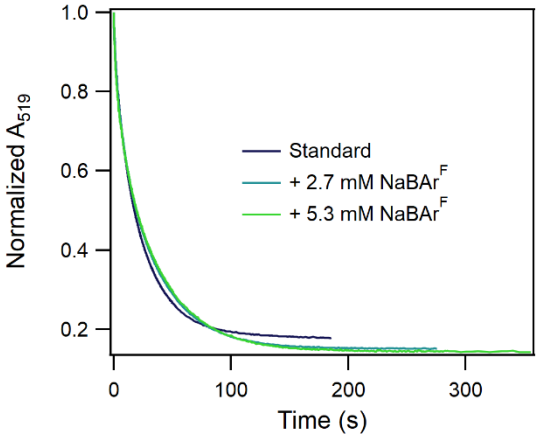

Figure D11. Traces are normalized to their initial absorbance. Standard sample contains [Ce atoms] = 4.7 mM, [DPPH] = 68 μM, and %Ce^{3+} of **Ce-L** stock is 25%. Other samples were prepared in the same way, but with varying concentrations of sodium tetrakis[3,5-bis(trifluoromethyl)phenyl]borate ($NaBAr^F$).

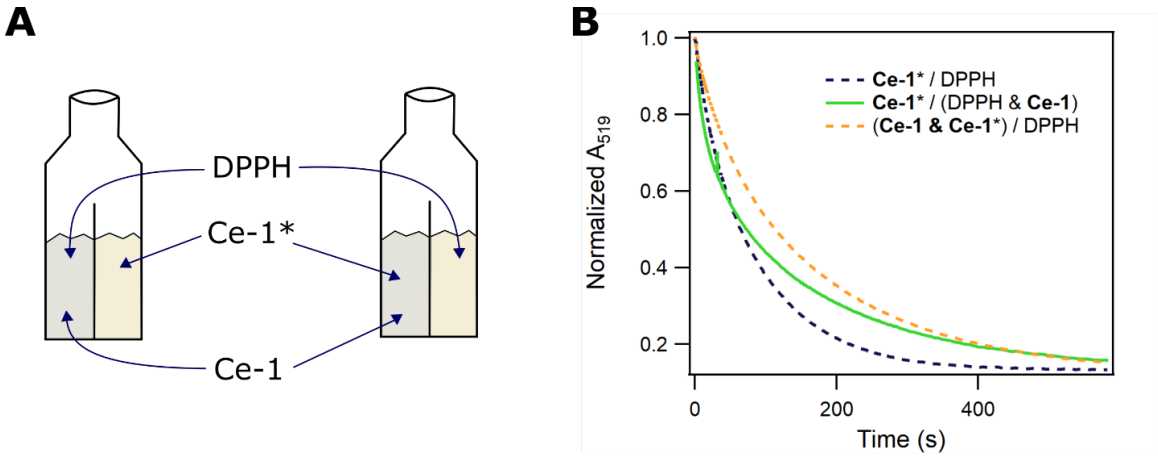

Figure D12. (**A**) Schematic of which stock solutions were added to which sides of the two tandem-mixing cell cuvettes used in the study. The left cell is denoted **Ce-1***/(DPPH & **Ce-1**) while the right is denoted (**Ce-1** & **Ce-1***)/DPPH to acknowledge which stock solutions are on each side. The concentration of (**B**) Kinetic traces for decay of DPPH absorbance in three samples. Sample **Ce-1***/DPPH contained [Ce atoms] = 0.93 mM, [DPPH] = 74 μM, and was reduced with H_2DCAQ such that the concentration of hydrogen atom equivalents was 0.37 mM. Sample **Ce-1***/(DPPH & **Ce-1**) contained [Ce atoms] = 1.8 mM, [DPPH] = 74 μM, and the concentration of added hydrogen atom equivalents was 0.37 mM. (**Ce-1** & **Ce-1***)/DPPH contained [Ce atoms] = 1.8 mM, [DPPH] = 74 μM, and the concentration of added hydrogen atom equivalents was 0.37 mM. Reactions were initiated through flipping the tandem mixing cells in the case of the cells described in (**A**), whereas for **Ce-1***/DPPH the reaction was initiated through the addition of the **Ce-1*** stock solution.

D.4 References

1. Agarwal, R. G.; Kim, H.-J.; Mayer, J. M., Nanoparticle O–H Bond Dissociation Free Energies from Equilibrium Measurements of Cerium Oxide Colloids. *J. Am. Chem. Soc.* **2021,** *143* (7), 2896-2907.